CAPITAL UNIVERSITY OF SCIENCE AND TECHNOLOGY, ISLAMABAD


# Design of a Rectangular Latent Heat Thermal Energy Storage Device

by

Muhammad Shahid Shafiq

A thesis submitted in partial fulfillment for the degree of Doctor of Philosophy

in the

Faculty of Engineering
Department of Mechanical Engineering

2023

# Design of a Rectangular Latent Heat Thermal Energy Storage Device

**By**

**Muhammad Shahid Shafiq**

**(DME153001)**

**Dr. Abhishek Dutta, Associate Professor**

**İzmir Institute of Technology, Türkiye**

**(Foreign Evaluator 1)**

**Dr. Jiang Yuting, Associate Professor**

**Harbin Engineering University, China**

**(Foreign Evaluator 2)**

**Dr. Muhammad Mahabat Khan**

**(Thesis Supervisor)**

**Dr. Muhammad Mahabat Khan**

**(Head, Department of Mechanical Engineering)**

**Dr. Imtiaz Ahmad Taj**

**(Dean, Faculty of Engineering)**

**DEPARTMENT OF MECHANICAL ENGINEERING**

**CAPITAL UNIVERSITY OF SCIENCE AND TECHNOLOGY**

**ISLAMABAD**

**2023**

*The Most Compassionate, taught the Quran, created humanity, taught them speech. The sun and the moon travel with precision. The stars and the trees bow down in submission. As for the sky, He raised it high, and set the balance of justice so that you may not transgress in the balance. Weigh with justice, and do not give short measure.*

*(Al-Quran, 55:1-9)*

# CAPITAL UNIVERSITY OF SCIENCE & TECHNOLOGY ISLAMABAD

Expressway, Kahuta Road, Zone-V, Islamabad
Phone:+92-51-111-555-666 Fax: +92-51-4486705
Email: info@cust.edu.pk Website: https://www.cust.edu.pk


## CERTIFICATE OF APPROVAL

This is to certify that the research work presented in the thesis, entitled "**Design of a Rectangular Latent Heat Thermal Energy Storage Device**" was conducted under the supervision of **Dr. Muhammad Mahabat Khan**. No part of this thesis has been submitted anywhere else for any other degree. This thesis is submitted to the **Department of Mechanical Engineering, Capital University of Science and Technology** in partial fulfillment of the requirements for the degree of Doctor in Philosophy in the field of **Mechanical Engineering**. The open defence of the thesis was conducted on **May 18, 2023**.

**Student Name :** Muhammad Shahid Shafiq
(DME153001)

---

The Examining Committee unanimously agrees to award PhD degree in the mentioned field.

**Examination Committee :**

(a) External Examiner 1: Dr. Muhammad Shehryar Manzoor
Professor
National Skills University, Islamabad

(b) External Examiner 2: Dr. Muzaffar Ali
Professor
UET Taxila, Taxila

(c) Internal Examiner : Dr. Mohammad Javed Hyder
Professor
CUST, Islamabad

**Supervisor Name :** Dr. Muhammad Mahabat Khan
Associate Professor
CUST, Islamabad

**Name of HoD :** Dr. Muhammad Mahabat Khan
Associate Professor
CUST, Islamabad

**Name of Dean :** Dr. Imtiaz Ahmed Taj
Professor
CUST, Islamabad

# AUTHOR'S DECLARATION

I, **Muhammad Shahid Shafiq (Registration No. DME153001)**, hereby state that my PhD thesis entitled, '**Design of a Rectangular Latent Heat Thermal Energy Storage Device**' is my own work and has not been submitted previously by me for taking any degree from Capital University of Science and Technology, Islamabad or anywhere else in the country/ world.

At any time, if my statement is found to be incorrect even after my graduation, the University has the right to withdraw my PhD Degree.

**(Muhammad Shahid Shafiq)**

Dated: 18 May, 2023

Registration No : DME153001

# PLAGIARISM UNDERTAKING

I solemnly declare that research work presented in the thesis titled "**Design of a Rectangular Latent Heat Thermal Energy Storage Device**" is solely my research work with no significant contribution from any other person. Small contribution/ help wherever taken has been duly acknowledged and that complete thesis has been written by me.

I understand the zero-tolerance policy of the HEC and Capital University of Science and Technology towards plagiarism. Therefore, I as an author of the above titled thesis declare that no portion of my thesis has been plagiarized and any material used as reference is properly referred/ cited.

I undertake that if I am found guilty of any formal plagiarism in the above titled thesis even after award of PhD Degree, the University reserves the right to withdraw/ revoke my PhD degree and that HEC and the University have the right to publish my name on the HEC/ University Website on which names of students are placed who submitted plagiarized thesis.

**(Muhammad Shahid Shafiq)**

Dated: 18 May, 2023

Registration No : DME153001

# *Plagiarism Undertaking*

I solemnly declare that research work presented in this thesis titled "**Design of PCM based Latent Heat Thermal Energy Storage Device**" is solely my research work with no significant contribution from any other person. Small contribution/help wherever taken has been duly acknowledged and that complete thesis has been written by me.

I understand the zero tolerance policy of the HEC and Capital University of Science and Technology towards plagiarism. Therefore, I as an author of the above titled thesis declare that no portion of my thesis has been plagiarized and any material used as reference is properly referred/cited.

I undertake that if I am found guilty of any formal plagiarism in the above titled thesis even after award of PhD degree, the University reserves the right to withdraw/revoke my PhD degree and that HEC and the University have the right to publish my name on the HEC/University website on which names of students are placed who submitted plagiarized work.

**(Muhammad Shahid Shafiq)**
Registration No: DME153001

# *List of Publications*

It is certified that following publication(s) have been made out of the research work that has been carried out for this thesis:-

1. **M. S. Shafiq**, M. M. Khan, and M. Irfan, "Performance enhancement of double-wall-heated rectangular latent thermal energy storage unit through effective design of fins," *Case Studies in Thermal Engineering*, vol. 27, no. May, p. 101339, 2021, doi: 10.1016/j.csite.2021.101339.

2. **M. S. Shafiq** and M. M. Khan, "Effects of fin length distribution functions and enclosure aspect ratio on latent thermal energy storage performance of dual-wall-heated unit," J. Energy Storage, vol. 53, 2022, doi: 10.1016/j.est.2022.105247.

**(Muhammad Shahid Shafiq)**
Registration No: DME153001

# *Acknowledgement*

First of all, I praise Allah, the Almighty for providing me with the opportunity and capability to carry out this research. Special thanks to my parents and family for their full support. I am also grateful to my supervisor Prof. Dr. Muhammad Mahabat Khan for his continuous guidance and valuable advice that helped a lot during my research.

The experimental work that was conducted during this research could not have been possible with the support from workshop officer Muhammad Raza and his team including lab technician Sheraz Kiani, staff Qaiser Mehmood and Zafar iqbal.

I would also like to thank Dr. Sultan Satti for providing necessary assistance to carry out Differential Scanning Calorimetry (DSC) for the measurement of thermal properties of Phase Change Material (PCM) Last but not least a special thanks to my boss Mr. Basit Hamid for supporting and accommodating my studies with the job.

**(Muhammad Shahid Shafiq)**

# *Abstract*

This study focuses on the design of a rectangular finned dual-wall heated Latent Heat Thermal Energy Storage (LHTES) unit. The objective is to develop a systematic approach and investigate the effects on the thermal performance of the system by varying fin lengths, fin displacement, fin thickness, and container geometry aspect ratio. Initially a reference experimental setup was manufactured and used as the basis of numerical validation. In this study stearic acid was used as Phase Change Material (PCM). For numerical investigation a 2D design was quantitatively examined by parametric variations in the LHTES device's design. Firstly, the design parameter variations of fins included angles (A), shapes (S), lengths (L) while maintaining constant PCM volume. The base case was modeled by six horizontal fins, three on each of the heated walls. Configuration-A, with fin angle-variations, significantly increased the melting time of PCM by 16% and reduced the averaged energy storage rate by 14.2%. The hybrid fin configuration-S, a combination of straight and angled type fins, showed appreciable improvement in thermal performance of LHTES device. The increase in melting rate was found to be 18% and average energy storage rate enhanced by 19.8%. The configuration-L, encompassing combinations of straight fins with different lengths and thicknesses while keeping constant PCM volume, was found to be most effective of all. The optimum case of configuration-L enhanced the melting performance of the LHTES by 39.5% and the average energy storage rate by 65.07%. The configuration-L was further improved by 12 horizontal fins, 6 on each of the isothermally heated walls. The fin lengths were arranged by employing linear, quadratic, cubic, and exponential distribution functions with decreasing slopes along the heated walls. Later on LHTES performance impacts of geometry aspect ratios of enclosure were investigated. Enthalpy-porosity model was employed for simulations and numerical results were validated against experimental results. Compared to the reference case, linear and quadratic fin configurations improved the PCM melting times by 31.7% and 24.3%, respectively. The corresponding average energy storage rates were enhanced by 46% and 31.4%, respectively. The corresponding average energy storage rates were enhanced by 46% and 31.4%, respectively. The exponential fin

configuration produced strong convection effects in PCM and improved the melting time and energy storage rates by 35.2% and 52.69%, respectively. Statistical and machine learning methods are used to identify the optimal configuration. In order to find optimal parameters that improve the thermal performance of the energy storage device, the design parameters for a thermal energy storage device were examined numerically. The design variables selected at the end of the studies were used to evaluate optimal values using Taguchi Method and later improved the prediction model by applying machine learning techniques. Exponential Gaussian Process Regression is found to predict the performance of LHTES device designed based on the base configuration and defined parameters.

**Keywords:** Latent Heat Storage, Phase-change Materials, Fin Geometry, Fin Arrangement, Thermal Energy Storage, Machine learning, LHTES Design

# Contents

# List of Figures

# List of Tables

# Glossary

**BTM** Battery Thermal Management. 30

**BTOE** Billion Tonnes of Oil Equivalent. xvi, 4

**CAD** Computer Aided Design. 54

**CFD** Computational Fluid Dynamics. 53

**DAQ** Data Acquisition. 56, 57, 60

**DSC** Differential Scanning Calorimetry. ix, 59

**GHG** Green House Gases. 8

**HTF** Heat Transfer Fluid. 19, 30, 41, 43, 44, 96

**LHTES** Latent Heat Thermal Energy Storage. x, xi, xvi, xvii, xx, 12– 18, 29, 31, 32, 35, 36, 39, 41– 45, 47, 49, 51, 52, 54, 56, 58, 59, 63, 64, 67, 83, 85– 88, 90, 91, 96, 97, 99, 100, 104– 106, 108, 109, 116, 117, 126– 132, 134, 136– 139, 148, 157, 175– 182, 207

**MF** Metal Foam. 33

**NEPCM** Nano Enhanced Phase Change Material. 38

**NZE** Net Zero Emissions. 9, 10

**PCM** Phase Change Material. ix, x, xiii, xvi, xvii, xix, xx, 2, 12– 16, 18– 50, 52– 61, 84, 86– 88, 90– 92, 95, 96, 98– 102, 105– 110, 116, 117, 120– 125, 127, 129, 132, 134, 136– 138, 148, 154– 160, 165, 167, 175, 177– 182, 207

**PEG** Polyethylene Glycol. 24

**PV** Photovoltaic. 38

**SHTES** Sensible Heat Thermal Energy Storage. 12

**SNR** Signal to noise ratio. 143

**TCTES** Thermochemical Thermal Energy Storage. 12

**TES** Thermal Energy Storage. xvi, 12, 13, 18, 19, 24, 27, 38

**TTX** Triplex Tube Heat Exchanger. xvi, 29, 30, 42, 44

# Nomenclature

| | |
|---|---|
| $\dot{Q}$ | heat transfer rate $(W)$ |
| $\overline{h}$ | Heat transfer coefficient $(W/m^2.K)$ |
| $\overline{Nu}$ | Nusselt number |
| $\zeta_i$ | $i^{th}$ input parameter in ML model |
| $A_r$ | Enclosure aspect ratio |
| $A_w$ | Effective heat transfer area $(m^2)$ |
| $c_{pl}$ | Specific heat capacity of liquid $(J/kg.K)$ |
| $c_{ps}$ | Specific heat capacity of solid $(J/kg.K)$ |
| $d_0$ | Distance between bottom fin and bottom wall $(mm)$ |
| $D_r$ | Depth of enclosure $(mm)$ |
| $E_{er}$ | Energy enhancment ratio |
| $E_{mr}$ | Melting enhancment ratio |
| $f_d$ | Distance between fins $(mm)$ |
| $f_l$ | Length of fin $(mm)$ |
| $f_n$ | Fin number $n$ |
| $f_t$ | Thickness of fin $(mm)$ |
| $H$ | Characteristic length $(m)$ |

$h$ Specific enthalpy of PCM $(J/kg)$

$H_r$ Height of enclosure $(mm)$

$h_sl$ Enthalpy of formation $(J/kg)$

$h_{sf}$ Latent heat capacity $(J/kg)$

$J$ Cost function of ML model

$k$ Thermal conductivity $(W/m.K)$

$NP_b$ Number of black pixels

$NP_f$ Number of pixels covered by fins

$NP_t$ Total number of pixels

$NP_w$ Number of white pixels

$NP_{pcm}$ Total number of PCM pixels

$p$ Pressure $(Pa)$

$Q_{total}$ Total stored energy $(J)$

$r_0$ Constant = 0.1, such that $d_0/H = r_0$

$Ra$ Rayleigh number

$Ste$ Stefan number

$T$ Temperature $(K)$

$T_e$ Final PCM temperature at the end of melting process $(K)$

$T_i$ Initial PCM temperature $(K)$

$T_l$ Liquidus temperature $(K)$

$T_m$ Melting PCM temperature $(K)$

$t_m$ Total melting time $(s)$

| | |
|---|---|
| $T_s$ | Solidus temperature $(K)$ |
| $T_w$ | Wall temperature $(K)$ |
| $ts_k$ | Melting time-saving ratio |
| $u$ | Velocity in x-direction $(m/s)$ |
| $v$ | Velocity in y-direction $(m/s)$ |
| $V_{pcm_l}$ | PCM solid volume per unit depth $(mm^3)$ |
| $V_{pcm_s}$ | PCM liquid volume per unit depth $(mm^3)$ |
| $V_{pcm}$ | PCM volume per unit depth $(mm^3/mm)$ |
| $W_r$ | Width of enclosure $(mm)$ |
| $\alpha$ | Thermal diffusivity $(m^2/s)$ |
| $\beta$ | Thermal expansion coefficient $(1/K)$ |
| $\gamma$ | Liquid fraction |
| $\gamma(t)$ | Liquid fraction at time t |
| $\gamma_k$ | Liquid fraction of case k |
| $\mu$ | Dynamic viscosity $(Pa.s)$ |
| $\mu$ | Dynamic viscosity of PCM $(Pa.s)$ |
| $\nu$ | Kinematic viscosity $(m^2/s)$ |
| $\omega_i$ | Weights of ML regreession model |
| $\rho$ | Density of PCM $(kg/m^3)$ |
| $\rho_l$ | Density of liquid phase $(kg/m^3)$ |
| $\rho_s$ | Density of solid phase $(kg/m^3)$ |
| $\tau_k$ | Melting time of case k $(s)$ |
| $\zeta_k$ | Energy of case k $(J/kg)$ |

# Chapter 1

# Introduction

## 1.1 Background

Industrial growth has happened exponentially over the past couple of decades impacting the global energy consumption. In the past decade it increased by 18% [1]. Fossil fuel is being consumed rapidly resulting in the shortage of fossil fuel [2] and a need to investigate alternative energy sources exists. As energy utilization increases, there is also a demand to determine ways to improve energy efficiency.

Fossil fuels make up the majority of the world's energy production, making them one of the main contributors to greenhouse gas emissions and global warming [3]. Therefore, a switch to renewable resources is necessary because of the dwindling fossil fuel reserves, rising annual energy consumption, and escalating environmental issues [4].

A major concern for energy savings in any field with high thermal demands is the conservation and management of thermal energy. One of these industries is the building sector, which today makes about 30% of the energy consumed in world [5, 6]. In many construction technologies, the existence of thermal energy storage indicates a more effective and lucrative operation. Among these technologies are thermal solar systems, domestic co-generation, etc., which typically include traditional hot water tanks to connect the supply and demand. These tanks can be

difficult to use in domestic settings, where there is generally a lack of space, due to the enormous water volumes and high aspect ratios they demand.

In the context of renewable energy, Phase Change Materials (PCMs) can be used to store excess energy generated from renewable sources, such as solar or wind power, for later use when the energy demand is higher or when the renewable source is not available. This helps to address the intermittent nature of some renewable energy technologies.

Figure 1.1 illustrates one potential application of PCMs in solar heating systems. During periods of abundant sunlight, solar energy is captured and used to heat the PCM, causing it to melt and store the thermal energy. Later, when solar radiation is insufficient or during periods of high energy demand, the PCM releases the stored energy by solidifying, thereby providing a continuous and stable heat supply. The energy is stored in PCM during latent thermal energy exchange that occurs during melting and/or solidification, enabling a higher thermal storage density [7].

## 1.2 Sources of Energy

There are many different types of energy sources that act as the driving factors for economic and societal growth as a whole. These energy sources can be classified into two major categories, renewable and non-renewable energy sources [9–11]. The total energy consumption of the world in 2021 was $165,320, TWh$ [12]. Fossil fuels accounted for 82% of primary energy [13].

### 1.2.1 Non-Renewable Energy Sources

These energy sources are finite, or scarce natural resources and usually take a long time to form or replenish [14]. Oil, coal, natural gas, and nuclear power are the principal non-renewable resources that are frequently used to generate energy [9, 14].

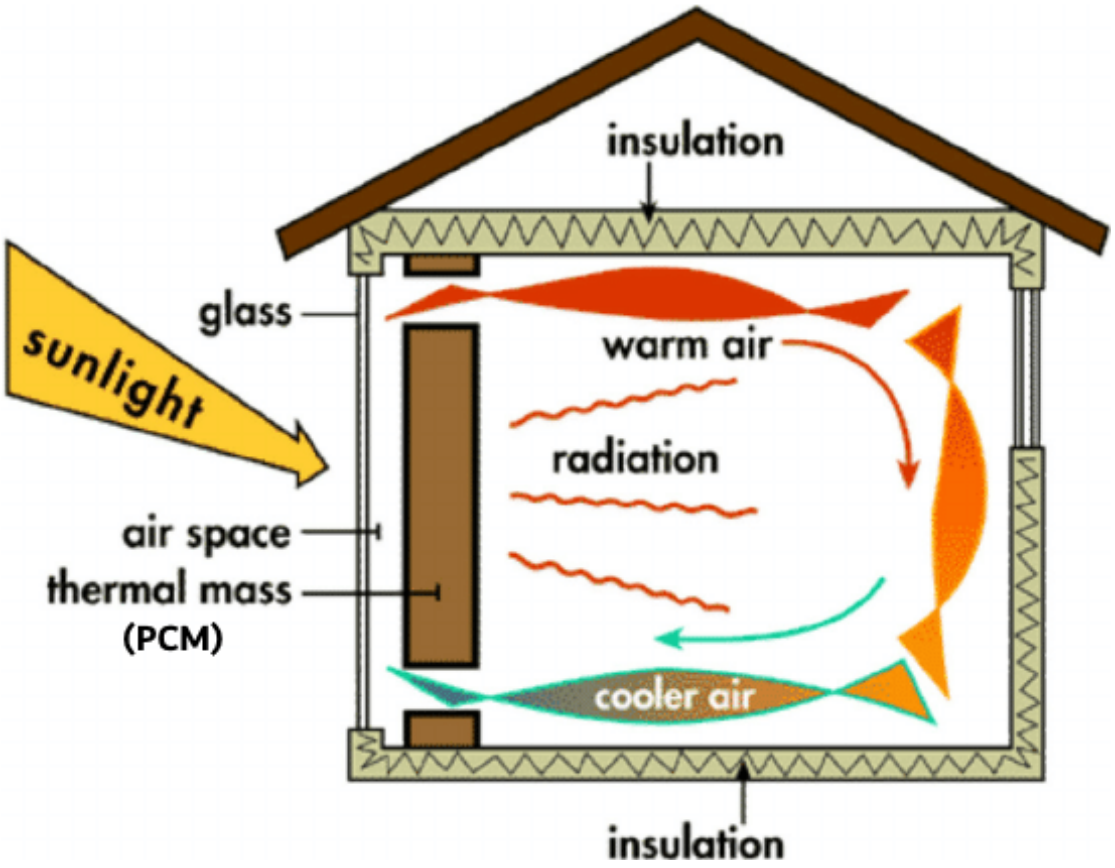


FIGURE 1.1: Passive solar heating using Phase Change Materials (PCMs) [8].

1. **Crude Oil:** The main components of crude oil, which is a naturally occurring highly hazardous combustible liquid, are hydrocarbons. The partial breakdown of living creatures that takes place in the rock strata of some geological formations results in oil. In 2021, the total world energy consumption based on oil was $51,170, TWh$ (31%) [12].

2. **Coal:** The sedimentary rock known as coal is combustible and is composed of fossilized plant material. Coal beds are layers or veins of amorphous carbon that are typically found in rock strata and contain a variety of organic and some inorganic substances. Coal is another very hazardous substance that is harmful to the environment. Coal is currently the main energy source for power plants, also known as coal-fired power plants. Total consumption of coal based world energy in 2021 was $44,473\,TWh$ (26.9%) in the world [12].

3. **Natural Gas:** Petroleum resources often contain methane-rich natural gas, which is another flammable mixture of hydrocarbon gases. It can be found

in coal beds as well as with other fossil fuels. It is produced by the decomposition of methanogenic organisms in bogs, landfills, and marshes. Higher temperatures are likely to provide more natural gas, while lower temperatures are likely to yield more petroleum. Natural gas is the least destructive of all fossil fuels, but it is still detrimental and getting access to it is become more and more difficult as easily accessible supplies are exhausted, as is the case with all other fossil fuels. The consumption of the third major fossil fuel source in 2021 was $40,375\,TWh$ (24.4%) in the world [12].

4. **Nuclear Power:** Nuclear fission, also known as controlled atom splitting, generates nuclear energy. Nuclear fission chain reactions are typically used in nuclear power plants to heat water, which then produces steam, which in turn generates electricity. One of the few elements that may easily fission is uranium, more especially uranium-235. Some people might consider this to be renewable, but it is not. Additionally, it is risky because the radioactive materials utilized and the radioactive waste they produce are exceedingly toxic for both people and the environment. $7,031\,TWh$ (4.3%) of the world energy demand was fulfilled by the nuclear power in 2021 [12]. In 2021 nuclear power generation increased by 4.2% [13].

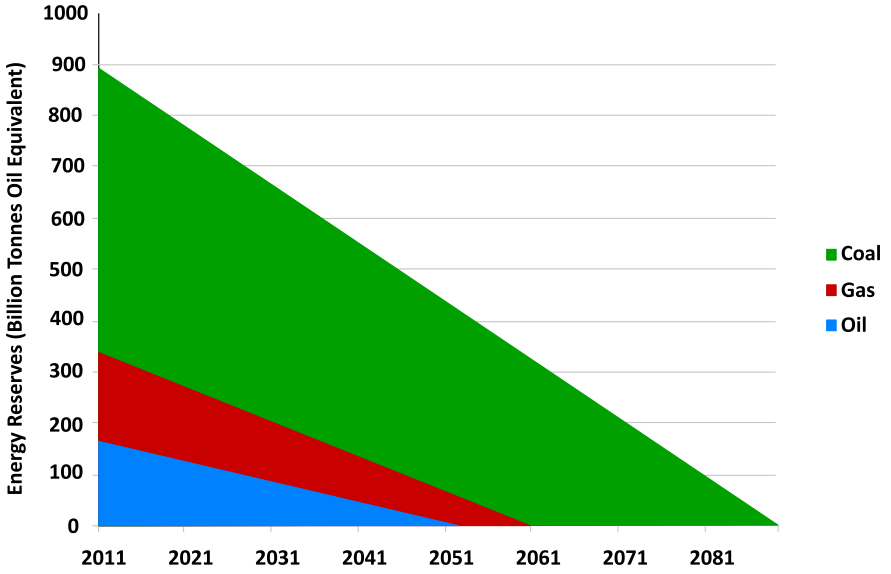


FIGURE 1.2: Energy reserves in Billion Tonnes of Oil Equivalent (BTOE) [15, 16]

Although these sources seem to be abundant, the supplies will diminish as we consume them. There will be a time, measured in decades, when these will run out as can bee seen in Figure 1.2. Shafiee and Topal [17] estimated that the world would run out of coal, oil, and gas in 107, 35, and 37 years, respectively. According to that forecast, coal would be the only fossil fuel available after 2042 until 2117. A 2019 report from Stanford University's Millennium Alliance for Humanity and the Biosphere presents a similar picture. The MAHB estimates that the world's coal reserves will run out by 2090, natural gas reserves by 2060, and oil reserves by 2052 [16].

### 1.2.2 Renewable Energy Sources

Renewable energy comes from natural sources that replace themselves more quickly than they are used up. Examples of such sources that are continuously replenished are the sun and the wind. There are many different types of renewable energy available to us[18]. Renewable primary energy increased by around 5.1 $EJ$ in 2021 – corresponding to an annual growth rate of 15%, stronger than the previous year's 9%, and higher than that of any other fuel in 2021 [13]. Usually naturally occurring phenomenon like solar, geothermal, wind, or ocean waves are involved in the derivation of energy. These energy sources are sustainable, eco-friendly, and will not pollute our planet. Solar, wind, water, geothermal, radiation, and biomass are the main renewable energy sources [11].

1. **Solar:** Humans have been using solar energy since the dawn of civilization. The three forms of solar energy are active, passive, and solar radiation. The fastest-growing power generating technology in the world at the moment is solar energy using photovoltaic or solar cells. In 2021, the total world energy consumption using solar technology was $2,702\,TWh$ (1.6%) [12].

2. **Wind:** Wind energy generates electricity by harnessing the wind's force to turn a generator. On land, wind turbines must be located in regions with strong winds, such as hilltops, wide-open spaces, and plains. Offshore

wind power has grown steadily over the years, with wind farms offering an excellent way to generate energy while avoiding many of the concerns about them being noisy or obtrusive on land. Of course, because of the hostile surroundings the turbines must operate in, offshore utilization has its own disadvantages [19]. Although wind energy is environmentally friendly and rising at a pace of 30% year, it is not always present in sufficient amounts everywhere. The total share of world energy consumption in 2021, based on wind was $4,872\,TWh$ (2.9%) [12].

3. **Hydroelectric Dams** Dams use hydro-power to generate electricity. Large turbines are turned by the force of moving water to produce energy, which is known as hydro-power. However, large hydroelectric dams of the modern era have an adverse effect on the environment because they cause the loss of natural habitat, alter the downstream riverbed, interfere with fish spawning, and even result in the extinction of fish and other species. In addition, they sometimes force people to abandon their farms, homes, and even entire cities and villages. The hydral energy source amounted to $11,183\,TWh$ (6.8%) of the total world energy consumption in 2021 [12].

4. **Tidal Hydro-power:** In this form of renewable energy, the water is released through a turbine that generates electricity in a manner akin to that of a hydroelectric dam as the tide recedes, filling the reservoir as the tide rises. With regard to this renewable energy, there are no current substantial environmental hazards [20, 21].

5. **Wave Hydro-power:** Wave power is the process of capturing energy from the motion of waves at the surface or from pressure changes induced by waves below the surface. This technique, which is comparable to wind energy, is also promising. Wave power is different from tidal power, which harnesses the energy of the current created by the Sun and Moon's gravitational attraction. Breaking waves, wind, the Coriolis effect, cabling, and variations in temperature and salinity are a few more forces that can cause currents.

After many trial projects, wave power is still not widely used for commercial applications as of 2022 [21–23].

6. **Geothermal:** Geothermal energy is produced by tapping into heat that is trapped beneath the earth's crust. This form of energy is typically affordable, dependable, largely sustainable, and generally eco-friendly. We can use highly heated water brought to the surface by drilling wells as a hydro thermal resource to run turbines and generate power. Pumping the steam and hot water back into the earth can reduce emissions, making this renewable resource greener [19, 21].

7. **Radiant Energy:** Solar radiation is a broad word for the electromagnetic radiation that the sun emits. It is also sometimes referred to as the solar resource or just sunshine. A multitude of devices can be used to collect solar radiation and transform it into useful forms of energy, such as heat and electricity. However, the technological viability and cost-effectiveness of these systems at a particular area depends on the solar resource available [24].

8. **BioMass:** The term "biomass" refers to biological material derived from recently extinct or alive species, including trees, landfill gases, and alcohol fuels produced from crops like corn. Two typical instances of biomass energy generation include the burning of grease or the use of ethanol made from corn to power a car. Contribution of biomass energy source was $12,177\,TWh$ (8%) of the total world energy consumption in 2021 [12].

## 1.3 Energy Consumption of the World

Primary energy consumption of the world by different sources is consolidated in Figure 1.3 [13]. It can be seen from the figure and Table 1.1, that bio fuels as energy source amounts to about 85% of the total sources. The nuclear and hydral sources are only 3% and 7% respectively. The total share of renewable energy sources is less than 5% which is significantly low as compared to the overall potential.

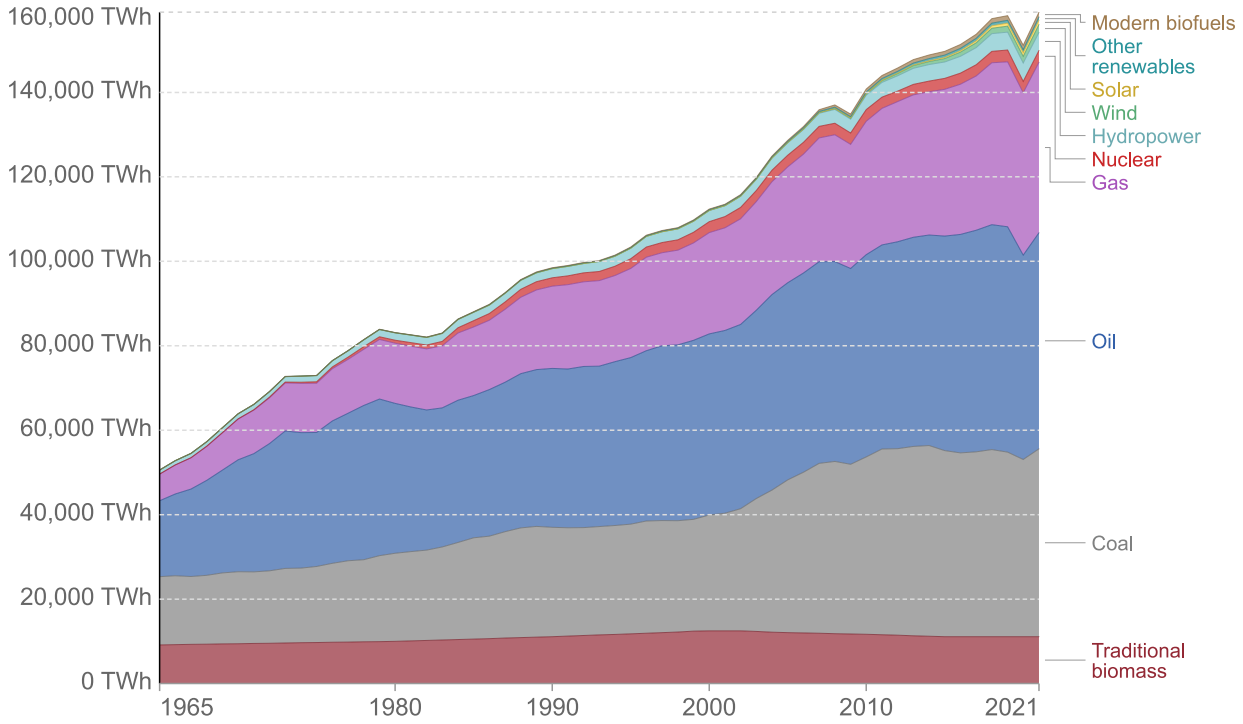


FIGURE 1.3: Primary world energy consumption by source in terawatt-hours (TWh). [13]

TABLE 1.1: Energy consumption by source of the world (2021) [12, 13]

| **Energy Source** | **Consumption (TWh)** | **Share (%)** |
|---|---|---|
| Oil | 51,170 | 82.3 |
| Coal | 44,473 | 31.0 |
| Gas | 40,375 | 26.9 |
| Nuclear | 7,031 | 4.3 |
| Hydro | 11,183 | 6.8 |
| Wind | 4,872 | 2.9 |
| Solar | 2,702 | 1.6 |
| Other | 3,514 | 2.1 |

## 1.4 Greenhouse Effect of Fossil Fuels

The extraction and burning of fossil fuel results in emission of green house gases (GHG). These include Carbon dioxide ($CO_2$), Methane ($CH_4$), Nitrous oxide ($N_2O$), and other Fluorine based gases like Hydrofluorocarbons, Perfluorocarbons, and Sulfer hexafluoride [25]. These Green House Gases (GHG) have an adverse effect on the natural world, including flora, fauna, and people, by polluting air, water, and soil. This effect may result in sickness, birth abnormalities, and human

mortality in addition to the extinction of some species and plants. Denchak [26] defined greenhouse gases, their sources, and their impact on the planet. The total contribution of each non-renewable source is summarized in the figure 1.4.

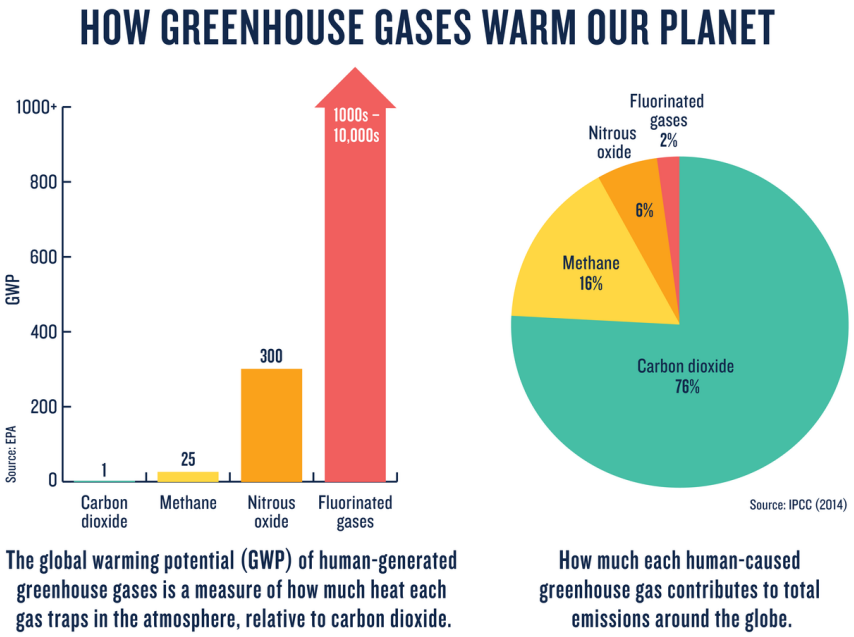


FIGURE 1.4: Greenhouse gases and their impact on planet [26]

.

## 1.5 Global Energy Requirements and Potential

The energy demand of the world is projected to rise more than 1000 $EJ$. The depletion of fossil reserves and need to reduce greenhouse gases impact necessitate adoption of renewable energy sources [27, 28]. Together, the building and construction industries account for 27% of all energy sector emissions and 30% of total global final energy consumption. Buildings and the construction of new buildings continue to use more energy as a result of increased energy access in developing nations, rising air conditioning demand in tropical regions, increased ownership and use of energy-intensive appliances, and the rapid increase in the area of buildings around the world [6]. Carbon dioxide ($CO_2$) emissions could be greatly reduced in the building sector by adoption of clean energy technology and

behavioral changes, which are supported by innovation initiatives. This will pave the way for the construction of zero-carbon structures [29].

In 2020, only 5% of newly constructed buildings were zero-carbon ready. While achieving the goals for a carbon-free building stock by 2050 (IEA's Net Zero Emissions (NZE)) would be difficult, it will also present enormous opportunities. According to the NZE Scenario, all newly constructed structures and those that have undergone retrofitting must be zero-carbon ready by 2030. Buildings must meet requirements for energy efficiency, low-emission fuel consumption, reporting of CO2 emissions based on life cycle, integration with electricity systems using high proportions of variable renewable energy sources, and climate change resistance [6, 30]. Figure 1.5 shows the energy consumption of the world to energy recoverable

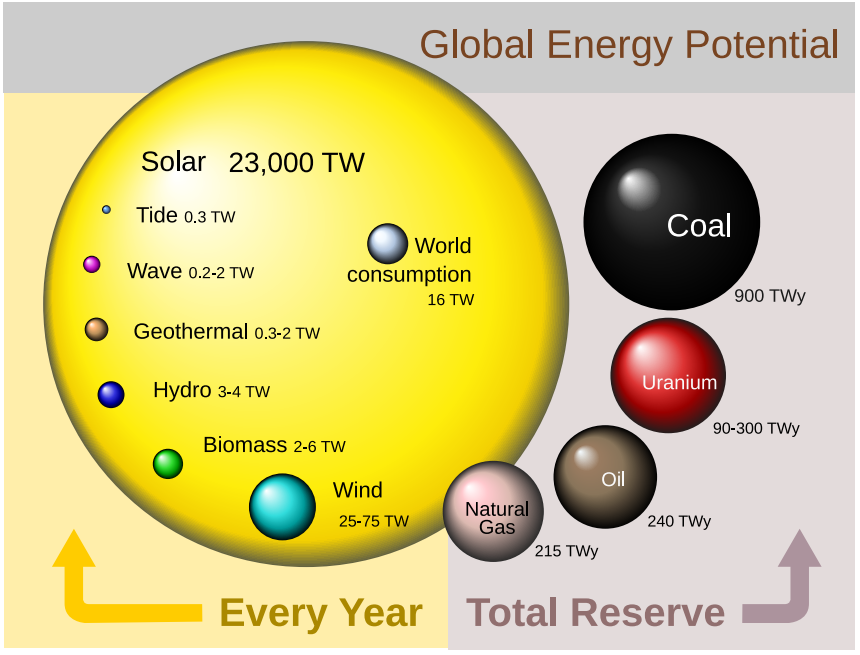


FIGURE 1.5: Global energy potential of different sources [31]

.

from various sources as reported by [31]. They have concluded that energy future of the planet would be solar. It can be seen from the figure that energy consumption of the world was 16 $TW$ and potential of wind energy is about five times higher than the consumption. Compared to potential of the solar energy it is less than

0.07%. The ratio of yearly consumption with respect to potential of these sources taken from the updated report in [32] is listed in Table 1.2.

TABLE 1.2: Energy potential of non-renewable and renewable sources [32].

| **Energy Source** | | **Potential** $(TW/y)$ | **Consumption Ratio** |
|---|---|---|---|
| **Non-Renewable** | Natural gas | 220 | 0.084 |
| | Petroleum | 335 | 0.055 |
| | Uranium | 185 | 0.10 |
| | Coal | 830 | 0.022 |
| **Renewable** | Solar | 23,000 | 0.00080 |
| | Wind | 75 | 0.25 |
| | Waves | 0.2 | 92.5 |
| | Biomass | 2 | 9.25 |
| | Hydro | 3 | 6.17 |
| | Geothermal | 0.2 | 92.5 |
| | Tidal | 0.3 | 61.67 |

Among the many types of renewable energy sources, solar energy is widely accessible [33, 34]. As demonstrated in Figure 1.6, the constant availability of solar energy throughout the day and during seasonal fluctuations is uncertain and limits its full potential adaptability. Therefore, it is necessary to store energy and use it later in order to meet demand for energy.

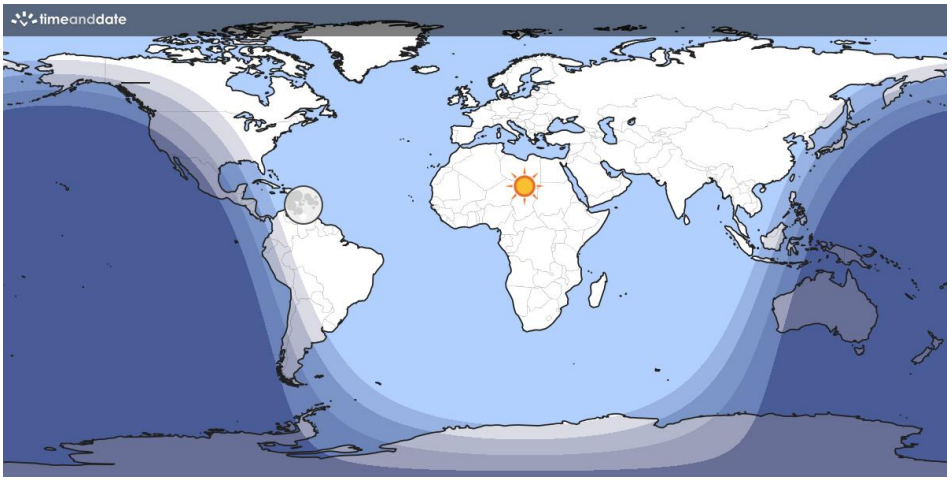


FIGURE 1.6: Day and night world map [35].

## 1.6 Thermal Energy Storage and Applications

Sensible Heat Thermal Energy Storage (SHTES), Latent Heat Thermal Energy Storage (LHTES), and Thermochemical Thermal Energy Storage (TCTES) are three different categories of Thermal Energy Storage (TES) systems. The simplest way to implement TES is with SHTES, but as shown in Figure 1.7, the heat energy that can be stored by this method is the least. Latent Heat Thermal Energy Storage (LHTES) systems pose the biggest technical risk even though they can store three to four times as much energy as SHTES and are commercially used. Additionally, TCTES is the most promising thermal energy storage approach, however due to technical challenges, the market has not fully adopted this technology. The heat storage potential of these three technologies is depicted in Figure 1.7. Depending on the application, one type may be used instead of the other [36].

A TES system can be used to store thermal energy from the sun or any other renewable sources [37, 38] that produce heat. These storage solutions fill the gap between supply and demand specially for building energy requirements for cooling and heating purposes. By storing the excess energy, these devices provide thermal energy during on and off-peak hours. PCMs are widely used in thermal energy storage systems due to their ability to store large amount of energy at nearly contact temperatures [39, 40]. During phase change of materials, major part of the energy is stored in form of latent heat [41] during the melting phase. This phase is also known as the charging phase of the thermal energy storage unit. During the discharging phase of TES device the stored energy is recovered and can be used in various applications.

Costa et al. [42] have described many applications of TES units. Space stations, air-crafts, and satellites could also be integrated with TES to utilize available energy. Refrigerated cargo trucks that carry temperature-sensitive items could be equipped with TES to enhance the efficiency of the equipped refrigeration system by sharing the heat transfer load. Solar energy is one of the freely available vast amount of energy. TES unit could be integrated with solar units to harness solar

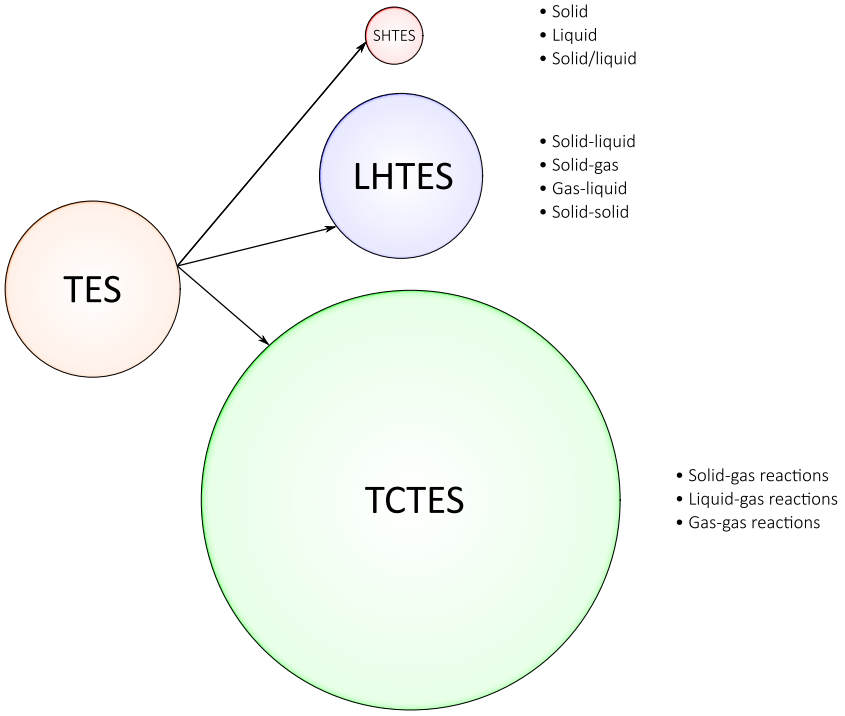


FIGURE 1.7: TES methods and their heat storage capacity [36].

energy. One of the most common applications for TES is in the heat transfer from the building for heating and cooling indoors. The unit could be installed in parallel to an active system and act as a backup energy system. The energy that goes to waste as a by-product of any industrial units could be preserved with the help of TES.

## 1.7 Thermal Energy Storage Device Design

The desirable PCM properties in a LHTES device are high heat of fusion, high thermal conductivity, high specific heat and density, long term reliability during repeated cycling, and dependable freezing behavior. The main limitations of the PCMs that are generally used for room or building application heating are low thermal conductivity and inefficient utilization of thermal energy.

In the design of rectangular LHTES unit following aspects could be studied.

- Longitudinal fins

- Circular fins
- Triangular fins
- Rectangular enclosure aspect ratio
- Orientation of fins
- Alignment of fins
- Varying wall heat flux
- Triangular fins

## 1.8 Problem Statement

Residential buildings consume 30% of the world-energy and contribute to more than $1/3^{rd}$ of the global greenhouse gas emissions [6]. Most of this energy is used for heating of the buildings. With the continuous increase in energy demand, the depletion of fossil fuels, and strict emission regulations, require a rapid incorporation of renewable resources into the energy mix. In this context, the PCM based Latent Thermal Energy Storage ( LHTES) systems can provide a clean solution for heating buildings by storing the heat from solar, geothermal and industrial waste heat sources. Although, the PCMs have high energy density, but low thermal conductivity which makes it difficult to transfer the heat into PCM based LHTES systems. Therefore, heat augmentation techniques in LHTES are paramount. The dominant design parameters that effect the performance of LHTES system are the container design, shape, orientation, and number of the fins. In this respect, double wall-heated rectangular LHTES systems are considered. To best of author's knowledge, these types of LHTES systems have not been studied yet and their parametric design optimization is still an open question.

## 1.9 Research Objectives

The main research objective of this study is to numerically design a PCM based rectangular latent thermal energy storage system embedded with horizontal rectangular fins with superior thermal performance. The analysis is based on enhancement of melting and energy storage rates of the LHTES device through optimization of it's design parameters. In this context, a numerical methodology was developed after validating against experimental results of the current study and from the literature. This numerical methodology was applied to:

- Identify key design parameters of the LHTES system.
- Develop a novel mathematical tool to investigate the effects of variation of key design parameters on the thermal performance of LHTES system.
- Optimize the primary design parameters of LHTES system and develop a machine learning model for melting performance prediction.

## 1.10 Research Contributions

The core contributions of this dissertation are as follows:

- The influence of different designs of the fins on the performance enhancement of a double-wall-heated rectangular latent heat thermal energy storage unit is studied numerically. The study included variation in fin angles, shapes, and lengths while maintaining constant PCM volume.
- A novel fin distribution tool based on mathematical functions (linear, quadratic, cubic, and exponential) is developed while keeping the volume of PCM and total fin area constant. The melting and energy storage performance enhancements of each of the fin distribution configuration is investigated in detail and optimal function is identified.

- The LHTES system is optimized by considering aspect ratio of the container, location of fins along the wall, and optimal mathematical fin distribution function. Taguchi optimization method is used with four level variation of each of the design parameter, forming an $L_{16}$ orthogonal array. A regression model is also developed by employing machine learning methods to predict the transient behavior of melting progression of PCM for a different design configuration based on parameters considered in this study.

## 1.11 Scope of this Study

In this study a prototype was designed and manufactured to conduct experimental studies. The experimental setup was used as a base design and results were used to establish a reference. These reference results were later used for the validation of numerical simulations. The temperature of heat transfer fluid (water) was set at $80°C$ and the PCM (pure Stearic Acid) has a melting temperature range of $54°C$ to $64°C$ [43]. Therefore, the working range of LHTES system considered in this work is limited to low-medium temperature ranges.

## 1.12 Structure of the Thesis

This thesis comprises of seven chapters. The major focus of this thesis is to give novel solutions to the design of dual-wall-heated LHTES system considering various fin topology. The chapter-wise description is given below:

**Chapter 1:** The domain of renewable energy resources and their increasing need in the energy mix is explained in this chapter. Different issues affecting the environment because of fossil fuel based energy resources are briefly discussed. Motivation for the research, objectives, and scope of the study are also stated in this chapter.

**Chapter 2:** This chapter gives a review of the research carried out in the domain of thermal energy storage and heat transfer enhancement methods proposed in the literature. Finally, a research gap in the previous work is identified, and a suggestion is made to fill it.

**Chapter 3:** In this study both experimental and numerical methods are employed. Chapter 3 thoroughly explains the experimental setup and procedure. The results of the experimental study are recorded for subsequent numerical study validation. The basic definitions, governing laws for fluid flows, continuity equation, momentum equation, and energy equation are described. The numerical model is developed and validation and verification of the techniques is also presented in this chapter.

**Chapter 4:** This chapter analyses simulation results of different fin design configurations of the dual-wall-heated rectangular LHTES device. The variations in fin orientation, fin length, and wall temperature are studied in this chapter.

**Chapter 5:** In this chapter a systematic investigation is performed to discover an optimal profile for the fin lengths using a mathematical function.

**Chapter 6:** In this chapter impact of aspect ratio of the rectangular enclosure of LHTES is investigated. Moreover, statistical Taguchi method is used to identify the optimized design parameters. Machine learning methods are employed to develop a regression model for the prediction of melting performance of LHTES systems.

**Chapter 7:** This chapter summarizes the overall thesis and draws conclusions along with few recommendations for future work are also stated.

# Chapter 2

# Literature Review

## 2.1 Introduction

A comprehensive literature survey was conducted to study the Phase Change Material (PCM) and their properties for the purpose of latent heat thermal energy storage device. The design of the shape and geometric parameters of Latent Heat Thermal Energy Storage (LHTES) unit were also investigated from the literature. Many of the studies discuss about different techniques to enhance heat transfer rate in the Phase Change Material (PCM) and improve thermal performance of Latent Heat Thermal Energy Storage (LHTES) devices.

## 2.2 Thermal Energy Storage

One of the effective methods to close the energy supply and demand gap is Thermal Energy Storage (TES), which stores heat in a material and releases it when it is needed. Solar thermal systems, waste heat recovery, district heating and cooling, thermal power plants, and buildings are only a few examples of the many real-world uses for thermal energy storage [44].

A composite PCM with hybrid graphene aerogel composed of graphene oxide, carbon nano-tubes, and paraffin wax was studied by Chen et al. [45] for solar thermal energy storage applications. They found that the composite PCM showed a comparable heat storage performance improvement compared to pure PCM. In order to increase the efficiency of solar thermal storage systems, this study recommended the creation and use of composite Phase Change Materials based on graphene aerogel and carbon nano-tubes that have strong thermal conductivity and absorbance properties. Campos-Celador et al. [46] have described a generic, simple method for designing Thermal Energy Storage (TES) that is appropriate for sensible and latent systems and have direct/indirect interface between the Heat Transfer Fluid (HTF) and storage media. The technique was broken down into four parts; describing (a) the thermal process and (b) TES system, (c) defining the TES system requirements and (d) determining the final design. The simplest and efficient way to improve the thermal performance of a TES device is to add fins that have the advantage of being easy to install and improve performance when in use [47]. PCMs have emerged as a potential technology for thermal energy storage due to their relative benefits over other forms of energy storage techniques. The performance of latent heat-based thermal energy storage systems is influenced by the design of heat exchanger as well as the thermophysical characteristics of PCM [48].

The influence of fin orientation on the thermal performance of a horizontal shell and tube latent heat storage unit were investigated numerically and experimentally by [49] for charging and discharging cycles. The annulus of the shell and tube were separated by a layer of stearic acid, which was employed as a phase-change material. In order to compare three distinct angular orientations of the exterior fins of the tube conveying the heat transfer fluid, a buoyancy-driven transient numerical approach was used. A-fin configuration was formed by the angle, whereas Y-fin configuration was developed. Due to improved natural convection effects, a considerable improvement in heat transfer rate for Y-fin arrangement was seen throughout the charging cycle. In comparison to the fin configuration, the Y-fin configuration enhanced the entire charging process for a heat transfer fluid of $358K$

by 51% and increased the latent heat storage unit's overall heat storage capacity by 10%.

## 2.3 Phase Change Materials

A key element in the energy business is effectively storing and transporting thermal energy. There have been numerous methods employed from the beginning of time to solve this problem, including heat exchangers, chemicals, and others. As research and industry improved, new composite materials known as PCMs were discovered. These materials proved to be exceptional for storing and transferring energy, but because they have low thermal conductivity, active and passive strategies were developed to address this issue. The PCM falls under the categories of both organic and inorganic materials. For a faster rate of heat transmission, the well-known PCM materials such as $Cu$, $Al_2O_3$, $Au$, $SiC$, $SiO_2$, and $TiO_2$ are taken into consideration [50, 51].

When PCM transforms from solid to liquid or from liquid to solid, thermal energy is transferred. This is referred to as a phase change or state change. These solid-liquid PCMs function initially like traditional storage materials; however, as they absorb heat, their temperature increases. PCM absorbs and releases heat at a practically constant temperature, in contrast to conventional (sensible) storage materials. Compared to conventional storage options like water, masonry, or rock, they store 5–14 times more heat per unit volume. It is known that several PCMs melt with a heat of fusion in any necessary range. However, these materials must have specific desired thermodynamic, kinetic, and chemical properties in order to be used as latent heat storage materials [7, 52].

Shape stabilization methods can be employed to stop leakage and improve the ability of PCMs to store energy. By micro-encapsulating the organic PCMs and integrating them into the matrix of the supporting materials, or by creating PCM with the solid-solid phase change, the shape stability can be attained [53].

PCM behave like a thermal battery, charging (storing) energy by melting and discharging (releasing) during solidification. These materials play an important role in the thermal energy storage unit related to domestic and industrial applications. PCMs have high energy storage density and can absorb or release thermal energy during the phase change process at nearly uniform temperature and pressure simultaneously [39]. PCMs can undergo different forms of phase transitions but solid-to-liquid phase transition is the most commonly used form of phase change.

## Solid-liquid phase change

Compared to sensible heat materials, this form of latent heat material allows for the storage of huge amounts of heat in a smaller volume and is based on the melting and solidification processes. The temperature remains constant during melting, often known as the melting temperature or phase change temperature. After melting is complete, sensible heat storage will facilitate additional heat transfer [54]. Latent

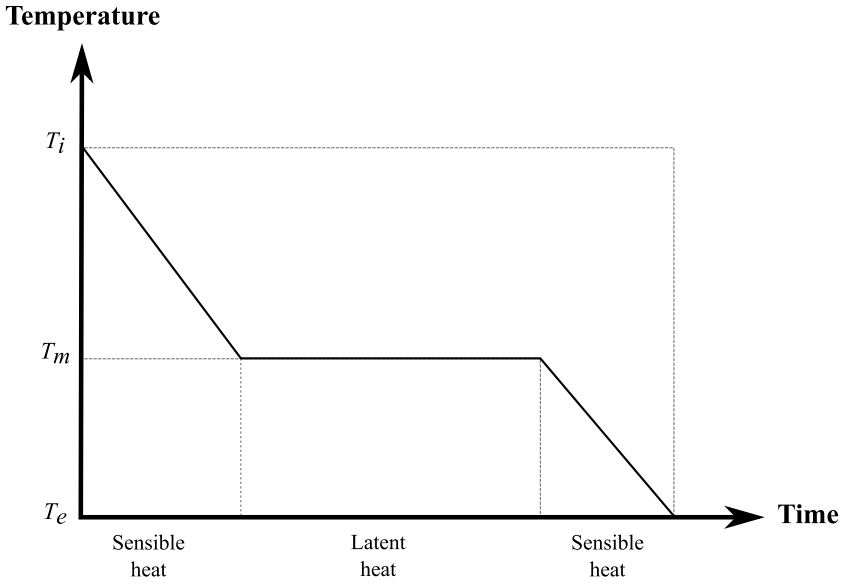


FIGURE 2.1: Temporal temperature variations in a typical melting process of PCM.

heat, which can be calculated by comparing the enthalpies of the two phases, is the heat transfer that occurs during melting or phase changes but cannot be quantified by temperature change because temperature is constant. Phase change enthalpy, melting enthalpy, or heat of fusion are terms used to describe the difference in

enthalpy in the event of solid-liquid phase change. A typical temperature-time plot during melting/charging of a PCM is depicted in Figure 2.1. It can be seen from the plot that during the phase change energy is absorbed by the material. This energy is stored that can be later recovered during discharging (solidification) phase. The temperature-time plot of a typical solidification is shown in Figure 2.2.

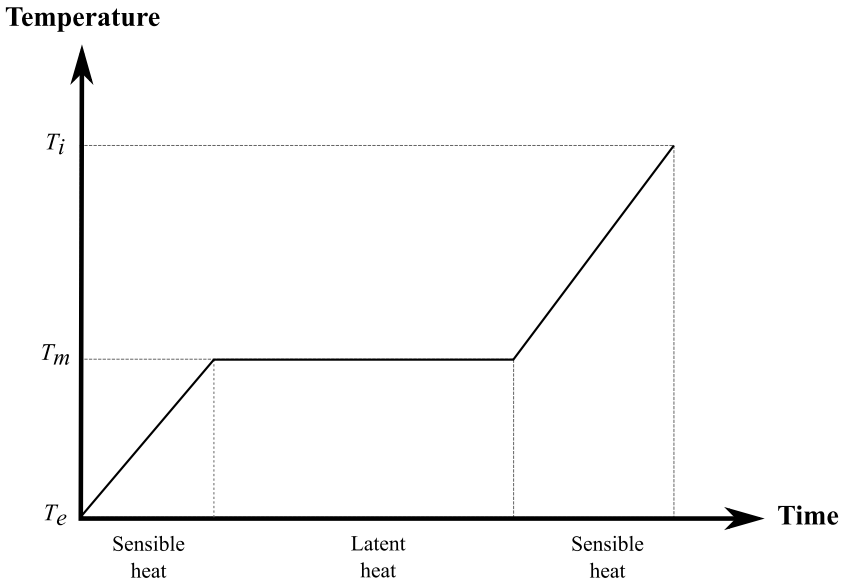


FIGURE 2.2: Temporal temperature variations in a typical solidification process of PCM.

### 2.3.1 Classification of PCM

PCM used in thermal energy units can be classified into three types [55] as depicted in Figure 2.3.

#### 2.3.1.1 Organic PCM

Organic materials have outstanding thermal properties. The melting is congruent and phase change temperature range is narrow. They exhibit self-nucleation and density of their energy is high. Most of the organic materials do not display phase segregation and they have very low or no super cooling [56]. These types of PCM

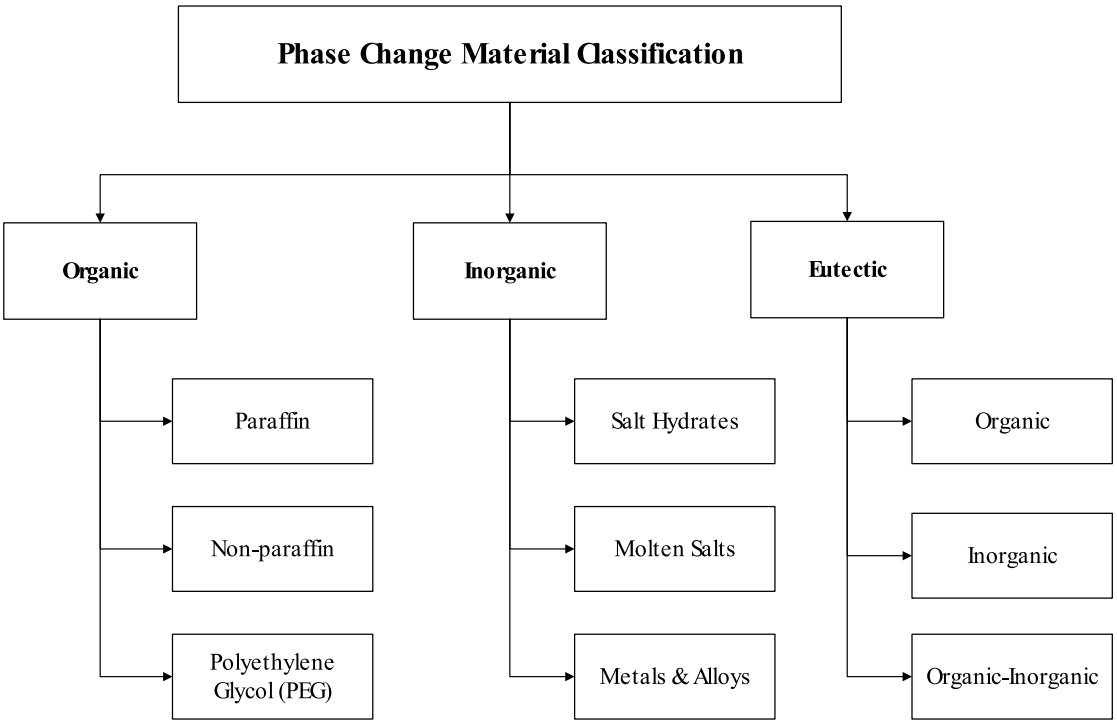


FIGURE 2.3: Phase Change Materials classification [55].

are suitable for conservation of energy in buildings, development of solar energy units, keeping batteries and electronic devices cool and textile industry etc. Organic PCMs are ideal candidate for storage units in domestic applications because of their low operating temperatures and higher fusion heat. The main disadvantage of organic materials is they have low thermal conductivity and leakage from the container upon melting [2], [7]. Research on overcoming these shortcomings has shown considerable progress.

Paraffin is one of the most widely used organic PCM. Paraffin is a mixture of $(C_nH_{2n+2})$. It has a low melting temperature in the range $18°C$ to $71°C$. It is cheaper to produce and is available at large scale. It is produced as a by-product during the refining of crude oil. It is used as PCM in thermal energy storage devices where energy from low temperature needs to be stored. The latent heat of Paraffins is $150J/g$ to $260J/g$.

Similarly, Fatty Acids (carboxyl acid $(CH_3(CH_2)_{2n}COOH)$ are are also commonly used organic PCM. Fatty acids include Capric acid, Lauric acid, Stearic acid, Myrstic acid, Palmitic acid, and Archidic acid. Generally all orgainc PCM have

low thermal conductivity which makes them ideal to store heat for long times but at the same time it becomes difficult to diffuse the heat with in the PCM. The melting range of fatty acids is $30°C$ to $74°C$ and they have latent heat of fusion between $140J/g$ to $280J/g$. They are also used to make eutectic mixtures.

When ethylene oxide and water condense, a polymer called Polyethylene Glycol (PEG) is created. In the presence of air, PEGs are sensitive to oxidative deterioration. Limiting PEG's exposure to high temperatures, oxygen, and/or adding an antioxidant can reduce the amount of breakdown. PEGs don't hydrolyze or degrade while they're stored. Along with paraffin and fatty acids, PEG is an organic PCM that exhibits a consistent phase change and a high nucleation rate [57]. PEG's chemical formula is typically written as $H-(O-CH_2-CH_2)_n-OH$. The melting range of PEGs is $19°C$ to $96°C$ and they have latent heat of fusion between $70J/g$ to $190J/g$. They are also used to make eutectic mixtures.

#### 2.3.1.2 Inorganic PCM

Inorganic materials have higher thermal conductivity. Inorganic materials are usually low cost and their latent heat capacity is higher than organic materials. Salt hydrates comprises of water and inorganic salts. The generic formula of salt hydrates is $(AB.nH_2O)$. They have poor nucleating ability and suffer from super cooling. The phase change process of Salt hydrates involves hydration and dehydration.

Another type of inorganic PCMs used for TES units are molten salts. Molten salts are high-temperature PCMs because they have melting temperatures in the range of $250°C$ and $1680°C$, and their heat of fusion values lie in the range of $68J/g$ to $1041J/g$. Primarily used between $100°C$ and $450°C$ in textile and food industry for low/medium temp steam generation. As the operating temperature range is high, molten salts are also used to generate steam for power generation. Aerospace and nuclear industry applications use fluorides as PCM. Some other examples of molten salts include chlorides, carbonates, nitrates, and sulfates.

Metals and Alloys are inorganic PCMs that have high thermal conductivity and heat storage per volume density is quite high for these materials. These PCMs generally have melting point higher than $300°C$ and they are compatible for high-temp TESU. Aluminum alloys, magnesium alloys, copper alloys are some examples of PCMs in this category.

#### 2.3.1.3 Eutectic Mixture PCM

As illustrated in Figure 2.3, eutectic PCMs are formed by combining two or more organic or inorganic materials. The components could be selected from same or different class of materials. The three type of eutectic mixture consist of organic-organic, inorganic-inorganic, and organic-inorganic depending on the type of material components. In many of the thermal storage applications binary and ternary mixtures of inorganic salts have been studied [58]. Eutectic mixtures give the opportunity to adjust phase change temperature. These do not segregate during melting or freezing. The thermal performance of eutectic mixtures is similar to that of the comprising components. Ionic liquids, that are medium temperature mixtures are produced from nitrate, sulfate, and chloride salts alkali and alkaline metals. The PCMs are grouped on the basis of their heat of fusion and melting temperature are shown in Figure 2.4.

### 2.3.2 Thermophysical Properties of PCM

Many heating, cooling, and power generation applications are covered by PCMs that have operating temperature ranges between $-20°C$ and $200°C$. The PCM is chosen based on the type of application and operating temperature range. Table 2.1 lists low, medium-low, medium, and high temperature range applications of PCM. A heat storage substance, a container that is compatible with the storage material, and a heat exchange surface are the minimum components that any latent heat TESS must have [55]. Mostly materials that show solid-liquid transition are used. A PCM should satisfy following properties for practical applications:

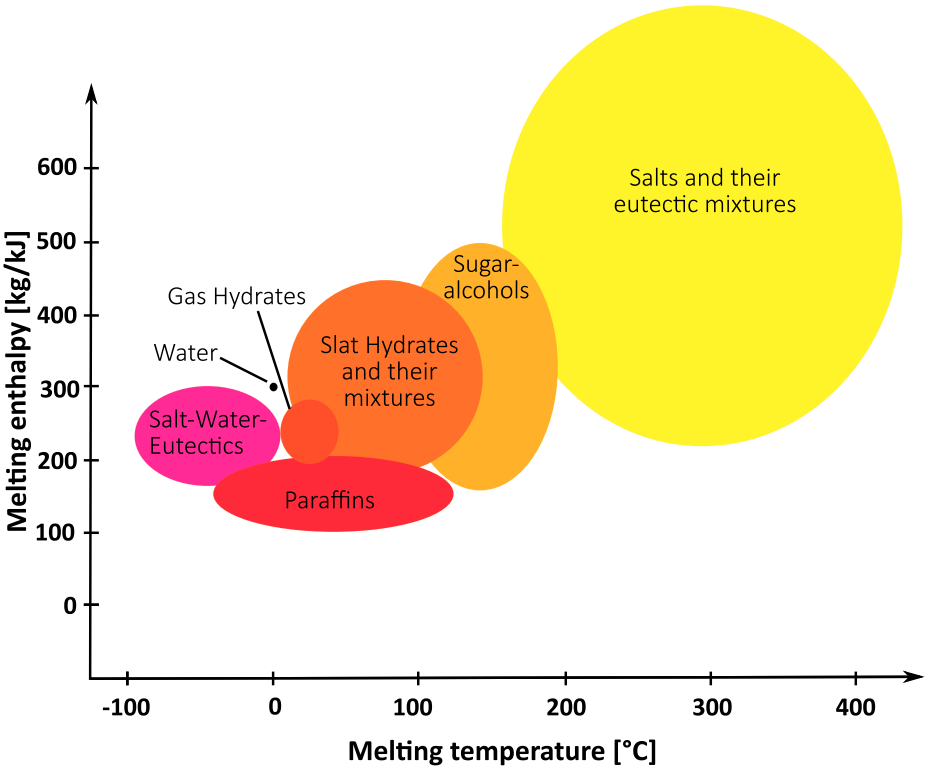


FIGURE 2.4: PCM with respect to heat of fusion [59].

- Melting-Point: It should have a suitable melting point that is easily attainable without any special energy requirements.
- Enthalpy: Phase change enthalpy for a good candidate PCM should be high.
- Specif heat: Similarly PCM should also possess high specific heat capacity.
- Conductivity: It is also required for PCMs to have high thermal conductivity.
- Density: Density of the PCM should be high as well.
- The PCMs with low volumetric strain and low vapor pressure are preferred.
- It is very important for PCMs not to have phase separation.
- Chemical: The chemical properties required for a good PCM are that it should not be toxic, it does not catch flame easily. It should bot be corrosive and must not pollute the environment.

TABLE 2.1: PCM operating temperature ranges and applications.

| **Temperature** | **Range** | **Applications** |
|---|---|---|
| Low | $-20°C$ *to* $5°C$ | Domestic refrigerator<br>Commercial refrigerated products |
| Medium-low | $5°C$ *to* $40°C$ | Free cooling<br>Building passive heating and cooling<br>Solar absorption chiller<br>Evaporative and radioactive cooling<br>Air conditioning system |
| Medium | $40°C$ *to* $80°C$ | Solar air heaters<br>Solar stills<br>Solar domestic hot water<br>Electric devices |
| High | $80°C$ *to* $200°C$ | Solar absorption cooling<br>On-site waste heat recovery<br>Off-site waste heat recovery<br>Solar thermal electricity generation |

- The PCM should have low or not super-cooling.
- Sufficient crystallization rate
- Phase transition: The PCMs should have reversible phase transition so that both charging and discharging cycles could be implemented.
- Economy: PCMs that are easily available, have low cost, are easily recyclable and abundantly available are better suited for TES applications.

Selecting a suitable solid-liquid PCM can be complex due to the absence of a single material that fulfills all desired properties. Researchers face common challenges, including super-cooling, phase separation, low thermal conductivity, and liquid leakage. Super-cooling occurs when a PCM remains in its liquid state below the expected melting temperature, which can be mitigated using nucleating agents or eutectic mixtures. Phase separation, where the liquid and solid phases of a PCM

separate, is addressed through encapsulation techniques and stable eutectic formulations. Low thermal conductivity in solid PCMs is tackled by incorporating high-conductivity materials, using composites or nano-structured PCMs, or creating porous structures for improved heat transfer. Lastly, liquid leakage concerns are addressed by employing encapsulation methods such as micro-encapsulation or macro-encapsulation. Overall, ongoing research and development efforts focus on finding innovative PCM formulations and encapsulation techniques to overcome these challenges and enhance the performance of thermal energy storage systems.

### 2.3.3 Thermal Energy Stored in PCM

In domestic heating applications, solid-liquid PCM is preferred over the others because in this phase change system the operating temperature is lower than any other system. The total amount of energy stored in the phase change process is comprised of sensible energy and latent energy. The expression in Equation (2.1) can be used to calculate the total stored energy[41].

$$Q = m[C_{sp}(T_m - Ti) + \Delta H + C_{lp}(T_e - T_m)] \tag{2.1}$$

where:

$$\begin{aligned} \text{Sensible energy in solid} &= mC_{sp}(T_m - Ti) \\ \text{Latent heat of fusion} &= m\Delta H \\ \text{Sensible energy in liquid} &= mC_{lp}(T_e - T_m) \end{aligned}$$

$T_m$, $T_i$, and $T_e$ are melting, initial and final temperature of PCM respectively. $m$ is mass, $C_{lp}$, and $C_sp$ are specific heat values of PCM for liquid and solid phases respectively. $Q$ is the total stored thermal energy.

### 2.3.4 PCM Limitations

The main drawback of organic PCMs is that these materials have low thermal conductivity [7]. There are two significant problems with organic PCMs. Organic solid-liquid PCM applications are constrained by low heat conductivity

and container leakage. Research on improving these PCMs' heat conductivity and reducing liquid leakage has advanced significantly in recent years. The next sections discuss several strategies and techniques for enhancing PCM's thermal conductivity and heat transfer rate in the thermal energy storage unit.

## 2.4 Heat Transfer Enhancement in PCM

Several different methods for heat transfer improvement exist. The objective of these methods is to enhance thermal conductivity of PCM so that heat transfer rate increases. This impact the phase change process and improves overall performance. One way to enhance conductivity is by adding materials with high conductivity such as metals, metal oxide nanoparticles, and carbon materials.

Another way of enhancing the heat transfer of PCM is by increasing the natural convection of liquid PCM. Commonly used thermal energy storage containers are tube-in-shell, triplex-tube and rectangular. Modifying the structure of the container can also help in improving the performance in LHTES [60]. Fins of different shapes like rectangular, cylindrical, spherical, and annular are commonly usually used to improve the thermal conductivity [61].

Heat transfer capability of PCM can also be enhanced by the use of heat pipes. Changing the geometrical configuration and materials also impact the performance of TESU. Thermal conductivity can also be improved through dispersion of nanoparticles having nominal sizes ranging from $1 - 100nm$[62] and are highly conductive. [63] have described several methods for heat transfer enhancement in thermal energy storage units. These methods can be generally classified into following categories as described in the subsequent paragraphs.

### 2.4.1 Using Fins to Enhance Heat Transfer

This is the most widely used method for enhancing heat transfer in thermal storage units. The addition of extended metal surfaces (fins) results in an increase in the

total surface area from which heat transfer takes place. These fins could be used in different shapes and configurations and their impact on the performance of thermal energy units has been extensively studied by Abdulateef et al. [64]. Figure 2.5 show different types of fins in a Triplex Tube Heat Exchanger (TTX) energy storage device investigated by them. This type of device comprises of three pipes. The inner and outer pipes contain HTF to carry heat to the PCM contained in the middle pipe.

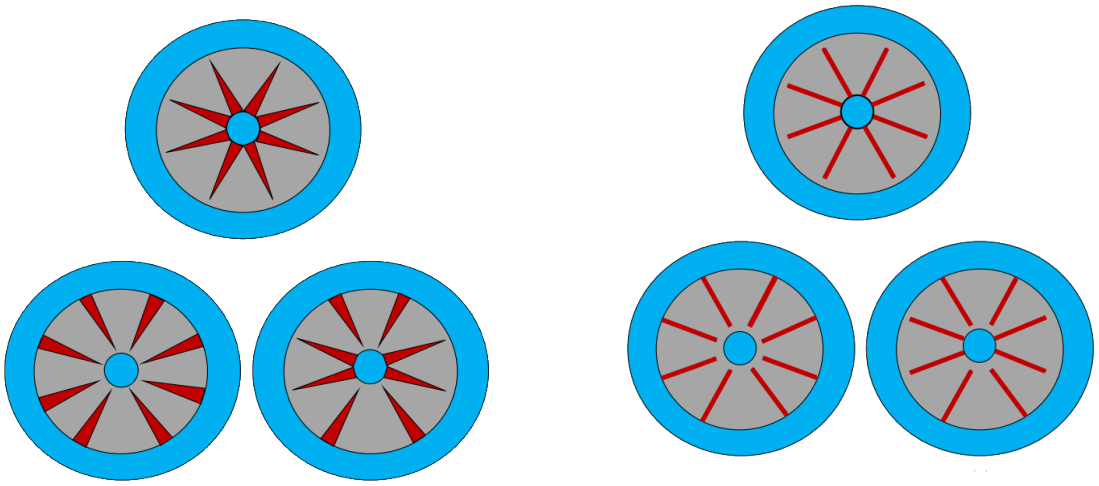

(a) (b)

FIGURE 2.5: (a) Internal and external triangular, and (b) Internal and external longitudinal fins in TTX [64]

### 2.4.2 Heat Pipes for Heat Transfer Enhancement

Heat pipes transfer high heat rates across small temperature gradients and act like thermal super conductors. The heat transfer fluid and PCM exchange energy by heat pipes which improves the over all performance of the unit. Heat pipe is frequently employed in Battery Thermal Management (BTM) systems that are PCM-based and aided because of its superior heat transmission properties [65, 66]. The heat pipe is filled with a working fluid and has three sections: one for evaporation, one for adiabatic cooling, and one for condensation. The working fluid will evaporate and produce vapor when the evaporation portion is heated.

The vapor then transports the heat from the battery to the condenser part, where the vapor fluid releases heat into the environment and condenses into liquid.

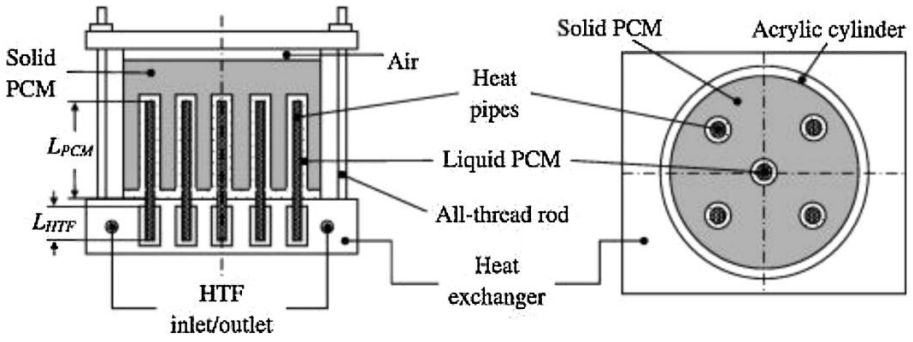


FIGURE 2.6: Cylindrical LHTES with several heat pipes [66].

The melting time of the PCM was examined using 3D computer analysis in a sinusoidal pipe placed into another pipe by Hakan et al. [67]. The system was heated from the inner pipe at various temperatures, and the other pipe was filled with PCM. The time-dependent governing equations were resolved using the finite volume technique. For the sinusoidal wall, four different scenarios were used to examine the impact on melting by geometry. Geometrical parameters had the most strong influence on the melting time. The increase in phase transition was observed as the amplitude ratio was raised. The effect of increasing wall temperature from $20°C$ to $60°C$ resulted in 46.77% reduction in melting time.

Abed et al. [68] numerically investigated a latent heat storage system with hemispherical and quarter-spherical fins (shown in Figure 2.7), this study intended to assess the melting properties of PCM. The PCM-based heat storage unit used a vertical triple-pipe heat exchanger to increase melting performance over a double-pipe system. To enhance heat transfer efficiency, the fins were also positioned inline and in staggered patterns. The heat storage rate increased by over 78% (from 35.6 to 63.5 W) when compared to the case without fins, cutting the melting time in half.

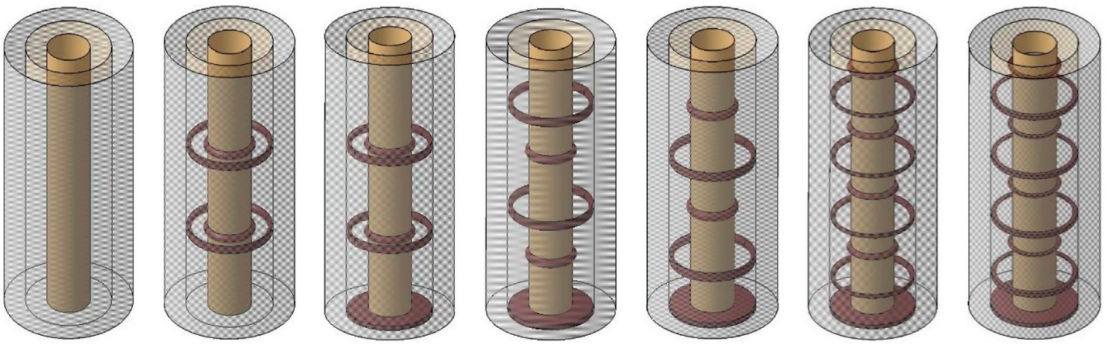

FIGURE 2.7: Hemispherical and quarter-spherical fins in a triple-pipe LHTES [68].

### 2.4.3 Creating Cascaded Storage

During the heat exchange process decrease in temperature difference causes poor heat transfer and this effect is unavoidable. Cascaded storage has been proposed to solve this problem [69]. Up to 30% enhancement in heat transfer has been observed by researches with the use of cascaded storage. Figure 2.8 shows a single stage and cascaded thermal storage units.

### 2.4.4 Improvement in Heat Transfer by Nanomaterials Additives

The improvement of the specific heat and thermal conductivity of PCMs has also been examined using nanoparticles [70], nanosheets, nanofibers, nanotubes, nanowires, nanorods, or droplets [71]. There are two possible ways to prepare the nanofluids: in one step or in two steps. The two-step method starts with the preparation of the nanoparticles using various processes, and then the dispersion of the nanoparticles in the fluids is accomplished through agitation techniques like magnetic agitation, ultrasonic agitation, high-shear mixing, homogenizing, or ball milling. In the one-step method, the production of nanoparticles and their dispersion in the fluid are simultaneous. The second strategy is the one that is most frequently employed since it is scalable and profitable. Carbon, particularly in the form of nanotubes, is one of the materials that is most frequently employed

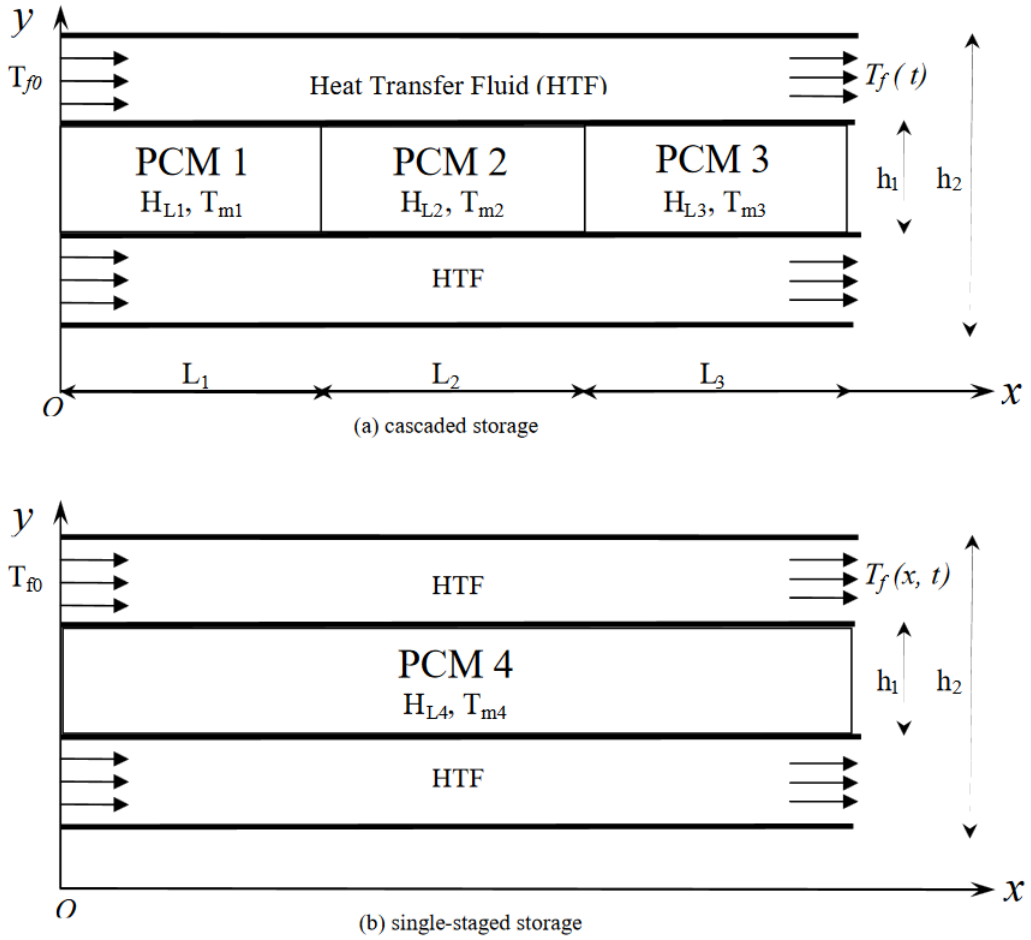


FIGURE 2.8: Single-staged Storage (SS) vs. Cascaded Storage (CS) [69].

for the enhancement of PCM properties. $TiO_2$, $Al_2O_3$, $SiO_2$, and Nano-Cu are the commonly used nano materials investigated by researchers for the improvement of thermal properties of PCM.

### 2.4.5 Metal Foams for Heat Transfer Improvement

The integration of open-cell Metal Foams (MFs) is one of the most effective ways to improve overall heat transfer performance of PCM by increasing thermal conductivity. MFs are thin, porous, lightweight metal objects that are typically flat or cylindrical in shape. Because it is porous, MF typically has a cellular structure with a high volume fraction of empty space [72, 73]. Figure 2.9 shows copper metal foam with different pore sizes.

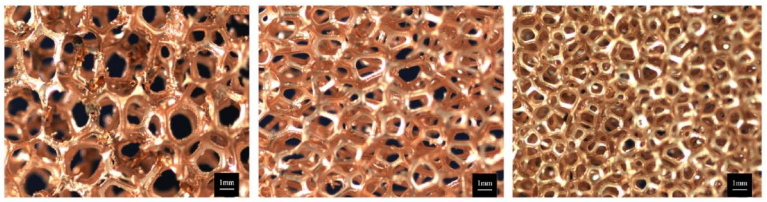

FIGURE 2.9: Images of metal foam with different pore sizes [73].

### 2.4.6 Encapsulation of PCMs

Encapsulation is the process by which a particle is surrounded by a covering substance or implanted in a homogeneous or heterogeneous matrix to create a capsule. The capsules can be constructed in an irregular shape or a standard shape, such as spherical, tubular, or oval. This procedure is one of the ways to deal with several PCM-related issues, such as low conductivity, thermal instability, and supercooling, which reduce the system's thermal efficiency and rate of heat release. In these methods PCM is covered by a shell of different type of material. Based on the size of the capsules these methods are classified as macro-encapsulation $(1 - 10mm)$, micro-encapsulation $(1 - 1000\mu m)$, and nano-encapsulation $(< 1\mu m)$. The encapsulated PCM's operation is depicted in Figure 2.10. The PCM serves as the core component, and the encasing material serves as the shell component. In the heated capsule, the PCM melts while the shell is still solid. During the melting and phase transition, the PCM's temperature stays constant, and depending on its thermophysical characteristics, it stores a certain amount of heat. The PCM returns to its initial solid form by releasing the absorbed heat when it cools below the melting point. The above mentioned methods help in improving the thermal conductivity of the PCM but they have some technical disadvantages. Nano-PCMs and encapsulated- PCMs are difficult to prepare and increase the cost of the LHTES. Moreover, nano- PCMs and metal foams reduce the overall energy capacity of the system. Joshi et al. [74] conducted an experimental and numerical study and have shown that the fins infused PCM accelerated the melting rate by 66.67% than the metal foam infused PCM [74] under the same mass of PCM. In another study Hayat et el. [75] showed that the heat storage rate was slightly improved by fins and nanoparticles until the complete melting of PCM. They also

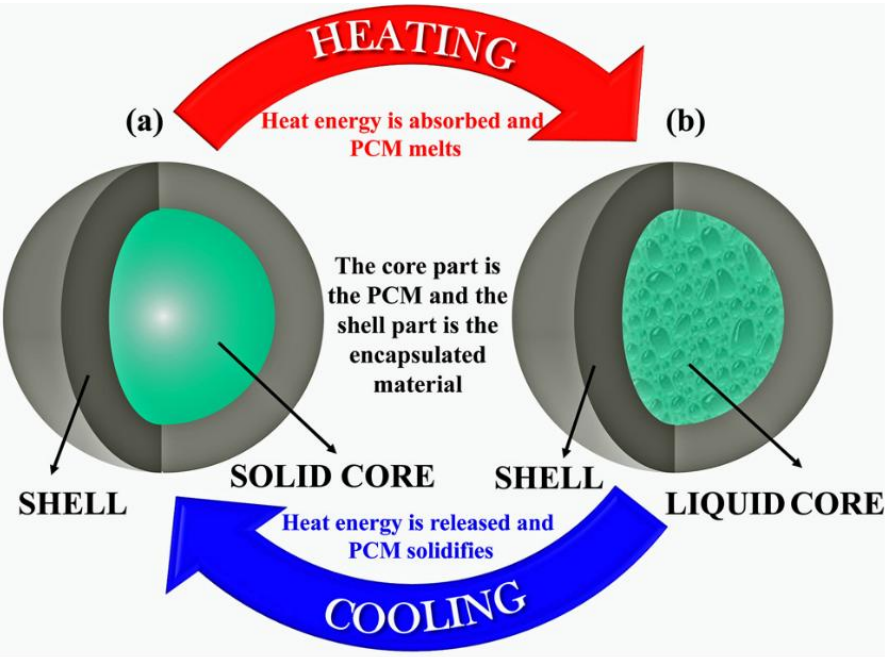


FIGURE 2.10: Working principal of the encapsulated PCM [71].

identified that by using 5 fins the total absorbed energy was increased by 10%. Moreover, after a complete meltdown, the total stored thermal energy in the PCM containing metal foam was about 85–95% of the total energy of the pure PCM [76].

## 2.5 Applications

In latent heat thermal-storage systems for heat pumps, solar engineering, and spacecraft thermal control applications, PCMs have been widely used. In the last ten years, PCM applications for building heating and cooling have been studied. Many PCMs exist and can melt and solidify at a wide range of temperatures, making them suitable for use in a wide range of applications.

### 2.5.1 Buildings

Since before 1980, PCMs have been taken into consideration for thermal storage in buildings. Wall-boards, shutters, under-floor heating systems, and ceiling

boards can now be used as a component of the building for heating and cooling applications thanks to PCM's implementation in Trombe walls, PCM wallboard, and PCM concrete systems.

De Gracia and Cabeza [77] studied active and passive PCM based thermal energy storage integrated in the building sector. They have identified and highlighted the advantages and drawbacks of each technology. Main advantages described by them are increase in efficiency, better reliability, reduced investment and running cost, and less pollution. The main drawbacks identified by the authors are low thermal conductivity of PCM and increase in volume in case of sensible thermal storage.

A parametric study for design optimization of and active LHTES system for space cooling was conducted by Ručevskis et al. [78]. PCM layer thickness, number of pipes, diameter of pipes, cooling duration, inlet water temperature, and weather conditions were the parameters they studied. They identified the improtance of each parameter in their numerical studies. The validity of PCMs as a Trombe wall has been examined through experimental and theoretical studies [79]. The phase change units are substantially smaller and lighter than water walls or mass Trombe walls for a given amount of heat storage. Calcium chloride hexahydrate (melting point 29.8°) was used as PCM by Bourdeau [80] to test two passive storage collector walls. He came to the conclusion that an 8.1 cm PCM wall performs marginally better thermally than a 40 cm masonry wall.

The idea of enhancing the thermal comfort of lightweight buildings by incorporating PCMs into the building structure has been examined in numerous research projects over the course of several decades [81, 82]. The ceiling boards, which are used for heating and cooling in buildings, are a crucial component of the roof. In order to discharge energy during peak hours, Bruno [83] created a mechanism that stored coolness in PCM during off-peak hours.

### 2.5.2 Solar Water Heating

The popularity of solar water heaters is growing [43, 84, 85] as a result of their low cost and ease of construction and maintenance. A built-in storage type water heater with a layer of PCM filled at the bottom was examined by Prakesh et al. [86]. In the presence of sunlight, the water warms up and radiates heat to the PCM below. Due to the buildup of energy in the form of latent heat, the PCM melts. When there is no sunlight, cold water is utilized instead of hot water, and the cold water receives its energy from the PCM. When the PCM changes from a liquid to a solid state, energy is released.

### 2.5.3 Solar Air Heating

In various investigations researchers have examined the effectiveness of air-based solar heating systems using phase change energy storage units. Their main goals were to ascertain the impact of PCM latent heat and melting temperature on the thermal performance of air-based solar heating systems.

Chaichan et al. [87] studied the effect of charging and discharging of PCM in a Trombe wall. They added $Al_2O_3$ nano particles in the paraffin wax of one wall. In their study they observed faster charging and discharging times. The exit air temperature of the wall with Nano- PCM was hotter by about 43% than the wall with plain PCM.

### 2.5.4 Solar Green House

As a component of the integrated greenhouse solar system, Hung and Toksoy [88] had designed and built a latent heat storage system with two alternative stacking configurations and air baffling. The main storage components were made of industrial cylindrical storage rods. The findings indicated that compared to rock or water storage, the developed latent storage devices revealed a much larger compact storage capacity.

In order to store solar energy for drying and curing processes as well as plant production, PCMs have also been employed in greenhouses [89]. A greenhouse energy storage was studied by Kern and Aldrich [90]. They used 1650 kg of $CaCl_2.6H_2O$ in aerosol cans each weighing 0.74 kg. Two stores with various amounts of PCM were employed, one inside and one outside the greenhouse, and PCM cans were arranged in a shop with a 22.86 mm gap between each one. The direction of air flow was switched for the energy-releasing procedure at night while the energy storage unit inside the greenhouse collected warm air from the ridge of the greenhouse during the day.

### 2.5.5 Photovoltaic Panels and Solar Stills

Numerical simulations were used by Sasidharan and Bandaru [91] to compare the thermal response and heat transport phenomena of Photovoltaic (PV)- Nano Enhanced Phase Change Material (NEPCM) and plain PV- PCM for different tilt angles. The $CuO$ nanoparticles chosen for NEPCM had mass concentrations of 1%, 3%, and 5%.

In order to determine the impact of mass concentration of nanoparticles and inclination, the thermal performance of PV-NEPCM at inclinations of $0°, 15°, 30°, and 45°$ was compared with a simple PV- PCM system. For PV- PCM and PV- NEPCM systems, the average temperature of PV, the liquid fraction and thermal energy stored in PCM, the pattern of isotherms and streamlines, and the performance of PV are compared. The results showed that the heat transfer rate of PCM was faster in all configurations in which nanoparticles were added.

Younes et el. [92] experimentally studied new rotating disc solar stills with various disc configurations, PCM thermal energy storage units, and the use of external reflectors. With a constant rotational speed of 0.1 rpm, three types of revolving discs—flat, finned, and corrugated—have been investigated. To maximize the water evaporation surface area and the exposed area to sun radiation, four revolving discs were employed on the back and side walls of the discs SS. According to

the findings, for flat, corrugated, and finned disc stainless steel, the productivity boost over standard stainless steel was 68%, 86%, and 106%, respectively. While using TES unit with NEPCM, productivity increased by 149% compared to the traditional solar stills.

## 2.6 Performance Enhancement

Many various techniques have been used in the literature to enhance LHTES device's thermal performance. The most widely used technique modifies the fins and container of the LHTES geometrically [93–95]. Shell and tube, spherical, and rectangular are typical geometric shapes in thermal energy storage systems [49, 96–99]. Rahimi et al. [100] have undertaken a thorough review based on key industrial applications, solution techniques, PCM components, and PCM enclosure geometries. Applications for Lead-Acid batteries, drying methods, food technology, thermal storage, and solar collectors are all included in this paper. They investigated the functionality of rectangular thermal energy storage units of the following shapes: square, rectangle, trapezoidal, triangular, and parallelogram.

### 2.6.1 Heat Transfer Enhancement Techniques

The biggest design challenge of PCM based LHTES systems is the low thermal conductivity of PCM. The majority of the techniques to overcome this are based on the different configurations of fins embedded in the PCM as shown in Figure 2.11. This selection is dependent on the simplicity, ease of fabrication, low cost of construction, and additional heat-transfer surface [101]. Another technique used for performance improvement in LHTES is enhancing the thermal conductivity of PCM. It involves mixing low density conductive materials with PCM that results in better thermal conductivity and higher heat exchange rate. The similar results are obtained by using nano PCM, that is developed by mixing different types of nano particles with PCM [102, 103]. KOK and GÜRTÜRK [104] studied the heat

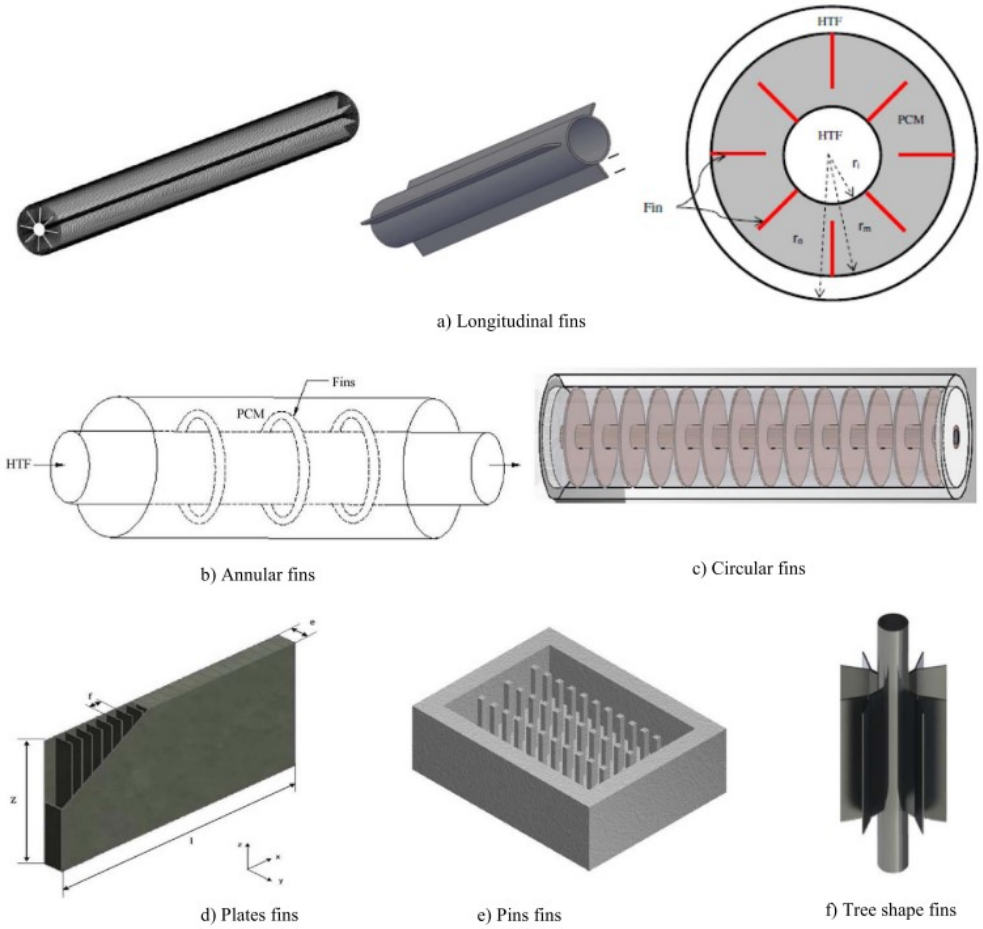


FIGURE 2.11: Different fin configurations [60].

transfer performance during the solidification of PCM and nano- PCMs ($Al_2O_3$ - $CuO$). They performed experimental and numerical studies with and without fins. Their findings showed that in the solidification process, due to over-cooling effect of PCMs, fins did not have significant effect. Base- PCM solidified in the heat storage tank in 10 minutes, but the solidification of the PCM with fins took 11 minutes. The heat storage tank's solidification using nano- PCM was completed in 13 minutes.

In an experimental study [105] authors studied the effect of surface areas of the heat transfer fins on the melting and solidification process of PCM in a thermal energy storage device. They identified that surface area of the fins had positive effects on heat transfer, but negatively effects natural convection current. They could obtain an improvement of 65% in the performance of the energy storage device with a specially designed fin.

In an another 3D numerical study, [106] combined Monte Carlo Ray-Trace (MCRT), Computational Fluid Dynamics (CFD), and thermal stress analysis with the static structural module of ANSYS to explore thermal performance and thermal stress studies of Parabolic Trough Collector (PTC) receiver. Initially they investigated how the material of the tube affected heat transfer. Thermal stresses and temperature gradients were compared. In the second phase, they used $Al_2O_3 - H_2O$ based nanofluid at different volume concentrations and examined the impact of nanoparticle addition on the Heat Transfer Fluid. A ratio of 1%–6% of nanoparticle volume concentration was found to enhance the ptc's thermal performance.

## 2.7 Geometric Modifications

The most common approach uses geometric alterations to the fins and container of the LHTES [93–95]. Shell and tube, spherical, and rectangular are typical geometric shapes in thermal energy storage systems [96–99]. Rectangular thermal energy storage units are chosen, however, due to its ease of manufacturing and installation, cost-effectiveness, and energy storage performance [107].

The current level of research on heat transport in a spherical shell is taken into account by [108]. The authors examined heat transmission in PCMs for restricted melting (solid PCM fixed inside the vessel), unconstrained melting and solidification (unfixed), and phase transition in finned shells. It was demonstrated that the restricted melting process as it exists was not well described. Some important recommendations they made are to use dimensionless forms for results and reliably measuring thermophysical properties of PCMs or mixtures closer to melting point.

### 2.7.1 Shell and Tube Configuration

Cylindrical pipes have a high efficiency in a small volume and are used in the majority of engineering systems, cylindrical shapes are thought to be the most

promising for the components of commercial heat exchangers. There are four different types of cylindrical PCM- LHTES container configurations. The first is a pipe model as shown in Figure 2.12a, in which the HTF flows via a single pipe while the PCM fills the shell. In the second type shown in Figure 2.12b, which is a cylinder, the PCM fills the tube while the HTF flows perpendicular to it. In the third model, the HTF flows through one side of a shell and tube while the PCM fills the other side [60].

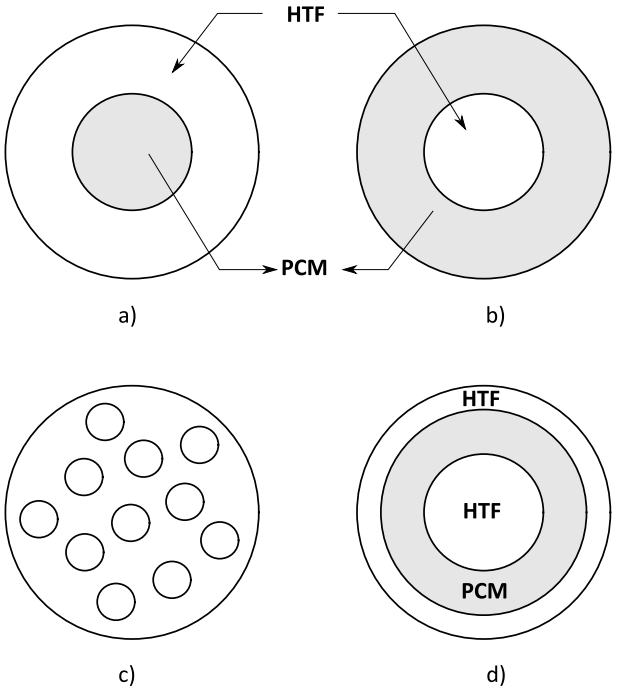


FIGURE 2.12: Types of shell n tube a) Tube b) Shell c) Pipes d) TTX.

Akgün et al. [109] experimentally analyzed a shell-n-tube type LHTES system. In their study they used three kinds of paraffin as PCM, with different melting temperatures. The heat transfer fluid used was water. They suggested a geometry with annular space and conical shell. In order to improve the performance that titled the outer surface of the container by 5°. They found the impact of Stefan and Reynolds numbers on melting and solidification behavior. It was revealed that the unique tube-in-shell storage design used in this investigation indicated excellent outcomes.

Malik et al. [38] numerically investigated the performance of a shell and tube LHTES unit subjected to fluctuating thermal cycles of waste heat. The waste heat was obtained from clinker cooling process (420K - 600K) as Cycle 1 & 2. The Cycle 3-5 were based on the internal combustion engines (360K - 780K). In their study, HITEC® industrial salt as PCM was used. They found that in Cycle 1 melting time was 41.6% higher than Cycle 2. Similarly, Cycle 5 accelerated the PCM melting by 37.4% and 33.3% compared to Cycle 3 and Cycle 4.

In another study, PCM melting enhancement was numerically studied using multiple tubes and modified shell designs by Qaiser et al. [98]. PCM was placed inside the heat-transfer fluid-carrying copper tubes and steel shell of the annulus. Using a single Y-fin HTF tube as the base case, two to five tubes were divided up into multiple configurations while maintaining constant PCM mass. Compared to the Base Case, the vertical double tube and triple tube V-configurations increased average heat transfer rates by 33.6% and 23.7%, respectively.

Qaiser et al. [110] numerically analyzed the effects of tube and shell geometric designs on the improvement of latent thermal energy storage system's thermal performance. HTF tubes were altered to include hexagonal, pentagonal, square, and triangular geometries as shown in Figure 2.13. All other tube configurations fell short of the performance of triangles with the vertex facing downward. In comparison to the base scenario, it increased the energy storage capacity by 3.72% and the PCM melting rate by 27.2% in thermal energy storage device. Moreover, several bottom vertex angle triangulated shell designs were also investigated. The shell's bottom vertex angle of 75° provided the greatest improvement. Compared to the base case, it increased the energy storage capacity by 23.7% while speeding up the PCM melting rate by 66.9%.

Sabir et al. [111] numerically investigated the performance of dimpled tubes with different geometric pitches under a fixed heat flux of $10\,kW/m^2$. The performance of improved tubes with ellipsoidal 0°, teardrop, and ellipsoidal 45° dimples of equivalent volumes was studied. It had been found that the variation in dimple pitch ($P$) and $Re$ had a substantial impact on the performance of dimpled tubes.

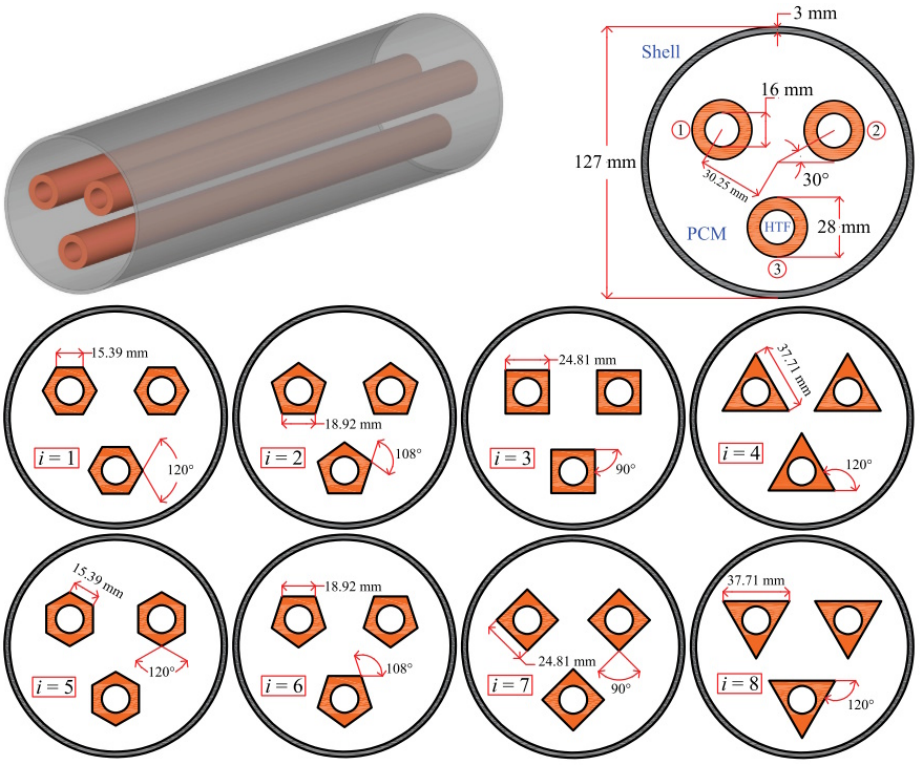


FIGURE 2.13: Multi-tube LHTES system model and geometric modifications [110].

The thermal-hydraulic performance was improved by 45.7% using ellipsoidal 45°, and 31.2% using teardrop dimpled tubes with the ideal pitch.

### 2.7.2 Triplex Tube Configuration

The triplex tube heat exchanger (TTHX), shown in Figure 2.12d, is another cylindrical arrangement in which the PCM fills the central tube and the HTF flows through the inner and outer tubes. In order to determine the effects of raising the HTF-inlet temperature on the melting and solidification of paraffin (RT50) as a PCM inside a shell and tube heat exchanger, Hosseini et al. [112] undertook a combined experimental and numerical investigation. According to their findings, the theoretical efficiency increased by 81.1% to 88.4% and by 79.7% to 81.4%, when the HTF-inlet temperature was raised from 70 degrees to 75°and then to 80°.

A novel fins configuration in a triplex tube heat exchanger was numerically investigated by Mahdi et al. [113]. They used a variety of fin configurations at different regions of heat exchanger. The new structure of fins was proposed in light of their findings. In order to determine the effectiveness of the suggested fin structure, three instances were compared: the proposed innovative case, the LHTES system with traditional fin system, and the LHTES system containing nanoparticles in the same storage volume of the heat exchanger. They suggested that improving the fin volume utilization as well as adopting a suitable fin arrangement between the upper and bottom halves of the domain could improve PCM melting in the TTX. Their findings demonstrated that the use of a relatively modest number of medium-sized fins at the upper half of the annulus enhanced convective heat flow into the PCM sufficiently, enabling faster melting of the PCM. Fakhar et al. [114] investigated the use of branched fins and nanoparticles to improve the melting process of PCM in a horizontally configured thermal energy storage unit. Different fin designs, including all-straight, single-branched, and double-branched, were analyzed, showing significant time savings of up to 45.9% and increased energy storage capacity. Furthermore, the addition of $Al_2O_3$ nanoparticles to the PCM further enhanced the melting performance, resulting in additional 26.8% time savings.

A PCM-based heat storage unit with vertical triple-pipe heat exchanger was used by Abed et al. [68] to increase melting performance over a double-pipe system. To enhance heat transfer efficiency, the fins were positioned in inline and staggered patterns. Both the upward and downward orientations were considered for the quarter-spherical fins. A faster rate of heat transfer was observed from the staggered fin layout. Moreover, the downward quarter-spherical fins with a staggered layout exhibited the best performance and the heat storage rate increased by over 78% compared to the case without fins, cutting the melting time in half.

Zhang et al. [115] created a mathematical model of PCM melting in triple-tube heat exchanger and tested against experimental data. The evolution and deformation of solid-liquid interfaces, the distribution of isotherms, the time-varying

profile of liquid fraction, and the average temperature over the course of the melting process were discussed in relation to the impact of various fin layouts and volume fractions of nanoparticles on the melting process.

The results showed that employing the improved techniques of innovative fins and nanoparticles improved the melting characteristic. Four different unique fins had melting times that were lowered by 80.35%, 77.62%, 77.33%, and 80.65%, respectively, when compared to the original structure. This was due to the system's improved heat transport as a result of the addition of fin configurations.

### 2.7.3 Rectangular Wall Heated Configuration

Due to their straightforward design, cost-effectiveness, and energy storage efficiency, rectangular thermal energy storage systems have garnered a lot of attention [107]. Applications for rectangular LHTES include solar collectors [116], solar stills for water desalination [117], power electronic equipment [118], large-scale heat storage tanks [104], space craft thermal control [119], and building materials such as walls, bricks, and shutters [120, 121].

The behaviour of PCM melting in a rectangular enclosure and the impact of adding horizontal fins were experimentally investigated by Kamkari and Shokouhmand [122]. The melting process was visualised to highlight both how crucial natural convection was to the melting process and how much partial fins may hasten it. In comparison to the basic case with no fins, they discovered a reduction in melting time of 18% for the 1-fin case and an improvement of 37% for the 3-fin arrangement.

For a rectangular LTESU heated from a single side, the effect of fin size and distribution on the buoyancy-driven heat transfer mechanism was quantitatively investigated by Biwole et al. [123]. For three hours, a steady heat flow of $1000 W/m^2$ was applied to one side of the enclosure to warm it up. Both the fin mass and the PCM mass were constant. The outcomes were contrasted with an un-finned reference case. The researchers came to the conclusion that larger surface areas

led to more overall heat transfer in the PCM and lower front plate temperatures. They deduced that if keeping the front temperature low was the design objective, the 16 fin layout would offer the optimal temperature management mechanism.

Ji et al. [124] examined the effects of different fin ratios of fins attached to the upper and bottom portions of the isothermally heated single wall in a numerical investigation of a rectangular thermal storage unit. The results demonstrated that natural convection significantly enhanced when the fin length ratio was less than 1.0 while it reduced in configurations with fin length ratios greater than 1.0. When the results were compared to the setup with a fin length ratio of 1.0, they showed a saving of 25% in melting time. Abdi et al. [125] numerically studied a rectangular LTESU with vertical fins. The fins were connected to the lower horizontal wall. The melting time was reduced by 12% in the case designed with long fins but it resulted in reduction of 6% energy storage capacity. This indicated an important aspect in the design of LTESU. Some design changes could positively affect one performance parameter while have a negative result on another performance parameter.

A vertical rectangular fin array on a vertical base was experimentally evaluated for its thermal performance by Yazicioglu and Yüncü [126]. They altered fin height and spacing in their investigation. They demonstrated how the geometric characteristics and the temperature difference between the base and environment affect the convective heat transfer rate. They experimented with 30 various arrangements and discovered that the ideal fin spacing fell between $10.4mm$ and $11.9mm$. A 41.28% improvement in the average heat transfer rate was the highest that was seen. The variance in fin thickness was not studied.

In another study, Bouhal et al. [127] numerically investigated the thermal performance of a rectangular LTESU enhanced with horizontal triangular partial fins. The rectangular shaped fins produced faster melting rates as compared to triangular fins. The results also manifested that the role of geometric configuration of the fins is very important in thermal performance enhancement of LHTES.

Similarly, [128] employed stepped fins to numerically investigate the melting performance of PCM enclosed in the rectangular LHTES. The enclosure was heated from single vertical wall. The results of the LHTES enhanced with stepped fins were compared to the case with straight horizontal fins. The impact of using downward stepped fins on PCM melting showed an improvement up to 65%. This configuration improved convection current on the upper part and enhanced heat transfer during the final phases of melting. In this study right angled fin steps were used where the parameters were changed uniformly. The study could be enhanced by allowing changing parameters for each step and investigated the thermal performance of the system.

Mahdi et al. [129] performed an experimental and numerical investigation of thermal energy storage performance of a rectangular LHTES by employing an innovative design that divided the rectangular plane into small partitions (1, 2, 8, 16, and 32). The idea was to trap the melting PCM in the partitions creating multiple melting fronts. The number of the partitions was varied based on the cavity aspect ratio with values 2, 1, 0.5, 0.25, 0.125, and 0.0625. They found that the optimal design was with 0.25 cavity ratio and 8 partitions. The performance improvement was observed with respect to a normal 1-partition cavity. It was found that melting process with 2, 4, 8, and 16 partitions showed an improvement of 31.2%, 53.6%, 65%, and 68% respectively. A similar study could be conducted by defining different shapes of the partitions, like square, triangular, or quadrilateral.

In another numerical study, Kasper et el. [130] studied different design parameters for improving melting and solidification performance of a finned rectangular thermal energy storage device. The parameters studied were cavity inclination and fin spacing to study the melting and freezing rates of the energy storage unit. Fekadu and Assaye [131] numerically investigated melting rate enhancement of PCM in a bottom wall heated rectangular enclosure keeping all other walls adiabatic. They studied the performance changes by varying number of fins and their angles to identify the best performing configuration. It was found that the optimal design with 2 fins reduced the melting time by 43%.

A parametric study was conducted by Arshad et al. [132] to investigate the performance of a heat sink by utilizing PCM and fins in applications for thermal management of electronic components. Two distinct volume fractions of 10% and 20% of plate-fin heat sinks with 10, 15 and 20 mm fin heights were chosen. RT-35HC was utilized as the PCM. At the heat sink base, a constant input power was applied to simulate the heat produced by an electronic device. They found that by increasing the fin height and quantity for both volume fractions of fins, a lower heat sink base temperature was attained. The 20 mm fin height of 20% volume fractions of fins demonstrated a superior reduction in heat sink base temperature when compared to the 10% volume fraction PCM filled finned heat sink. However, a 20 mm fin height with a 10% volume percentage of fins was projected for the higher phase completion time during melting. Greater fin height and fin count result in a faster melting rate.

In another study shape and position of fins were used to investigate the thermal performance of rectangular LTESU by Sinaga et al. [133]. In their study lauric acid was used as PCM. In the first stage of their study three positions for rectangular fins were considered. They observed that the best results were obtained when fins were located at the lower half of enclosure. The second stage of their study considered two trapezoidal and one triangular shaped fins. The optimum positions obtained from the first stage results were used for fin placement. Their results concluded that triangular shaped fins produced best results.

Wang et al. [134] numerically studied "L" shaped fin in a rectangular enclosure instead of simple horizontal fins. In their study, the enclosure was heated from the one side wall and ratio of horizontal and vertical segments of the "L" geometry and orientation of the the fins were used variable parameters. They found that these parameters had a significant impact on the thermal performance of the LHTES. The best case in their research was found to be the one where fin was mounted to the lower side of the wall and had $40mm$ horizontal and $20mm$ vertical dimensions for the "L" shape. They showed 45% improvement in melting time compared to the reference case with two horizontal fins.

Kamkari et el. investigated experimentally the melting rate of PCM in a single wall heated rectangular enclosure[135]. The orientation angles of the enclosure were varied from 0° to 90°. The vertically oriented (90°) case was selected as a reference for comparison of results. A 35% and 53% reduction in total melting times for 45° and 0° orientations, respectively, was observed. Additional enhancement of up to 35% was achieved when wall temperatures were increased from 55°C to 70°C.

In another experimental study, Kamkari and Groulx [136] used lauric acid to investigate the impact of orientation of a finned rectangular chamber that was heated from one side wall. The increased convection and lower melting time was observed in enclosure with vertical configuration than the horizontal configuration.

In another study of a rectangular thermal energy device that was inclined at different angles and filled with lauric acid and paraffin wax, thermal performance was analyzed experimentally by Shathe and Dhoble [137]. They varied the enclosure angle with respect to the horizontal plane from 30°, 60°, to 90°, and concluded that as the inclination angle is increased, natural convection increased and resulted in higher melting rate.

In a numerical investigation of a rectangular PCM storage unit, effects of changing aspect ratio (Height to Width ratio) were studied for performance enhancement [138]. In this study different sides of the enclosure were heated and elaborated comparison was conducted to analyze the PCM melting rate. The best melting time was reported for enclosure whose aspect ratio was less than 1.25 and that was heated from bottom side.

To speed up the melting of PCM, three conductive fins were connected to the heated bottom wall in various locations of a horizontal rectangular enclosure and numerically studied by Laouer et al. [139]. To examine their impact on melting rate, several dimensionless fin lengths ($a/H = 0.25, 0.50, and 0.75$) and dimensionless fin positions ($b/L = 0.15, 0.25, 0.35, and 0.75$) were taken into consideration as parameters.

Finding the ideal fin lengths and spacing between them was the key goal in order to get the maximum storage performance. The entire melting period was reduced by 15.1%, 40.7%, and 70.1%, respectively, when the ratio of fin lengths of $a/H$ was increased from 0.25 to 0.75. When PCM was completely melted, the optimal compromise position ratio for short fins at $a/H = 0.25$ was $b/L = 0.48$; however, when $a/H > 0.50$, it was $b/L = 0.35$.

To comprehend the effect of fins on the thermal performance of rectangular storage tanks that are positioned vertically and horizontally, a parametric research was carried out by Safari et al. [140] keeping the mass of PCM in the tank and the fin volume constant during numeric simulations. In their findings, they implied that longer, thinner fins were preferable than shorter, thicker fins for increasing melting rate. It was determined that adding more fins did not always speed up melting for horizontal enclosures with fin lengths of 25 and $35mm$. When nine $45mm$ long fins were utilized in a horizontal enclosure, the highest melting time decrease compared to the 3-fin vertical enclosure with a fin length of $25mm$ was 75.1%.

Barthwal et al. [141] studied rectangular, triangular, and Y-type fins for two storage/sink enclosure orientations: upright ($\theta = 90°$) and inclined ($\theta = 35°$). In addition, three fin configurations—equal, decreasing, and increasing-stepped were examined based on how the fins were arranged along the enclosure height. Based on variables, the time enhancement ratio, suppression ratio, liquid fraction, temperature distribution, melt velocity magnitude, storage capacity/rate, and enhancement in Nusselt number, the performance of each storage unit (orientation/fin-type/fin-arrangement) was evaluated. For inclined and vertical enclosures, respectively, equal and increasing-stepped Y-fin designs produced the largest time enhancement ratios of 42.38% and 29.86%. Additionally, as compared to other fin types, Y-fins-based enclosure provided a higher average suppression ratio. Nusselt number was found to increase by 2.56, 2.67, and 2.64 times for upright enclosures with rectangular, triangular, and Y-shaped fins, respectively.

To speed up the melting of phase-change materials, Xu et al. [142] investigated the structural parameters of longitudinal rectangular fins utilized in a horizontal shell-and-tube latent heat storage unit while taking into account the natural convection during melting process. A new coupling approach between genetic algorithms and computational fluid dynamics was created due to the phase-change heat-transfer optimization problem's excessive non-linearity and high computational cost. The ideal construction characteristics, including the length, width, and placement of each fin, were explored along with the impacts of the fins' thermal conductivity, filling rate, and number. In their results, they found the ideal dimensionless fin length and fin angle to be around 0.96 and 0.2 respectively.

## 2.8 Conclusion

From the above studies, it is concluded that fin configurations and container configuration including shape, have an influence on the melting process. These are important parameters in the design of for a LHTES. To the best of author's investigation and knowledge, no studies in the literature, described previously, investigated qualitative and quantitative effects of fin-distribution in a rectangular cavity using mathematical functions on the performance of energy storage behavior of LHTES using stearic acid as PCM and isothermally heated from side walls. This study, therefore, investigated the impact of different fin configurations that are defined by using mathematical functions and the resulting model is numerically studied to investigate the thermal response in terms of melting time and heat transfer storage rate of rectangular LHTES.

First an experimental setup is used to study the melting behavior of the rectangular enclosure with fins connected to isothermal side walls. A reference numerical study was performed to set the parameters for numerical analysis matching with the experimental results. Furthermore, numerical studies were performed by varying different design parameters. The volume of PCM was kept constant in all current studies. Additionally, the effect of aspect ratio of the cavity, and the variation in

the wall temperature of LHTES are also analyzed for melting and thermal energy performance enhancements.

Finally two new correlations, one for melting $Fo$ (Fourier number) with respect to $Ste$ (Stefan number) and the second one for $\bar{Nu}$ (average Nusselt number) with respect to $Ra$ (Rayleigh number), are developed. A wide range of operating temperature could use these correlations for studying the behavior of the system for different applications.

# Chapter 3

# Experimental Study and Numerical Formulation

## 3.1 Introduction

In this study, various latent heat thermal energy storage devices were modeled by varying different design parameters, such as, fin thickness, fin length, fin orientation, fin displacement, and container geometry aspect ratio. A reference case with designed and manufactured. It had six fins with uniform length, thickness and displacement along the heated walls. The chamber and fins were heated from side walls. Multiple experiments were performed to observe the melting process and transient behavior of Phase Change Material (PCM) temperature and liquid front was recorded. In order to investigate the thermal performance the design changes were made to the reference case and studied numerically using Computational Fluid Dynamics (CFD) software. Initially reference case was replicated numerically and numerical parameters were adjusted so that the results are congruent to the experimental results. This enabled to execute further numerical studies with higher confidence. Overall, this study represents a comprehensive approach to investigating the thermal performance of Latent Heat Thermal Energy Storage (LHTES) devices, combining experimental observations, numerical simulations,

and sensitivity analyses. The findings contribute to the advancement of energy storage technologies and pave the way for more efficient and sustainable utilization of thermal energy resources.

## 3.2 Experimental Setup

The experimental setup was designed with the help of Computer Aided Design (CAD) software Autodesk Fusion 360. The design was used to manufactured the model Latent Heat Thermal Energy Storage (LHTES) unit as per specifications. The main design elements were LHTES chamber, heat exchangers, and fins as shown in Figure 3.1.

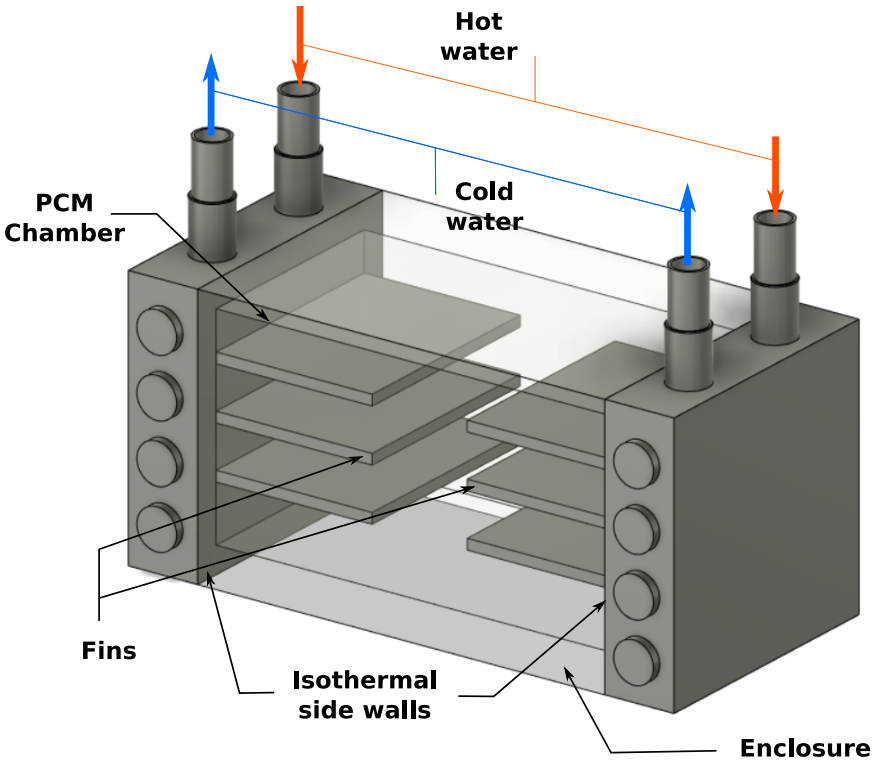


FIGURE 3.1: 3D isometric view of design of experimental LHTES device .

The dimensions of the device are shown in Figure 3.2. The chamber was made of 25$mm$ thick acrylic. The both sides of the chamber were connected with Aluminum based heated walls on which Aluminum fins were attached. The enclosure was filled with PCM in liquid state. The mass of PCM filled in the chamber was

$3.4kg$ and its volume per depth was $0.0282mm^3/mm$. In order to provide isothermal temperature to these walls, hot water based Aluminum heat exchangers were connected to these walls. The hot water at the required temperature was circulated through these exchangers that transferred the heat through conduction to the hot walls, then to fins and eventually to PCM. To monitor the temperature distribution and evolution of the immediate solid-liquid interface, a rectangular thermal storage experimental unit was devised and built as mentioned in the preceding paragraphs. In Figure 3.3, the experimental setup's schematic and the heat exchanger that was utilized to transmit heat to the PCM are displayed.

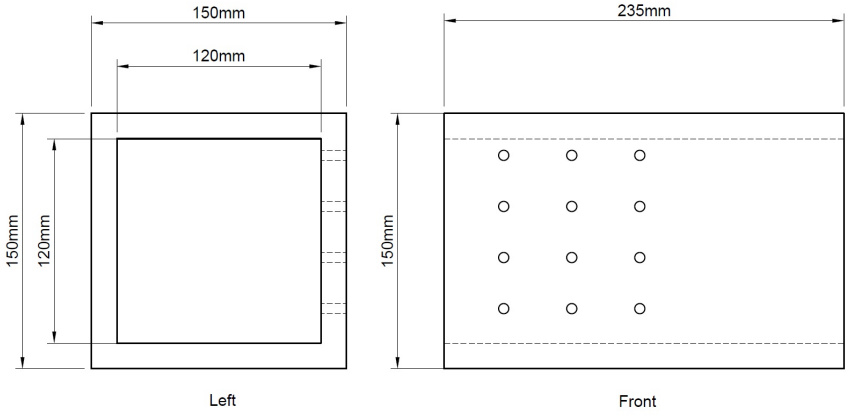


(a)

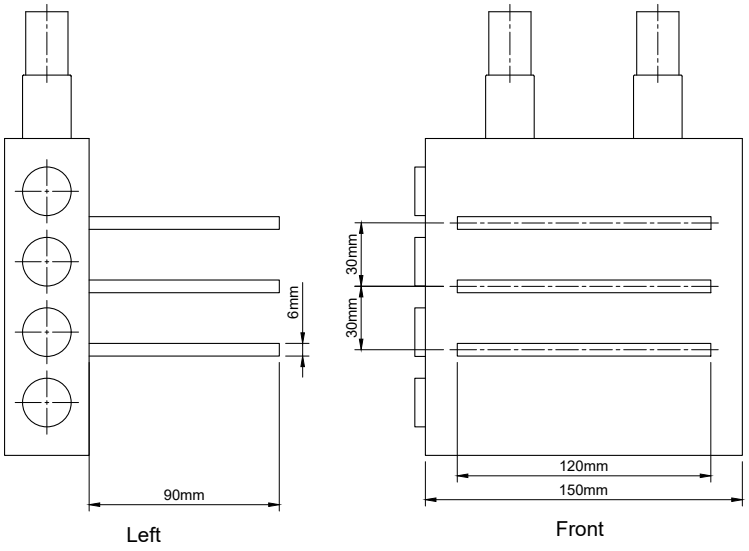


(b)

FIGURE 3.2: Schematic drawing of (a) PCM enclosure and (b) Heat exchanger and fins.

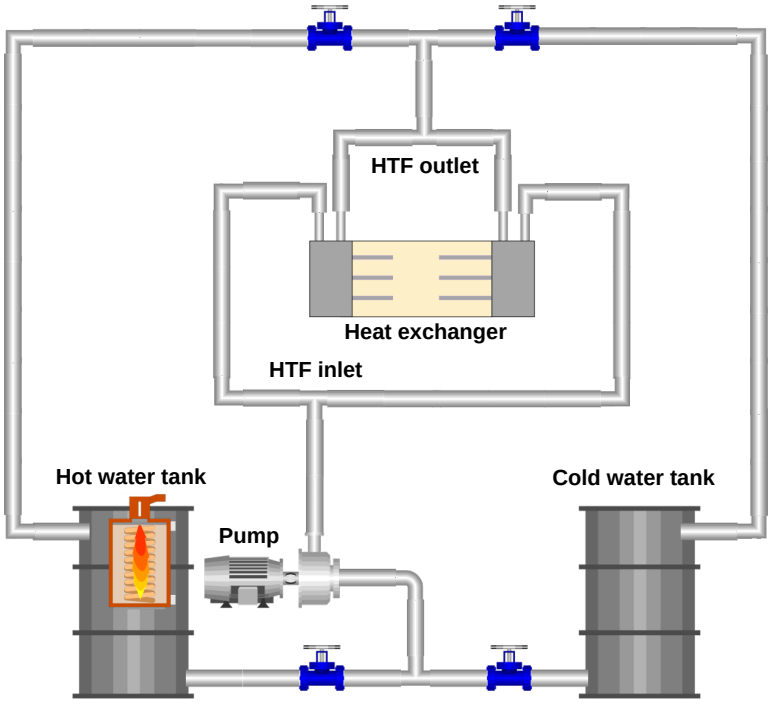


FIGURE 3.3: Schematic view of experimental setup.

The rectangular enclosure's dimensions were $235mm$ in width, $125mm$ in height, and $125mm$ in length. The fins that are connected to the walls were $6mm$ thick, $90mm$ wide, and $120mm$ long as shown in Figure 3.2.

To provide heat at a constant temperature, heat exchangers made of $35mm$ thick high conductive aluminum slabs were attached to the enclosure's side walls. Water circulating within these slabs was used to achieve isothermal temperature as shown in Figure 3.4. A valve system connected the hot and cold constant temperature water tanks to the heat exchangers. The enclosure's remaining walls were built from translucent acrylic sheets that were $12mm$ thick. The transparent walls allowed for the visualization of the melting process and the photography of melt-fraction. The acrylic's low thermal conductivity reduced heat loss from the enclosure. Glass wool sheet ($k = 0.042, W/m.K$ [143, 144]) connected to the lateral faces served as additional insulation. The hot water tank delivered hot water that was in the range between $70°C$ and $90°C$. Four $1500\,W$ heaters, electronic thermostat STC-100A temperature controller with NTC type temperature sensor implanted in the water bath, and thermal regulator with a $\pm 0.5°C$ accuracy were part of the PID temperature control system.

(a)

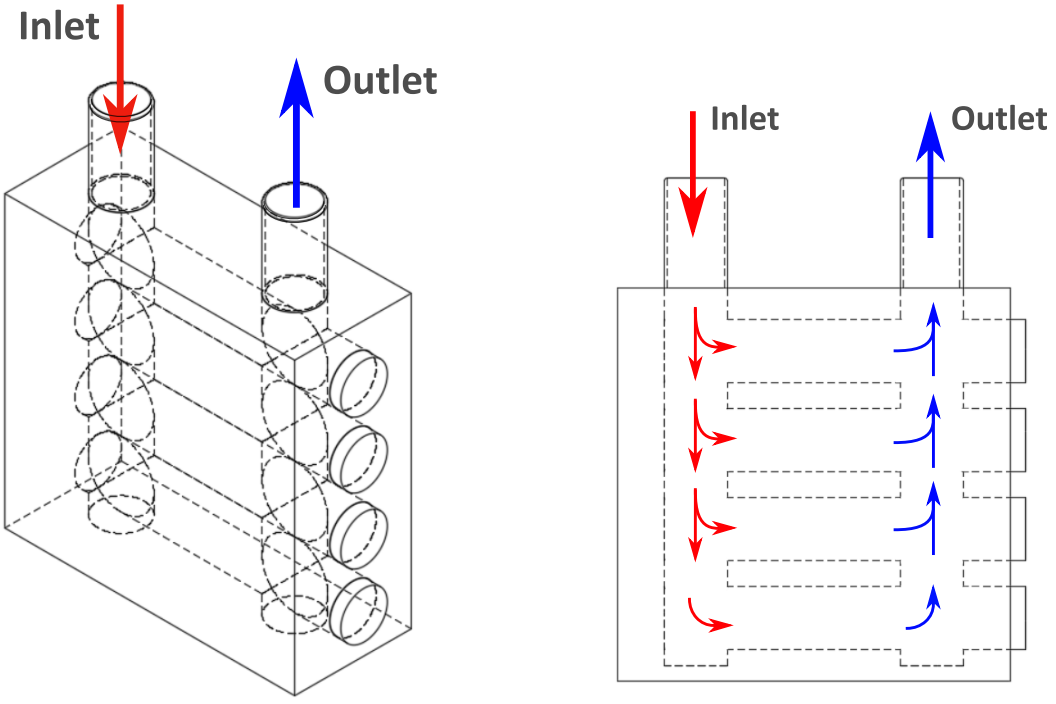


(b) (c)

FIGURE 3.4: Heat exchanger and water flow through its inner channels (a) Photograph of heat exchangers, (b) 3D Cad model, and (c) Front view.

To gauge the temperature distribution inside the container, there were twelve K-type thermocouples with a precision of ±0.5 °C. These thermocouples were positioned so that their sensors were at the enclosure's vertical mid-plane and these were placed in four rows and three columns. This configuration made it possible to see the PCM's temperature distribution in the LHTES in an appropriate manner. The sixteen-channel Data Acquisition (DAQ) system was wired with

(a)

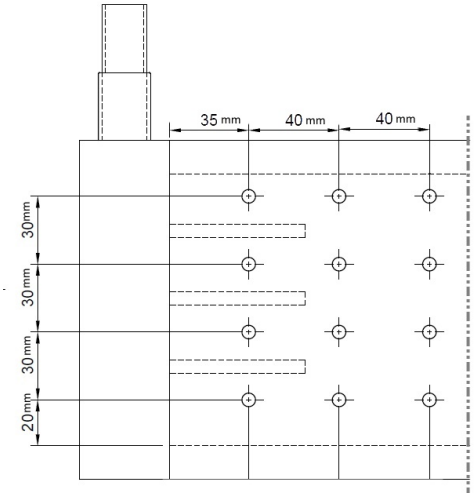


(b)

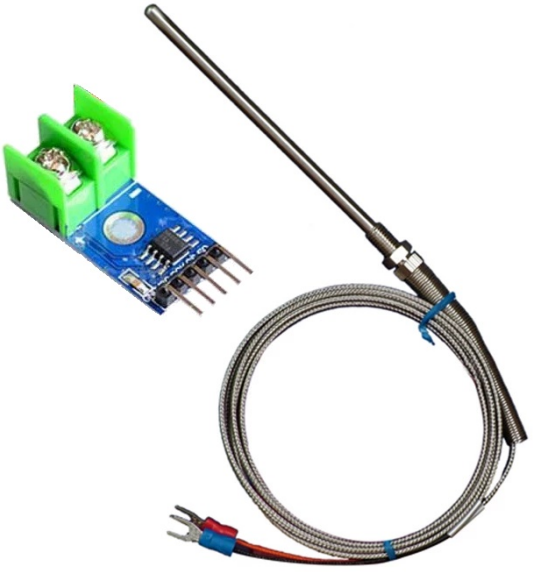

(c)

FIGURE 3.5: (a) PCM filled LHTES, (b) Placement of thermocouples, (c) K-Type thermocouple and MAX6675 module.

connections for all thermocouples. The DAQ was connected to the laptop using serial port interface. At predetermined intervals, the data was recorded on the computer using Serial Port Monitor software.

Photographs of the latent heat thermal storage device, placement of thermocouples and a closeup of K-Type thermocouple with MAX6675 module for temperature reading are shown in Figure 3.5. The experimental apparatus included a heat exchanger, a rectangular PCM enclosure, and hot and cold water tanks with

constant temperature supply. Temperature regulation was provided via a temperature controller (SP100), and temperature measurements were recorded using a 16-channel data acquisition system. A circulation pump was used to move the water through the plumbing system. Snapshots of the PCM during the melting process were taken using a digital camera (NIKON 3500). Data processing and analysis were done on the laptop.

In this study, a chemically stable, non-toxic and having a high latent heat of fusion PCM stearic acid was used. Due to its operating temperature range, stearic acid can be employed in medium-temperature thermal storage applications. Stearic acid is translucent in the liquid phase but has a white tint in the solid form. This color contrast made it simple to distinguish between the two phases and helped during the melting process to follow the interface, see Figure 3.6. The heat exchanger with LHTES, hot and cold water baths, water flow loops, thermocouples, and a temperature controller can be seen in Figure 3.5. Thermal properties

(a) (b)

FIGURE 3.6: (a) Solid and (b) liquid phases of stearic acid ( PCM).

of stearic acid including melting temperature range, latent heat of solid–liquid phase change and specific heat capacity were determined by Differential Scanning Calorimetry (DSC). The DSC thermal analyses were performed with a heating rate of 5°C/min in the temperature range from 20°$C$ to 70°$C$.

The onset melting temperature of the PCM is obtained as the intersection point between the tangent line at the point of the maximum slope of the DSC peak, and the base line taking into account the change of heat capacity between the solid and the liquid phases, as shown in Figure 3.7. Melting temperature range was measured with an accuracy of ±0.2 °C. The latent heat of solid–liquid phase change was calculated by numerical integration of the area under the peak of the DSC curve. Figure 3.7 shows the DSC heating thermogram of stearic acid. Some of the thermal properties were obtained from literature. All of the thermal properties of stearic acid are shown in Table 3.1. The components of the experimental setup are shown in the Figure 3.8.

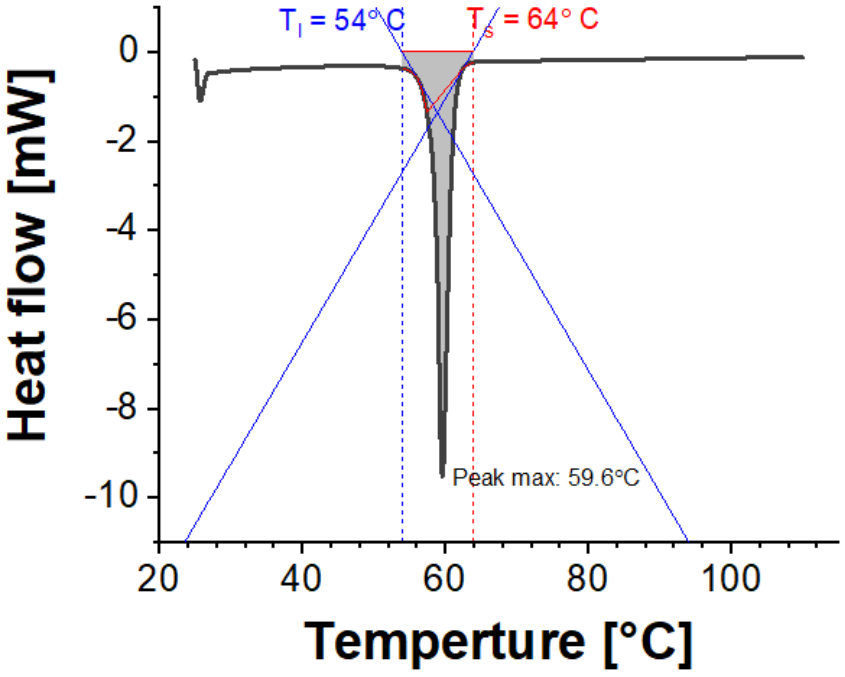


FIGURE 3.7: DSC heating thermogram of stearic acid.

The water in the hot tank was heated to $Tw = 85°C$ by $6kW$ heater. Temperature controller was used that maintained the temperature at the configured value. When required water temperature was obtained, the hot water was circulated through the heat exchanger at the start of the experiment. In order to visualize the melt-front, photographs were taken at regular intervals. The front face insulation of the enclosure was periodically removed for this purpose. Temperatures were logged using thermocouples and DAQ system every second. The solid form

TABLE 3.1: Thermophysical properties of Stearic acid [96].

| **Property** | **Symbol** | **Value** |
|---|---|---|
| Liquidus temperature | $T_l$ | 327.1 $K$ |
| Solidus temperature | $T_s$ | 337.5 $K$ |
| Density (solid) | $\rho_s$ | 1150 $kg/m^3$ |
| Density (liquid) | $\rho_l$ | 1008 $kg/m^3$ |
| Specific heat capacity (solid) | $c_{ps}$ | 2830 $J/kg.K$ |
| Specific heat capacity (liquid) | $c_{pl}$ | 2380 $J/kg.K$ |
| Latent heat capacity | $h_{sf}$ | 186500 $J/kg$ |
| Thermal conductivity | $k$ | 0.18 $W/m.K$ |
| Dynamic viscosity | $\mu$ | 0.0078 $Pa.s$ |
| Thermal expansion coefficient | $\beta$ | 0.00081 $1/K$ |

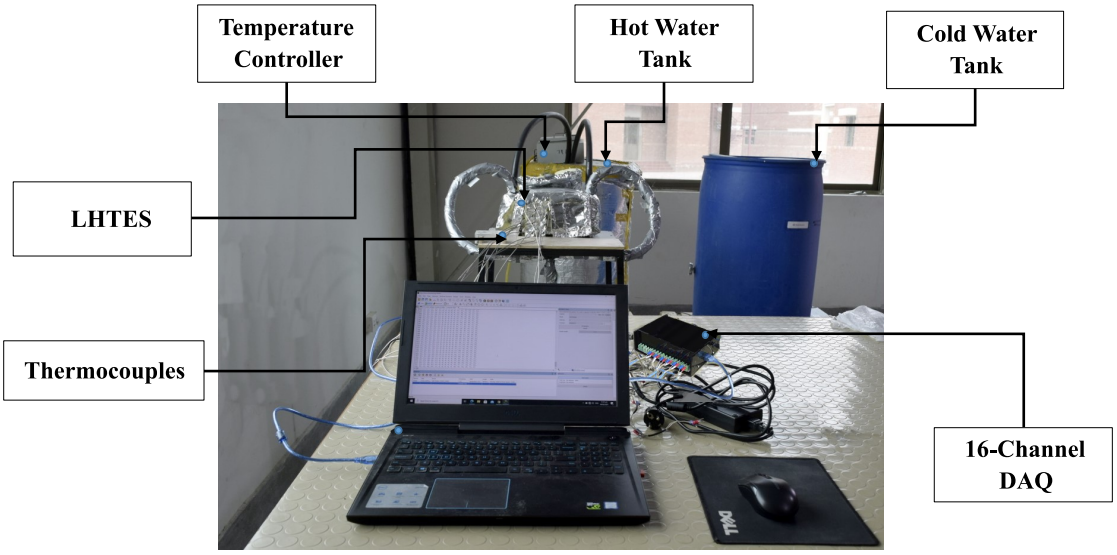


FIGURE 3.8: Components of the experimental apparatus.

of the stearic acid is a white powder. The melted PCM was poured into the enclosure gradually in a layer by layer manner so that each layer height did not exceed 1 cm. Each layer was allowed to solidify completely and then the next layer was added until the whole enclosure was filled with the solid PCM. The objective of this filling procedure was to ensure that no air pocket was formed inside the solid PCM.

In order to establish a constant initial thermal condition for all the experiments, cold water at room temperature (20 °C) was circulated through the heat exchangers attached to the side walls of the enclosure, to provide a uniform temperature in

the initial solid PCM prior to the start of each experiment. Water circulation was continued until all thermo-couple readings were uniform within 1 °C.

The experiments were started by circulating the water at required temperature through the heat exchanger. For visualizing the melt front, the insulation of the front face of the enclosure was periodically removed and photographs were taken at time intervals of approximately 10 min.

Temperature distributions at the vertical mid-plane of the enclosure were logged every second. There were two experimental runs performed in the lab. In the first experiment HTF temperature was set as $Tw = 85°C$ and in the second experiment it was set as $Tw = 75°C$. The experiments were conducted till 70% of the PCM was melted and analyses were performed on the recorded data.

## 3.3 Uncertainty Analysis

The inherent mistakes that occur during experimental measurements always have an impact on the reliability of the particular measuring devices, which has an impact on the uncertainties of the experimental results. The propagation of uncertainty in the outcome is influenced by the uncertainties of independent variables, according to Kline and McClintock's uncertainty analysis technique [145].

The uncertainty of result $U$ is achieved by suitably combining the uncertainties of independent variables $U(x_i)$ as follows, assuming that the final result is derived from independent variables $x_1$, $x_2$,..., $x_n$.

$$\begin{aligned} M &= f(x_1, x_2, ..., x_n) \\ U(M) &= \sqrt{\sum_{i=1}^{n} (\frac{\partial f}{\partial x} U(x_i))^2} \end{aligned} \tag{3.1}$$

The independent variables in the experiment were temperature and liquid fraction. The time is measured at fixed intervals when liquid fraction was evaluated. The

uncertainties ($\sigma$) in these variables are shown in Equation (3.2).

$$\begin{aligned} \sigma_{Lf} &= \pm 5\% \\ \sigma_T &= \pm 0.5^{\circ}C \end{aligned} \tag{3.2}$$

The melt fraction uncertainty is found to be 5% and the total absorbed energy uncertainty to be 7%.

## 3.4 Post Processing of Experimental Results

As explained earlier, during the experiments of melting process, snapshots of the PCM enclosure were taken at regular intervals. Photographs of initial, intermediate, and final stages of the melting process are shown in Figure 3.9.

### 3.4.1 Interface Detection and Image Based Liquid Fraction Estimation of PCM

The snapshot shown in Figure 3.10a illustrates the state of PCM in the enclosure after 45 minutes in the melting process. The photograph was processed and converted to black and white binary image for evaluating liquid fraction as shown in Figure 3.10b. The black area indicates the liquid phase of PCM while white area shows solid phase and metallic fins. The liquid fraction was calculated using the procedure described in subsequent paragraphs.

As shown in Figure 3.11, the (black and white) image was used to find the total number of pixels ($NP_t$), number of black pixels ($NP_b$), number of white pixels ($NP_w$), and number of pixels covered by fins ($NP_f$) using the image processing software **paint.net 5.0.2** and **GIMP 2.10**. The image processing included correcting the rotations and skewness of the photograph so that front face of the LHTES system is clearly visible. The extra objects captured in the image were removed by cropping and focusing on the face of chamber (see Figure 3.9).

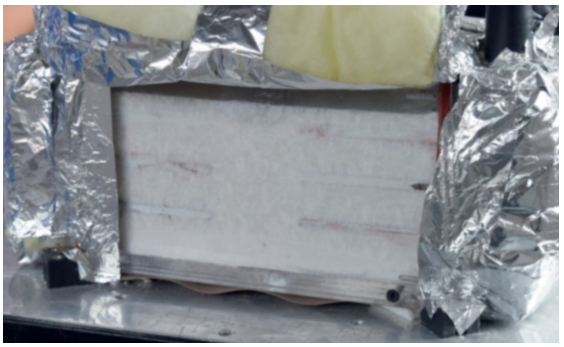

(a)

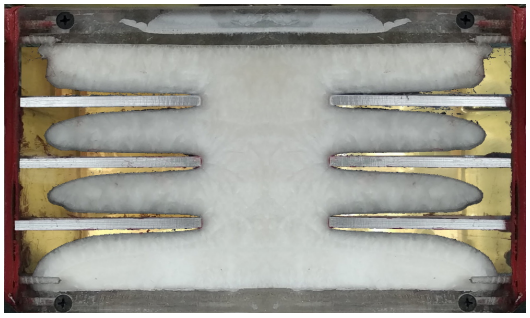

(b)

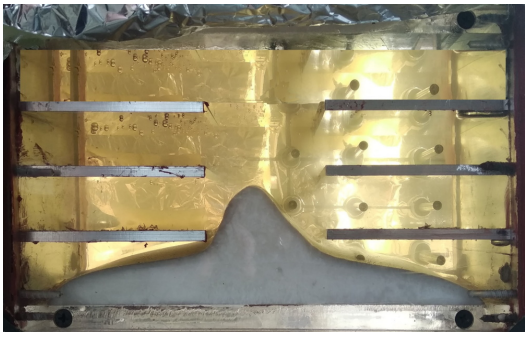

(c)

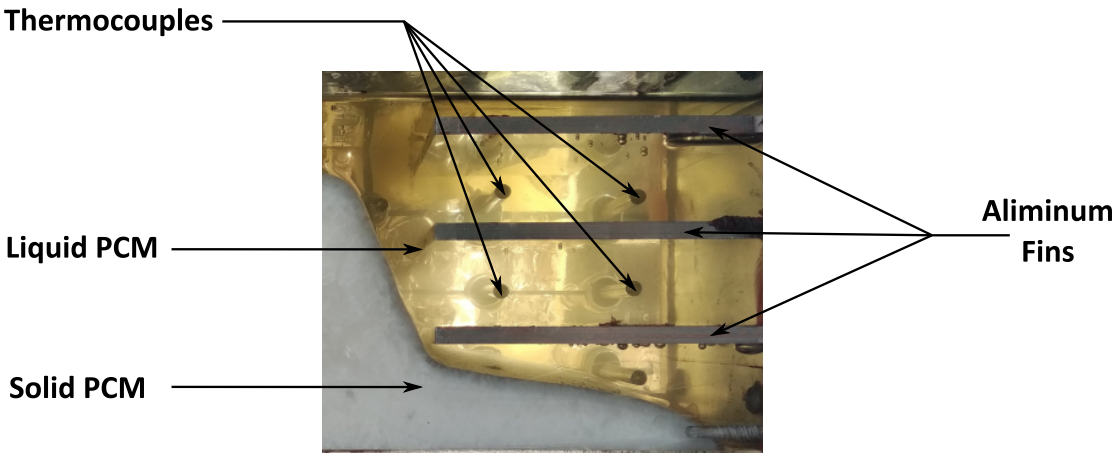


(d)

FIGURE 3.9: (a) PCM in enclosure, (b) initial and (c) final stages of PCM melting in LHTES (d) Phases of PCM and fins.

Furthermore, full-color images were converted to gray-scale images and then to binary images. This enabled evaluation of solid and liquid interfaces and the ratios of each phase of the PCM. The volume of solid and liquid phases is calculated using

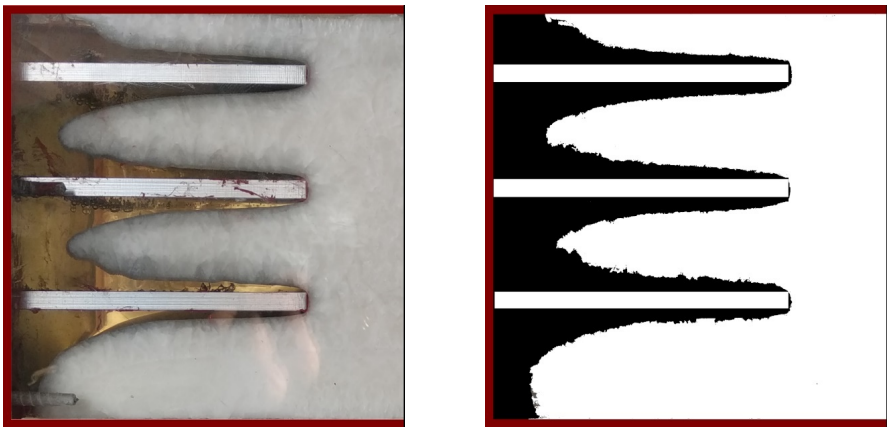

(a) (b)

FIGURE 3.10: Melting front at t=45 min (a) digital camera snapshot and (b) processed black and white image.

the expressions in eq. (3.3) and eq. (3.4).

$$\text{Liquid phase} = PCM_l = \frac{NP_b}{NP_t} \tag{3.3}$$

$$\text{Solid phase} = PCM_s = \frac{NP_w - NP_f}{NP_t} \tag{3.4}$$

The process was performed for each recorded time (t) for which snapshots were taken. The liquid fraction was calculated using Equation 3.5:

$$\gamma(t) = \frac{PCM_l(t)}{PCM_s(t) + PCM_l(t)} \tag{3.5}$$

Where $NP_l$ and $NP_{pcm}$ are the number of pixels with 0 values representing liquid phase and the total number of pixels representing PCM (solid + liquid) in the digital image respectively.

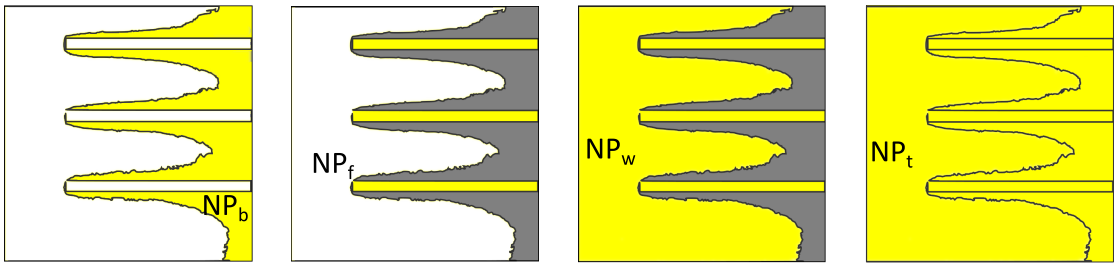


(a) (b) (c) (d)

FIGURE 3.11: Pixel-shading representing (a) all pixels (b) white pixels (c) fin-pixels (d) black pixels.

TABLE 3.2: X and Y coordinates of thermocouples on the LHTES enclosure and temperature reading at t=45 min.

| **Therocouple** | **X (mm)** | **Y (mm)** | **Temperature** ($^{\circ}C$) |
|---|---|---|---|
| $T_1$ | 35 | 20 | 57 |
| $T_2$ | 75 | 20 | 46 |
| $T_3$ | 110 | 20 | 33 |
| $T_4$ | 35 | 50 | 69 |
| $T_5$ | 75 | 50 | 68 |
| $T_6$ | 110 | 50 | 41 |
| $T_7$ | 35 | 80 | 77 |
| $T_8$ | 75 | 80 | 71 |
| $T_9$ | 110 | 80 | 52 |
| $T_{10}$ | 35 | 110 | 71 |
| $T_{11}$ | 75 | 110 | 62 |
| $T_{12}$ | 110 | 110 | 49 |

The results of image processing of liquid front of PCM for four different time steps are shown in Figure 3.12. These snapshots demonstrate the melting progression and movement of the melting front.

### 3.4.2 Temperature Variations in PCM

In order to record instantaneous temperature of PCM during the melting process 12 K-type thermocouples were installed in the central plane of the PCM inside the enclosure through holes in the back face of the enclosure. The locations of these thermocouples are shown in Figure 3.13. The corresponding X and Y coordinates are recorded in Table 3.2.

In order to generate temperature contours at a certain time step, the temperature readings from these thermocouples were used to perform 2D interpolation and plot the results to obtain temperature contours. Last column in Table 3.2 lists temperature readings at time t = 45 min. MATLAB R2019b was used to interpolate intermediate temperatures and obtain contours as shown in Figure 3.14.

(a) (b)

FIGURE 3.12: Melting front at different time steps (a) photographs and (b) digitally processed frames.

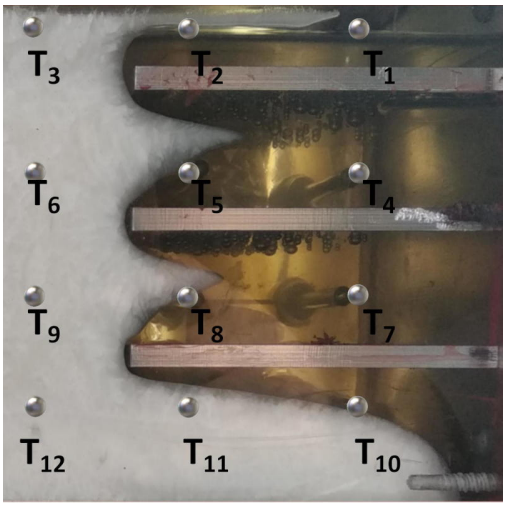


FIGURE 3.13: Thermo-couple locations and numbering.

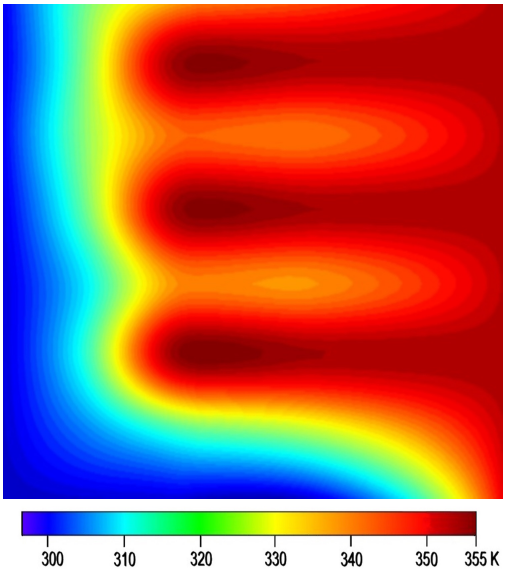


FIGURE 3.14: Interpolated temperature contour at t=45 min.

### 3.4.3 Assessment of Heat Transfer in PCM

The total energy absorbed by the PCM during the melting process is calculated by the following equation:

$$Q(t) = Q_{sensible}(t) + Q_{latent}(t) \tag{3.6}$$

For a differential volume $\Delta V_{pcm}$ at time t, the above expression can be broken down into following four elements: Sensible heat gain in the liquid phase by the

initial solid PCM.

$$Q_1(t) = \rho_s \, c_{ps}(T_{solidus} - T_0)\Delta V_{pcm_l} \tag{3.7}$$

Sensible heat gain in the liquid phase by the melted PCM.

$$Q_2(t) = \rho_l \, c_{pl}(T_{ml} - T_{solidus})\Delta V_{pcm_l} \tag{3.8}$$

Sensible heating of the solid phase.

$$Q_3(t) = \rho_s \, c_{ps}(T_{ms} - T_0)\Delta V_{pcm_s} \tag{3.9}$$

Latent heat during phase change of liquid PCM.

$$Q_4(t) = \rho_l \, h_{sl} \, \Delta V_{pcm_l} \tag{3.10}$$

Total heat:

$$Q(t) = Q_1(t) + Q_2(t) + Q_3(t) + Q_4(t) \tag{3.11}$$

The heat transfer rate during time interval $\Delta t$ is calculated using following expression:

$$\dot{Q}(t) = \frac{Q(t + \Delta t) - Q(t)}{\Delta t} \tag{3.12}$$

The average heat transfer rater during the melting process is defined as:

$$\bar{\dot{Q}}(t) = \frac{1}{t_{total}} \int \dot{Q}(t) \, dt \tag{3.13}$$

Table 3.3 provides the results of the calculated total thermal energy and heat transfer rate at four specific time steps. These values offer insights into the dynamic behavior of the system's thermal energy and the rate at which heat is transferred. By examining the data at different time intervals, it is possible to track changes in the thermal energy over time and assess the efficiency of the heat transfer process. These results are valuable for evaluating the performance of the system, optimizing its design, and ensuring the desired thermal outcomes are achieved within the specified time frames.

TABLE 3.3: Total energy and heat transfer rate at specific times.

| **Time** (min) | $\mathbf{Q_t}$ $(kJ)$ | $\dot{\mathbf{Q}}_\mathbf{t}$ $(W)$ |
|---|---|---|
| 25 | 471.06 | 314.05 |
| 45 | 534.79 | 198.06 |
| 65 | 549.03 | 140.77 |
| 80 | 591.74 | 123.27 |

The initial PCM temperature was 18°C. A modified Stefan number Ste* is defined as given in eq. (3.14) which accounts sensible heating of both phases of the PCM.

$$Ste^* = \frac{(c_p s(T_m - T_i) + c_p l(T_w - T_m)}{h_s l} \tag{3.14}$$

The natural convection effect intensity is calculated by Rayleigh number as:

$$Ra = \frac{g\beta(T_w - T_m)}{\nu\alpha} \tag{3.15}$$

For present study $Ste$ and $Ra$ were evaluated to be 1.487 and $1.43\times10^9$ respectively.

### 3.4.4 Experimental Results and Discussion

The Figure 3.15 shows the liquid front and temperature contours at four different times into the melting process. Temperature contours are generated in MATLAB by linear interpolation of the data obtained from the thermo-couples readings.

The evolution of the solid-liquid interface observed at specific times during melting of PCM is illustrated in Figure 3.15. The liquid fraction for all measurements was calculated and is shown as a plot in Figure 3.16. Temperature measurements within PCM was recorded by thermo-couples. The average temperature of all thermocouple readings is shown in Figure 3.17.

Thermal behavior of PCM melting in the finned enclosure heated from side walls is analyzed through the temperature history of the PCM. Figure 3.18 illustrates temperature histories of the all thermo-couple readings. Both side walls are maintained at $85°C$. At the beginning all thermo-couples are submerged in the solid

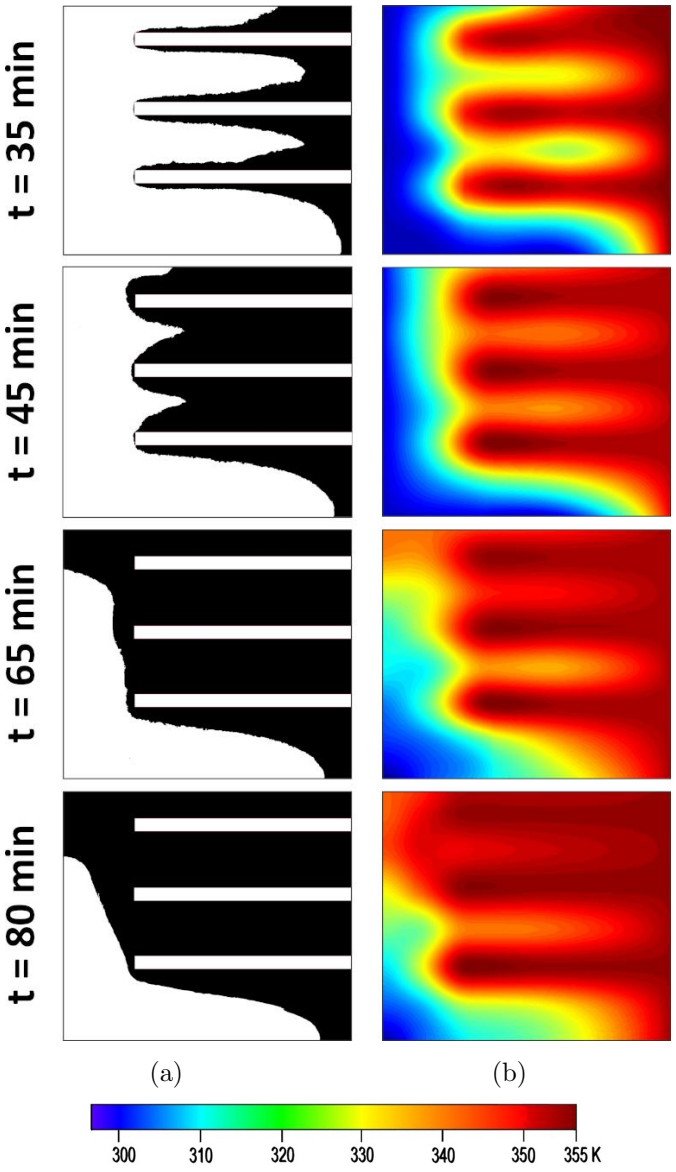


FIGURE 3.15: (a) Binary images of liquid fraction and (b) temperature contours at different times.

PCM and heat is transferred through conduction from the heated walls. The temperatures gradually increase until PCM reaches melting point. There are sudden increases in the temperature indicating that melt front is touching thermo-couples. After that the temperature increase is gradual again until the end of the process. The maximum temperature reached during the melting process is $82°C$. The transient variation of heat transfer rate is shown in Figure 3.19. There is a sharp decrease in heat transfer rate during the early stage of melting. This is due to the close contact melting heat transfer [45]. As the thickness of liquid PCM layer

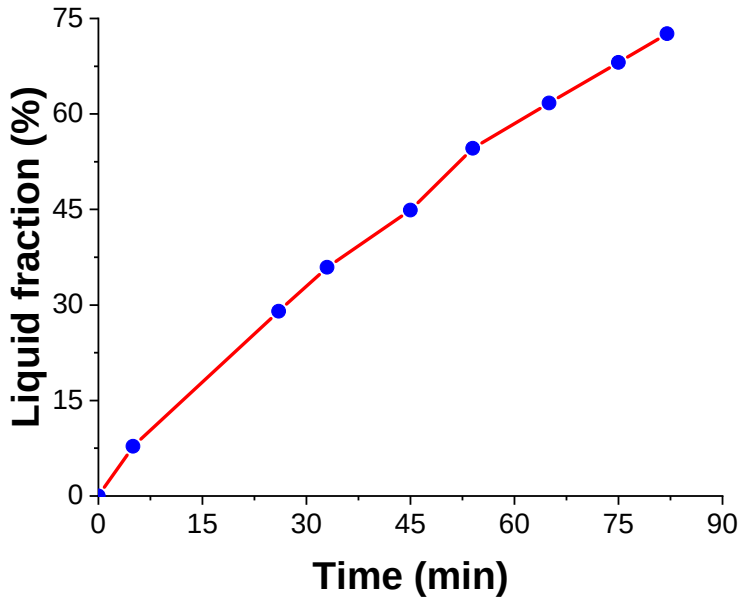


FIGURE 3.16: Temporal progress of melting fraction.

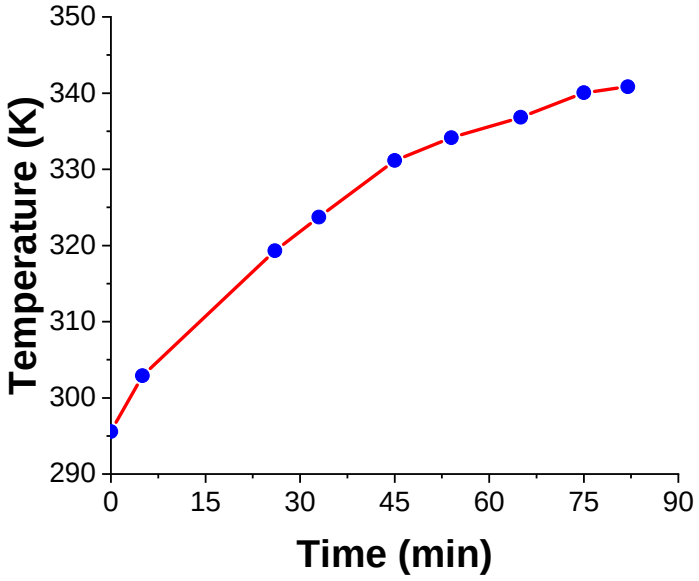


FIGURE 3.17: Temporal progress of averaged temperature.

increases, heat transfer rate decreases. The final heat transfer rate is 123 W. The deviation from initial to final heat transfer rate is 86%.

The visual inspection of the PCM during melting process showed that in the early stages heat conduction is dominant. The melting occurs parallel to the heated walls during this phase. Natural convection flow develops as liquid layers grows that is

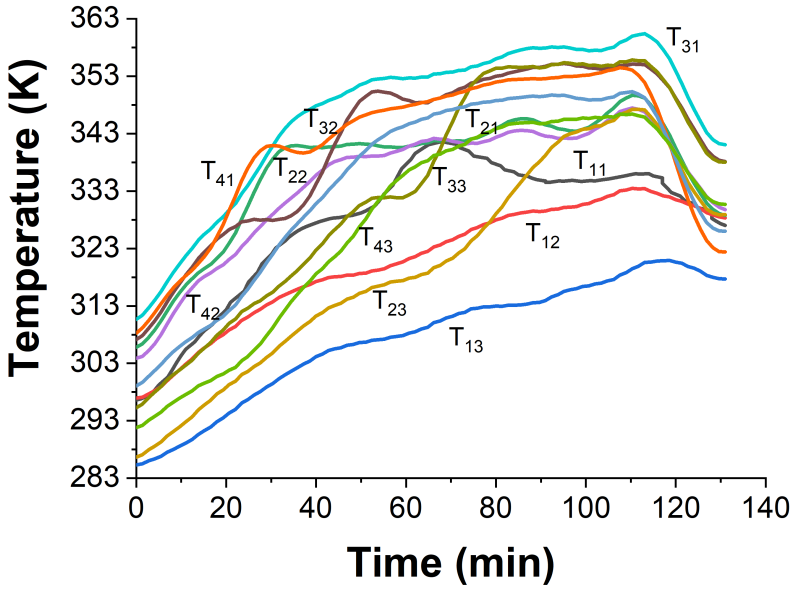


FIGURE 3.18: Local temperature variations in the PCM during melting process.

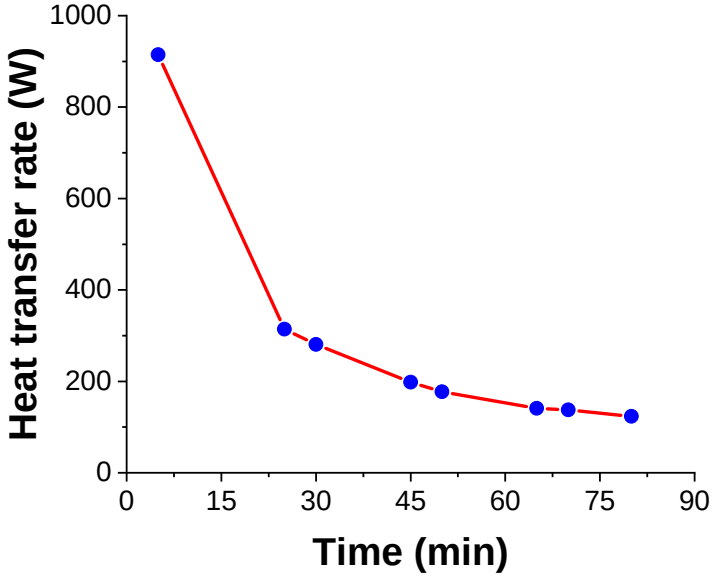


FIGURE 3.19: Temporal variations in time-averaged heat transfer rate of the PCM.

apparent from the wavy shape of the solid-liquid interface in the photographs of the melt front shown in Figure 3.12. The prototype LHTES unit can be used to calculate requirements for heating a room. Consider a sample case of heating a typical room of $10ft \times 10ft \times 8ft$ dimensions by $10°C$. Ignoring heat losses from the room, the expression in Equation (3.16) can be used to calculate the required

amount of energy.

$$U = m_a \, c_{p_a} \, \Delta t \tag{3.16}$$

where $m_a$, $c_{p_a}$ are mass and heat capacity of air to raise the temperature by $\Delta T$ degrees.

If $Q$ is the thermal capacity of the LHTES then the number of required units would be:

$$N = U/Q \tag{3.17}$$

Based on the room size and energy requirements, mass of PCM, the size and number of of LHTES can be adjusted.

## 3.5 Development of a Numerical Model

### 3.5.1 Computational Domain and PCM Thermo-physical Properties

The computational domain used in the numerical study is shown in Figure 3.20. The side walls were isothermal with three fins attached to each side. The adiabatic model was used for the other two walls as they were well insulated. The width and height of the domain were $W_r = 150$ mm and $H_r = 120$ mm, respectively. The thickness of the fins was $f_t = 1.25$ mm and length of fins was defined as $f_l = 40$ mm. The PCM in the domain is Stearic acid, and Table 3.1 lists all thermophysical properties required during numerical simulations.

The base case is the same as described by Shafiq et al. [146]. It is a rectangular enclosure with three fins connected to each wall. An additional reference model was designed in this study with 6 fins attached to both side walls to accurately compare results of this study with a reference having same number of fins. The length and thickness of the fins were $f_l = 40mm$ and $f_t = 1.25mm$, respectively.

For the improvement of the melting time and energy storage, different rectangular LTESU designs are proposed. The reference designed is varied by changing the fin lengths from top to bottom based on different mathematical functions. The length and thickness of the fins are adjusted so that the PCM volume ($V_{PCM}$) remains constant for all these designs. Numerical simulations for the planar 2D geometries are performed for all the design configurations and comparison of the results are analyzed with the reference case.

### 3.5.2 Assumptions and Simplifications

For the purpose of numerical solution, simplifications were made to account for the complex, unstable, and nonlinear nature of the phase change material (PCM)

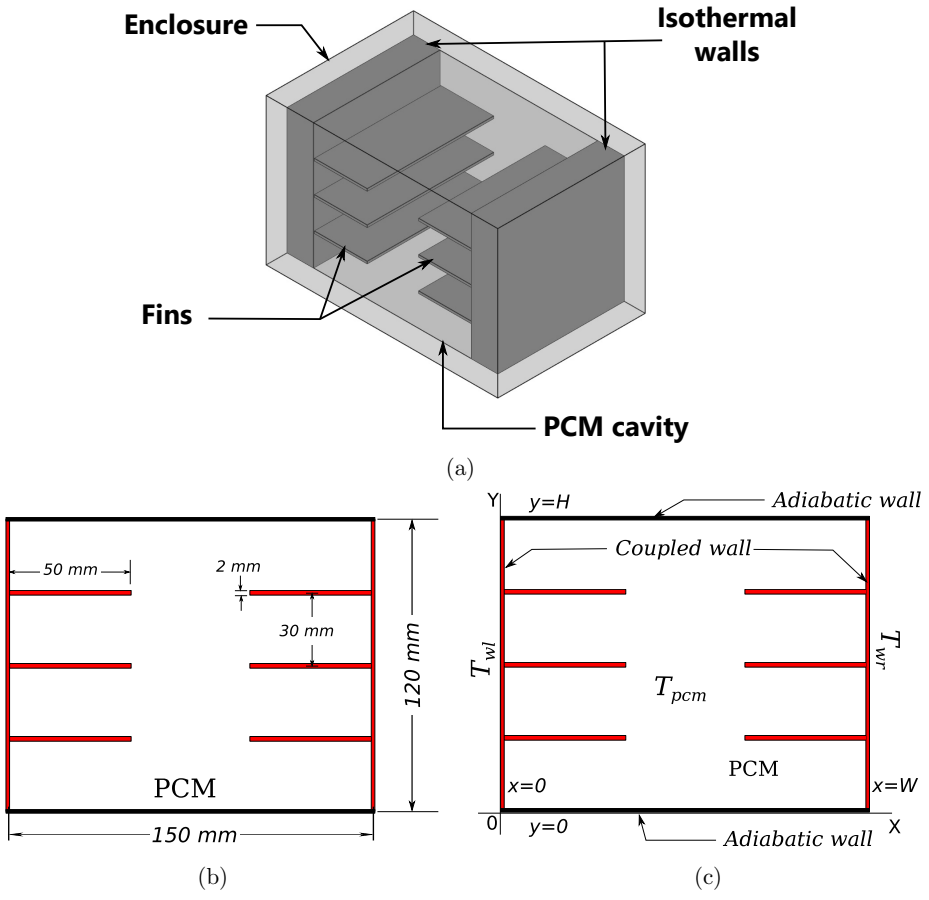


FIGURE 3.20: Computational domain (a) 3D Model, (b) 2D model dimensions (c) Boundary conditions.

melting process. It was assumed that the PCM in its liquid form behaves as a Newtonian fluid with laminar flow during the melting process. This assumption allowed for the application of well-established fluid flow equations to model the PCM's behavior. Additionally, the PCM was assumed to be homogeneous and incompressible throughout the system. This assumption simplified the modeling process by disregarding any spatial variations or compressibility effects within the PCM. It allowed for the use of simpler mathematical equations and facilitated the numerical analysis.

Moreover, the thermophysical properties of the PCM were considered to remain constant over the temperature range examined in this study. While this assumption may not hold true in all cases, it provides a reasonable approximation for systems where the PCM's properties do not vary significantly within the temperature range of interest. By assuming constant properties, the numerical model could avoid the additional complexity associated with accounting for temperature-dependent variations in properties.

Furthermore, different properties were assigned to the solid and liquid phases of the PCM. This differentiation was necessary to accurately represent the distinct thermal and flow characteristics of each phase. The numerical model accounted for these phase-specific properties to capture the behavior of the PCM during the melting process accurately. Additionally, a thin layer known as the mushy zone was considered to act as an interface between the solid and liquid phases of the PCM. This mushy zone represented the region where both solidification and melting occurred simultaneously. By describing the mushy zone as a combination of PCM phases, the numerical model aimed to capture the transitional behavior of the PCM during the phase change process.

These simplifications and assumptions enabled the development of a numerical model that could effectively simulate the melting process of the PCM within the latent heat thermal energy storage device. While these simplifications may introduce some level of error or deviation from real-world conditions, they allowed

for a computationally feasible and practical approach to analyzing the system's thermal behavior and performance.

The effect of variation in density is approximated by Boussinesq technique that is represented in the governing equations to model buoyancy source term. The change in volume of PCM during the course of melting can be neglected in the Boussinesq approximation and in the governing equations constant mean density is used. This approximation allows a simplified constant volume approach in 2D domain. In order to solve the problem an enthalpy porosity numerical methodology is used. This method has been validated by [147, 148] for the complex Volume of Fluid approach in 3D domain with variable volume.

### 3.5.3 Mathematical Model

The governing equations of the flow of liquid PCM are described by the conservation of mass, conservation of momentum, and conservation of energy as shown in Equations (3.18), (3.19), and (3.22).

$$\frac{\partial \rho}{\partial t} + \frac{\partial (\rho u)}{\partial x} + \frac{\partial (\rho v)}{\partial y} = 0 \tag{3.18}$$

In this equation, $u$ and $v$ are $x$ and $y$ components of velocity. $\rho$ denotes the density of the PCM and $t$ represents time. The momentum for $x$ and $y$ directions is defined by the Equation (3.19).

$$\begin{aligned}
\frac{\partial (\rho u)}{\partial t} + \frac{\partial (\rho u u)}{\partial x} + \frac{\partial (\rho v u)}{\partial y} &= -\frac{\partial p}{\partial x} + \frac{\partial}{\partial x}(\mu \frac{\partial u}{\partial x}) + \frac{\partial}{\partial y}(\mu \frac{\partial u}{\partial y}) + Au \\
\frac{\partial (\rho v)}{\partial t} + \frac{\partial (\rho u v)}{\partial x} + \frac{\partial (\rho v v)}{\partial y} &= -\frac{\partial p}{\partial y} + \frac{\partial}{\partial x}(\mu \frac{\partial v}{\partial x}) + \frac{\partial}{\partial y}(\mu \frac{\partial v}{\partial y}) + Av + \rho g \beta (T - T_l)
\end{aligned} \tag{3.19}$$

where $p$ is pressure and dynamic viscosity of PCM is denoted by $\mu$. $g$ represents gravity and coefficient of thermal expansion is denoted by $\beta$. The instantaneous and liquidus temperature of PCM are represented by $T$ and $T_l$ respectively.

The buoyancy source term $\rho g\beta(T - T_l)$ is used to incorporate the effect of density variation due to temperature in the momentum equation through Boussinesq approximation. The effects of momentum variations by buoyancy are included by momentum source terms $Au$ and $Av$. The porosity function $A$ is defined by Equation (3.20) [149].

$$A = C\frac{(1-\gamma)^2}{\gamma^3 + \epsilon} \tag{3.20}$$

The mushy zone is used to define liquid-solid interface. The damping effect of velocity in this region is controlled by a mushy zone constant $C$. The value of $C$ lies between $10^4$ and $10^7$ [150]. Higher the value of $C$, more is the velocity damping. In the current study, $C$ is defined as $10^5$.

This value results in a good match for results obtained in experimental studies and numerical simulations. In order to avoid division by zero, a small number is added in the denominator to prevent the source term $A$ becoming infinite at $\gamma = 0$. A typical of $\epsilon$ is 0.001. Liquid fraction, $\gamma$, is calculated as given below:

$$\gamma = \begin{cases} 0, & T < T_s \\ \dfrac{(T - T_s)}{(T_l - T_s)}, & T_s < T < T_l \\ 1, & T > T_l \end{cases} \tag{3.21}$$

The following equation expresses conservation of energy of PCM:

$$\frac{\partial(\rho h)}{\partial t} + \frac{\partial(\rho u h)}{\partial x} + \frac{\partial(\rho v h)}{\partial y} = \frac{\partial}{\partial x}(k\frac{\partial T}{\partial x}) + \frac{\partial}{\partial y}(k\frac{\partial T}{\partial y}) \tag{3.22}$$

where thermal conductivity of PCM is denoted by $k$. Specific enthalpy $h$ for different PCM zones (solid, liquid, and mushy) during the melting process is evaluated

as follows:

$$h = \begin{cases} \int_{T_{ref}}^{T} c_{p_s} dT, & T < T_s \\ \int_{T_{ref}}^{T_s} c_{p_s} dT + \gamma \Delta H, & T_s < T < T_l \\ \int_{T_{ref}}^{T_s} c_{p_s} dT + \Delta H + \int_{T_l}^{T} c_{p_l} dT, & T > T_l \end{cases} \tag{3.23}$$

As described by Rathod et al. [61], a linear variation can be considered for $C_p$ between solid phase and liquid phase of stearic acid during the melting process.

### 3.5.4 Non-Dimensional Numbers

For generic analysis of the PCM melting behavior, non-dimensional numbers are used. These number are Nusselt Number, Rayleigh Number, Stefan Number, and Fourier Number as are defined by the expressions in eqs. (3.24) and (3.27) to (3.29).

$$\overline{Nu} = \frac{\overline{h} H}{k} \tag{3.24}$$

$\overline{h}$ is the heat transfer coefficient averaged over the surface and it is calculated as

$$\overline{h} = \frac{Q_{total}}{A_w (T_w - T_m) \Delta t} \tag{3.25}$$

$Q_{total}$ is the total thermal energy stored by the PCM in total melting time $\Delta t$. The total heat transfer surface area $A_w$ is calculated as

$$A_w = 2(H_r \times D_r) + 2n(f_l \times D_r) \tag{3.26}$$

The length of the fin is defined by $l_f$ and count of fins is represented by $n$. The enclosure height and depth are denoted by $H_r$ and $D_r$ respectively in the above

relation.

$$Ra = \frac{g\beta(T_w - T_m)H^3}{\nu\alpha} \tag{3.27}$$

where $\nu = \frac{\mu}{\rho}$ is kinematic viscosity and $\alpha = \frac{k}{c_p\rho}$ is the coefficient of thermal diffusivity. In this expression $H$ is the characteristic length of the heated wall.

$$Ste = \frac{c_{pl}(T_w - T_m)}{h_{sl}} \tag{3.28}$$

where latent heat of fusion is defined by $h_{sl}$ and specific heat is represented by $c_{pl}$ for the liquid PCM.

$$Fo = \frac{\alpha t}{H^2} \tag{3.29}$$

### 3.5.5 Numerical Schemes

All of the numerical simulations in this work were performed using ANSYS Fluent 19.0. The problem was modeled as a transient melting in two dimensions. Diffusion terms in the governing equations were discretized using a second order central differencing technique. The MUSCL scheme, a combination of second-order upwind and central differencing techniques, was used to discretize the convective terms. With this method, problems with significant gradients and discontinuities provided highly precise numerical solutions. The SIMPLE algorithm was used to handle the connection of pressure and velocity. The PRESTO scheme was used to calculate pressure correlations. The discretization of temporal terms used a second order implicit technique that is unconditionally stable. The convergence criteria during each time step of the numerical simulation, scaled residuals less than $10^{-6}$ are defined for all governing equations.

### 3.5.6 Initial and Boundary Conditions

PCM's initial temperature was set to $300K$. A constant temperature of $353K$ was set up for the side isothermal walls. The other two walls were defined as adiabatic. The linked wall heat transfer and no slip velocity boundary constraints

were used to define the interface between the enclosure body and PCM. Conduction heat transfer was enabled on the enclosure's walls and fins so that heat can be transferred from the heated surfaces to the PCM. These conditions are listed in the Table 3.4.

TABLE 3.4: Initial and boundary conditions.

| **Condition** | **Definition** |
|---|---|
| Initial PCM temperature | $T_0 = 300K$ |
| Isothermal heated walls temperature | $T_w = 353K$ |
| Top and bottom wall conditions | $q_w = 0$ |
| Boundary constraints at PCM - Enclosure interface | no slip |

### 3.5.7 Mesh Independence

In order to select an appropriate mesh grid resolution for the studies, a grid convergence study was performed using the base case. The study was performed with mesh element sizes of $2mm$, $1mm$, $0.75mm$, $0.6mm$, $0.55mm$, and $0.5mm$. Figures 3.21a to 3.21c show the results of the grid convergence study. The plot in Figure 3.21a and the error analysis in Figure 3.21c indicate that the grid size finer than $0.55mm$ does not improve the solution. The $(E_n)_i$ is used to calculate instantaneous percentage error using the following relation:

$$(E_n)_i = \left| \frac{(\gamma_{n+1})_i - (\gamma_n)_i}{(\gamma_{n+1})_i} \right| \times 100 \tag{3.30}$$

where $n$ is the grid element size, $i$ is time step, and $\gamma$ represents liquid fraction. In this expression, $n$ changes from 1 - 6 corresponding to the grid element sizes. For each grid element size $n$, the average percentage error $\overline{E_n}$ is calculated by:

$$\overline{E_n} = \frac{\sum (E_n)_i}{N_{step}} \tag{3.31}$$

where number of time steps are denoted by $N_{step}$. The percentage error vs time is plotted Figure 3.21b. It can be seen in the plot that as grid element size is decreased, the percentage error also decreases. Figure 3.21c shows the average

percentage error for different grid element sizes. The same behavior is observed in this plot as well. It can be seen that as grid element size is decreased, the average percentage error is reduced as well.

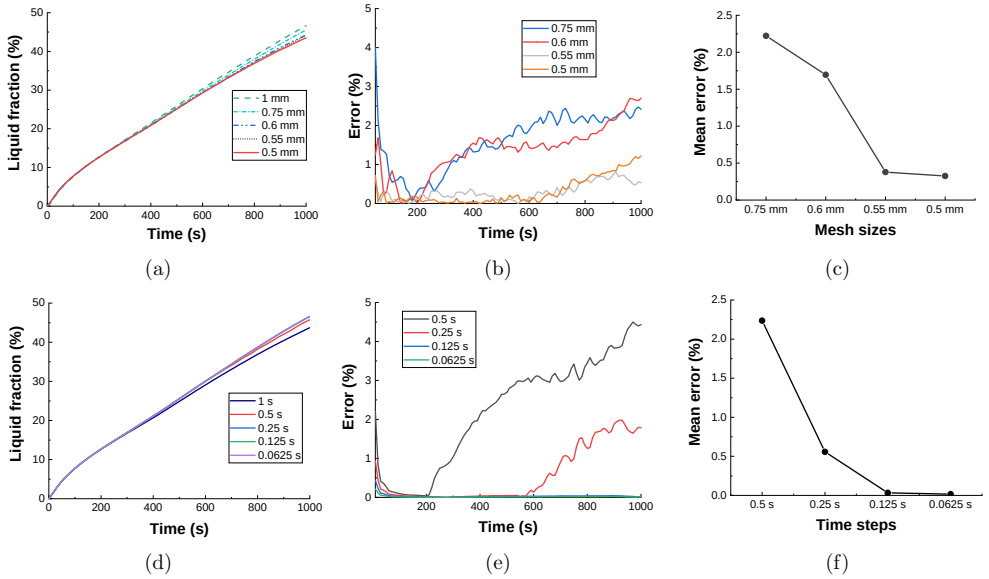


FIGURE 3.21: Validation of numerical results (a)-(c) mesh independence (d)-(f) time step independence.

### 3.5.8 Time-step Independence

A similar study was performed to find an appropriate time-step so that the simulations results are independent of the time-step size. For this, five different time-step sizes $1s$, $0.5s$, $0.25s$, $0.125s$, and $0.0625s$ were chosen. The results of the study are shown in Figures 3.21d and 3.21e. $0.125s$ was selected as the optimal time-step.

Any further decrease in step size, did not improve the results, but required additional computational cost. Equations (3.30) and (3.31) were used to calculate errors in the time-step study similar to the grid convergence study. It can be seen in the plots that both the running percentage error and the average percentage error approach to zero for time-step size of $0.125s$ or smaller.

### 3.5.9 Validation of Numerical Methodology

The numerical solution strategy and mathematical formulation are validated against the results of the experimental study described previously and also from literature. The subsequent sections provides detailed analysis and comparison of numerical and experimental results Figure 3.22 shows comparison of liquid front progression in numerical and experimental studies. It can be seen in the figure that liquid fronts mostly match in numerical and experimental cases. At later time, after $t = 60min$, it is observed that the top part of PCM takes longer to melt in the numerical study compared to the experimental results. Figure 3.23 shows time history of temperature and liquid fraction for these studies. The liquid fraction and temperature numerical results are within 10% and 2% respectively of the results obtained experimentally.

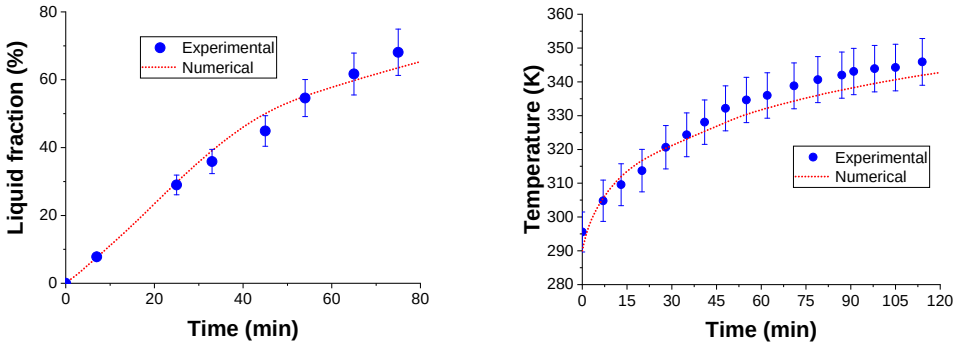


(a) (b)

FIGURE 3.23: Experimental and numerical results (a) liquid fraction (b) temperature.

### 3.5.10 Comparison of the Results from Current Numerical Methodology and Literature

The experimental study of Kamkari et al. [136] was also used to validate the numerical methodology. A numerical model identical to as described in their experiments was set up and solved numerically. They used Lauric acid as PCM. The initial and boundary conditions were setup and corresponding thermo-physical

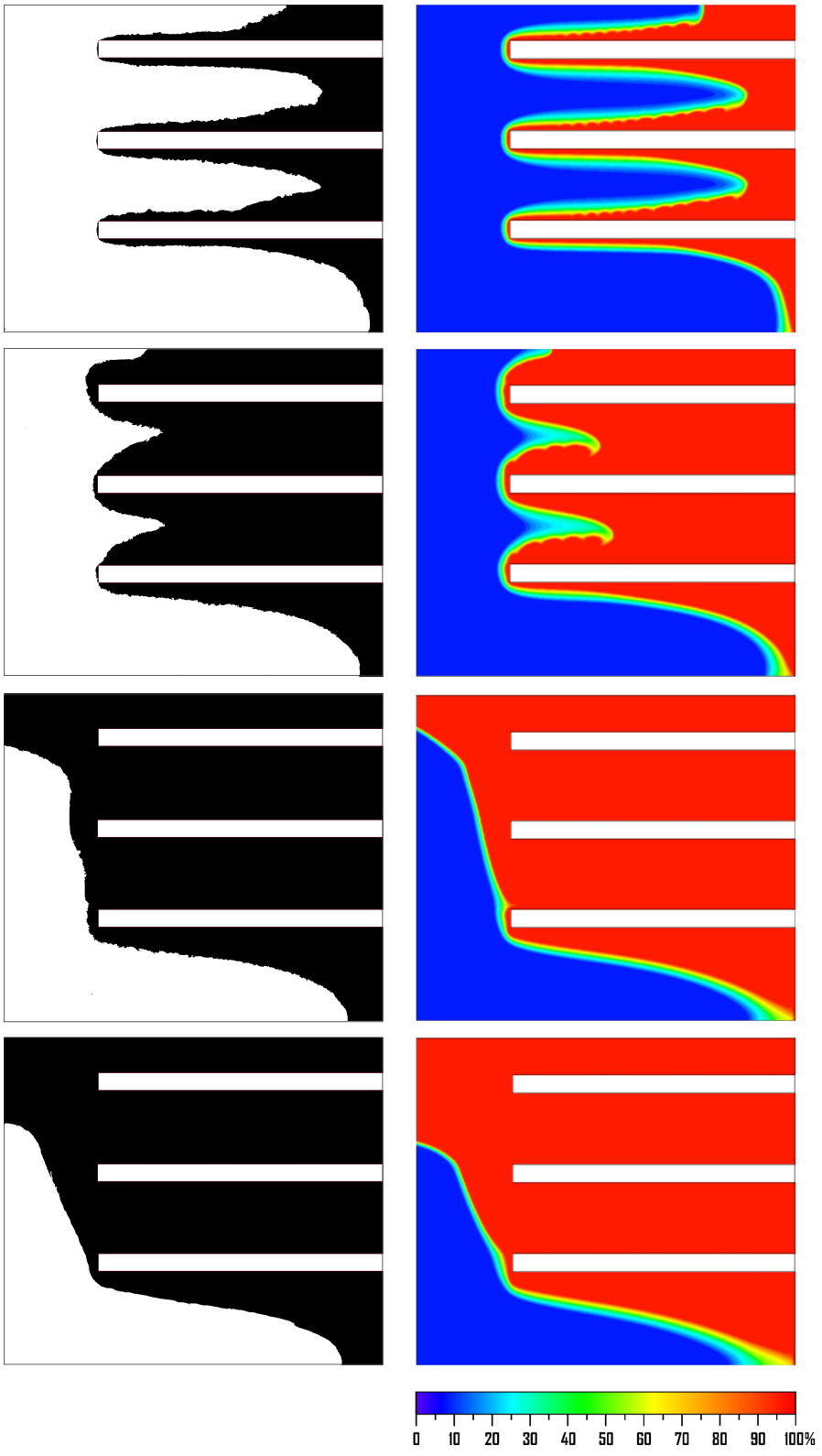


(a) (b)

FIGURE 3.22: Comparison of (a) experimental and (b) numerical melting fronts of the PCM.

properties were defined as in the experimental setup. Temperature of the right wall was set as $343K$, and all other walls were kept adiabatic. The same values for mesh element size and time-step size were used for the numerical simulation.

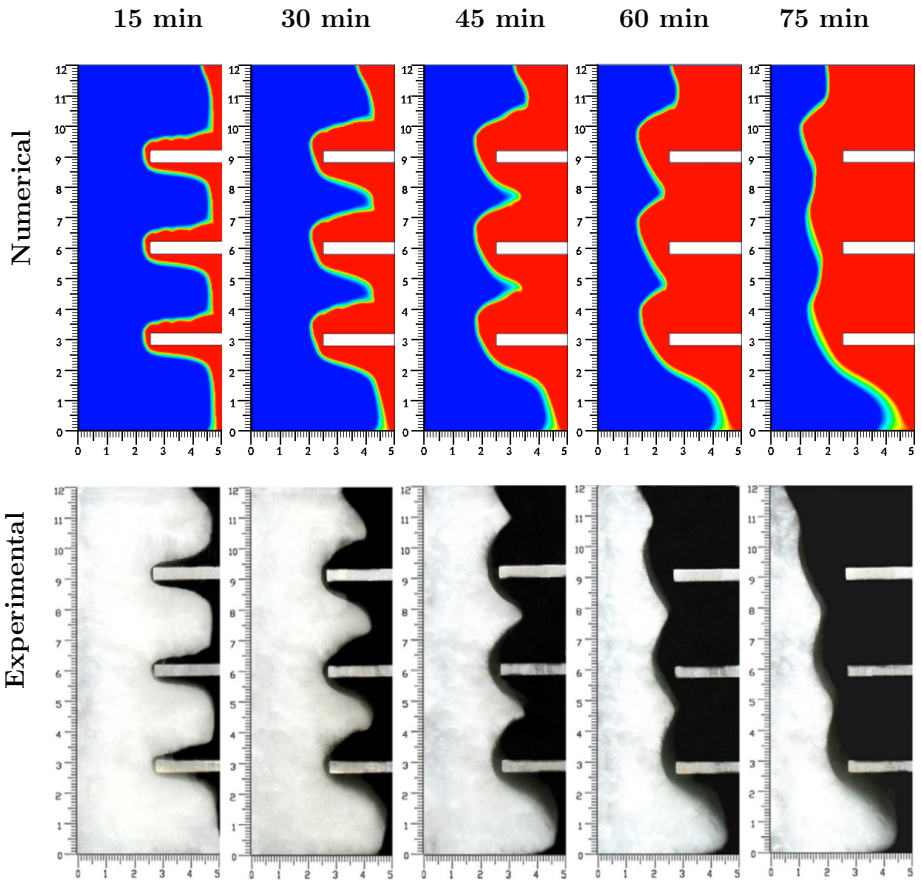


FIGURE 3.24: Contours of numerical and experimental [136] results.

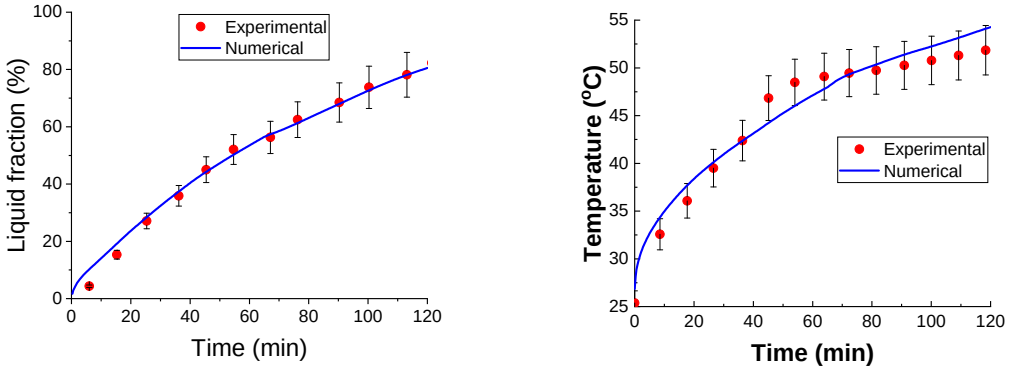


(a) (b)

FIGURE 3.25: Melt fraction and temperature comparison of numerical and experimental [136] results.

Numerical and experimental results are compared by visualization of the melt fraction at different times as shown in Figure 3.24. It can be seen in the figure experimental results and present numerical results match well. The melting front is captured with adequate accuracy and our numerical solution is justified.

The liquid fraction and temperature are plotted with respect to time for the experiments and the numerical solution and are shown in Figures 3.25a and 3.25b. The performance of the numerical methodology can be analyzed with the help of these plots. It can be seen that the plots agree very closely with the experimental data. There was 2% and 5% average error for liquid fraction and average temperature respectively. The maximum error was below 10% for both cases.

## 3.6 Conclusion

The experimental investigation was conducted in order to study the melting process and thermal behavior of a rectangular LHTES device heated from both side walls. During the experiment, liquid melting front was recorded by taking photographs of the melting process at specified time intervals.

Thermocouples were used to record transient temperature measurements. These photographs were later processed to evaluate the liquid fraction and heat transfer rates were evaluated from the temperature measurements. Based on the study following observations were made:

1. During the melting process of the PCM, a visual inspection revealed that heat conduction initially dominates. The melting occurs parallel to the heated walls, indicating the influence of heat transfer through conduction. However, as the process progresses, natural convection begins to develop. This is evident from the wavy shape observed in the photographs of the solid-liquid interface at the melt front, indicating the formation of liquid layers and the onset of convective flow.

2. The transient history of the liquid fraction progress demonstrated the presence of three distinct melting regions: fast, moderate, and slow melting. The average melting rates for these regions were determined to be 27.8 g/min, 25.5 g/min, and 18 g/min, respectively. This observation highlights the varying rates at which different portions of the PCM transition from solid to liquid, indicating the importance of considering the temporal behavior of the melting process.

3. A notable observation was the close agreement between the numerical simulations and experimental results regarding the advancement of the liquid front. This alignment suggests that the numerical model accurately captures the melting behavior of the PCM, validating its capability to simulate and predict the progression of the liquid phase front.

These findings provide valuable insights into the melting behavior of the PCM, emphasizing the significance of heat conduction, natural convection, and temporal variations in the melting process. The agreement between the numerical and experimental results further enhances the confidence in the simulation model, demonstrating its utility for studying and analyzing the melting characteristics of the PCM system.

# Chapter 4

# Investigation of Orientation, Shape and Length of Fins

## 4.1 Introduction

In this section, the simulation results of various fin designs and configurations installed on the isothermal side walls of the rectangular Latent Heat Thermal Energy Storage (LHTES) device are presented. The objective of these simulations is to enhance the thermal performance of the system. Several performance indicators are defined and analyzed to assess the effectiveness of the studied designs, with melting time and energy storage being the key indicators under consideration. All simulation results are compared against the reference case, which is depicted in Figure 3.20. By comparing the performance of different configurations to the reference case, the relative improvements or shortcomings can be identified. The best-performing configuration among the studied designs is then further analyzed to investigate the effects of wall temperature variation on the melting performance. This analysis aims to understand how changes in wall temperature impact the thermal behavior and efficiency of the system.

Moreover, correlations are proposed to predict the non-dimensional melting time and average Nusselt number for different wall temperatures. These correlations

provide a simplified way to estimate the melting time and heat transfer characteristics based on the wall temperature, allowing for quick assessments and preliminary design considerations.

Additionally, the coupling effect of various parameters is considered in Chapter 6, where parameter optimization is carried out. This optimization process explores the interactions between different design parameters and seeks to identify the optimal combination that maximizes the thermal performance and energy storage capacity of the LHTES device. By presenting these simulation results, analyzing the best-performing configuration, and proposing correlations, this study contributes to a deeper understanding of the thermal behavior and performance of the LHTES device. The findings offer valuable insights for the design and optimization of similar systems, facilitating their practical implementation and enhancing their overall efficiency.

## 4.2 Design Configurations

To enhance the melting and thermal energy storage performances of the reference case, several designs of the rectangular LHTES were investigated by varying parameters comprising of orientation, shape, and length of fin. These parameters were so adjusted that the Phase Change Material (PCM) volume ($V_{PCM}$) remained constant for all of the designs. Three groups of designs were studied to analyze the effect of the defined parameters on the thermal performance of LHTES unit.

The designs in which the number of fins, fin length, and fin thickness are same as that of the reference case, but the angular orientation was varied were grouped in "A" configuration as shown in Figure 4.1a. "S" configuration comprised of designs which contained straight fins and a combination of straight and angled sections as shown in Figure 4.1b. In the third "L" configuration, the designs were having different fin lengths. The Phase Change Material (PCM) volume was managed to be constant by adjusting the thickness and number of fins as shown in Figure 4.2. The geometric details and topology of the fins for all the design cases are listed

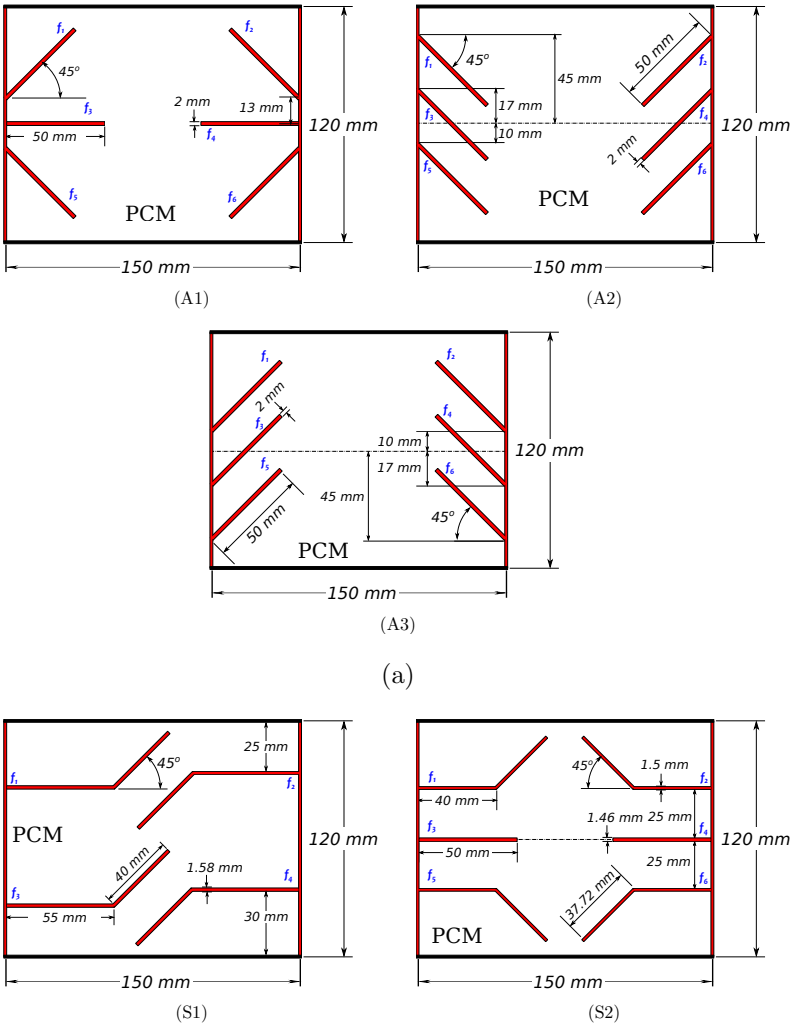


FIGURE 4.1: Computational domain (a) Angle, and (b) Shape configurations.

in Table 4.1. Numerical simulations were performed for the 2D planar geometries of all the designs discussed above and results were compared with that of the reference case results.

For the sake of completeness, a zero-fin case was also simulated and the results were compared with the reference case to observe the favorable effects of fins on the thermal performance of the LHTES device. The contour plots of liquid fraction and temperature are presented for both the cases in Figure 4.3 at five different time instances during the melting process. The impact of fins on the melting process can clearly be seen in these frames depicting faster melting of the PCM for the finned reference case. Initially, the heat is conducted from

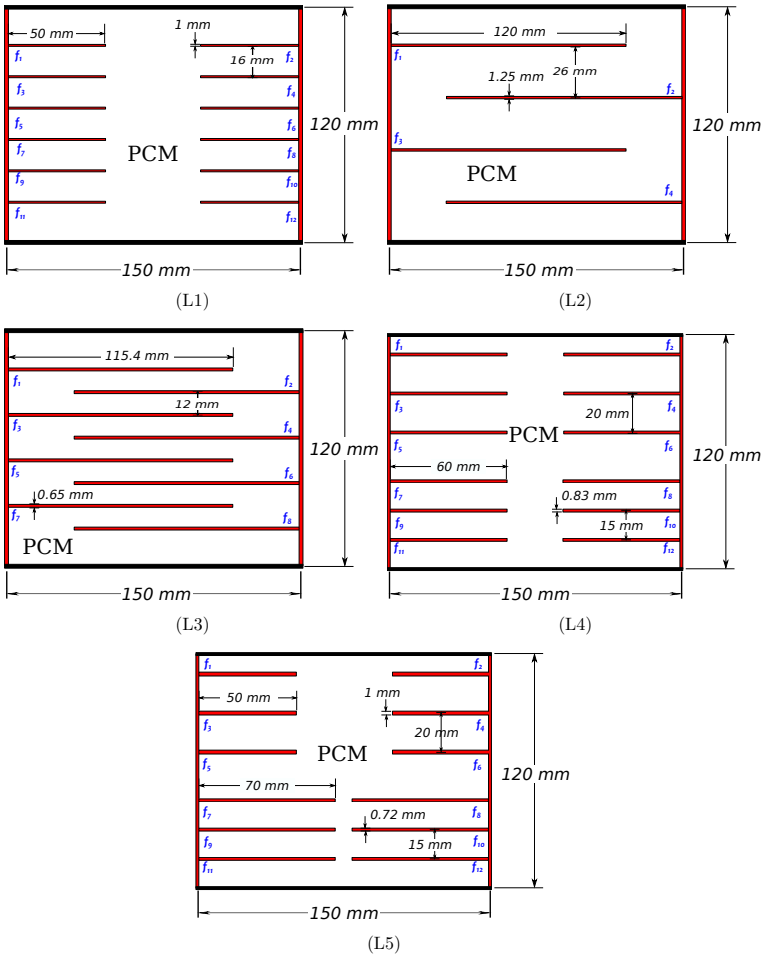


FIGURE 4.2: Computational domain for fin-length configurations.

the isothermal walls to the solid PCM to melt it. The layer of melted PCM then rises due to density gradient based buoyancy driven currents. As a result, the convection currents sweeps the melted PCM alongside the walls and heated surfaces towards the upper portion of the LHTES device and enhance the melting rate of the PCM. This can be seen in the liquid fraction contour plots at t = 20 min for both the cases. The reference case shows several localized melting zones and the corresponding convection currents generated from the hot fin surfaces. These convection currents agitate the flow and enhance the melting process.

Additionally, this also mixes the PCM and results uniform temperatures. This can be observed from the temperature contour plots of the reference case at $t = 20min$ where the temperatures on the upper side of the fins are lower but uniform, however, the lower side regions of the fins are at high temperature. As the time

TABLE 4.1: Topology and geometric properties of fins.

| **Case** | **Fin** | **Length** $(mm)$ | **Thickness** $(mm)$ | **Area** $(mm^2)$ | **Topology** |
|---|---|---|---|---|---|
| Case A1 | 1, 2 | 50 | 2 | 200 | 45° up |
| | 3, 4 | 50 | 2 | 200 | horizontal |
| | 5, 6 | 50 | 2 | 200 | 45° down |
| Case A2 | 1-6 | 50 | 2 | 600 | 45° down |
| Case A3 | 1-6 | 50 | 2 | 600 | 45° up |
| Case S1 | 1, 3 | 55 + 40 | 1.58 | 380 | horizontal + 45° up |
| | 2, 4 | 55 + 40 | 1.58 | 380 | horizontal + 45° down |
| Case S2 | 1, 2 | 40 + 38 | 1.46 | 312 | horizontal + 45° up |
| | 3, 4 | 50 | 1.46 | 200 | horizontal |
| | 5, 6 | 40 + 38 | 1.46 | 312 | horizontal + 45° down |
| Case L1 | 1-12 | 50 | 1 | 1200 | horizontal |
| Case L2 | 1-4 | 120 | 1.25 | 960 | horizontal |
| Case L3 | 1-8 | 115.4 | 0.6 | 1846 | horizontal |
| Case L4 | 1-12 | 60 | 0.83 | 1440 | horizontal |
| Case L5 | 1-6 | 50 | 1 | 600 | horizontal |
| | 7-12 | 70 | 0.72 | 840 | horizontal |

progresses, the thickness of the liquid layer increases and eventually the liquid layers from both sides merges and forms a cloud of liquid PCM on top of the solid as visible at t = 40 min.

As the liquid PCM layer grows, the convection currents are still continuously generated but these die out without significant contribution towards the melting enhancement resulting in the slower melting progress. This can be observed for the zero-fin case between the times 40 min to 80 min. The reference case, on the other hand, quickly melts a major chunk of the PCM due to the fins embedded into it; once all PCM around the fins is melted the melting progresses slower. Zero-fin case still holds large quantity of solid PCM at $t = 80min$, whereas finned reference case almost melts whole body of PCM at that time.

The corresponding temperature contours also suggest that the reference case has stored considerable amount of energy at that time as compared to zero-fin case which is still at low temperature. The melting phenomena and the corresponding thermal characteristics were further analyzed by plotting the temporal variation

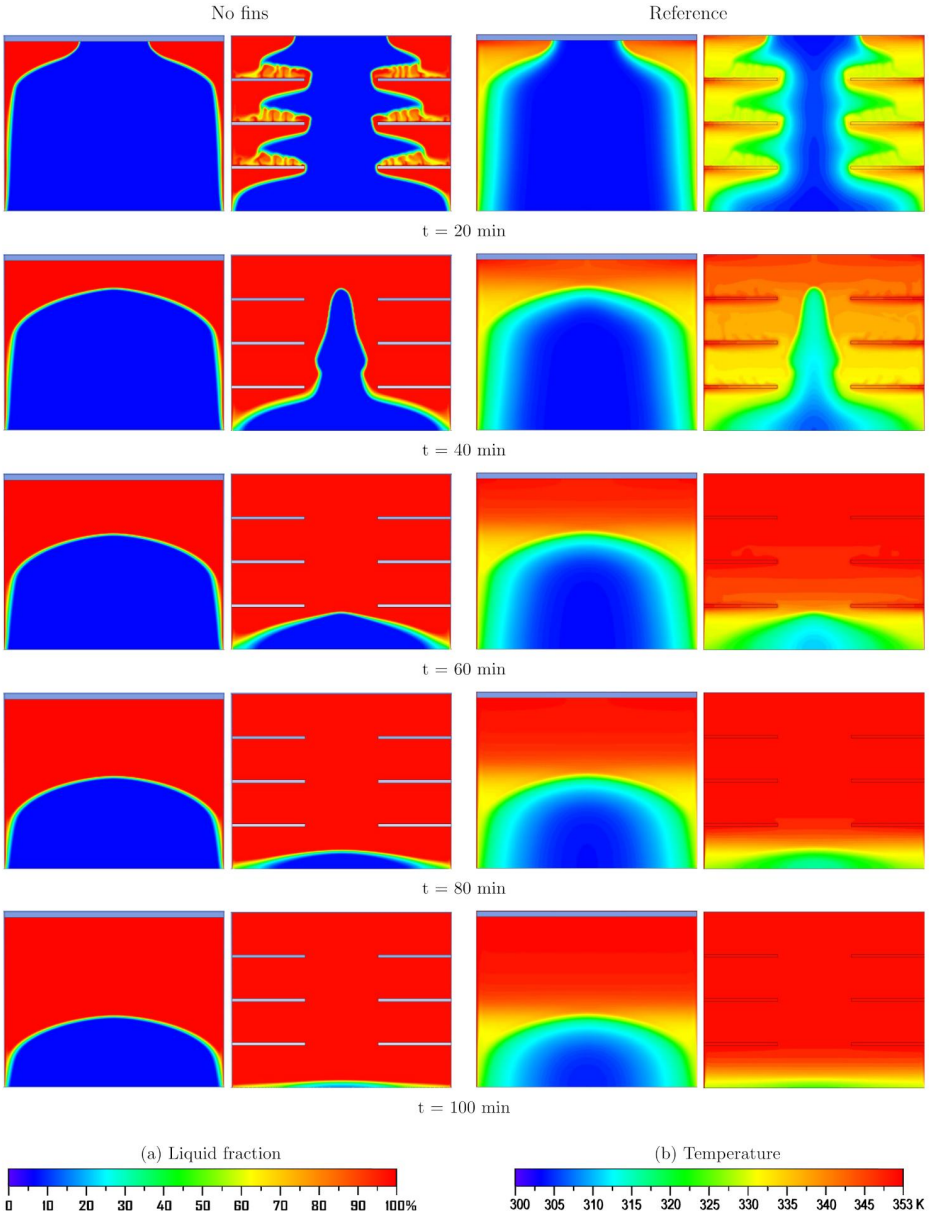


FIGURE 4.3: Contour plots of liquid fraction and temperature for 0-fin and reference designs at five different time instances.

of the liquid fraction, temperature, and energy storage as shown in Figure 4.4a to 4.4c. The zero-fin case maintains an almost constant slope till t = 100 min which is followed by a very smooth decreasing trend. The reference case melts quite faster initially as compared to the zero-fin case melting 70% of the PCM in initial 37 minutes. This is then followed by a gradually decreasing trend which is due to the fact that all PCM around the hot surfaces is melted.

The time to completely melt the PCM for zero-fin and the reference case is 205

and 115 minutes, respectively. This represents 44% improvement in the melting time for the reference case over the zero-fin case. The temperature plots follow a similar trend as that of the liquid fraction.

It can be seen that the rise in temperature is faster in case of the reference case compared to the zero-fin case. After 37 minutes into the melting process which corresponds to 70% melting of the reference case, the average PCM temperatures are $335K$ and $316K$ for reference case and zero-fin case, respectively. At complete melting time t = 115 min for reference case, the average PCM temperature for zero-fin case is only 340K, whereas, it is 351 K for the reference case. The energy storage curves exactly follow the trends of the liquid fraction.

The maximum energy storage capacity of LHTES considered in this case is 330 kJ/kg which corresponds to the complete melting of the PCM. The storage rate is, however, quite different and is dictated by the melting rate. At $t = 115min$ which corresponds to the complete melting of the reference case, the energy stored for the zero-fin and the reference case is $250kJ/kg$ and $330kJ/kg$, respectively.

## 4.3 Analysis of Configuration Cases A1, A2, and A3

Three designs of LHTES are simulated using different angular orientations of the fins by keeping their lengths and thicknesses constant. These angular arrangements significantly effect the thermal performance characteristics of the LHTES due to different depths of penetrations of the fins into the PCM and their roles in creating convection currents. Contour plots of liquid fraction and temperature for all three configurations are presented at different time instances in Figures 4.5 and 4.6, respectively.

During the initial times, i.e., till t = 10 min, the PCM around the heat transfer surfaces gets melted at the same rate for all three configurations due to conduction dominated heat transfer as shown in Figure 4.7a. This is then followed by the

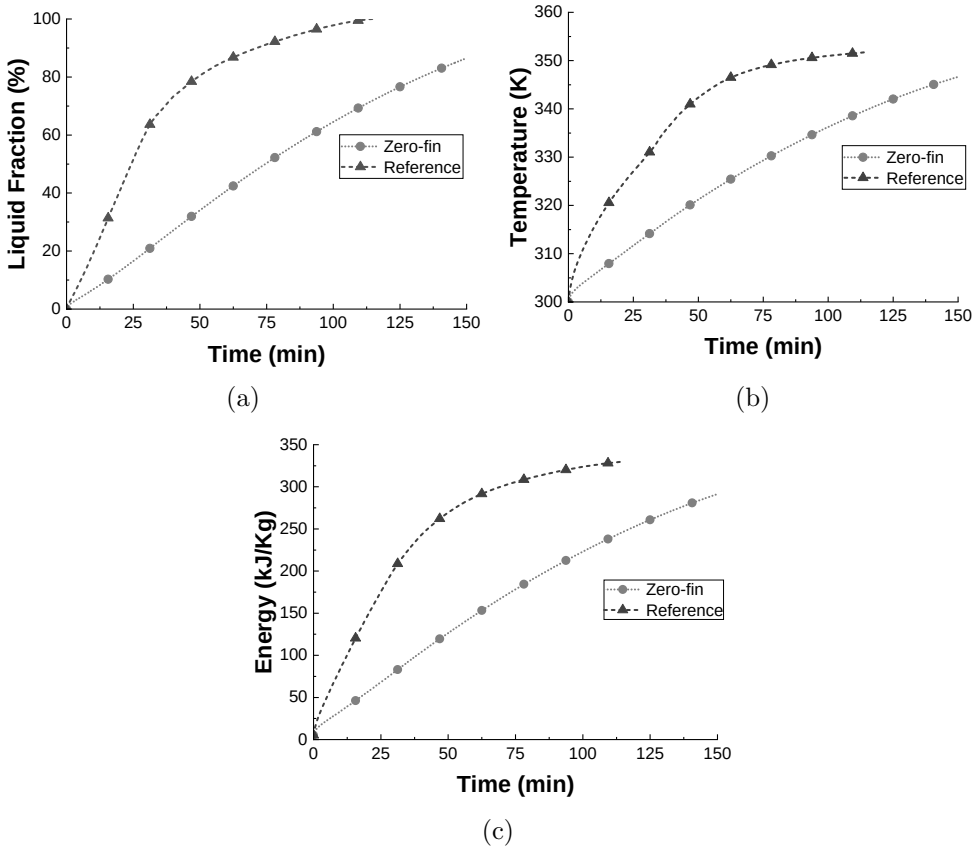


FIGURE 4.4: Comparison of (a) liquid fraction (b) temperature and (c) thermal energy for zero fin and reference configurations.

creation of buoyancy driven convective currents in the molten PCM as shown by the contour plots of liquid fraction at t = 20 min.

The upward oriented fins for the A3 design supports these convective currents and results in a faster melting. In contrast, the downward oriented fins of A2 design oppose these currents and causes slower melting as well as generation of higher temperature zones underneath the fins as shown in the temperature contour plots. Design A1 is a mix of upwards, downward and horizontally oriented fins. The horizontal fins present an advantage for this design because it penetrates more into the PCM and transfers heat deep into the solid PCM.

At t = 40 min, A1 design is maintaining the faster melting trend by utilizing the convection currents, whereas, A2 and A3 designs have lost the melting pace because the convective currents are no more helpful to melt the a large mass of PCM lying away from the convection zones. For $t = 60 - 100min$, the rest of the

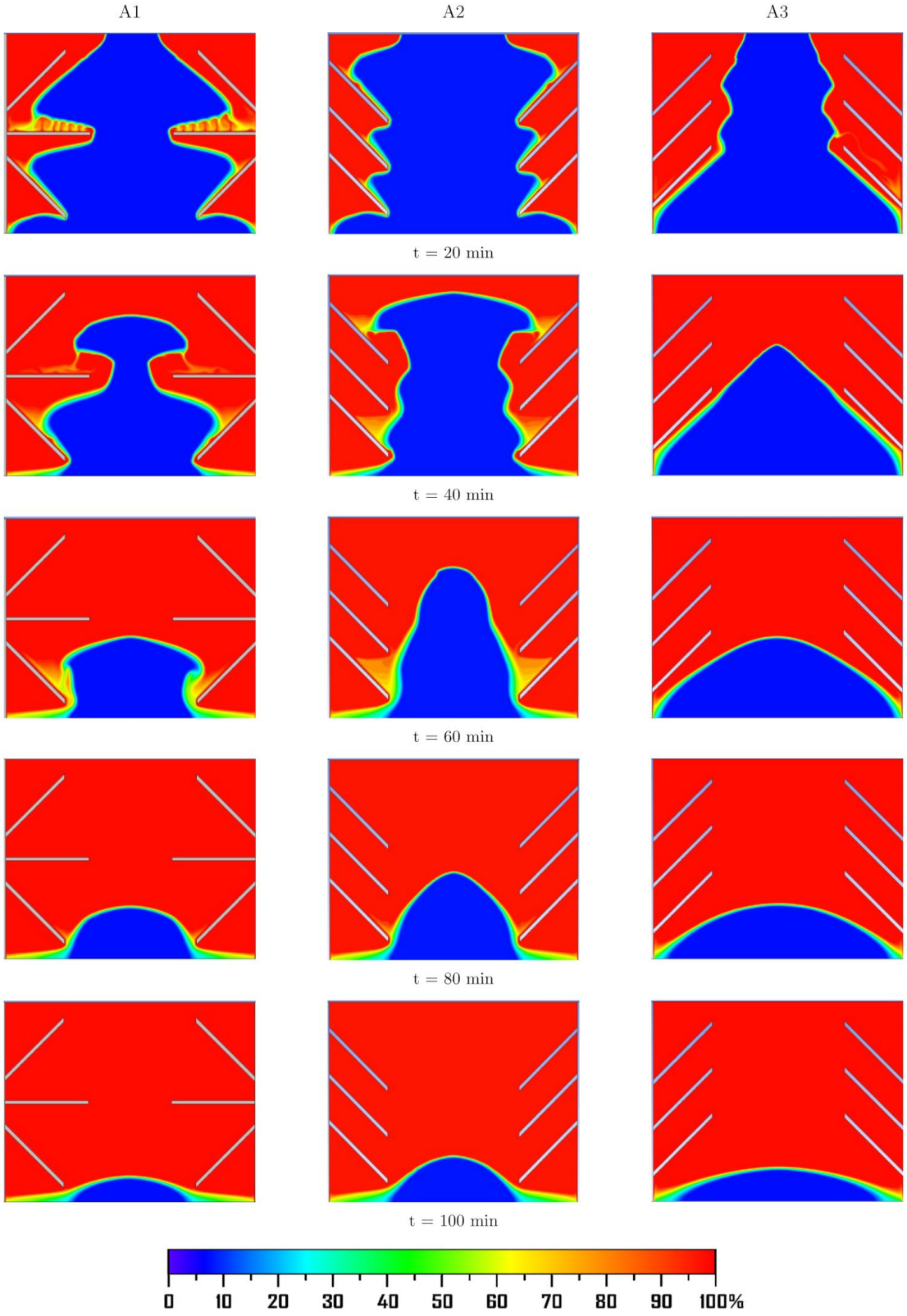


FIGURE 4.5: Liquid fraction contour plots for "A" configuration.

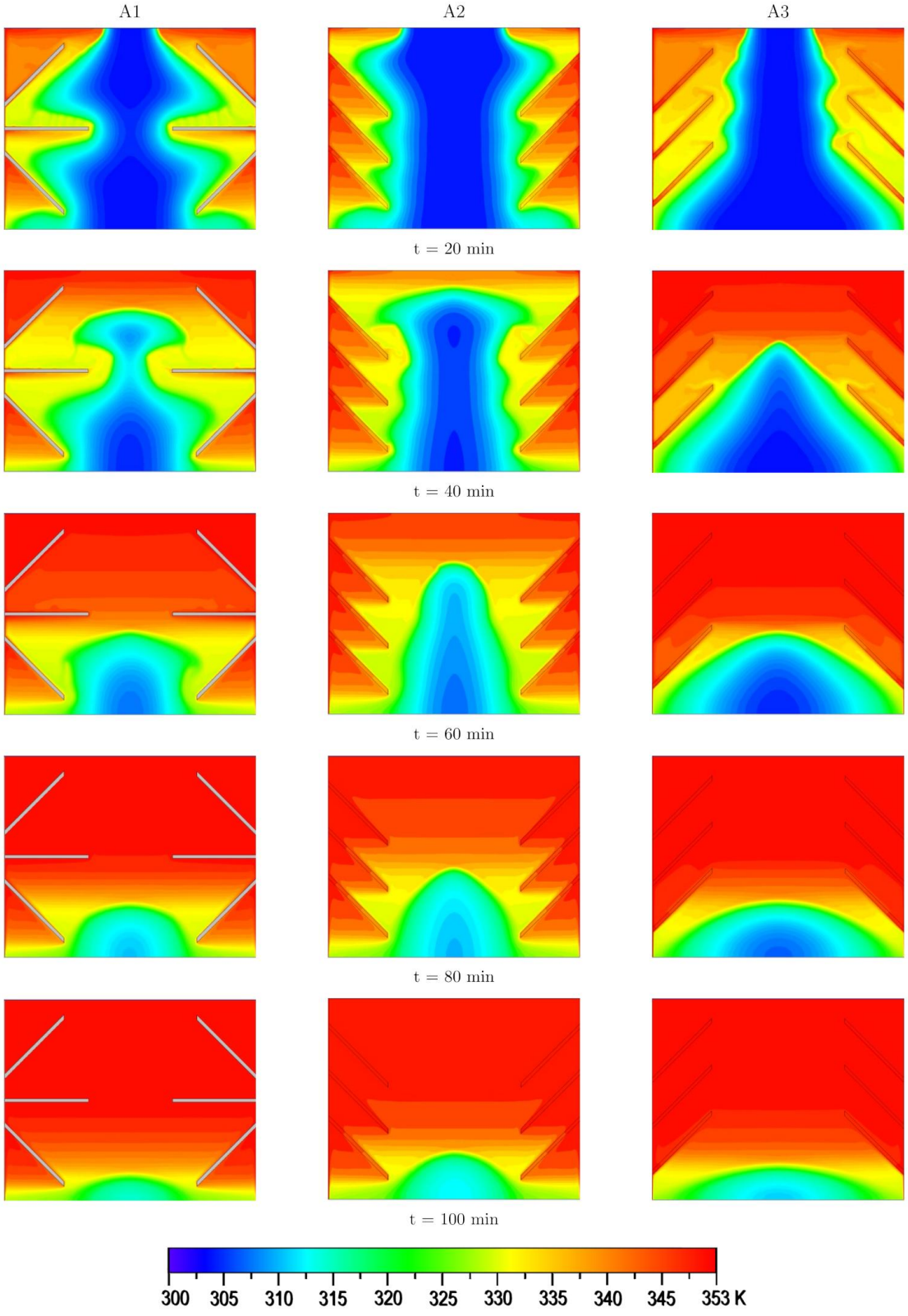


FIGURE 4.6: Temperature contour plots for "A" configuration.

solid PCM continues to melt slowly mostly through conduction heat transfer for all the three cases. Temperature contour plots indicates localized high temperature zones where the liquid PCM gets trapped initially and continuously gets heated. These zones then continuously build up and fill the whole region containing the melted PCM. To quantify the melting trends and thermal behaviors relative to the reference case, line plots for the temporal variation of liquid fraction, temperature, and energy storage are presented in Figure 4.7a to 4.7c for all three cases along with the reference case.

It can be observed from the liquid fraction plots that nearly 20% of the PCM gets melted for all the cases in the initial 10 minutes. Design A3 maintains the faster melting pace due to the favorable slope of the fins till $t = 20min$, but afterwards, it slows down and eventually approach the trend of the A2 design. Design A1, although, performing moderate during the initial 30 minutes, ends up best with the minimum melting time among the three designs. All the three designs, however, prove to be inferior to the reference case. Design A1 took 16% more time to complete the melting cycle as compared to the reference case. The average PCM temperature trends, shown in Figure 4.7b, also demonstrate that the temperature rise for all designs of A configuration is slower than that of the reference case.

The temperature profile for all cases almost matches with the reference case till $t = 20min$. The design A2 shows a sudden decline in the temperature profile and remain almost linear till $t = 90min$. The A1 and A3 designs continue with the same rate till $t = 50min$. Afterwards, design A3 illustrates decline in the average temperature values and approaches with the rate of A2 design at 110 minute.

The energy storage trends, shown in Figure 4.7c, also follow the melting path: more the melting time more time a design takes to store the maximum amount of energy. The energy storage rate in cases A1 and A3 proceed at a similar rate till $t = 40min$. The rate for A3 starts to decline while energy storage rate in A1 continues at the same rate till $t = 60min$ and then starts to gradually slow down

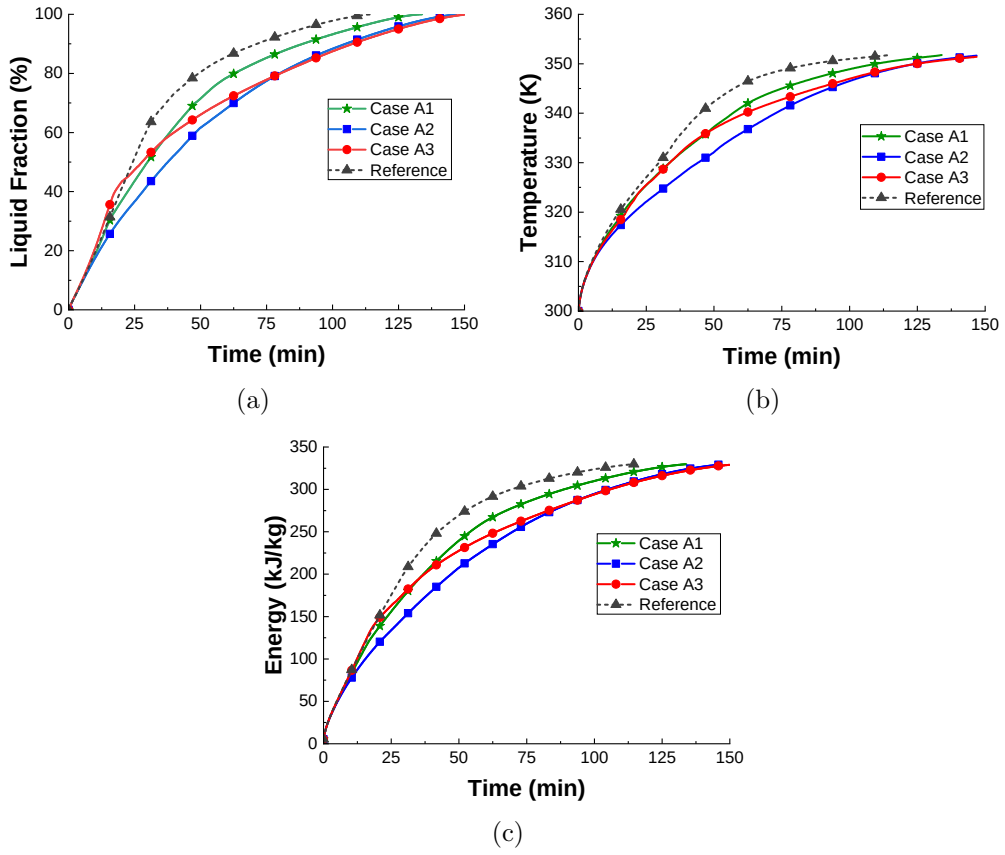


FIGURE 4.7: Comparison of (a) liquid fraction, (b) temperature and (c) thermal energy for A1, A2, and A3 configurations.

after that. The energy rate for all A cases is slower than reference case as can be seen in the Figure 4.7c.

## 4.4 Analysis of Configuration Cases S1 and S2

S configuration deals with the shape modifications of the fins in LHTES and include two variants named as S1 and S2. The dimensional details of these designs are shown in Figure 4.1b. Numerical simulations are performed and results are presented in the form of contour plots of liquid fraction and temperature as shown in Figure 4.8. Furthermore, to quantitatively analyze these results against the reference case, the time history of the liquid fraction, temperature, and energy storage is presented in Figures 4.9a to 4.9c for both the designs along with the results of reference case. The trends of liquid fraction, shown in Figure 4.9a,

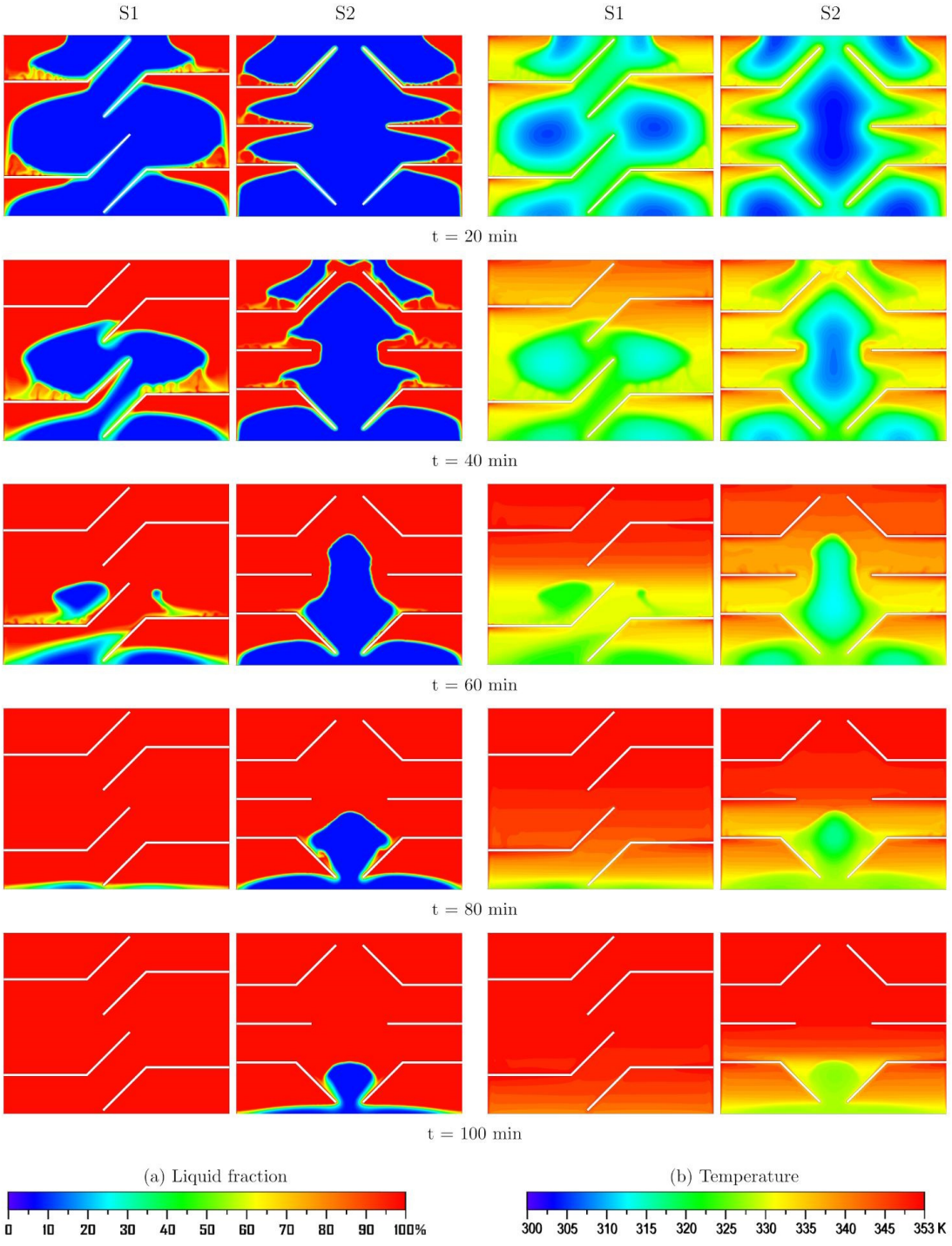


FIGURE 4.8: Contour plots of liquid fraction and temperature for S1 and S2 configurations at five different time instances.

indicate that the design S1 performs better compared to S2 reporting higher liquid fraction values from the start of the melting till complete melting. This is due to the fact that the S1 design configuration creates more convection current due to

buoyancy effects which reinforce each other and results in faster melting rates.

The S2 design configuration of fins poses a disadvantage as indicated by a decrease in the melting rate shown in Figure 4.9a because the solid body of PCM lying vertically at the center of the LHTES is away from the fins and melts slowly. Also, the central region of this configuration acts to suppress the convective currents and slows down the melting. In contrast, the design S1 has fewer but longer fins and their bent ends are parallel to each other handling the middle vertical portion of the LHTES effectively. The melting is faster compared to S2. After 30 minutes,

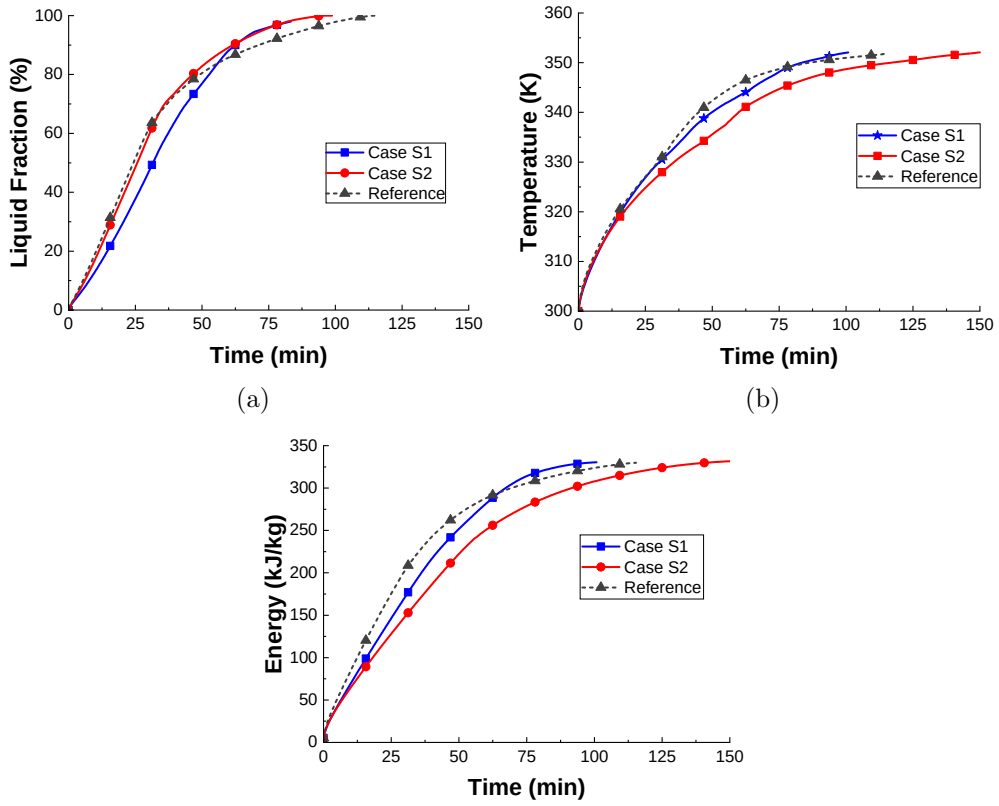


FIGURE 4.9: Comparison of (a) liquid fraction (b) temperature and (c) thermal energy for S1 and S2 configurations.

melting rate in S1 design further increases and difference in melting rate of S1 and S2 increases till 80 minutes into melting. Furthermore, the temperature of the melted portion continuously rise as time progresses, ultimately approaching the temperature of the Heat Transfer Fluid (HTF) where it has stored maximum

possible energy. The profiles of average PCM temperature are presented in Figure 4.9b.

During the initial 18 minutes into melting process the rise in temperature is almost same and matches closely with the rate of reference case. This corresponds to conduction dominant heat transfer and the average temperature in LHTES reaches about $318K$ at this time. The average temperature decreases for S2 as compared to S1 and maintains the decreasing trend. At $t = 94min$ which corresponds to complete melting of S1, the average PCM temperature for S1 approaches $351K$. At the same instant of time the temperature for design S2 is $348K$. The energy storage rates follow the trends of the melting rates as obvious.

The trends in Figure 4.9c indicate that S1 design performs better than the reference case, whereas, S2 design proves inferior to the reference case. The melting rate for both S1 and S2 is slower compared to the reference case in the beginning of the melting till t = 60 min. After that point in time S1 configuration achieves faster melting rate than the reference case and remains high till the end of melting. The melting rate of S2 remains lower than the reference case for the complete melting process. The trends in the figure show that the total melting is accelerated by 18% for design S1. Design S2 took 29% more time to complete melting cycle compared to the reference case.

## 4.5 Analysis of Configuration Cases L1, L2, L3, L4, and L5

A set of five designs, named as L1, L2, L3, L4, and L5, is proposed by varying the lengths, thicknesses and arrangement of fins in the LHTES as shown in Figure 4.2. The surface area of the fins exposed to the PCM changes as the lengths and thicknesses of fins are changed and ultimately affect the thermal performance of the unit. For a unit meter depth of the LHTES, the surface areas for L1, L2,

L3, L4, and L5 designs are 1.2 $m^2/m$, 0.96 $m^2/m$, 2.0 $m^2/m$, 1.44 $m^2/m$ and 1.44 $m^2/m$, respectively.

Contour plots of liquid fraction and temperature are presented in Figure 4.10 and 4.11, respectively, for all the designs at five different time instances during the melting life cycle. Furthermore, transient variation of the liquid fraction, temperature, and energy storage for all five designs along with the reference case is illustrated in Figure 4.12a to 4.12c in the form of line plots for the quantitative comparative analysis.

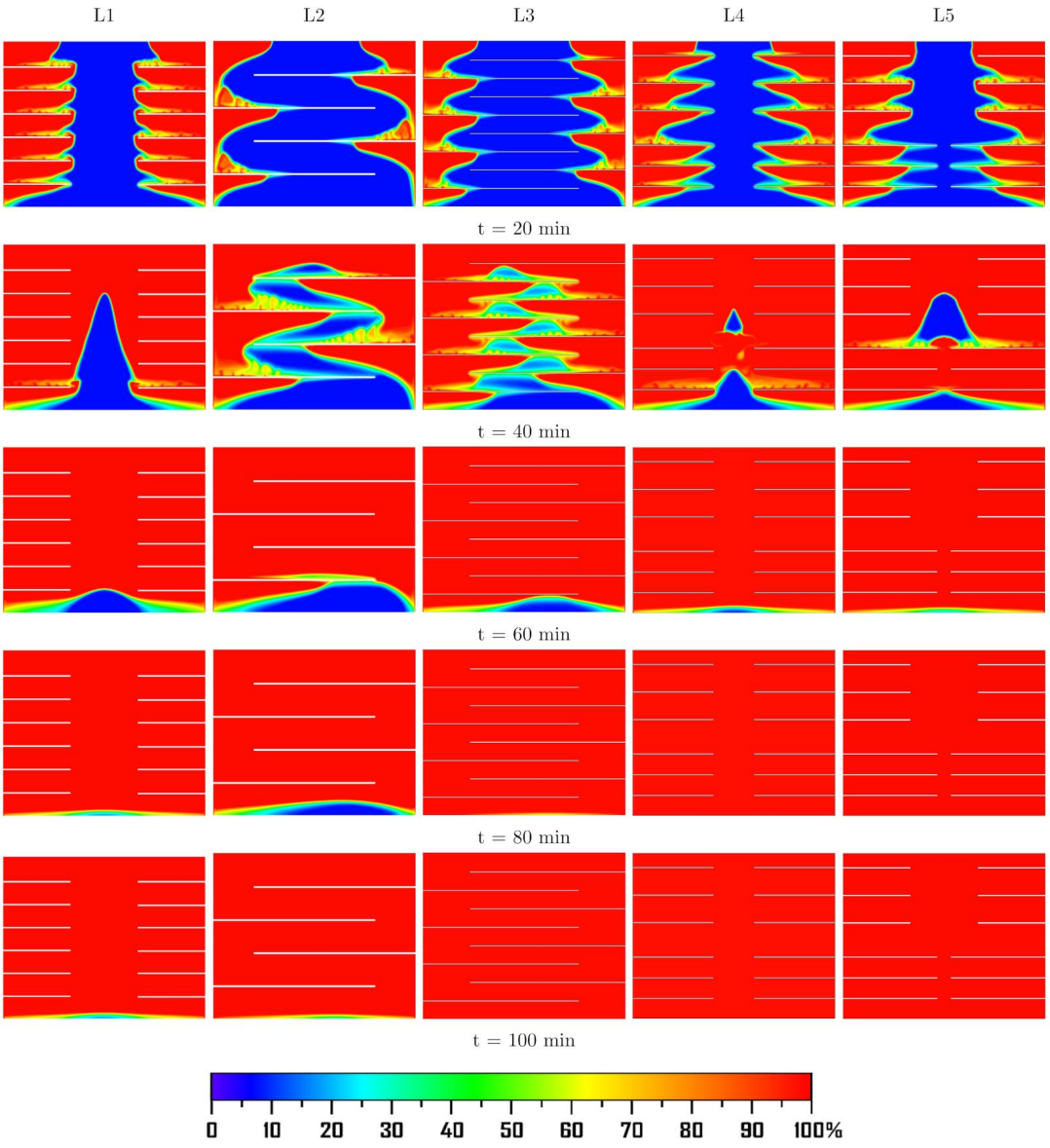


FIGURE 4.10: Contour plots of liquid fraction of "L" configurations at five different time instances.

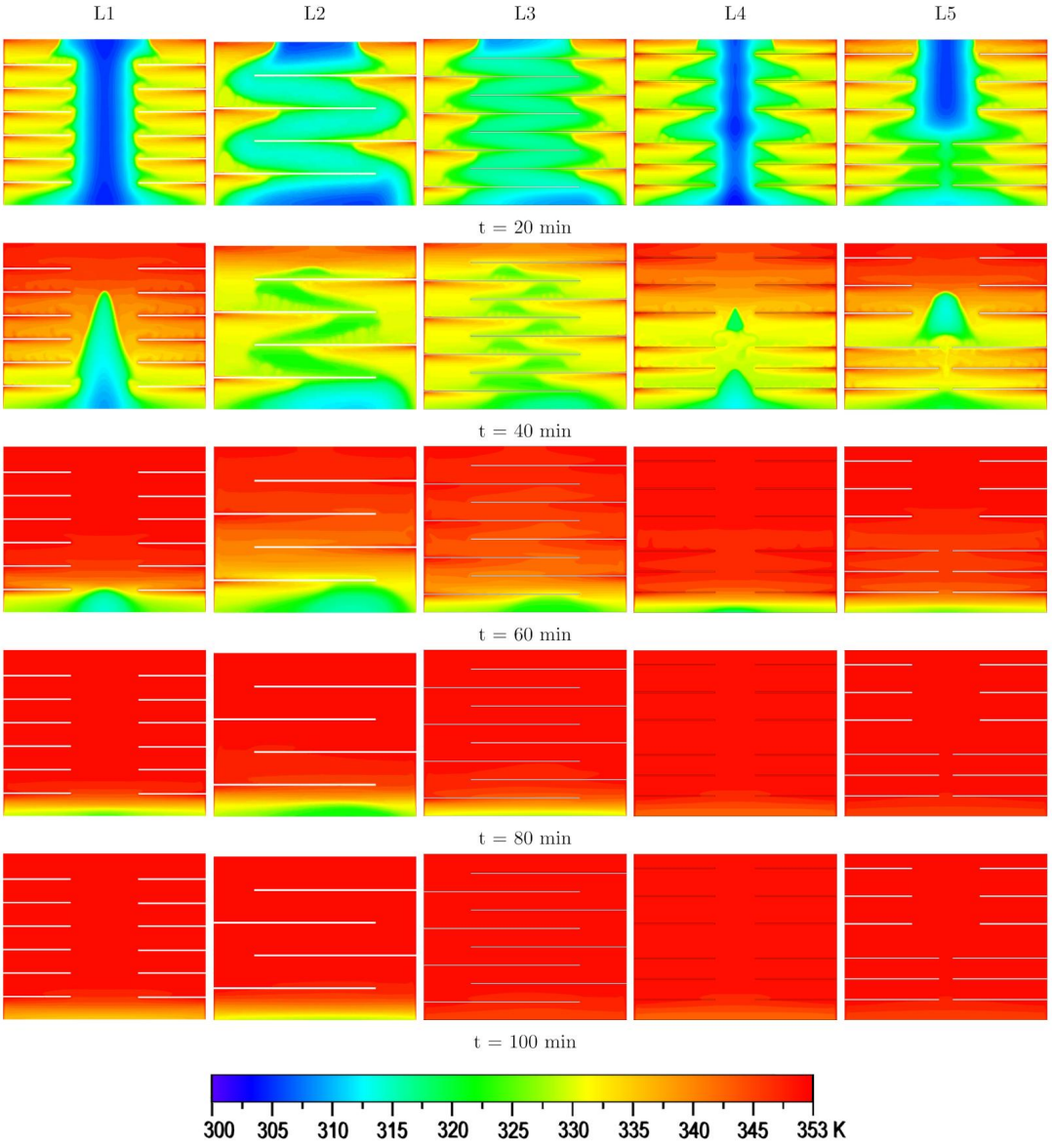


FIGURE 4.11: Contour plots of temperature of "L" configurations at five different time instances.

Trends of liquid fraction for all the designs, shown in Figure 4.12a, indicate a significant change in the slope which manifests a decrease in the melting rate due to switching from the convection to the conduction dominated heat transfer. L5 is the best performing design although the surface area is not the maximum. This is because of the intelligent arrangement of the fins in the LHTES and the generation of strong convection currents by the lower six longer fins which melt the whole PCM on the upfront.

L4 design has same heat transfer surface area as that of L5 but it finished up second, taking a bit more time than L5 design. The is attributed to the intelligent arrangement of the fins in L5 case. It can be concluded that in addition to the heating area exposed to PCM, the fin topology also impact the performance. L3 design has the largest heat transfer surface area and longer fins, however, the melting pace is slower initially because it takes more time to conduct heat to the farther end of the fins as shown by the melting and temperature contour plots at t = 20 min. The melting rate gains the momentum as the currents approach the respective upper heated fins at t = 40 min.

L1 design has a large number of small-sized fins which uniformly transfers heat to the PCM and quickly melts it thereby creating convective currents which eventually melts all the PCM around the fins as shown by the contour plots at t = 20 min. However, there is significant area at the center of the LHTES which is unattended and the PCM melts slowly due to conduction through t = 30 - 60 min interval. This design stands fourth on the performance ranking.

Design L2 is the last in the list taking maximum time to melt the PCM among the five proposed designs. Two main reasons are: the smallest heat transfer surface area and fewer but longer fins. It is interesting to note that this design, though marginally, still performs better than the reference case like the other four designs. Temperature contour plots illustrate significantly low temperatures for L2 design as compared to other design at t = 40 min.

The transient temperature plots, shown in Figure 4.12b, demonstrate similar trends of all the five cases. Except for case L2, the average PCM temperature values are greater than that of the reference case for all other cases and remain higher throughout the melting cycle. At t = 35 minute which corresponds to 80% melting of the best performing case L5, the average temperatures for L2 and L3 designs are 333K and 335K, respectively. For all other L designs the average PCM temperature is 339 K at that time.

The average temperature increase rate is faster during the sensible heat transfer phase while it is relatively slower during latent heat transfer phase. The energy

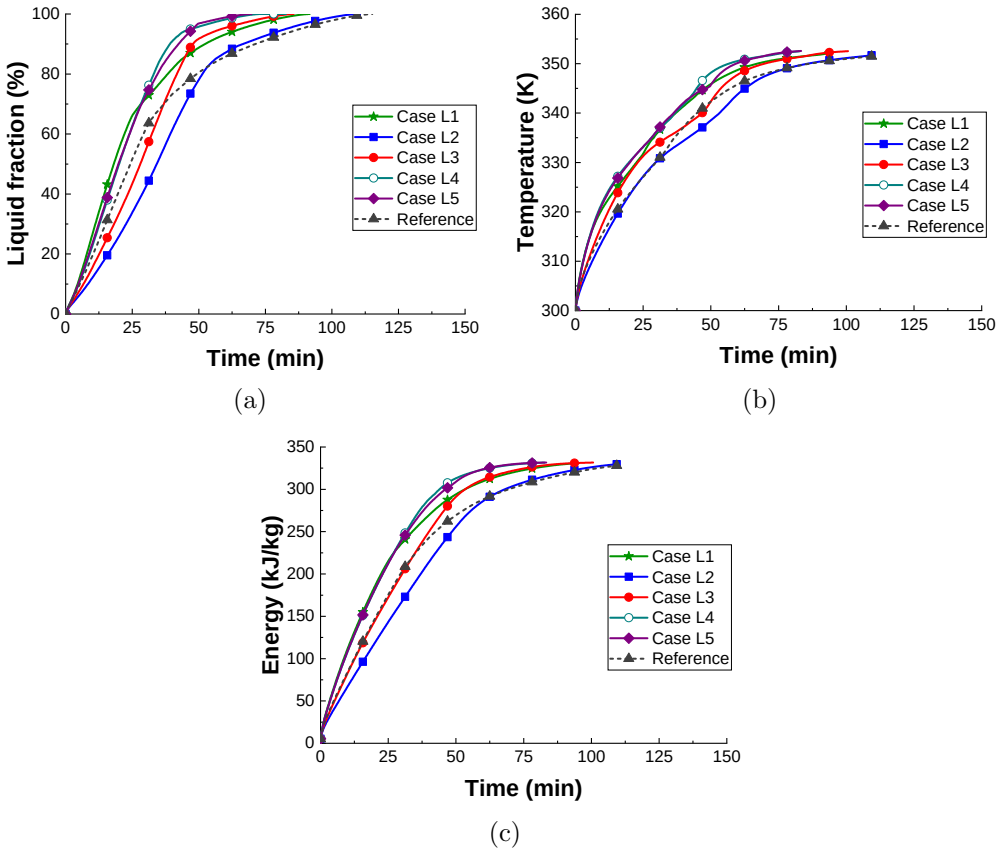


FIGURE 4.12: Comparison of (a) liquid fraction, (b) temperature and (c) thermal energy for L configurations.

storage plots, shown in Figure 4.12c, follow the trends of the liquid fraction both of which are guided by the temperature values. Quantitatively, L1, L2, L3, L4, and L5 designs accelerated the melting due to better heat transfer performance saving 20%, 5%, 26%, 36%, and 39% time, respectively, compared to the reference case for complete melting of the PCM.

## 4.6 Flow Characteristics and Interface Velocity

The melting process was further examined by investigating the flow characteristics of the PCM during the phase change. In addition to analyzing the liquid fraction and temperature contours, the average velocity of the vortices generated during natural convection was studied. As the melting progressed, the melted PCM rose to the top of the system due to convection. The solid PCM adjacent to the heat

source received heat and generated additional vortices, which combined with the previously developed vortices, thereby enhancing the natural convection and heat transfer rate within the system.

The state of velocities in different fin configurations at various time steps is depicted in Figures 4.13, 4.14, and 4.15. These figures provide a visual representation of the velocity distribution within the PCM as it undergoes the melting process.

The average velocity of the liquid PCM gradually increased and reached a maximum as the natural convection became stronger. During the later stages of melting, as the liquid fraction increased, the convection weakened, resulting in decrease in the average PCM velocity.

To quantify the maximum average interface velocity at different time steps, these values were recorded and compiled in Table 4.2. This table provides a comprehensive overview of the velocity characteristics during various stages of the melting process.

TABLE 4.2: Streamline average velocities for A,S, and L configurations.

| **Time** ($min$) | **Average streamline velocity** ($mm/s$) | | | | | | |
|---|---|---|---|---|---|---|---|
| | A1 | A2 | A3 | S1 | S2 | 0-fin | Ref |
| 20 | 2.60 | 1.75 | 0.45 | 2.80 | 2.30 | 3.48 | 2.20 |
| 40 | 3.20 | 3.25 | 3.60 | 3.40 | 3.80 | 3.56 | 4.63 |
| 60 | 2.10 | 2.84 | 2.30 | 1.40 | 2.00 | 3.23 | 1.76 |
| 70 | 1.30 | 2.12 | 2.07 | 1.30 | 1.20 | 2.82 | 1.38 |

By analyzing the flow characteristics, velocity profiles, and convection patterns within the PCM, this study offers insights into the dynamic behavior of the system during the melting process. These findings contribute to a better understanding of the heat transfer mechanisms and can aid in the optimization of fin configurations and overall system design for improved thermal performance.

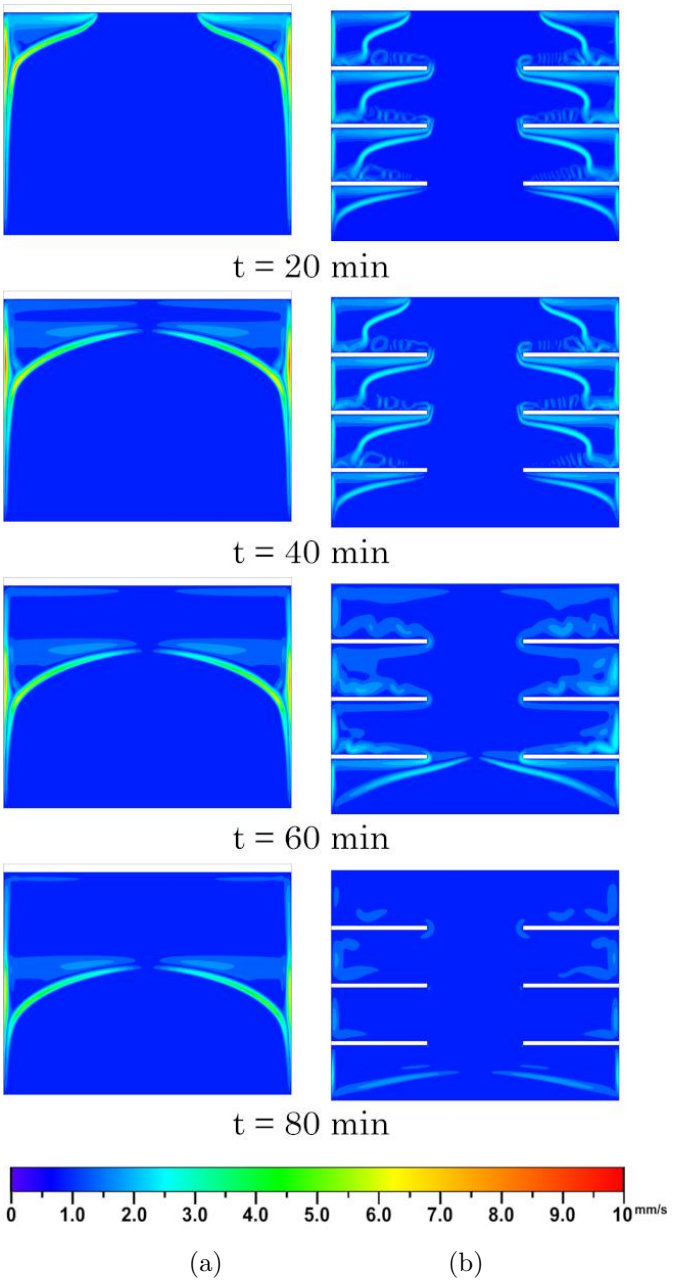


FIGURE 4.13: Velocity contour plots for (a) 0-fin and (b) reference configurations.

## 4.7 Comparative Performance Analysis of Different Design Configurations

Various performance indicators are defined for the overall and transient thermal performance analysis of different LHTES designs. These are the percentage time saving, melting and energy enhancement ratios and the energy transfer rates.

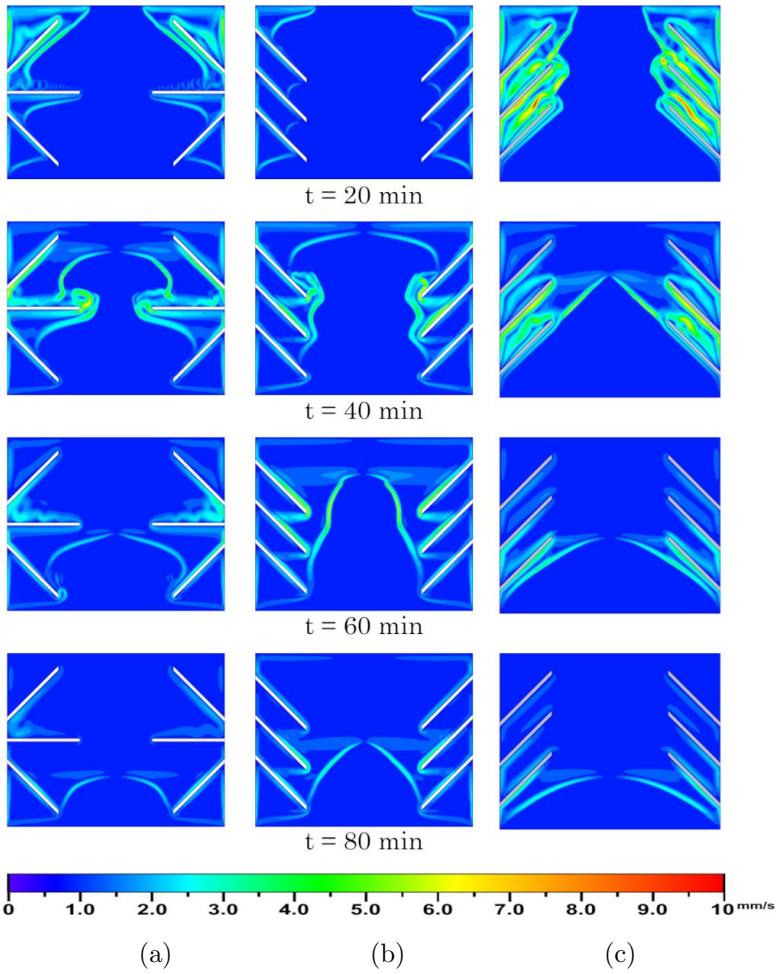


FIGURE 4.14: Velocity contour plots for (a) A1, (b) A2, and (c) A3 configurations.

These performance indicators are based on the melting time and energy storage rates discussed in detail in the previous sections for different design configurations.

### 4.7.1 Melting Time and Time Saving

Numerical results obtained for the complete melting time of PCM for different fin designs are compared and analyzed in this section. A parameter relevant to the melting time is the time saving which quantifies how fast a particular fin design melts the PCM compared to the reference case. The lower the melting time, more is the time saving and better is the thermal performance of LHTES. The time saving is defined as shown in (4.1).

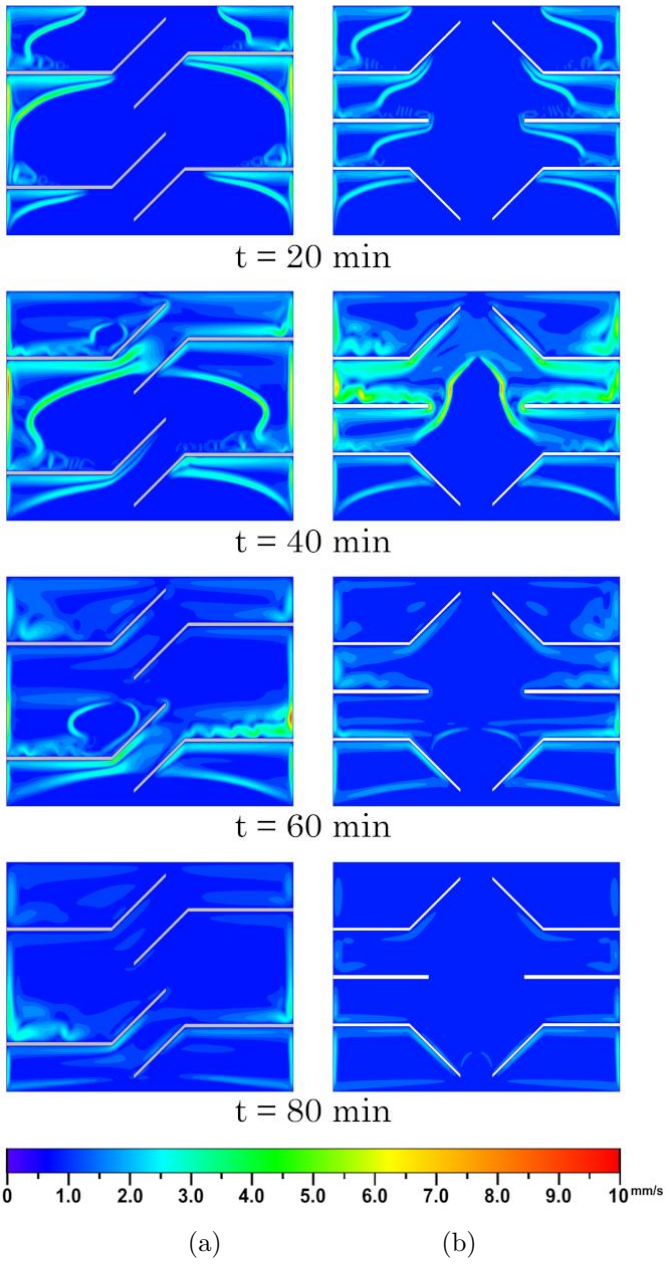


FIGURE 4.15: Velocity contour plots for S configurations.

$$ts_k = \frac{\tau_0 - \tau_k}{\tau_0} * 100 \tag{4.1}$$

where $ts_k$ is the time saving for case $k$ and $\tau_0$ and $\tau_k$ are the complete melting times of the reference case and case $k$, respectively. Melting times and time savings for all designs of LHTES units discussed so far are presented Figure 4.16 and listed in Table 4.3.

It can be observed that the no fin case takes maximum time of 205 minutes for

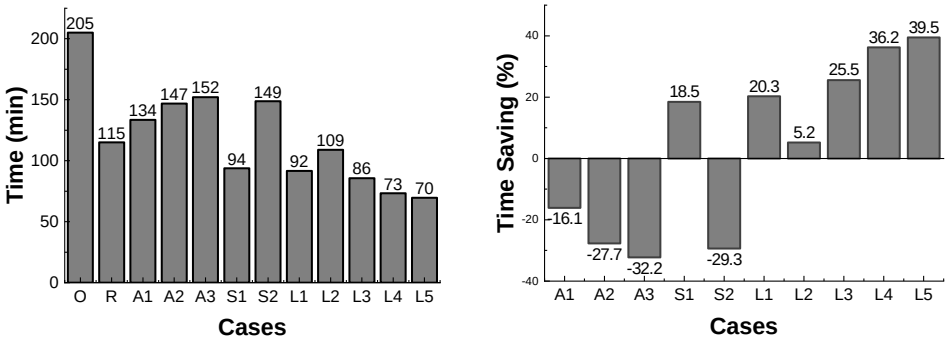


(a) (b)

FIGURE 4.16: (a) Total melting time and (a) Melting enhancement ratio.

complete melting, whereas, the reference case takes 115 minutes. All variants of "A" configuration take more time to melt than the reference case, hence, got negative values of time saving.

The evaluation of different designs, including "S" and "L" configurations, showed that most designs outperformed the reference case in terms of melting time, except for the S2 design. Among all the designs, L5 emerged as the best overall, taking 70 minutes to completely melt the PCM and resulting in a significant time-saving value of 39%. These findings highlight the impact of design modifications on the efficiency of the melting process. The successful performance of the L5 design underscores the importance of selecting an appropriate configuration for optimizing melting, offering potential benefits such as increased productivity and energy savings. The comparative analysis of different designs provides valuable insights into design considerations and can guide the development of more efficient thermal energy storage systems.

### 4.7.2 Performance Enhancement Ratios

Melting and energy enhancement ratios are defined to monitor the transient variation of the melting and energy storage characteristics of the proposed designs with respect to the reference case. These ratios are mathematically expressed as shown

TABLE 4.3: Melting times and improvement ratios for various fin designs.

| **Configuration** | **Fin surface area** ($mm^2$) | **Melting time** (min) | **Enhancement ratio** |
|---|---|---|---|
| Zero-Fin | 600 | 205.00 | - |
| Reference | 600 | 115.00 | - |
| Case A1 | 600 | 133.54 | -16.1% |
| Case A2 | 600 | 146.87 | -27.7% |
| Case A3 | 600 | 152.08 | -32.2% |
| Case S1 | 760 | 93.75 | 18.5% |
| Case S2 | 824 | 148.75 | -29.3% |
| Case L1 | 1200 | 91.67 | 20.3% |
| Case L2 | 960 | 109.00 | 5.2% |
| Case L3 | 1846 | 85.63 | 25.5% |
| Case L4 | 1440 | 73.33 | 36.2% |
| Case L5 | 1440 | 69.58 | 39.5% |

in Equations (4.2) and (4.3).

$$E_{mr}(t) = \frac{\gamma_k(t)}{\gamma_0(t)} \tag{4.2}$$

$$E_{er}(t) = \frac{\zeta_k(t)}{\zeta_0(t)} \tag{4.3}$$

where $E_{mr}(t)$ and $E_{er}(t)$ are the melting and energy enhancement ratios at any time $t$, respectively. $\gamma$ represents the liquid fraction while $\zeta$ denotes the energy storage in kJ. The subscripts 0 and $k$ define the reference case and case $k$, respectively. Figures 4.17a to 4.17c illustrate the melting enhancement ratio plots for all three configurations while energy enhancement ratios are plotted in Figure 4.18a to 4.18c over the complete melting time.

Melting enhancement ratio plots for configuration A reveal that all the variants perform inferior to the reference case throughout the melting life cycle except for the design A3 which shows $E_{mr}(t) > 1.0$ for the initial 20 minutes. This is attributed to the upward sloped fins of design A3 which supports the convection

currents and quickly melts the PCM in the beginning. Later on, the PCM settling below the fins melt slowly powered by conduction as explained earlier.

For S configuration, the melting rates of both the variants are slower than the reference case as indicated by the $E_{mr}(t) < 1.0$ values despite having more heat transfer surface area than reference case. The reason being the longer fins taking more time to heat up throughout. S1 design starts performing better than the reference case after t = 60 minutes. This is because the heat is now conducted to the end of the fins and the convective currents generated add up and reinforce each other to accelerate the melting.

Among the L configuration designs, L1, L4, and L5 perform better than the reference case. L2 design, however, performs comparable to the reference case for t $\geq$ 50 min. L3 design shows improved performance at t = 40 min and remains better than reference case till complete melting.

Heat transfer surface areas are significantly larger for L configuration than the reference case which enhance melting. The peak of $E_{mr}(t)$ curve attains as high as 1.38 for L1 design at t = 10 min then drops below other curves except that of L2.

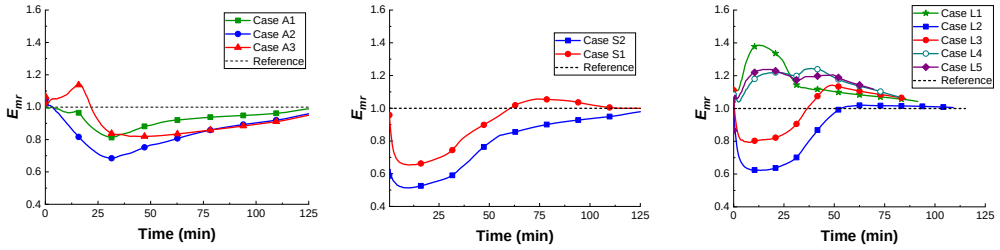


FIGURE 4.17: Melting enhancement ratio $E_{mr}$ for (a) A, (b) S, and (c) L Configurations

Energy enhancement ratios, plotted in Figure 4.18a to 4.18c, are dependent on the transient energy storage characteristics of the proposed designs with respect to the reference case. The energy storage can be sensible or latent depending on whether the PCM melts or not. The melting of PCM is governed by the thermal characteristics of the LHTES, i.e., heat transfer surface area, arrangement of

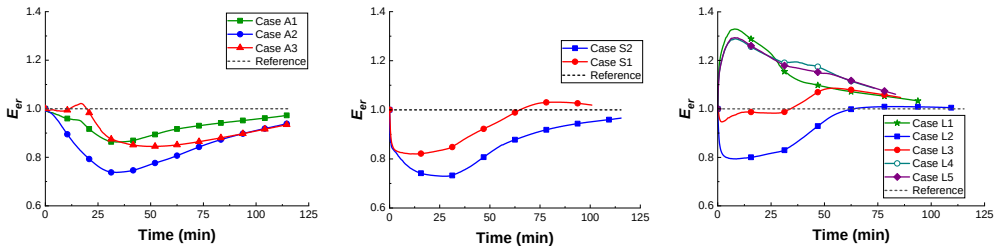


FIGURE 4.18: Energy enhancement ratio $E_{er}$ for (a) A, (b) S, and (c) L Configurations.

fins, etc. Hence it can be concluded that the energy enhancement ratio trends will qualitatively be governed by the melting enhancement ratio. All designs of A configuration have $E_{er}(t) < 1.0$ throughout the melting cycle except one spike with a value greater than 1 for A3 design. S1 design of S configuration has $E_{er}(t) > 1.0$ after t = 65 minutes whereas S2 design performs inferior to the reference case on the scale of energy enhancement ratio. L1, L4 and L5 designs of L configuration have $E_{er}(t) > 1.0$ throughout the melting time.

### 4.7.3 Heat Transfer Rate

The melting progression and the corresponding energy storage rate of any LHTES design is governed by the heat transfer rate. Higher the heat transfer rate, quicker is the energy stored in the LHTES. Therefore, it is a fundamental parameter to be considered while designing a LHTES for heat transfer enhancement. Mathematically, it is expressed as

$$\dot{Q}(t) = \frac{Q(t + \Delta t) - Q(t)}{\Delta t} \tag{4.4}$$

where $\dot{Q}(t)$ is the heat transfer rate at time $t$ while $Q(t)$ and $Q(t + \Delta t)$ represent the energy stored in the LHTES at time $t$ and $t + \Delta t$, respectively. Figure 4.19a to 4.19c illustrates the heat transfer rates for all the proposed design configurations plotted over the complete melting time along with the reference case. It can be

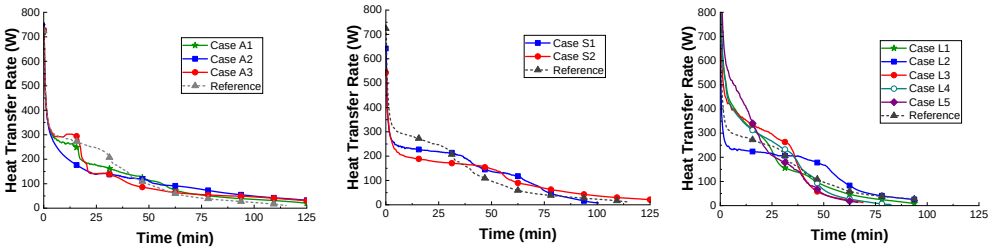


FIGURE 4.19: Heat transfer rate $\dot{Q}$, for A, S, and L.

observed that during the initial stages of the melting process the temperature difference between the hot surfaces and the PCM is high resulting in high heat transfer rates.

As the melting progresses, the thickness of the melted liquid layer increases around the heated surfaces decreasing the temperature gradient between the heated wall and PCM causing a reduction in the heat transfer rates. For A configuration, the heat transfer rates of all the designs are lesser than the reference case during the initial 40 minutes interval which resulted in comparatively slower melting and energy storage rates as discussed previously.

Heat transfer rates of the S1 and S2 designs are less than the reference case for the initial 30 minutes but it then outperforms the reference case for the next 50 minutes. All designs of L configuration have higher heat transfer rates compared to the reference case during the initial 20 minutes into the melting process except for the L2 design. All these trends are truly reflected in the melting and the energy storage trend of the respective designs. To quantitatively compare the heat transfer rates of different designs over the complete melting time, average heat transfer rate is defined as

$$\dot{Q} = \frac{Q_{total}}{t_m} \tag{4.5}$$

Where $Q_{total}$ is the energy stored by the PCM when completely melted and $t_m$ is the time taken to completely melt the PCM. The average energy storage rate for

all cases are shown in Figure 4.20. The average energy storage rate of the reference case is 47.8 W.

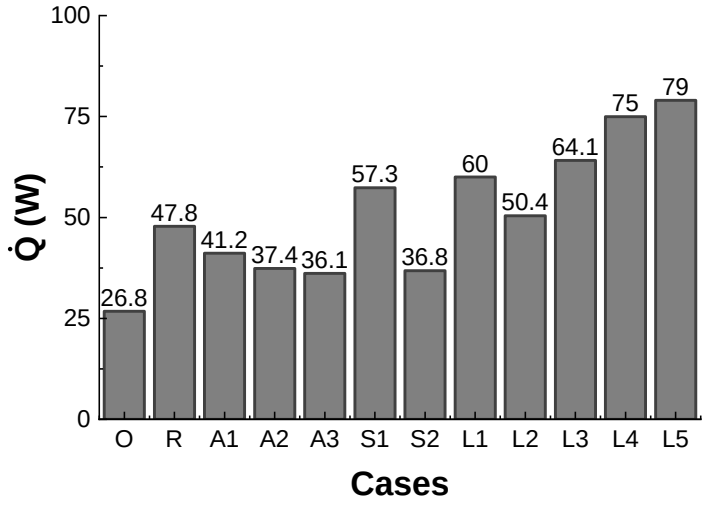


FIGURE 4.20: Energy storage rate for all cases.

All design variants of A configuration have $\dot{Q}$ values less than that of the reference case, whereas, the S and L configuration designs show higher average heat transfer rate values than the reference case except for the S2 design. L5 design is the best among all designs on the basis of $\dot{Q}$ achieving a value of 208 W with L4 being the next in the list at 197 W. The results are presented in Table 4.4.

TABLE 4.4: Average energy storage rate.

| **Configuration** | **Melting time** (min) | **Storage rate** (W) |
|---|---|---|
| Zero | 205 | 26.8 |
| Reference | 115 | 47.8 |
| Case A1 | 133.54 | 41.2 |
| Case A2 | 146.87 | 37.4 |
| Case A3 | 152.08 | 26.1 |
| Case S1 | 93.75 | 57.3 |
| Case S2 | 148.75 | 36.8 |
| Case L1 | 91.67 | 60 |
| Case L2 | 109 | 50.4 |
| Case L3 | 85.63 | 64.1 |
| Case L4 | 73.33 | 75 |
| Case L5 | 69.58 | 79 |

Based on the analysis of all the performance indicators discussed, it can be concluded that the L5 design is the best performing among all designs.

## 4.8 Effect of Wall Temperature

The optimum design L5 is further studied by varying the isothermal wall temperature to analyze its impact on the thermal performance of the heat storage device. Five different cases are simulated with wall temperatures of 343 K, 348 K, 353 K, 358 K, and 363 K and the results are compared with the reference case results at 353 K. The reference case melts completely in 115 minutes. Table 4.5 presents the complete melting time and the percentage time saving results for all the cases. The melting time decreases as the isothermal wall temperature is increased. The higher wall temperature results larger temperature gradients resulting in the faster heat transfer and consequently smaller melting time.

For $T_w = 343$ K, the complete melting time is 128.54 min which is greater than the reference case value, hence, resulting in negative time saving. The rest of the cases melt faster than the reference case resulting in positive values of time saving. The plots of melting and energy enhancement ratios are presented in Figure 4.21a and 4.21b. For a wall temperature of 343 K, both $E_{mr}$ and $E_{er}$ values are less than 1.0 throughout the melting process, whereas, for 348 K these values are comparable to reference case values. All other cases have enhancement ratio values greater than 1.0. The instantaneous heat transfer rate is illustrated in Figure 4.21c. A linear increasing trend is observed for the total average energy storage rate because of an increase in the sensible energy storage content. This increasing average energy storage trend is justified by an increase in the heat transfer rates for higher wall temperature cases.

TABLE 4.5: Effects of varying wall temperature on melting time, time saving and average energy storage rate for design L5.

| **Temperature** (K) | **Melting time** (min) | **Time saving** (%) | **Storage rate** (W) |
|---|---|---|---|
| 343 | 129 | -11.8 | 39.8 |
| 348 | 83.3 | 27.5 | 63.64 |
| 353 | 69.6 | 39.5 | 79 |
| 358 | 55.8 | 51.5 | 100.97 |
| 363 | 48.3 | 58 | 120.66 |

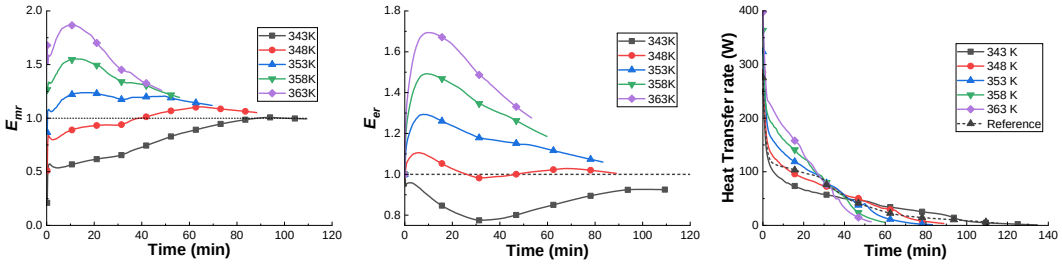


FIGURE 4.21: Effects of varying wall temperature on the temporal variation of the (a) melting enhancement ratio (b) energy enhancement ratio and (c) heat transfer rate for design L5 in comparison with the reference case results.

The numerical results of the melting time and mean convective heat transfer coefficients for different wall temperatures are provided in Table 4.6 in the form of non-dimensional numbers. These non-dimensional numbers offer a normalized representation of the results, enabling comparisons and generalizations across different conditions. The mean convective heat transfer coefficient is expressed in terms of the non-dimensional Nusselt number, denoted as $\overline{Nu}$.

The wall temperature is represented by the Rayleigh number, denoted as $Ra$, and the Stefan number, denoted as $St_e$. These non-dimensional numbers allow for a standardized assessment of the convective heat transfer characteristics, facilitating comparisons between different configurations and wall temperature variations.

The non-dimensional melting time of the PCM is represented by the melting Fourier number, denoted as $Fo$. This non-dimensional number quantifies the rate of melting in relation to the thermal properties and geometry of the system. By using the melting Fourier number, the melting time can be analyzed and compared across different designs and operating conditions . The definitions of these non-dimensional numbers, namely the Nusselt number, Rayleigh number, Stefan number, and melting Fourier number, are provided in equations 3.24, 3.27, 3.28, and 3.29, respectively. These equations establish the mathematical relationships and formulas used to calculate the non-dimensional numbers and aid in the interpretation of the numerical results.

By presenting the results in non-dimensional form and providing the corresponding definitions, this study offers a standardized framework for analyzing and comparing the thermal performance of different configurations and wall temperature variations within the latent heat thermal energy storage system.

TABLE 4.6: $\overline{Nu}$, $Ra$, $Ste$ and $Fo$ numbers for design L5 at different wall temperatures.

| $\mathbf{T_w}(K)$ | $\overline{\mathbf{Nu}}$ | **Ra** | **Ste** | **Fo** |
|---|---|---|---|---|
| 343 | 57.85 | $8.658 \times 10^7$ | 0.0753 | 0.06485 |
| 348 | 78.28 | $1.599 \times 10^8$ | 0.1391 | 0.04449 |
| 353 | 93.09 | $2.333 \times 10^8$ | 0.2029 | 0.03505 |
| 358 | 108.95 | $3.067 \times 10^8$ | 0.2667 | 0.02823 |
| 363 | 119.86 | $3.801 \times 10^8$ | 0.3305 | 0.02434 |

To further elaborate on the analysis and correlation presented in Figure 4.22a and Equation (4.6), we can discuss the implications of the relationship between dimensionless melting time ($Fo$) and Stefan Number ($Ste$) in the context of changing wall temperature.

$$Fo = a_1 Ste^{-b_1} \tag{4.6}$$

Where $a_1$ and $b_1$ are constants which are equal to 0.01221, and 0.6479, respectively.

The plot in Figure 4.22a demonstrates that as the Stefan Number increases, indicating a higher rate of heat transfer from the wall to the melting material, the melting time (represented by $Fo$) decreases. This makes intuitive sense, as a higher heat transfer rate would accelerate the melting process.

However, the decreasing trend observed in the plot is non-linear. Initially, when the Stefan Number is relatively low, the reduction in melting time is significant with an increase in $Ste$. As $Ste$ continues to increase, the gradient of the decreasing trend slows down, indicating that the diminishing returns of heat transfer on the melting time become more pronounced. In other words, the additional heat transferred at higher $Ste$ values has a diminishing impact on further reducing the melting time.

To approximate this non-linear relationship between $Fo$ and $Ste$, the proposed correlation given in Equation (4.6) can be utilized. This equation provides a mathematical expression that captures the general trend observed in the plot. However, it's important to note that the specific coefficients and functional form of the correlation would need to be determined through data fitting or theoretical analysis specific to the system being studied.

It's worth mentioning that the correlation in Equation (4.6) might not capture all the intricacies of the melting process and the effect of changing wall temperature. It serves as an approximation or an empirical relationship that provides a reasonable estimation of the relationship between $Fo$ and $Ste$ based on the observed trend in the data.

By using this correlation, researchers and engineers can make predictions or estimations regarding the melting performance for different values of $Ste$ without conducting extensive experiments. However, it's important to validate the correlation against experimental or numerical data to ensure its accuracy and applicability to the specific system under consideration.

Overall, the analysis and correlation presented in Figure 4.22a and Equation (4.6) provide insights into the effect of changing wall temperature, as indicated by the Stefan Number, on the dimensionless melting time. This information can be valuable for designing and optimizing processes involving melting phenomena.

To further discuss the analysis and correlation presented in Figure 4.22b and Equation (4.7), we can delve into the implications of the relationship between the average Nusselt number and Rayleigh number when varying wall temperature in the context of natural convection.

The plot in Figure 4.22b demonstrates that as the Rayleigh number increases, indicating a higher driving force for natural convection, the average Nusselt number also increases. The Nusselt number characterizes the convective heat transfer coefficient, and an increase in the average Nusselt number suggests a more efficient

heat transfer process.

$$\overline{Nu} = a_2 Ra^{b_2} \tag{4.7}$$

Where $a_2$ and $b_2$ are constants which are equal to 0.00663, and 0.49624, respectively.

However, similar to the melting performance analysis discussed earlier, the trend observed between the average Nusselt number and Rayleigh number is non-linear. Initially, as the Rayleigh number increases, the average Nusselt number rises significantly. This indicates that the convective heat transfer enhances considerably with increasing Rayleigh numbers, which typically occur with higher temperature differences or lower viscosity fluids.

As the Rayleigh number continues to increase, the rate at which the average Nusselt number rises slows down. This behavior suggests that the diminishing returns of convective heat transfer become more apparent at higher Rayleigh numbers. In other words, the additional heat transfer resulting from the increased driving force of natural convection has a diminishing impact on further increasing the average Nusselt number.

To approximate this non-linear relationship between the average Nusselt number and Rayleigh number, the proposed correlation given in Equation (4.7) can be utilized. This equation provides a mathematical expression that captures the general trend observed in the plot. However, as with the previous correlation, the specific coefficients and functional form of this correlation need to be determined through data fitting or theoretical analysis specific to the system being studied.

It's important to note that the correlation in Equation (4.7) serves as an approximation or empirical relationship that represents the general behavior observed in the data. It may not capture all the complexities and intricacies associated with natural convection and the effect of varying wall temperature. Therefore, validation against experimental or numerical data is essential to ensure its accuracy and applicability to the specific system under consideration.

By utilizing this correlation, researchers and engineers can estimate the average Nusselt number for different Rayleigh numbers without conducting extensive experiments. This information is valuable for designing and optimizing heat transfer systems involving natural convection.

In summary, the analysis and correlation presented in Figure 4.22b and Equation (4.7) provide insights into the effect of varying wall temperature, as indicated by the Rayleigh number, on the average Nusselt number in the context of natural convection. This information can aid in understanding and predicting heat transfer performance in situations where natural convection plays a significant role.

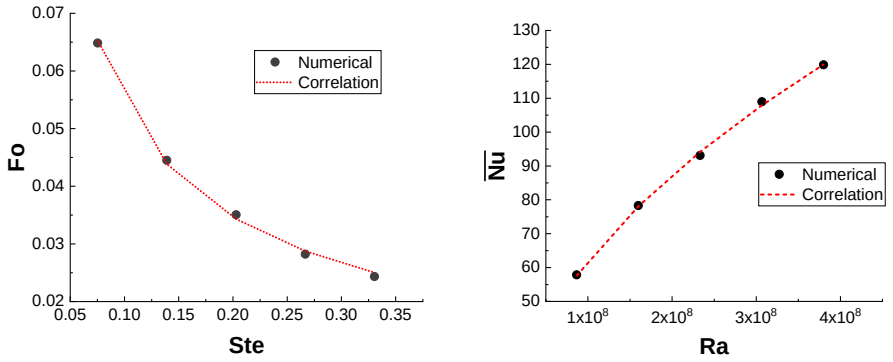


FIGURE 4.22: Correlations (a) ($Fo$ number) vs ($Ste$ number) and (b) $\overline{Nu}$ number vs. $Ra$ number.

## 4.9 Conclusion

This chapter discussed the numerical study performed to study the enhancement of the thermal performance of a rectangular shaped latent heat storage device based on fin variations. The device was modeled as a 2D planar geometry whose both side walls were kept at constant temperature of 353 K, Stearic acid was used as PCM filled in the cavity. Extended surfaces in the form of fins were employed to accelerate the heat transfer from the isothermal walls to the PCM for energy storage. Various fin-parameters were varied, including the number of fins,

their lengths, thicknesses, orientations and positions at the isothermal walls. The proposed designs were grouped under three configurations: the designs in which fin-orientations were varied are grouped under "A" configuration, the designs with fin-shape variations are categorized as "S" configuration and the designs in which lengths and number of fins were predominantly varied are collected under the "L" configuration. The performance of the proposed design configurations were compared against a six-fin reference case.

The target performance parameters were the melting time, percentage time saving, melting and energy enhancement ratios and the heat transfer rates. It was observed that the reference case took 115 minutes for complete melting of PCM. All "A" configuration designs took longer than 115 minutes to completely melt PCM, resulting in the negative time saving values. Moreover, the melting and energy enhancement ratio were less than 1.0 for the majority of the melting time duration.

Furthermore, the average energy storage rate was less than the reference case value of 126 $W$. The "S" configuration designs showed a mixed behavior: S1 design clearly performing better than the reference case resulting in the time saving of 18% and average energy storage rate of 151 $W$. S2 design, however, performed inferior to the reference case on all the defined performance metrics. All five designs of "L" configuration performed better than the reference case; the surface area, arrangement and number of fins being decisive factors.

The percentage time savings for L1, L2, L3, L4 and L5 designs came out to be 20%, 5%, 26%, 36% and 39%, respectively. The average energy storage rate of the corresponding designs were 158 $W$, 133 $W$, 169 $W$, 197 $W$ and 208 $W$, respectively. Design L5 proved to be the optimum design based on both the scales of melting time and energy storage, yielding maximum values of time saving and average energy storage rate, respectively.

# Chapter 5

# Investigation of Optimal Fin Arrangement using Mathematical Functions

## 5.1 Introduction

In previous chapter it was concluded that fin length had a very strong impact on the Phase Change Material (PCM) melting process in the Latent Heat Thermal Energy Storage (LHTES) unit. As described previously, that PCM melting process has different heat transfer phases, conduction and convection. Initially, conduction is strong when all PCM is in solid phase. After initial melting of PCM along the heated surfaces, natural convection becomes the major contributor to heat transfer in the fluid.

As melting process proceeds, the melting PCM rises to the top hot region and solid PCM settles to the bottom of the container. The convection is weak and PCM only melts due to conduction. As thermal conductivity of PCM is low, the last phase of melting is very slow. It was also found in the previous chapter, that if variable fin lengths with short fins at the top half of the heated walls and longer

fins at the bottom half of the heated walls were used, the overall improvement in the thermal performance of LHTES device was observed.

Moreover, it was also found in the literature [124, 128, 151] that the PCM melting rate can be positively increased by having a short top fin and a long bottom fin. This arrangement was found to enhance heat transfer to the solid PCM settled near the bottom wall of the thermal energy storage. It was observed in the literature that most of the fin design enhancements were performed rather randomly and without any systematic study. A need was identified to investigate a systematic model for the fin arrangement profile where top fins are short and bottom fins are long.

Therefore, based on the effectiveness of the fin design enhancements four different mathematical functions were proposed in this study. A systematic study is carried out to identify the optimum fin design function efficiently and effectively. In this chapter investigation is performed to discover an optimal profile for the fin length. The simplest engineering approach for such investigation is application of models that can be described mathematically. Therefor, simple basic mathematical functions are employed to generate fin length profiles and thermal performance is analyzed based on the LHTES designs using these fin length profiles.

The purpose of investigating the optimal fin arrangement using mathematical functions is to determine the most effective and efficient way of fin designs that can transfer heat from one medium to another. By varying parameters such as the fin spacing, thickness, and shape, engineers can use mathematical modeling to identify the optimal fin arrangement that minimizes heat transfer resistance and maximizes thermal performance.

The investigation of optimal fin arrangement using mathematical functions is therefore an important aspect of engineering design, as it can help to improve the energy efficiency and performance of a wide range of industrial and consumer products that rely on heat transfer. The optimal profile that produced best melting characteristic of the PCM in LHTES device is selected for subsequent study

of the effects of additional parameters (fin thickness and geometry aspect ratio) during the melting process.

## 5.2 Fin Length Variations

Four different types of variations of the function $y = f(x)$, as shown in Figure 5.1 are modeled to obtain different sub-models for studying the effects on thermal performance. the maximum length of the fins was constrained to be $max(f_l) <= W/2$. Moreover, the minimum and maximum fin to fin distances were $5mm$ and $20mm$, respectively.

### 5.2.1 Linear Function

The linear functions used to calculate fin lengths are shown in the following equation 5.1. Figure 5.1a illustrates the function representing the dimensions of the enclosure. The length of the fins is obtained by evaluating the $x$ value at fixed $y$ positions and applying the scaling to the enclosure geometry.

$$\begin{aligned} y &= y_0 - A(x - x_0) \\ x &= x_0 - \frac{y - y_0}{A} \end{aligned} \tag{5.1}$$

### 5.2.2 Quadratic Function

The quadratic functions are represented in the Equation (5.2) below, which is used to calculate the fin length and is shown in Figure 5.1b corresponding to the dimensions of the enclosure.

$$\begin{aligned} y &= y_0 + A(x - x_0)^2 \\ x &= x_0 - \sqrt{\frac{y - y_0}{A}} \end{aligned} \tag{5.2}$$

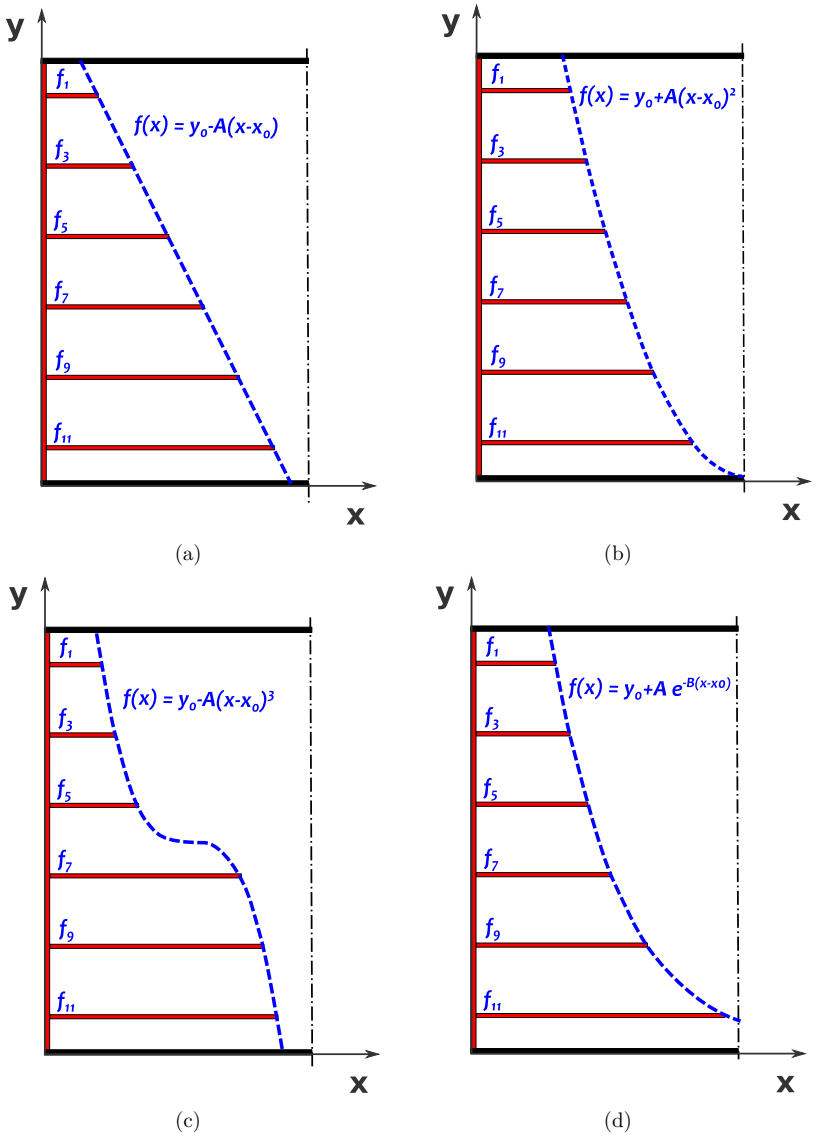


FIGURE 5.1: Function based fin length variation (a) linear (b) quadratic, (c) cubic (d) exponential.

### 5.2.3 Cubic Function

The Equation (5.3) and Figure 5.1c are used to compute the fin-lengths for the cubic function variation case.

$$\begin{aligned} y &= y_0 - A(x - x_0)^3 \\ x &= x_0 + \sqrt[3]{\frac{y - y_0}{A}} \end{aligned} \tag{5.3}$$

### 5.2.4 Exponential Function

The last variant uses an exponential function to model fin length as a function of vertical position within the enclosure. The functions for the expressions $x$ and $y$ are given in the Equation (5.4) and shown in Figure 5.1d.

$$\begin{aligned} y &= y_0 + Ae^{-B(x-x_0)} \\ x &= x_0 - \frac{1}{B}\ln(\frac{y-y_0}{A}) \end{aligned} \tag{5.4}$$

The fin lengths calculated using these functions are represented graphically in Figure 5.2. The graphical representation provides an opportunity to compare distribution of fin lengths in different cases. The parameters $[x_0, y_0, A, B]$, used in these functions are listed in Table 5.1.

In all of the above cases, the same vertical $(y)$ positions are used and the corresponding $x$ values are calculated and the scaled fin length is evaluated. The surface area per unit depth of fins exposed to PCM is $480mm^2$ and fin thickness is $1.25mm$. PCM volume per unit depth of the container is $17400mm^2$.

TABLE 5.1: Function parameters.

| **Parameter** | **Linear** | **Quadratic** | **Cubic** | **Exponential** |
|---|---|---|---|---|
| $x_0$ | 4 | 4 | 4 | 4 |
| $y_0$ | 6 | 6 | 6 | 0 |
| $A$ | 2 | 0.32 | 0.8 | 4.67 |
| $B$ | NA | NA | NA | 0.5 |

TABLE 5.2: Fin lengths $(mm)$ for different function based configurations.

| **Fin location** $(y)$ | **Linear** | **Quadratic** | **Cubic** | **Exponential** |
|---|---|---|---|---|
| 10.00 | 65.00 | 59.93 | 65.00 | 70.83 |
| 30.00 | 55.00 | 48.89 | 61.09 | 48.86 |
| 50.00 | 45.00 | 41.29 | 54.62 | 38.64 |
| 70.00 | 35.00 | 35.11 | 25.38 | 31.91 |
| 90.00 | 25.00 | 29.78 | 18.91 | 26.89 |
| 110.00 | 15.00 | 25.00 | 15.00 | 22.87 |

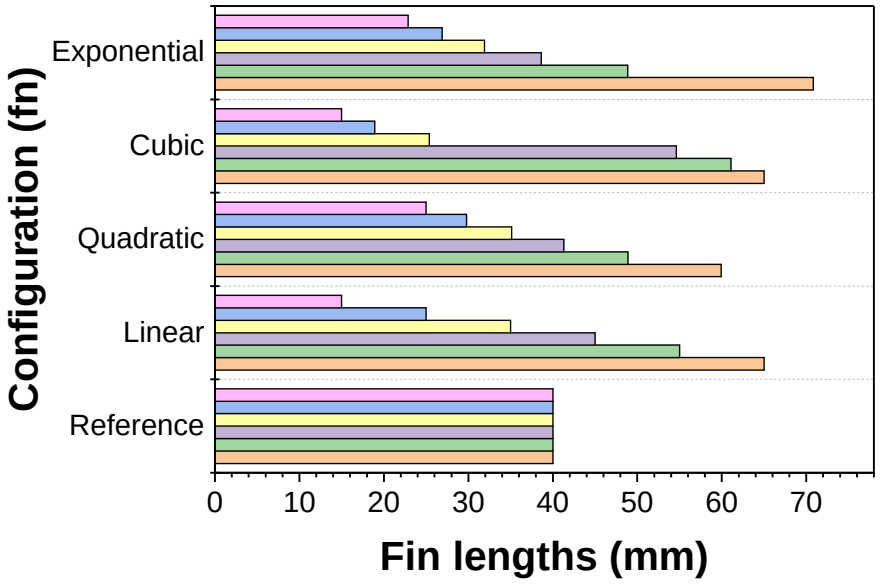


FIGURE 5.2: Graphical representation of function based fin lengths.

## 5.3 Analysis of Melting Process

As shown in the modeling section, fin lengths are varied from top to bottom. The length of the fins increases as fin position of the fin changes from top to bottom. In the initial phase of melting process, heat conduction is dominant. As PCM melts the liquid rises to the top and the convection currents caused by buoyancy help transfer heat in the melting process. Solid PCM at the bottom is melted by the thermal conduction of the fins at the bottom during the last stages of the melting process. In all cases, the fins at the bottom are longer and conduct more heat to PCM, helping to accelerate the melting process at this stage. The overall intelligent configuration of the fins help the convection currents transfer heat more efficiently compared to the base and reference cases having fins of uniform length.

### 5.3.1 Liquid Fraction and Temperature Contours

Figure 5.3 shows the evolution of the liquid fraction, temperature, and energy storage for the PCM melting process in the double-walled heated, rectangular enclosure with different fin arrangements based on different functions, as explained

previously in the modeling section. The graph shows that at the beginning of the melting process, the reference case is faster. Linear, quadratic, and exponential function based fin configurations show almost identical behavior for these parameters. Although the melting rate is slower at the beginning than the reference case, it gradually improves and exceeds the melting rate of the reference case after 70 minutes and remains higher until the end of the melting process.

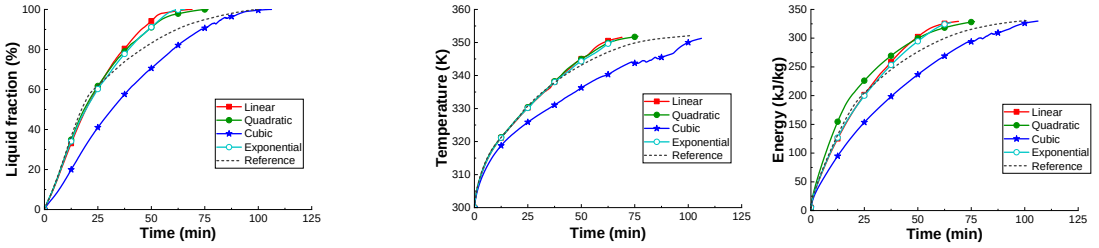


(a) (b) (c)

FIGURE 5.3: Transient behavior of (a) liquid fraction, (b) temperature, (c) and thermal energy for function based fin configurations.

The identical behavior of the melting process for linear, quadratic, and exponential fin arrangements can also be seen in the contours of the liquid fraction shown in Figure 5.4. These contours show that as the melting starts, the PCM is melted by heat conduction from the fins. The liquid fraction of PCM increased with melting progress and convection heat transfer began to dominate by the vortexes formed along the fins, enhancing heat transfer into PCM. The melted PCM close to the walls formed liquid walls on both sides, as seen in the snapshots at $t = 20min$. Except for the cubic fin configuration, the liquid at the top of both walls melted and merged at $t = 40min$. After 60 minutes into the melting process cubic fin configuration still had solid PCM, while most of the PCM had melted for the other configurations. The temperature contours for these cases at same time steps are shown in Figure 5.5.

### 5.3.2 Flow Characteristics and Interface Velocity

The melting process was further analyzed by investigation of the flow characteristics of the PCM during phase change. In addition to the liquid fraction and

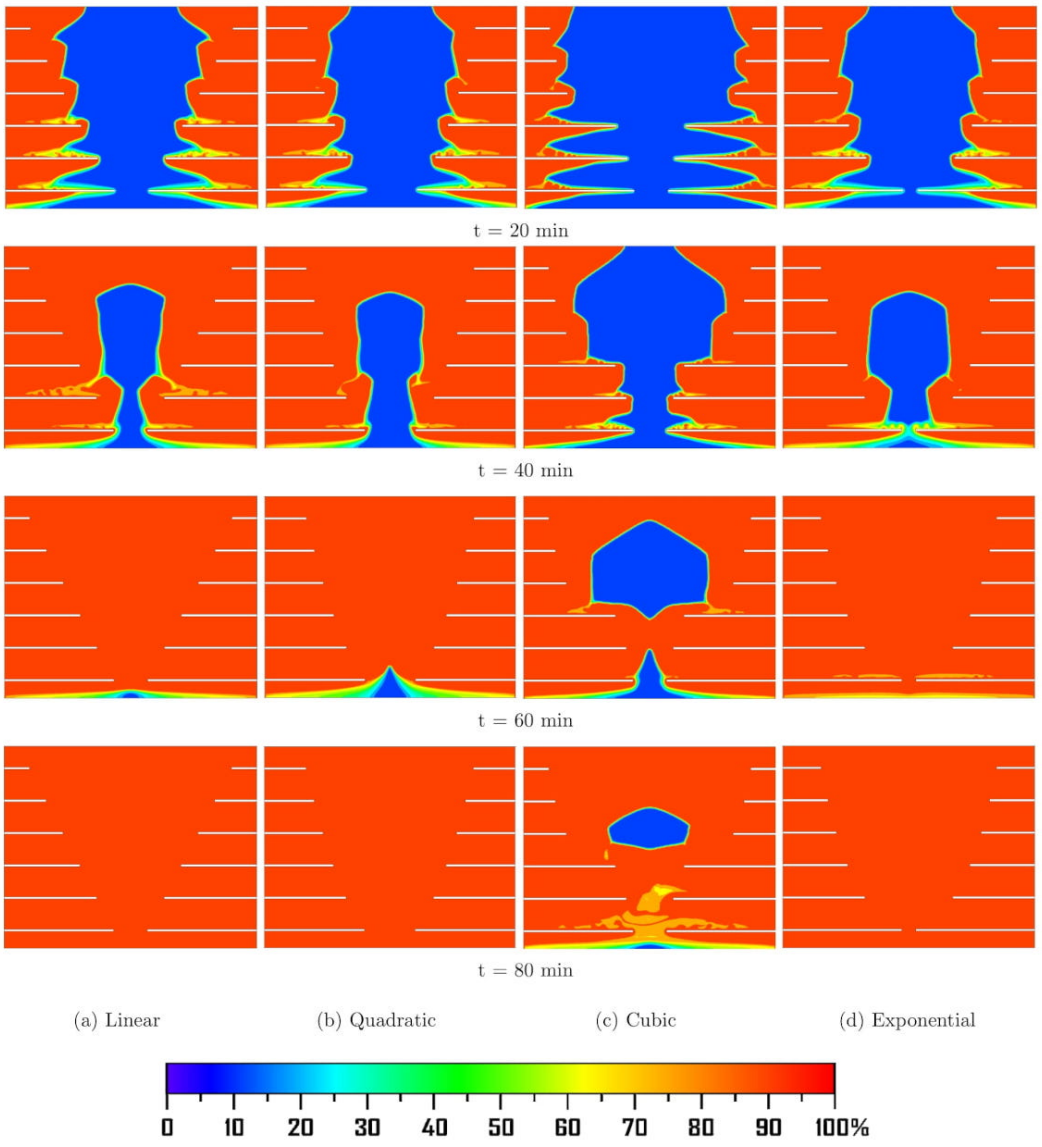


FIGURE 5.4: Liquid fraction contour plots for (a) linear, (b) quadratic, (c) cubic, and (d) exponential cases.

temperature contours, the average velocity of the vortices developed during natural convection phase was also studied. As melting progressed, the melted PCM rose to the top due to convection. The solid PCM adjacent to heat source received heat and developed more vortices that rose and combined with the previously developed vortices strengthening natural convection and heat transfer rate. State of velocities in different fin configurations at different time steps are shown in Figure 5.6. The average velocity of liquid PCM gradually increase and reach a

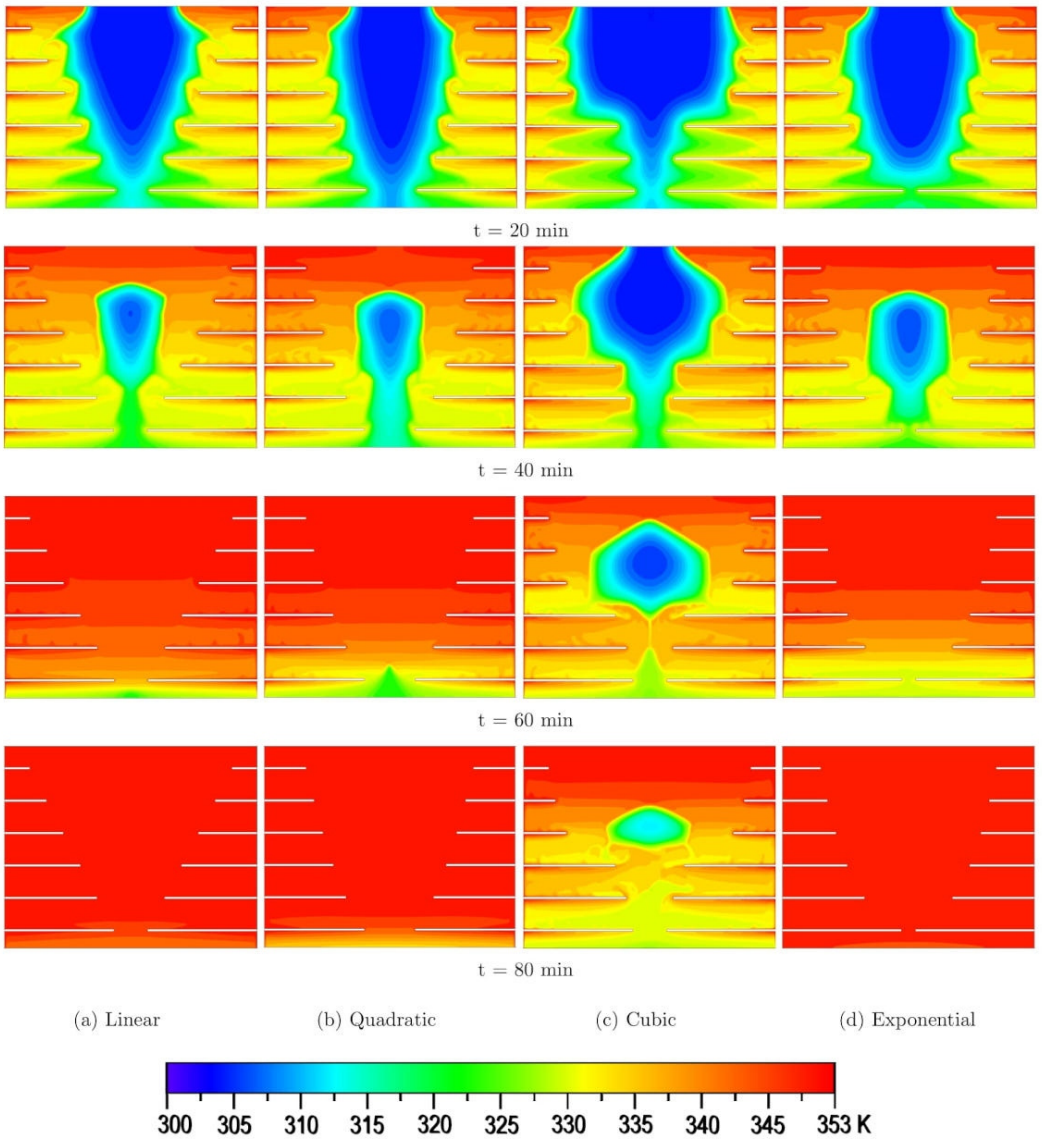


FIGURE 5.5: Temperature contour plots of all configuration at four different time instances.

maximum as natural convection got strong. During the later stages of melting, as liquid fraction increased, the weakened convection was manifested by decrease in the average PCM velocity. In the linear configuration, maximum velocity was reached at around $t = 30min$ and by $t = 45min$, melted liquid from both sides combined and developed a cloud layer at the top of the enclosure.

The comparison of various configurations revealed that in the case of cubic configuration, vortices are smaller than the other cases at any specific time step. At time $t = 20min$, that vortices from fin sections grow larger than fin lengths in

most of the configuration but they are smaller for cubic fin arrangement. As the heat is trapped in the heat pockets in case of cubic configurations, it resulted in slow heat transfer to the solid PCM and affected the progression of solid liquid interface. At time $t = 40min$, except for cubic fin arrangement, all other cases show that vortices have grown large enough to merge with the other side of the enclosure forming a cloud of liquid at the top region of the chamber.

Cubic configuration is slow and this phase is reached around $t = 60min$ in this case. By that time melting is almost complete in the other configurations. The similar behavior was seen in case of quadratic and exponential configuration with appropriate difference in amount of liquid PCM and maximum velocity reached at the time step shown in the figure.

The Figure 5.6 shows that in case of linear, quadratic, and exponential fin arrangements, the vortices are developed early in the melting process and quickly rise towards the top region. This increased convective heat transfer in case of these configurations. In case of the cubic fin arrangement, the transition of phase from conduction heat transfer to convection heat transfer was slow and vortices were seen after $t = 60min$. The complete melting was reached around 1 hour in the other cases, whereas in the case of cubic configuration, the melting took more that 80 min to complete.

Moreover, it can be seen that the melting interface progression is faster than cubic case in all other cases. Even though the PCM melting is slow in cubic fin configuration, at time $t = 80min$ the maximum velocity of the vortices is around $9mm/s$ that was higher than other cases. The maximum vortex velocity reached was $8.5mm/s$, $6.3mm/s$, and $6.4mm/s$, in linear, quadratic, and exponential configurations.

Compared to cubic configuration case, the melting progression is uniform as can be seen in the Figure 5.6. This is a direct result of enhanced natural convection effects, and thus faster melting of PCM is observed in these cases. The average interface velocity values for various time steps have been recorded and listed in Table 5.3.

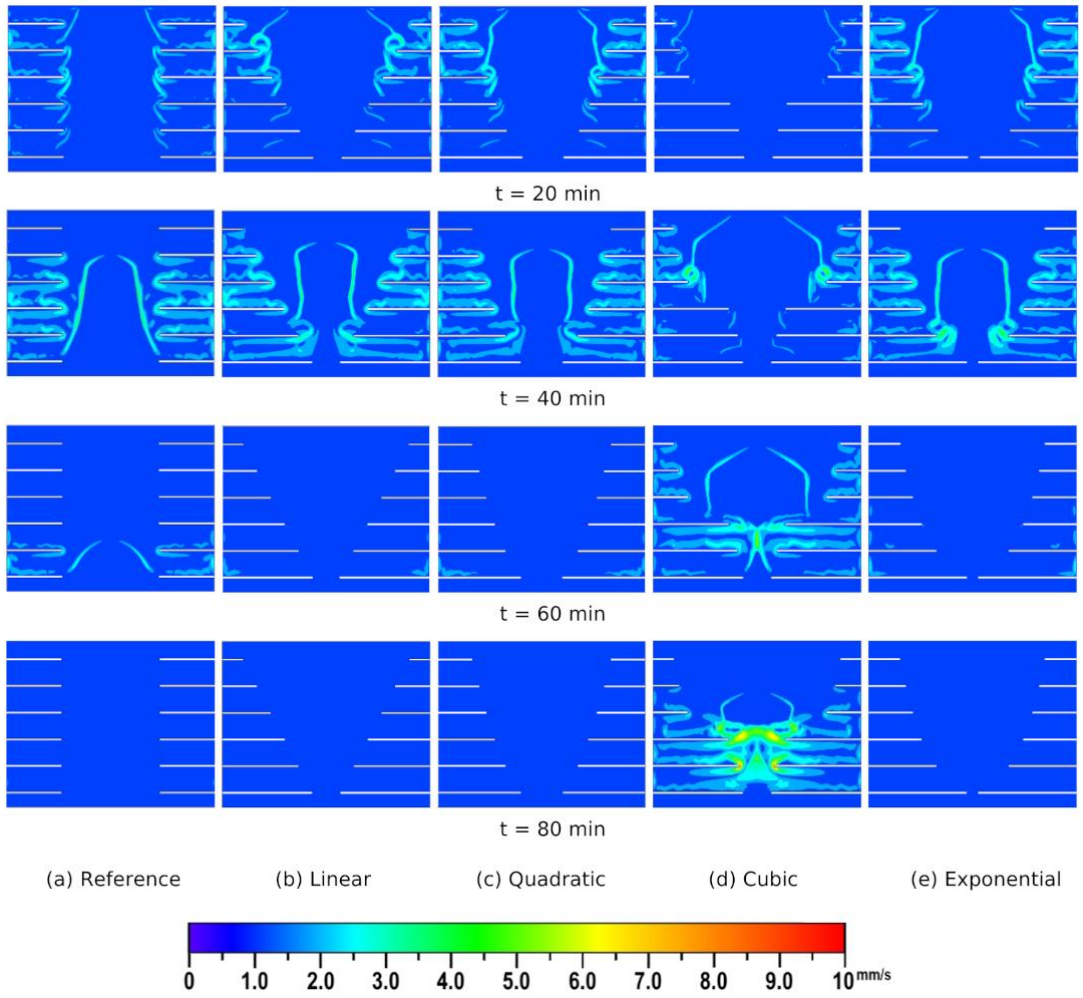


FIGURE 5.6: Velocity contour plots for (a) linear, (b) quadratic, (c) cubic, and (d) exponential cases.

## 5.4 Performance Analysis

In this section, we will discuss different performance indicators that are commonly used for analyzing the performance of various LHTES designs with different fin configurations. These indicators provide valuable insights into the efficiency and effectiveness of the LHTES systems. The four key performance indicators we will focus on are:

1. Melting Enhancement Ratio: This indicator compares the melting time of an LHTES system with fins to that of a reference system without fins. The

TABLE 5.3: Streamline average velocities of different configurations.

| **Time** $(min)$ | **Average streamline velocity** $(mm/s)$ | | | | |
|---|---|---|---|---|---|
| | **Reference** | **Linear** | **Quadratic** | **Cubic** | **Exponential** |
| 10 | 0.1122 | 0.1207 | 0.1140 | 0.0582 | 0.1249 |
| 20 | 0.3687 | 0.3573 | 0.3876 | 0.1413 | 0.3819 |
| 30 | 0.7396 | 0.6961 | 0.7270 | 0.2688 | 0.6462 |
| 40 | 0.5777 | 0.6643 | 0.5961 | 0.3983 | 0.5913 |
| 50 | 0.3953 | 0.5373 | 0.4505 | 0.4996 | 0.4642 |
| 60 | 0.2377 | 0.2359 | 0.2239 | 0.6021 | 0.2187 |
| 70 | 0.1485 | 0.1616 | 0.1454 | 0.7285 | 0.1615 |
| 80 | 0.1010 | - | - | 0.8657 | 0.1154 |
| 90 | 0.0827 | - | - | 0.4467 | 0.0896 |

melting enhancement ratio quantifies the improvement achieved in the melting process due to the presence of fins. It is calculated as the ratio of the melting time of the reference system to the melting time of the finned system. A higher melting enhancement ratio indicates a more efficient melting process with the presence of fins.

2. Energy Enhancement Ratio: Similar to the melting enhancement ratio, the energy enhancement ratio compares the energy discharge or storage capacity of an LHTES system with fins to that of a reference system without fins. It is calculated as the ratio of the energy storage capacity or energy discharge rate of the reference system to that of the finned system. A higher energy enhancement ratio indicates an improved energy storage or discharge performance with the use of fins.

3. Percentage Time Saving: This indicator quantifies the time savings achieved by utilizing fin configurations in LHTES systems. It is calculated as the percentage reduction in the melting or solidification time of the finned system compared to the reference system without fins. A higher percentage time saving indicates a more significant reduction in the required time for melting or solidification, resulting in enhanced system performance.

4. Energy Transfer Rates: Energy transfer rates provide information about the rate at which energy is transferred during the melting or solidification process. These rates can be expressed as the amount of energy transferred per unit time or as the power input or output of the LHTES system. Energy transfer rates are crucial in evaluating the dynamic performance and power requirements of LHTES systems with different fin configurations.

These performance indicators collectively offer a comprehensive analysis of the effectiveness and efficiency of LHTES systems with various fin configurations. By comparing these indicators for different designs, researchers and engineers can make informed decisions regarding the selection and optimization of fin configurations to maximize the performance of LHTES systems in terms of melting efficiency, energy storage capacity, time savings, and energy transfer rates.

### 5.4.1 Melting Time and Time Saving

As mentioned previously, melting time is one the important performance indicators considered in the analysis of LHTES design. A related parameter melting time saving, defined by (4.1), measures the relative improvement or degradation of the performance compared to the reference or base cases. The positive values indicate better thermal performance. Table 5.4 lists values for melting times and time savings for all cases of LHTES design configurations. In the base case with no fins, PCM completely melted in $115min$, where as the reference case defined in the current study melted in $100.83min$.

Linear, quadratic, and exponential function based configurations improved the melting performance and complete melting was obtained in less time than the reference. The melting performance of the cubic function based configuration was very poor compared to the reference case and resulted in negative time saving. The best performing case in this study was the one where fin lengths had exponential based distribution. It took $65.33min$ to completely melt the PCM and 35% time saving was obtained in this case compared with the reference case.

The exponential fin configuration in this study improved the melting performance by 6% compared to the best case performance of intelligent fin arrangement as described in previous chapter. The corresponding improvement in melting with respect to the base case was 43%.

TABLE 5.4: Melting times and improvement ratios for various fin designs.

| **Configuration** | **Melting time** (min) | **Improvement ratio** |
|---|---|---|
| Reference | 100.83 | - |
| Linear | 68.83 | 31.7% |
| Quadratic | 67 | 33.6% |
| Cubic | 106 | -5.1% |
| Exponential | 65.33 | 35.2% |

### 5.4.2 Performance Enhancement Ratios

Other performance analysis indicators considered in this study are melting enhancement ratio and energy enhancement ratio. These are defined by Equation 4.2 and (4.3), respectively. These parameters indicate how fast or slow melting rate and energy storage rate are obtained for a particular design case $k$ compared to reference and base cases. The transient variation of the performance of the proposed designs compared with the reference case are examined by defining these enhancement ratios. Figure 5.7a shows the performance enhancement ratio of melting rate, whereas, Figure 5.7b manifests energy enhancement ratio, for different LHTES design configurations.

All designs configuration have $E_{mr}(t) > 1.0$ in the beginning of the melting process except the configuration with cubic fin arrangement. As melting progressed, the ratio decreased for all cases and even dropped below the reference case by $t = 5min$ for all cases. After about 10 minutes of melting process, the melting rate started to rise as natural convection increased. At about time $t = 30min$ the rate of melting for linear, quadratic, and exponential configurations surpassed the references case.

The peak melting rate for linear and exponential cases was obtained at time $t = 55min$. The exponential configuration reached the peak at about $60min$

of the process. The cubic configuration never reached higher melting rate than the reference case throughout the melting process. The highest melting enhancement ratios compared to the reference case were 1.142, 1.138, and 1.117 for linear, quadratic, and exponential cases respectively.

Heat transfer surface area and placement of fins are important characteristics of the LHTES design. The energy enhancement ratio trends indicate the impact of the design parameters on the thermal behavior of the energy storage unit. It can be seen from the plots that all configurations initially have $E_{er}(t) < 1.0$. Except for cubic configuration energy storage performance improvement was observed for linear, quadratic, and exponential configurations.

The energy storage enhancement higher than the reference case was observed at about $t = 30min$ for linear, quadratic, and exponential configurations. The maximum enhancement ratio compared to the reference case was 1.1 obtained for the linear configuration case and it was reached at about $t = 55min$.

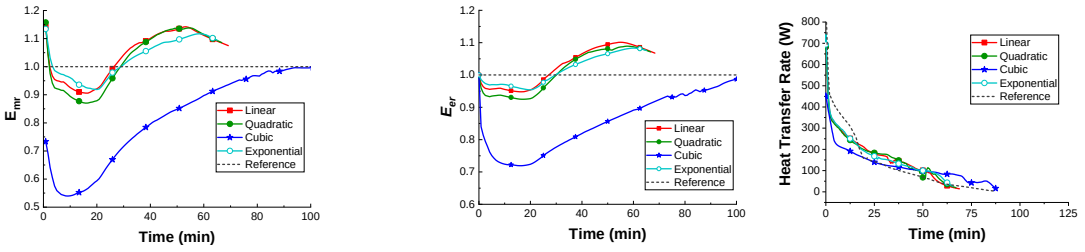


(a) (b) (c)

FIGURE 5.7: Enhancement ratios and heat transfer rate (a) melting enhancement ratio $E_{mr}$, (b) energy enhancement ratio $E_{er}$, and (c) power $\dot{Q}$.

### 5.4.3 Heat Transfer Rate

The heat transfer rate in the LHTES has an important impact on the melting and energy storage rates. Higher values of the heat transfer rate indicate that charging will be faster for LHTES. It is, therefore, a critical parameter considered in the design of LHTES. Heat transfer rate is evaluated by the expression defined by Equation (4.4).

The instantaneous heat transfer rate is represented by $\dot{Q}(t)$ and is shown in Figure 5.7c for all studied cases. It can be seen from the plot that high heat transfer rate is observed in the beginning of the melting process.

The temperature difference between the PCM and heated wall was high at that time and resulted this higher rate. The liquid PCM layer increased around the hot fins and walls as melting progressed. The higher temperature of PCM resulted in lower gradient between the hot wall and PCM causing lower heat transfer rates. These trends can be easily seen in the plot of the Figure 5.7c. Heat transfer rate calculated by the expression in (4.5) was used for quantitative comparison with the reference and other design cases.

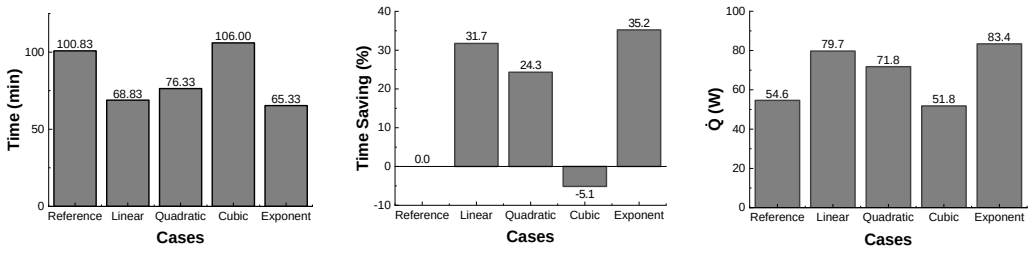


(a) (b) (c)

FIGURE 5.8: Performance indicator (a) melting time, (b) melting time saving, and (c) average energy storage rate.

The average energy storage rate of the reference case was $54.6W$. The base case from the previous study had an average energy storage rate of $47.86W$. The rates for all design cases are shown in Figure 5.8. It is seen that $\dot{Q}$ was better than that of the reference case for all cases except the case with cubic function based fin-length configuration.

The best performing case was the design with exponential function based fin design. The value of $\dot{Q}$ for exponential design case was $83.4W$, while quadratic function based design was the next in the list resulting in heat transfer rate of $81.6W$. The heat transfer rate for linear and cubic cases was $79.7W$ and $51.9W$ respectively. Based on the analysis of all the performance indicators discussed, it can be concluded that the exponential function based design was the best performing amongst all designs.

## 5.5 Effect of Wall Temperature

The best performing model is chosen to study the effect of changing wall temperature on the LHTES performance and develop correlations. The case studied are with wall temperatures of $343K$, $348K$, $353K$, $358K$, $363K$, and $368K$. Table 5.5 lists the values of melting time and total energy storage rate after the completion of melting process.

The melting time deceases with the increase in wall temperature as it resulted in higher heat transfer rate. The total stored energy in the LHTES comprises of sensible heat energy and latent heat energy. When the wall temperature is raised, heat transfer rate increased, resulting in higher energy storage. The latent heat energy remains same but sensible heat energy increases with the increase in wall temperature. This is reflected in the values listed in Table 5.5.

TABLE 5.5: Melting times and improvement ratios for different wall temperatures.

| **Wall temperature** (K) | **Melting time** (min) | **Storage rate** (W) |
|---|---|---|
| 343 | 82.71 | 61.92 |
| 348 | 56.25 | 94.28 |
| 353 | 43.75 | 125.23 |
| 358 | 36.25 | 155.60 |
| 363 | 31.04 | 186.62 |
| 368 | 26.88 | 220.77 |

### 5.5.1 Development of Correlations

It is important to represent the melting time and heat transfer rate of LHTES device as the functions of non-dimensional numbers to quantify the variations of design parameters and boundary conditions.

Representing the melting time and heat transfer rate of an LHTES device as functions of non-dimensional numbers is indeed crucial for quantifying the variations of design parameters and boundary conditions. Non-dimensional numbers allow

for the development of useful correlations that can provide a quick and reasonably accurate estimation of the thermal performance of similar LHTES units.

By using non-dimensional numbers, the dependence on specific system dimensions and operating conditions can be eliminated, allowing for a more general and transferable analysis. These non-dimensional numbers are typically derived based on the governing equations and physical properties relevant to the system.

For example, in the context of melting time, one commonly used non-dimensional number is the Stefan number ($Ste$), which represents the ratio of latent heat transfer to conductive heat transfer. It relates the rate of heat transfer during the phase change process to the temperature gradient across the material. By plotting the melting time as a function of the Stefan number, the effects of different design parameters and boundary conditions can be captured in a dimensionless manner.

Similarly, for heat transfer rate analysis, non-dimensional numbers such as the Nusselt number ($Nu$) and the Rayleigh number ($Ra$) are often utilized. The Nusselt number represents the convective heat transfer coefficient normalized by the conductive heat transfer coefficient, providing a measure of the efficiency of convective heat transfer. The Rayleigh number, on the other hand, characterizes the relative importance of buoyancy-driven convection to conductive heat transfer in a fluid.

By plotting the heat transfer rate as a function of these non-dimensional numbers, correlations can be established to estimate the heat transfer performance for various design configurations and operating conditions. These correlations allow for a quick estimation of the thermal behavior of LHTES devices without the need for extensive computational or experimental efforts.

In summary, the use of non-dimensional numbers to represent melting time and heat transfer rate in LHTES devices is essential for quantifying variations in design parameters and boundary conditions. These non-dimensional representations

enable the development of correlations that facilitate efficient and accurate estimation of thermal performance across different latent thermal energy storage units.

TABLE 5.6: $\overline{Nu}$, $Ra$, $Ste$ and $Fo$ numbers at different wall temperatures.

| $\mathbf{T_w}(K)$ | $\overline{\mathbf{Nu}}$ | **Ra** | **Ste** | **Fo** |
|---|---|---|---|---|
| 343 | 87.1 | $2.738 \times 10^9$ | 0.0753 | 0.00417 |
| 348 | 118.83 | $5.058 \times 10^9$ | 0.1391 | 0.00283 |
| 353 | 142.90 | $7.378 \times 10^9$ | 0.2029 | 0.00220 |
| 358 | 162.25 | $9.698 \times 10^9$ | 0.2667 | 0.00183 |
| 363 | 179.15 | $1.202 \times 10^{10}$ | 0.3305 | 0.00156 |
| 368 | 196.35 | $1.434 \times 10^{10}$ | 0.3943 | 0.00135 |

All the relevant non-dimensional number are defined in section 3.5.4. Fourier number $Fo$ is used to represent the non-dimensional melting time of the PCM. These non-dimensional quantities are defined in eqs. (3.24) and (3.27) to (3.29). Table 5.6 lists all results calculated for non-dimensional numbers at different wall temperatures.

Figure 5.9a shows as plot of Fourier number (dimensionless melting time) ($Fo$) vs Stefan number ($Ste$). This plot is used to study the effect of wall temperature on the melting performance. The trend indicates that a decrease in the melting time is observed with the increase in Stefan number.

The gradient of non-linear trend gradually slows down as $Ste$ increases. The Equation (5.5) approximately correlates the trend of $Fo$ versus $Ste$.

$$Fo = a_1 Ste^{-b_1} \qquad (7.530 \times 10^{-2} \leq Ste \leq 3.943 \times 10^{-1}) \tag{5.5}$$

Where $a_1$ and $b_1$ are constants which are equal to $7.56715 \times 10^{-4}$, and 0.6619, respectively.

To approximate the behavior of the average Nusselt number versus the Rayleigh number, a correlation is developed. This correlation provides a useful tool for estimating the convective heat transfer characteristics in natural convection scenarios. Figure 5.9b depicts the effect of the wall temperature on natural convection,

demonstrating that an increase in the Rayleigh number corresponds to an increase in the average Nusselt number.

However, it is important to note that this relationship is non-linear, with the average Nusselt number gradually declining as the Rayleigh number continues to increase. This non-linear trend highlights the complex nature of natural convection heat transfer phenomena and emphasizes the need for accurate correlations to predict and analyze convective heat transfer in various practical applications.

$$\overline{Nu} = a_2 Ra^{b_2} \qquad (2.738 \times 10^9 \leq Ra \leq 1.434 \times 10^{10}) \tag{5.6}$$

Where $a_2$ and $b_2$ are constants whose values are equal to 0.00233, and 0.48485, respectively. The coefficient of determination, $R^2$ for both of these correlations is 99%. Tables 5.7 and 5.8 lists corresponding values for $F_o$ and $\overline{Nu}$ evaluated by the correlations.

TABLE 5.7: Maximum error in $Fo$ vs $Ste$ correlation.

| **Ste** | $\mathbf{F_o}(Simulation)$ | $\mathbf{F_o}(correlation)$ | **Error**(%) |
|---|---|---|---|
| 0.0753 | 0.00417 | 0.00419 | 0.53 |
| 0.1391 | 0.00283 | 0.00279 | 1.33 |
| 0.2029 | 0.00220 | 0.00218 | 1.14 |
| 0.2667 | 0.00183 | 0.00181 | 0.82 |
| 0.3305 | 0.00156 | 0.00157 | 0.94 |
| 0.3943 | 0.00135 | 0.00140 | 3.78 |

The maximum error for correlations in eqs. (5.5) and (5.6) is 3.78% and 0.73%. These correlations could be used for LHTES performance estimation with reasonable accuracy for a wide range of wall temperature applications.

TABLE 5.8: Maximum error in $\overline{Nu}$ vs $Ra$ correlation.

| **Ra** | $\overline{\mathbf{Nu}}(Simulation)$ | $\overline{\mathbf{Nu}}(correlation)$ | **Error**(%) |
|---|---|---|---|
| $2.738 \times 10^9$ | 87.1 | 87.71 | 0.71 |
| $5.058 \times 10^9$ | 118.83 | 118.12 | 0.59 |
| $7.378 \times 10^9$ | 142.90 | 141.85 | 0.73 |
| $9.698 \times 10^9$ | 162.25 | 161.96 | 0.18 |
| $1.202 \times 10^{10}$ | 179.15 | 179.72 | 0.32 |
| $1.434 \times 10^{10}$ | 196.35 | 195.77 | 0.29 |

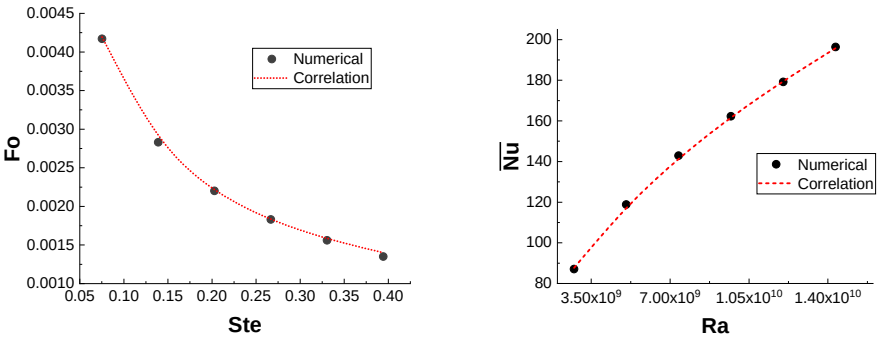


(a) (b)

FIGURE 5.9: Proposed correlations (a) $Fo$ vs $Ste$, (b) $\overline{Nu}$ vs $Ra$.

## 5.6 Conclusion

In this numerical study, design of a rectangular thermal energy storage device was investigated for thermal performance improvements. A 2D model was developed for the geometry of LHTES with isothermal side walls. A constant temperature of $353K$ is initially set to heat the PCM in the enclosure.

Stearic acid was used as PCM and fins were connected to the isothermal walls forming extended surfaces to accelerate the heat transfer from walls to the PCM for improved heat transfer. Fin lengths were calculated using different functions $x = g(y)$ mapped to the enclosure frontal plane. $Y$ coordinate represented vertical location on the heated wall and $x$ was evaluated to return fin lengths at each of the isothermal wall. The performance results obtained from the configuration of the new designs were compared with the base case of the previous study and a reference case of the current study. The reference for current study had six fins of uniform length that were attached to each isothermal wall. The target parameters for performance comparison were same as were used in the previous study described in the last chapter. The melting time of PCM of the base case from the previous study was $115min$, while the reference case in this study took $100.8min$ for complete melting of PCM. The key points drawn from this study are described below.

i Total melting times were 68.83$min$, 76.33$min$, 106$min$, and 65.33$min$ for linear, quadratic, cubic, and exponential cases respectively. It was observed that during the melting process, enhancement ratios less than 1.0 were observed for melting and energy for most of the duration of the process. Moreover, for the case where fin lengths were calculated using cubic functions, the energy storage rate was 51.8$W$, that was slower than 54.6$W$, the result obtained for the reference case. All other cases resulted in improved energy storage rate. The percentage time savings for linear, quadratic, and exponential function based designs came out to be 31.7%, 24.3%, and 35.2%, respectively. The corresponding average energy storage rate for LHTES designs resulted in 79.7$W$, 71.8$W$, and 83.4$W$, respectively.

ii The best performing design was further studied by changing the isothermal wall temperature from 343$K$ to 368$K$ with 5$K$ interval. An increase in the wall temperature decreased the PCM melting time and enhanced average energy storage rate. Empirical correlations are proposed to predict non-dimensional Fourier number and the average Nusselt number over the range of isothermal wall temperatures.

# Chapter 6

# Optimization of LHTES Design Parameters and Machine Learning Regression Modeling

## 6.1 Introduction

It has been established in the previous chapters that various fin parameters like thickness, length, orientation, and distribution along the heated walls impact thermal performance of Latent Heat Thermal Energy Storage (LHTES) devices. In this chapter impact of aspect ratio of the rectangular enclosure of LHTES is investigated. In preceding chapters fin thickness was not independently studied. The fin length and fin thickness are interdependent due to the constraint of constant Phase Change Material (PCM) volume throughout this study.

In Chapter 4, different fin designs based on lengths and shapes were studied. Later in Chapter 5, fin length distribution functions were investigated and the optimum exponential function was identified. In Chapter 6 the spread factor of the exponential fin length distribution function was further explored which was controlled through fin thickness. Therefore, fin thickness was one of the three independent

factors used in the design optimization of LHTES. The emphasis of the investigation in the previous chapters was orientation, shape, and arrangements of fins in the LHTES system. These parameters were thoroughly studied in previous chapters, highlighting the importance of these parameters in improving the thermal performance of the system. By varying the orientation, shape, and arrangement of the fins, it is possible to identify the optimal design parameters that minimize heat transfer resistance and maximize thermal performance.

It was also found that exponential function was the optimal fin design function. However, the spread factor of fin lengths that is controlled by the fin thickness was yet to be investigated. In this chapter, effect of fin thickness on the thermal performance of LHTES is studied. Fin thickness plays a critical role in determining the heat transfer characteristics of a fin. In particular, the thickness of fins affects the rate at which heat is conducted through the material, and can also impact the rate of convective heat transfer between the fin and PCM.

By studying the effects of fin thickness, engineers can gain insights into how this parameter impacts heat transfer performance, and can use this information to optimize the design of heat transfer devices. Furthermore, statistical technique, Taguchi method is used to investigate the optimization of design parameters.

The Taguchi method is a powerful and effective optimization approach that has been extensively used for finding the optimal values of parameters for a single objective function. One of the key advantages of the Taguchi method over the other optimization methods is its ability to produce robust designs while requiring fewer simulation runs to achieve the same level of optimization. This makes it a cost-effective, simple, and flexible tool to find optimal designs.

The method has recently been applied to CFD applications [142, 152–156] and found to be an effective tool in parametric optimization of thermal energy storage systems.

The Taguchi method involves the use of experimental design and statistical analysis to identify the most important factors affecting the performance of a product

or process and to determine the optimal levels for each factor. It uses a structured approach to testing and optimization, which can help ensure that results are reliable and consistent.

Machine learning methods are employed to develop a regression model for the prediction of melting performance of LHTES device. The use of machine learning methods for regression analysis can help to improve the accuracy and reliability of predictions for the melting performance of LHTES devices, which is important for optimizing their design and performance. One of the benefits of using machine learning methods for regression analysis is that they can be used to capture non-linear relationships between the input and output variables, which may be difficult or impossible to model using traditional regression techniques. This can be particularly useful in complex systems where the relationships between variables are not well understood.

## 6.2 Optimization of Design Parameters

In chapter 4 fin shape, angle, and lengths were studied while keeping the geometry of the rectangular container constant. During all these simulations, the LHTES design parameters were modeled such that the volume of the PCM remained fixed. The results showed that the orientation of the fins could positively or negatively impact the melting rate. It was also found that larger heat transfer area provided better heat transfer rate. The best performing model was the one in which fin-lengths of the top and bottom halves were different. The fins in the top half were shorter than the one in the lower half of the rectangular chamber. This intelligent arrangement of fins improved the thermal performance of LHTES system.

In chapter 5 fin length variation, fin thickness, and container geometry aspect ratio were investigated and their impact on the thermal performance of LHTES was studied. The fins lengths on the heated walls were designed based on linear, quadratic, cubic, and exponential distribution functions. The results concluded

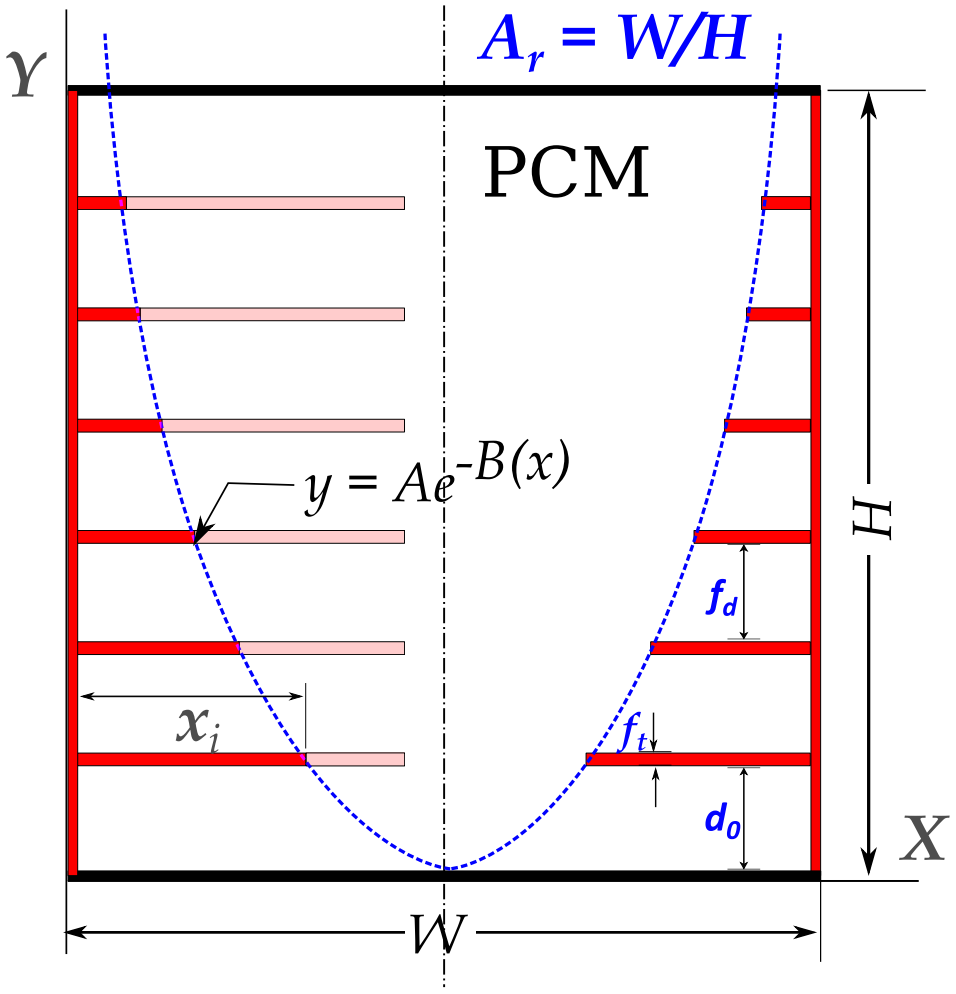


FIGURE 6.1: Graphical representation of design parameters.

that the model of LHTES with exponential function based distribution of fin lengths produced the best results.

In this chapter a comprehensive optimization study of simplified design parameters with two objective functions and 3 factors have been performed. The two objectives were minimization of melting time and maximization of energy storage in the LHTES.

The displacement among fins attached to the heated walls, fin thickness, and geometry aspect ratio were the used factors for optimizations as shown in Figure 6.1. In the figure, $d_0$ is displacement of the bottom most fin from the horizontal insulated wall at the bottom. This displacement is derived from the ratio $r_0 = d_0/H = 0.1$. During the analysis, exponential function based fin length distribution storage units design were modeled as was established during the initial

investigation stages. Table 6.1 lists all the design parameters finalized based on the studies described earlier.

TABLE 6.1: LHTES device design parameters.

| **Parameter** | **Symbol** | **Range** |
|---|---|---|
| Fin distance | $f_d$ | 5mm to 20mm |
| Fin thickness | $f_t$ | $1.2mm$ to $2.0mm$ |
| Geometry aspect ratio | $A_r$ | 0.5 to 1.5 |

To ensure the availability of optimization results when studying the effect of aspect ratio, distance among fins, and fin thickness on thermal performances, it is important to consider the interdependence of these parameters. In other words, the optimization process should take into account the interactions between these parameters and the resulting effects on thermal performance.

One way to achieve this is to use a design of experiments (DOE) approach, such as the Taguchi method, to identify the optimal parameter values for each of the parameters while minimizing the impact of their interactions. In the Taguchi method, a set of orthogonal arrays is used to evaluate the effects of each parameter and their interactions on the thermal performance of the fin design. Another approach is to use a response surface methodology (RSM) to model the complex relationships between the parameters and the thermal performance. RSM uses statistical techniques to construct a mathematical model that predicts the response variable (thermal performance) as a function of the input parameters (aspect ratio, distance among fins, and fin thickness).

In both cases, it is important to carefully select the range of values for each parameter and the number of experiments or simulations to be performed. This can help to ensure that the optimization results are reliable and accurate, even in the presence of interdependent parameters.

Overall, to ensure the availability of optimization results when studying the effect of aspect ratio, distance among fins, and fin thickness on thermal performances, it is important to use appropriate methods and techniques that account for the

interdependence of these parameters and their impact on the overall thermal performance of the fin design.

## 6.3 Optimal Parmeter Selection Using Taguchi Method

The Taguchi method is a powerful optimization technique that has been widely utilized for determining the optimal values of parameters for a single objective function [157–159]. It offers the advantage of requiring fewer experiments to identify the optimal settings for factors that influence the output responses. An additional analysis technique, called analysis of variance (ANOVA), is often employed to assess the contribution of the optimized parameters to the overall outcomes.

To better understand the workflow of the current investigation, a flowchart depicting the steps taken can be seen in Figure 6.2. This flowchart provides a visual representation of the actions and decisions made during the application of the Taguchi method. The Taguchi method typically consists of several stages, including:

1. Problem Definition: Clearly defining the objective function and the factors that influence it.

2. Design of Experiments (DOE): Determining the experimental plan by selecting the levels and combinations of factors to be tested.

3. Conducting Experiments: Performing the experiments based on the defined plan and recording the corresponding responses.

4. Data Analysis: Analyzing the experimental data using statistical techniques, such as ANOVA, to determine the most influential factors and their optimal levels.

5. Optimization: Identifying the optimal parameter settings based on the analysis results and selecting the levels that yield the best performance.

   Confirmation Test: Conducting additional experiments to validate the optimal parameter settings obtained from the previous step.

By following these steps, the Taguchi method helps researchers or engineers efficiently identify the optimal parameter values for a given objective function while minimizing the number of experiments required.

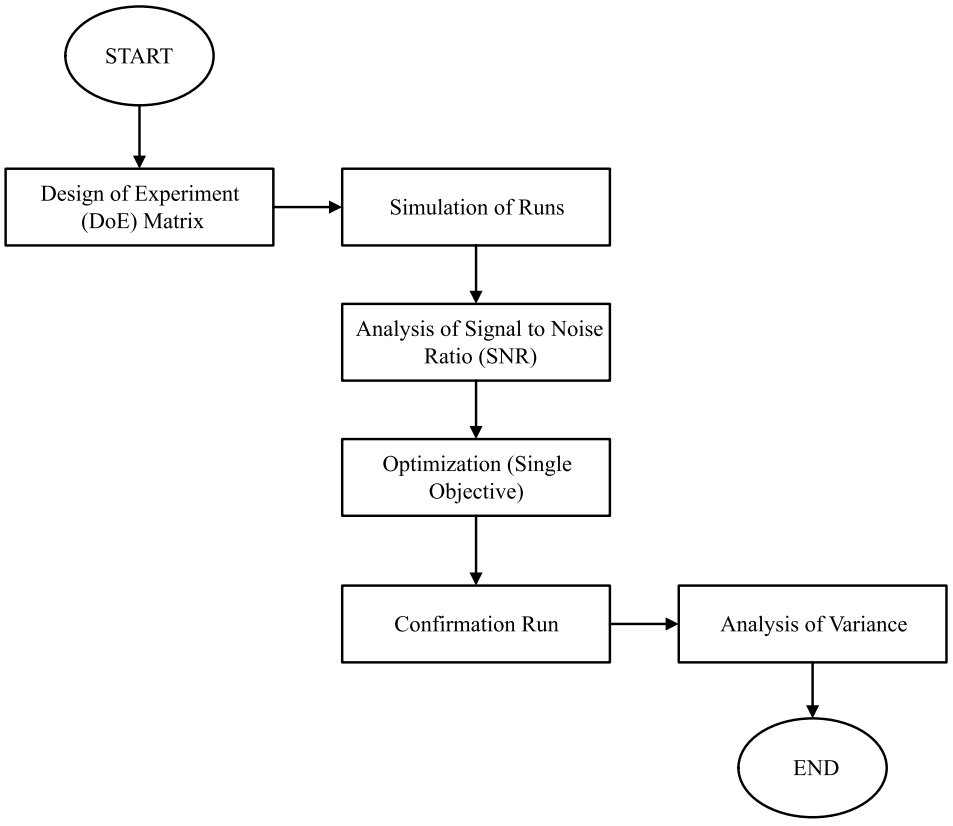


FIGURE 6.2: Flowchart of the Taguchi method.

### 6.3.1 Design of Experiments

Orthogonal arrays are used in Taguchi method to derive optimal subset of a full factorial experiment matrix. By reducing the number of experiments, the time and cost are greatly saved. The analysis of the influencing factors and their levels is performed after all the experiments in the DoE matrix have been run [160].

Orthogonal array consisting of 3 factors and 4 levels each was formed in the study as listed in Table 6.2. In case of factorial design we would need to run $4^3 = 64$ experiments. However, with Taguchi method the number of experiments is reduced to 16 ($L_{16}$) as listed in Table 6.3 in which is a 75% reduction in the total number of experiments of the full factorial design.

TABLE 6.2: Factors and levels for Taguchi analysis.

| **Factors** | **Levels** | | | |
|---|---|---|---|---|
| | 1 | 2 | 3 | 4 |
| $f_d(mm)$ | 5 | 10 | 15 | 20 |
| $A_r$ | 0.5 | 1.2 | 1.25 | 1.5 |
| $f_t(mm)$ | 1.2 | 1.25 | 1.5 | 2.0 |

TABLE 6.3: Taguchi orthogonal array ($L_{16}$).

| **Experiment No.** | **Factors** | | |
|---|---|---|---|
| | $f_d$ | $A_r$ | $f_t$ |
| 1 | 5 | 0.50 | 1.20 |
| 2 | 5 | 1.00 | 1.25 |
| 3 | 5 | 1.25 | 1.50 |
| 4 | 5 | 1.50 | 2.00 |
| 5 | 10 | 0.50 | 1.25 |
| 6 | 10 | 1.00 | 1.20 |
| 7 | 10 | 1.25 | 2.00 |
| 8 | 10 | 1.50 | 1.50 |
| 9 | 15 | 0.50 | 1.50 |
| 10 | 15 | 1.00 | 2.00 |
| 11 | 15 | 1.25 | 1.20 |
| 12 | 15 | 1.50 | 1.25 |
| 13 | 20 | 0.50 | 2.00 |
| 14 | 20 | 1.00 | 1.50 |
| 15 | 20 | 1.25 | 1.25 |
| 16 | 20 | 1.50 | 1.20 |

### 6.3.2 Evaluation of Signal to Noise Ratio (SNR)

Each design in the Table 6.3 was simulated. At the end of the melting process, the total melting time ($m_t$) and stored energy ($Q_t$) were recorded. The best value of the

parameter values is indicated by highest signal to noise ratio (SNR). In this study our objective was to determine the lowest melting time ($t_m$) and highest energy storage ($Q_t$). Equations (6.1) and (6.2) are used for calculating SNR values.

$$SNR = -10\ log(\frac{1}{n}\sum_{i=1}^{n}\frac{1}{Y_i^2}) \tag{6.1}$$

$$SNR = -10\ log(\frac{1}{n}\sum_{i=1}^{n}Y_i^2) \tag{6.2}$$

In these equations, $Y_i$ denotes either $m_t$ or $Q_t$ depending upon for which result SNR is being evaluated. $n$ is the number of observation which is 1 in the current study. The computed values were used for the construction of Taguchi relations and ranking table.

### 6.3.3 Analysis based on Melting Time Means

Equation (6.2) is utilized to calculate the Signal to noise ratio (SNR) values. SNR is a measure of the quality of a signal, representing the ratio of the desired signal power to the noise power. In the context of the current investigation, Equation (6.2) is employed to quantify the SNR values associated with the experimental outcomes. The calculated SNR values are reported in Table 6.4. This table provides a comprehensive overview of the obtained results, showcasing the SNR values corresponding to different parameter settings or experimental conditions.

By examining the SNR values, researchers can assess the impact of various factors on the signal quality and determine the optimal parameter combination that maximizes the SNR. It can be inferred that the SNR values in Table 6.4 serve as indicators of signal quality and are used to evaluate the performance of different parameter settings or configurations. Overall, Equation (6.2) and the corresponding results in Table 6.4 play a crucial role in assessing the signal quality and determining the optimal parameter values within the framework of the Taguchi method.

TABLE 6.4: Melting time results obtained by numerical study and Taguchi method.

| **No.** | **Factors** | | | **Result** | **SNR** | **Means** |
|---|---|---|---|---|---|---|
| | $f_d$ | $A_r$ | $f_t$ | | | |
| 1 | 5 | 0.50 | 1.20 | 4050.00 | -72.15 | 4050.00 |
| 2 | 5 | 1.00 | 1.25 | 4412.50 | -72.89 | 4412.50 |
| 3 | 5 | 1.25 | 1.50 | 5681.25 | -75.09 | 5681.25 |
| 4 | 5 | 1.50 | 2.00 | 6737.50 | -76.57 | 6737.50 |
| 5 | 10 | 0.50 | 1.25 | 2793.75 | -68.92 | 2793.75 |
| 6 | 10 | 1.00 | 1.20 | 3062.50 | -69.72 | 3062.50 |
| 7 | 10 | 1.25 | 2.00 | 5050.00 | -74.07 | 5050.00 |
| 8 | 10 | 1.50 | 1.50 | 5500.00 | -74.81 | 5500.00 |
| 9 | 15 | 0.50 | 1.50 | 2025.00 | -66.12 | 2025.00 |
| 10 | 15 | 1.00 | 2.00 | 4450.00 | -72.97 | 4450.00 |
| 11 | 15 | 1.25 | 1.20 | 3650.00 | -71.25 | 3650.00 |
| 12 | 15 | 1.50 | 1.25 | 4175.00 | -72.41 | 4175.00 |
| 13 | 20 | 0.50 | 2.00 | 2131.25 | -66.57 | 2131.25 |
| 14 | 20 | 1.00 | 1.50 | 3387.50 | -70.60 | 3387.50 |
| 15 | 20 | 1.25 | 1.25 | 3631.25 | -71.20 | 3631.25 |
| 16 | 20 | 1.50 | 1.20 | 4075.00 | -72.20 | 4075.00 |

Tables 6.5 and 6.6 show the impact of every design parameter on the melting time of thermal energy storage unit using SNR and means respectively. It can be seen from the table that aspect ratio of the container geometry was the most important design parameter effecting the melting time. This factor has the first rank of significance. The second important parameter was distance among fins. The fin thickness was the least significant design parameter.

TABLE 6.5: Response table for signal to noise ratios.

| **Level** | $\mathbf{f}_d$ | $\mathbf{A}_r$ | $\mathbf{f}_t$ |
|---|---|---|---|
| 1 | -74.18 | -68.44 | -71.33 |
| 2 | -71.88 | -71.55 | -71.36 |
| 3 | -70.69 | -72.90 | -71.66 |
| 4 | -70.14 | -74.00 | -72.54 |
| Delta | 4.03 | 5.55 | 1.21 |
| Rank | 2 | 1 | 3 |

The results obtained from the application of the Taguchi method for each parameter and level are visually presented in Figure 6.3. These figures display main

TABLE 6.6: Response table for means.

| **Level** | $\mathbf{f}_d$ | $\mathbf{A}_r$ | $\mathbf{f}_t$ |
|---|---|---|---|
| 1 | 5220 | 2750 | 3709 |
| 2 | 4102 | 3828 | 3753 |
| 3 | 3575 | 4503 | 4148 |
| 4 | 3306 | 5122 | 4592 |
| Delta | 1914 | 2372 | 883 |
| Rank | 2 | 1 | 3 |

effects plots for Signal-to-Noise (S/N) ratios and means, providing a graphical representation of the impact of different parameter levels on the response variable.

By analyzing the main effects plots and means plots in Figure 6.3, researchers can identify the optimal design parameters. The selection of the optimal parameter level is typically based on the principle of choosing the design level that corresponds to the minimum mean value. In other words, the parameter level that yields the lowest mean response is considered as the optimal choice according to the Taguchi method.

The specific values of the optimal design parameters determined through this analysis are listed in Table 6.7. This table serves as a concise summary of the identified optimal parameter settings, providing the necessary information for reproducing or implementing the optimized design in practical applications.The Taguchi method has facilitated the identification of the most favorable parameter settings for achieving the desired outcome.

TABLE 6.7: Optimal design parameters

| **Description** | **Symbol** | **Value** |
|---|---|---|
| Fin displacement | $f_d$ | 20 $mm$ |
| Geometry aspect ratio | $A_r$ | 0.5 |
| Fin thickness | $f_t$ | 1.20 $mm$ |

In summary, the main effects plots and means plots depicted in Figure 6.3 have aided in determining the optimal design parameters through the Taguchi method. The corresponding optimal values for the parameters are summarized in Table 6.7, providing valuable insights for implementing the optimized design.

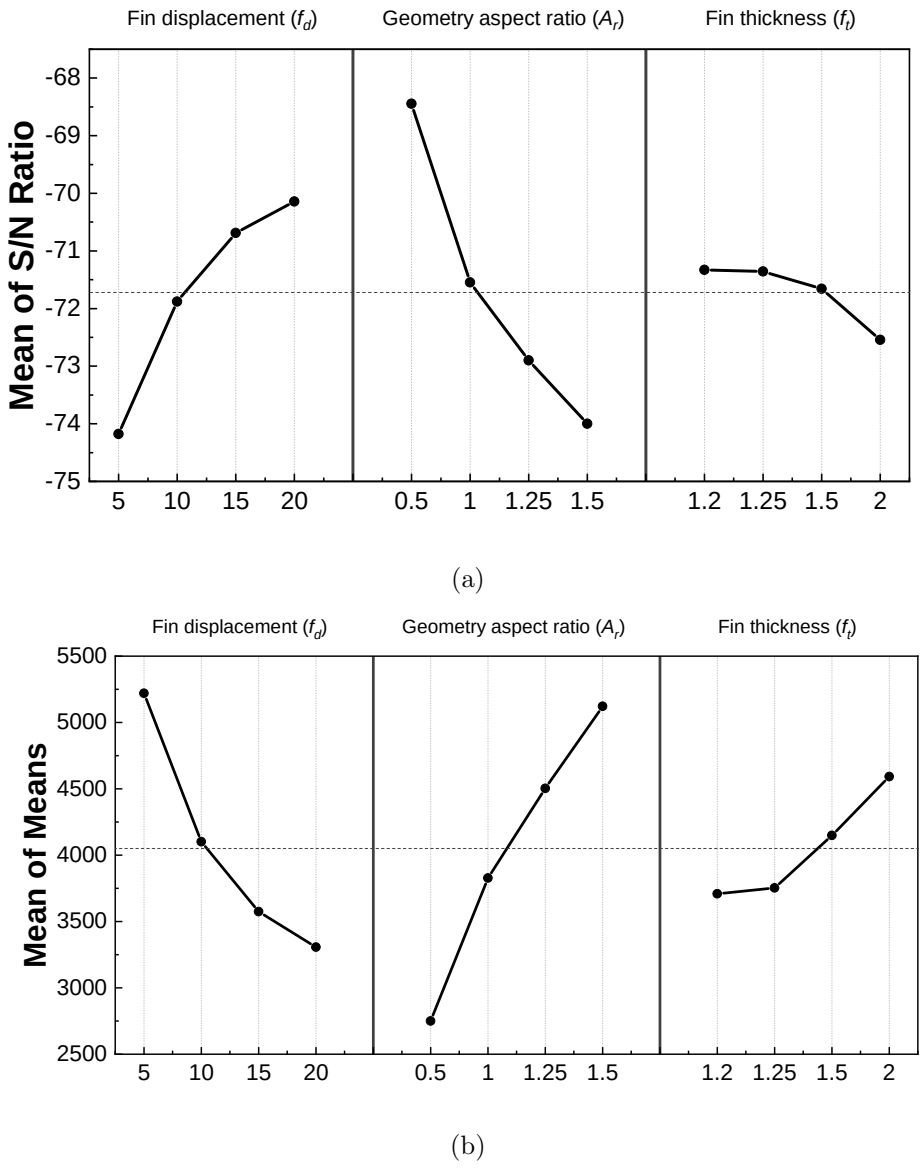


FIGURE 6.3: Graphical representation of Taguchi analysis (a) Main effects plot for S/N ratios (b) Main effects plot for means.

The optimal design case, obtained from the Taguchi method, represents one of the $4^3$ possible designs. It is important to note that in this particular case, the design did not align with the $L_{16}$ orthogonal array. Therefore, an additional simulation was conducted using the identified optimal parameters.

To facilitate a visual comparison between the optimal configuration and the reference and initial exponential fin distribution configurations, Figure 6.4 has been provided. This graphical illustration offers a clear visual assessment of the performance of the optimal configuration in relation to the other configurations.

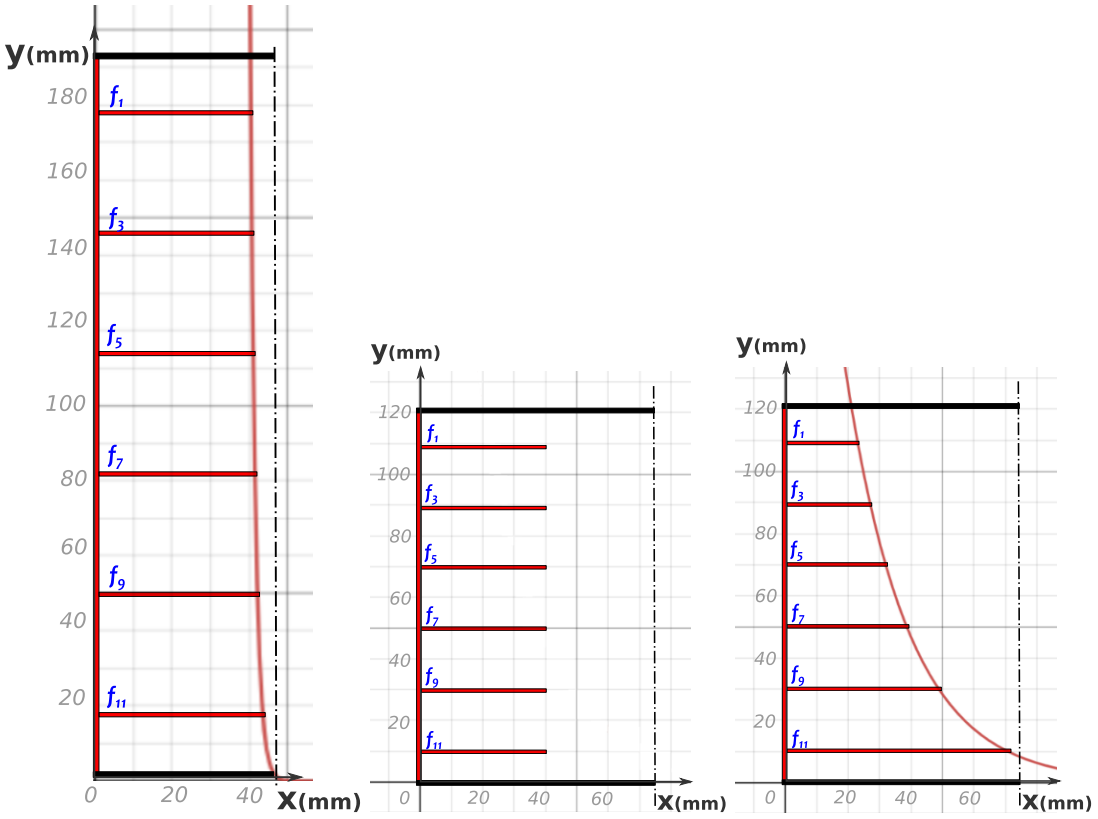


FIGURE 6.4: Graphical representation of (a) optimal configuration in comparison with (b) reference and (c) configurations.

By plotting relevant performance metrics or indicators on the graph, such as melting time, energy enhancement ratio, percentage time saving, or heat transfer rate, one can visually observe the differences and improvements achieved by the optimal configuration compared to the reference and initial exponential fin distribution configurations. The specific metrics to be included in the graph would depend on the objectives and requirements of the analysis.

The graph allows for a side-by-side comparison of the different configurations, making it easier to evaluate the performance of each design. This visual assessment provides a quick and intuitive understanding of the advantages and disadvantages of the configurations and helps identify the most effective design for the given criteria.

Additionally, the graph can be enhanced by incorporating error bars or confidence

intervals to indicate the uncertainty associated with the performance metrics, particularly if the data is obtained from experimental measurements or numerical simulations.

By utilizing Figure 6.4, researchers and engineers can gain valuable insights into the relative performance of different configurations and make informed decisions regarding the selection and optimization of fin designs for LHTES systems.

Furthermore, the results of this simulation are summarized in Table 6.8. The table presents the obtained values and demonstrates that the predicted value closely matches the actual value. The error in the prediction is calculated to be 2.12%, indicating a high level of accuracy in the predicted outcome.

In summary, the additional simulation conducted with the optimal parameters obtained from the Taguchi method is visually illustrated in Figure 6.4, and the corresponding results are listed in Table 6.8. The close agreement between the predicted and actual values, with an error of only 2.12%, demonstrates the effectiveness of the Taguchi method in identifying an optimized design configuration.

TABLE 6.8: Results for estimated and optimum design based on Taguchi method.

| | **Factors** | | | **Results at 95% LF** ($s$) | |
|---|---|---|---|---|---|
| **Model** | $\mathbf{f}_d(mm)$ | $\mathbf{A}_r$ | $\mathbf{f}_t(mm)$ | Simulated | Predicted |
| Reference | 20 | 1.25 | 1.25 | 4525 | - |
| Exponential | 20 | 1.25 | 1.25 | 3250 | - |
| Optimal | 20 | 0.5 | 1.2 | 1700 | 1664 |

It can be seem from these results that the optimal design obtained by Taguchi analysis is 62.43% better than the reference case and 47.69% improvement is seen with respect to the design with exponential function based fin distribution from the previous chapter. The total melting time for the optimal design was 45.8 minutes and the total energy stored was 330362.72 $kJ/kg$. The optimal energy storage rate obtained was 120 $W$.

### 6.3.4 Response Surface Plots

The results obtained from the DoE matrix constructed in the Taguchi method were used to plot 3D response surfaces. Three types of surfaces were plotted to observe the impact of design parameters on the melting time of PCM in LHTES device. Figure 6.5 shows the impact of fin displacement and geometry aspect ratio on the melting time. It can be seen that melting time reduces with lower aspect ratio and higher fin displacement. The optimal point seen in the plot is in the corner opposite to the origin.

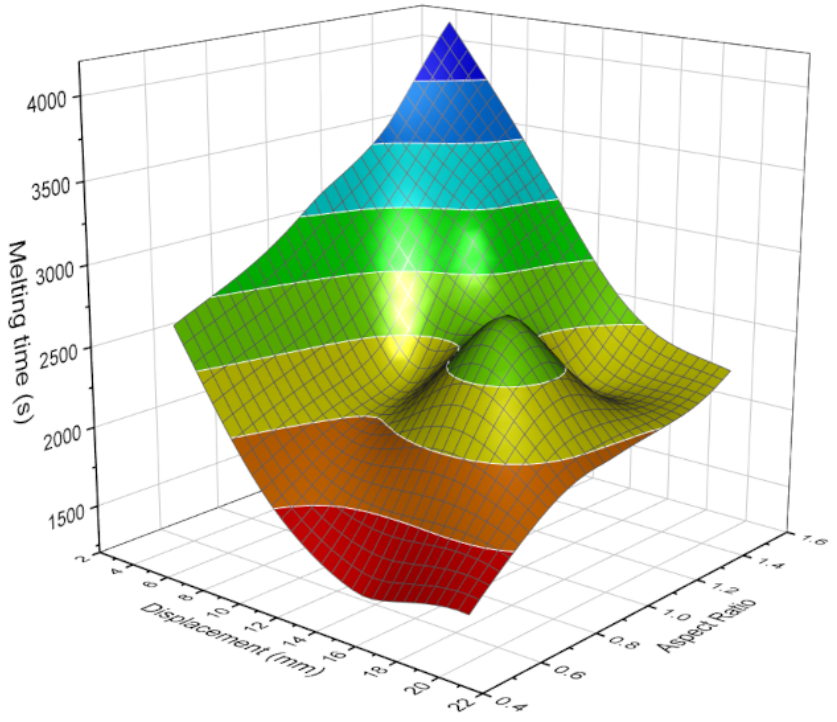


FIGURE 6.5: Response surface of $m_t$ vs. $f_d$ and $A_r$.

The effect of fin displacement and fin thickness on the melting time is shown in Figure 6.6. Two local minima can be observed in the response surface plot that occur near the area where fin thickness and fin displacement is low. The other local minimum point can be seen at the large fin displacement and low fin thickness.

The last surface plot shown in Figure 6.7 illustrates the correlation of fin thickness and thermal energy storage device's geometry aspect ratio on the melting time. Two local minima can be seen in the response surface plot in this case as well.

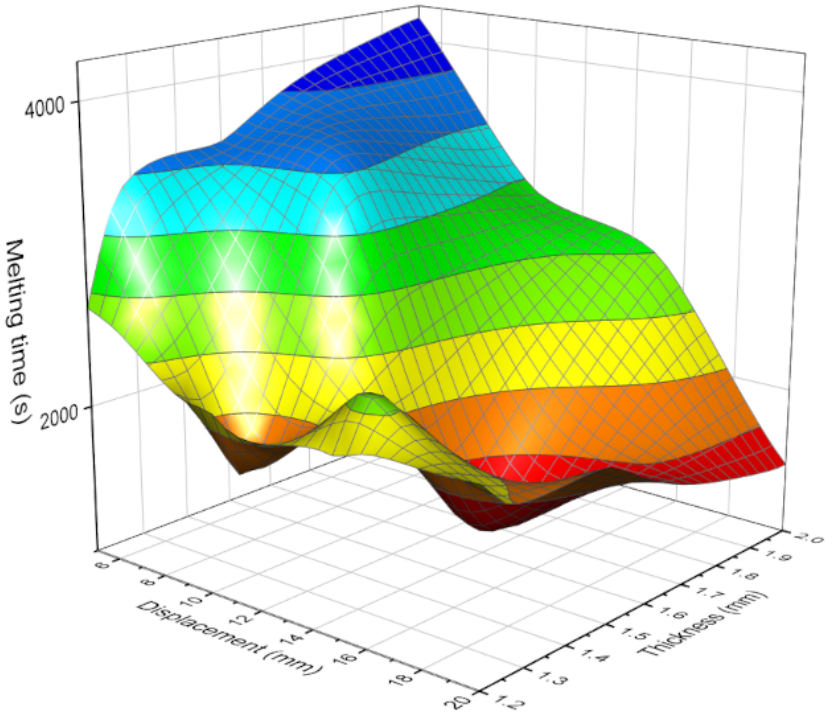


FIGURE 6.6: Response surface of $m_t$ vs. $f_d$ and $f_t$.

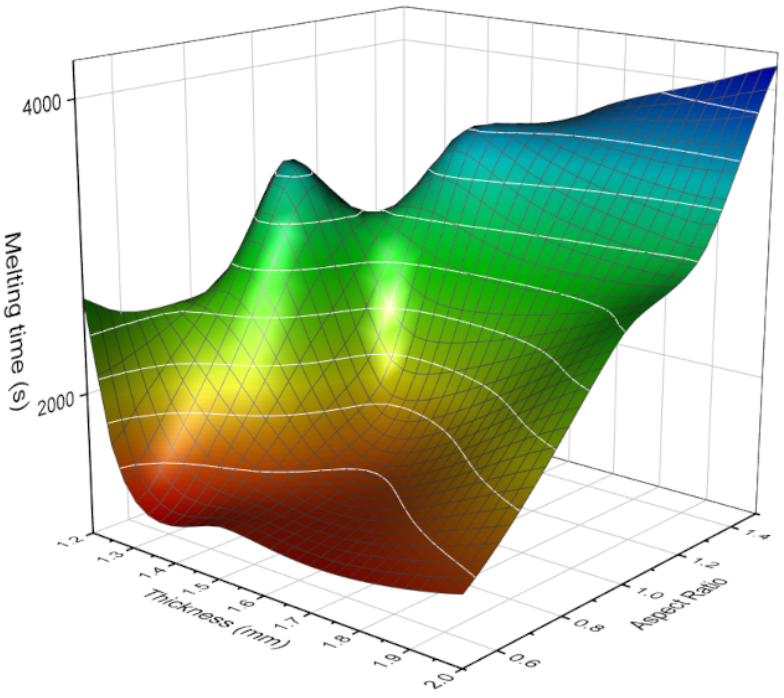


FIGURE 6.7: Response surface of $m_t$ vs. $A_r$ and $f_t$.

Both of these minima are close to geometry aspect ratio value close to 0.5. The corresponding fin thickness values are around $1.5mm$ and $1.9mm$.

It can be concluded all parameters namely, geometry aspect ratio $A_r$, fin displacement $f_d$, and fin thickness $f_t$ has an effect on the thermal performance of the LHTES system. It can be concluded from the combined effect of these parameters that the optimal value lies near smaller geometry aspect ratio, larger fin displacement as fin thickness values in the range of 1.2 to 1.5. There is a need to find the optimum values for these parameters. The subsequent sections is a statistical analysis of the results using Taguchi method to identify the optimal parameters and predict the performance of a design configuration for given set of design variables. Machine learning techniques are utilized to improve the prediction model.

### 6.3.5 Correlation of Exponential Function Parameter B vs. Fin Thickness

In this section a correlation is developed between the exponential function-parameter B and design parameters $f_t$ of LHTES. The parameter is converted to a dimensionless quantity before developing the correlation. The dimensionless parameter $f_t{}'$ is evaluated as given in equation (6.3).

$$f_t{}' = f_t/H \tag{6.3}$$

The corresponding dimensionless quantities are evaluated using the above expressions and listed in Table 6.9. The correlation by fitting a curve through these dimensionless values and the result is shown in Equation (6.4) below:

$$B = a\,(f_t{}')^b \tag{6.4}$$

where,

$$a = 5.284 \times 10^{-8}$$

$$b = -3.2051$$

TABLE 6.9: Dimensionless quantities

| $f_t$ | $f_t\prime$ | B |
|---|---|---|
| 1.20 | 0.00633 | 0.60481 |
| 1.25 | 0.00932 | 0.116012 |
| 1.50 | 0.01250 | 0.072727 |
| 2.00 | 0.01826 | 0.051421 |
| 1.20 | 0.00894 | 0.138131 |
| 1.25 | 0.00659 | 0.51883 |
| 1.50 | 0.01369 | 0.067751 |
| 2.00 | 0.01667 | 0.067982 |
| 1.20 | 0.01000 | 0.109544 |
| 1.25 | 0.01141 | 0.084451 |
| 1.50 | 0.00791 | 0.29144 |
| 2.00 | 0.01491 | 0.089421 |
| 1.20 | 0.01095 | 0.092684 |
| 1.25 | 0.01042 | 0.109831 |
| 1.50 | 0.01118 | 0.11721 |
| 2.00 | 0.01054 | 0.19177 |

The fitting of the developed correlation, which predicts the thermal performance of the LHTES system, is visually depicted in Figure 6.8. This figure showcases the close agreement between the predicted values from the correlation and the corresponding empirical values.

By closely examining Figure 6.8, it can be observed that the developed correlation accurately captures the relationship between the design variables and the thermal performance of the LHTES system. The predicted values closely align with the empirical values, indicating that the correlation effectively captures the underlying patterns and trends in the data.

The close fit between the developed correlation and the empirical values in Figure 6.8 signifies the reliability and accuracy of the predictive model. It implies that the correlation can be utilized to estimate the thermal performance of the LHTES system for various design configurations, thereby enabling engineers and researchers to make informed decisions and optimize the system's design.

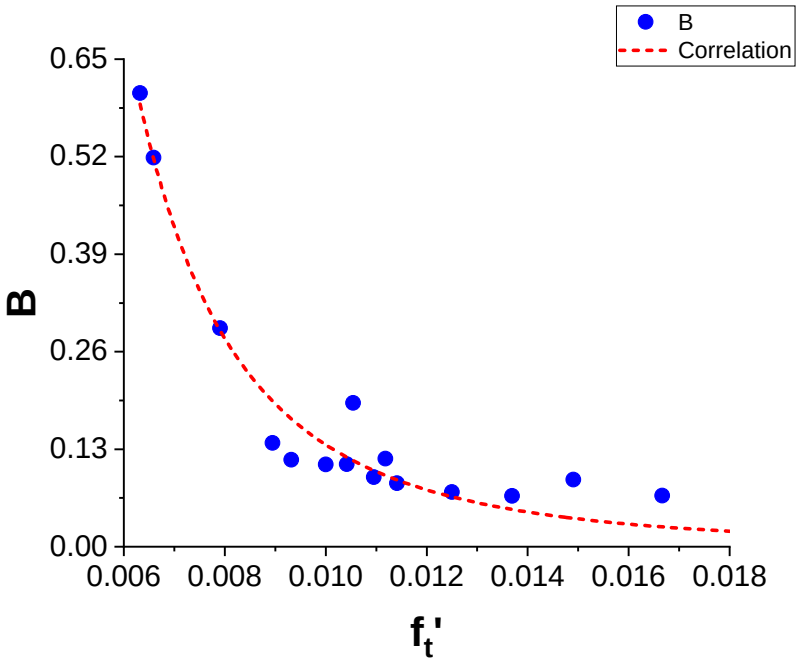


FIGURE 6.8: Correlation between exponential parameter B and $f_t{}'$.

### 6.3.6 ANOVA

The analysis of variance (ANOVA) is carried out for the evaluation of relative contribution effects of the parameters on $m_t$ and $Q_t$. The SNR data calculated by Taguchi method is used by ANOVA. 95% $F_{test}$ is selected in this study as the confidence level of the statistical analysis to ensure reliability of the method. If the calculated $F_{test}$ value is higher than $F_{3,6,0.05} = 4.76$ value, the relevant parameter is statistically significant.

TABLE 6.10: Analysis of variance for means.

| **Source** | **DF** | **Seq SS** | **Adj SS** | **Adj MS** | **F** | **P** |
|---|---|---|---|---|---|---|
| Fin displacement ($f_d$) | 3 | 8604307 | 8604307 | 2868102 | 12.34 | 0.006 |
| Aspect ratio ($A_r$) | 3 | 12373857 | 12373857 | 4124619 | 17.75 | 0.002 |
| Fin thickness ($f_t$) | 3 | 2031260 | 2031260 | 677087 | 2.91 | 0.123 |
| Residual Error | 6 | 1394160 | 1394160 | 232360 | | |
| Total | 15 | 24403584 | | | | |

It can been seen from Table 6.10 that the most significant factors influencing the melting time are container geometry aspect ratio ($A_r$) and displacement of fins ($f_d$) on the heated walls in the design of a LHTES device. The $P$ values for these

factor are less than 0.05. The percentage contributions of $f_d$, $A_r$, and $f_t$ on the melting time ($m_t$) were 35 %, 50 %, and 8.32 % respectively.

### 6.3.7 Development of a Linear Regression Model

A predictive mathematical model was developed for melting time ($m_t$) as a function of $f_d$, $A_r$, and $f_t$ using linear regression analysis. The model obtained from the regression analysis is shown in Equation (6.5).

$$m_t = 1438 - 125.4 f_d + 2375 A_r + 1114 f_t \quad (R^2 = 90.95\%) \tag{6.5}$$

Coefficient of determination $R^2$, that varies from 0 to 1, was used to check the capability of the developed model. A value closer to 1 indicates a good fit between the dependent and independent variables. In our case, the developed regression model for $m_t$ had $R^2 = 90.95\%$.

Moreover, the normal probability plot of residuals shown in Figure 6.9 was used to check the significance of the coefficients in the predicted model. The straight line meant that the residual errors in the model were normally distributed and coefficients in the model are significant. It was observed that the residuals fall near the straight line which implies that the coefficient models are significant.

## 6.4 Thermal Performance Analysis of Taguchi $L_{16}$ Configurations

In this section, thermal behavior of simulations performed for each Taguchi trial is studied. Figure 6.10 shows enclosure geometry aspect ratio variations used in the simulation of these configurations. In these figures, $f_n$ represents fin numbers from top to bottom. In the figure, the odd numbered fins are on the left heated wall while the even numbered fins are attached to right heated wall.

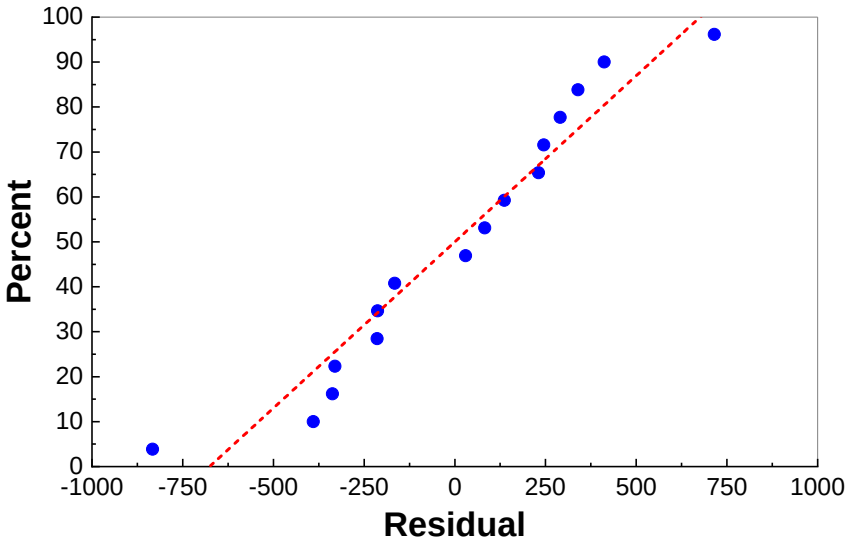


FIGURE 6.9: Normal probability plot of the residuals for melting time.

The function parameters $A$ and $B$, in Equation (6.6) were adjusted appropriately so that the resultant fin configuration conforms to the requirements of constant PCM volume and other design parameters.

$$y = y_0 + Ae^{-B(x-x_0)} \tag{6.6}$$

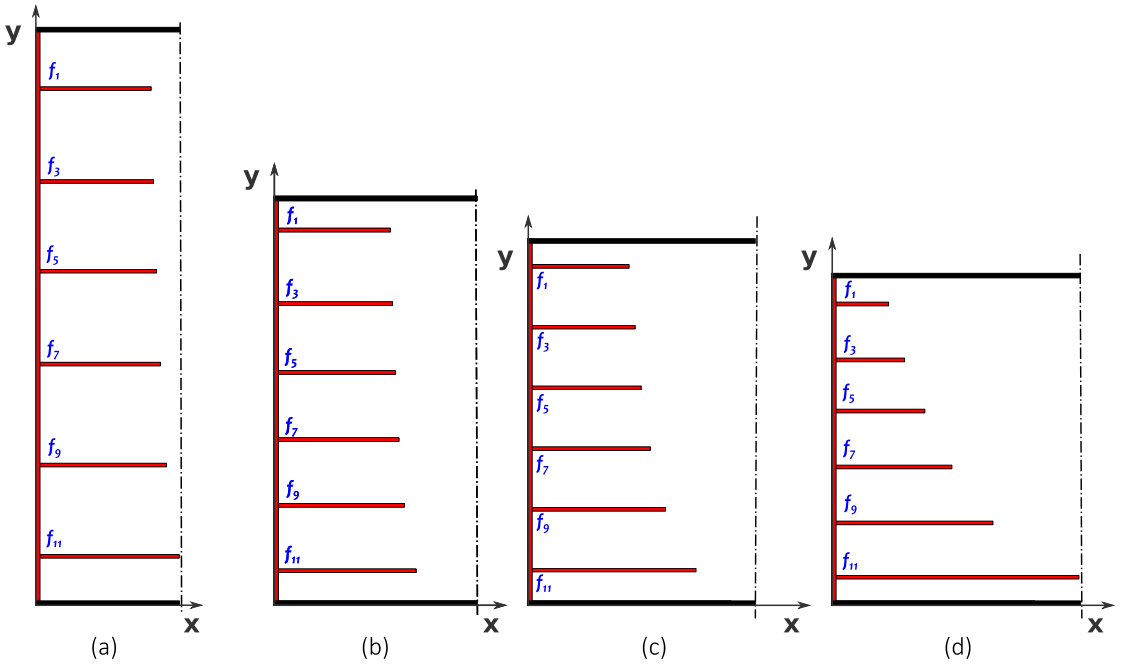


FIGURE 6.10: Variation of enclosure geometry aspect ratio (a) $A_r = 0.5$, (b) $A_r = 1.0$, (c) $A_r = 1.25$, (d) $A_r = 1.5$.

For each enclosure design, these parameters were adjusted and corresponding fin lengths were evaluated. Table 6.11 lists values for these parameters identified for each trial. These parameter values were used in the expression defined in eq. (5.4) to calculate the corresponding fin lengths. The table also lists the fin lengths calculated for all design configurations described in the Taguchi DOE matrix. For the sake of simplicity, constant values $y_0 = 0$, $A = 1.0$, and $x_0 = W_r/2$ were used to evaluate the $B$ parameter in the expression shown in 5.4.

The last of the table contains the configuration of the optimal design as a result of the Taguchi analysis. The graphical representation of the lengths is shown in Figure 6.11 for four different cases of fin displacements $f_d = [5, 10, 15, 20]$.

TABLE 6.11: Function parameters ($y_0 = \mathbf{0}$, $A = \mathbf{1.0}$) and corresponding fin lengths for all Taguchi $L_{16}$ DOE cases.

| **Configuration** | | | **Function** | | **Fin length** | | | | | |
|---|---|---|---|---|---|---|---|---|---|---|
| $f_d$ | $A_r$ | $f_t$ | $x_0$ | $B$ | $f_l$ | $f_3$ | $f_5$ | $f_7$ | $f_9$ | $f_{11}$ |
| 5 | 0.50 | 1.20 | 47.43 | 0.605 | 40.80 | 41.05 | 41.35 | 41.72 | 42.20 | 42.87 |
| 5 | 1.00 | 1.25 | 67.08 | 0.116 | 35.47 | 36.80 | 38.37 | 40.30 | 42.78 | 46.27 |
| 5 | 1.25 | 1.50 | 75.00 | 0.073 | 26.11 | 28.23 | 30.74 | 33.81 | 37.76 | 43.34 |
| 5 | 1.50 | 2.00 | 82.16 | 0.051 | 14.79 | 17.79 | 21.33 | 25.67 | 31.27 | 39.15 |
| 10 | 0.50 | 1.25 | 47.43 | 0.519 | 38.66 | 39.01 | 39.44 | 40.00 | 40.78 | 42.11 |
| 10 | 1.00 | 1.20 | 67.08 | 0.138 | 36.63 | 37.95 | 39.57 | 41.65 | 44.59 | 49.60 |
| 10 | 1.25 | 2.00 | 75.00 | 0.068 | 14.77 | 17.46 | 20.74 | 24.97 | 30.93 | 41.13 |
| 10 | 1.50 | 1.50 | 82.16 | 0.068 | 23.07 | 25.76 | 29.06 | 33.30 | 39.29 | 49.52 |
| 15 | 0.50 | 1.50 | 47.43 | 0.291 | 30.62 | 31.28 | 32.11 | 33.20 | 34.82 | 37.96 |
| 15 | 1.00 | 2.00 | 67.08 | 0.089 | 16.15 | 18.32 | 21.02 | 24.58 | 29.84 | 40.08 |
| 15 | 1.25 | 1.20 | 75.00 | 0.110 | 34.44 | 36.22 | 38.42 | 41.33 | 45.62 | 53.98 |
| 15 | 1.50 | 1.25 | 82.16 | 0.084 | 30.63 | 32.93 | 35.79 | 39.56 | 45.12 | 55.97 |
| 20 | 0.50 | 2.00 | 47.43 | 0.192 | 20.53 | 21.58 | 22.89 | 24.65 | 27.31 | 33.04 |
| 20 | 1.00 | 1.50 | 67.08 | 0.117 | 26.03 | 27.74 | 29.88 | 32.75 | 37.11 | 46.49 |
| 20 | 1.25 | 1.25 | 75.00 | 0.110 | 32.20 | 34.03 | 36.32 | 39.38 | 44.03 | 54.04 |
| 20 | 1.50 | 1.20 | 82.16 | 0.093 | 32.43 | 34.59 | 37.30 | 40.93 | 46.45 | 58.30 |
| 20 | 0.50 | 1.25 | 47.43 | 0.579 | 38.52 | 38.87 | 39.30 | 39.88 | 40.77 | 42.66 |

The contours of melting fraction and temperature for the Taguchi DOE matrix base design cases are shown in From Figures 6.12, 6.13, 6.14 and 6.15. It can be seen from these contours that the cases with smaller fin displacement have fins close to each other and this configuration cause heat to be trapped around the

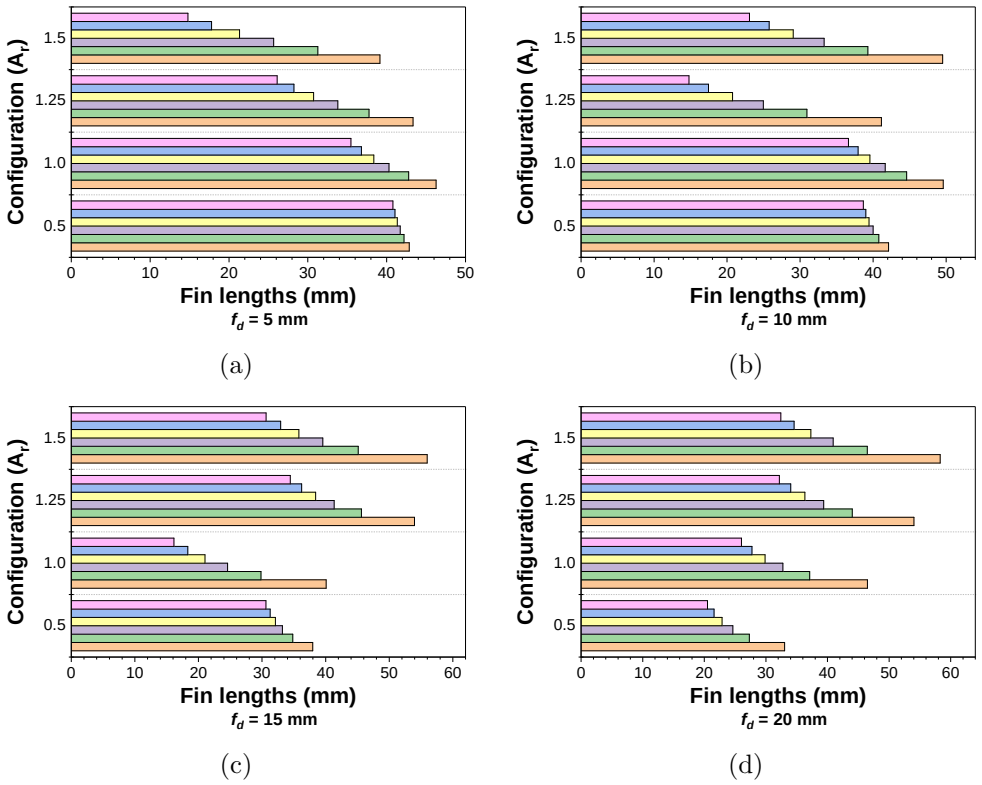


FIGURE 6.11: Graphical representation of fin lengths for different geometry aspect ratio, fin displacement (a) $f_d = 5mm$ (b) $f_d = 10mm$ (c) $f_d = 15mm$ (d) $f_d = 20mm$.

fins, resulting in slower natural convection and slow melting of PCM. The cases where fin displacements is large, fins are uniformly distributed along the heated walls and result in much better heat transfer, higher rate of natural convection and faster melting.

Another observation based on the geometry aspect ratio of the rectangular LHTES is that the performance of the thermal energy storage device with higher aspect ratio (Figure 6.12) is lower than the LHTES device with smaller aspect ratio (Figure 6.15). The total melting time and energy storage rate for these cases are shown in Figure 6.16a and 6.16b respectively.

The transient progression of melt-fraction, and stored energy in all of the cases are shown in Figure 6.17 and Figure 6.19 respectively. The best melting rate in all configuration groups shown in the figure is obtained for $f_d = 20mm$.

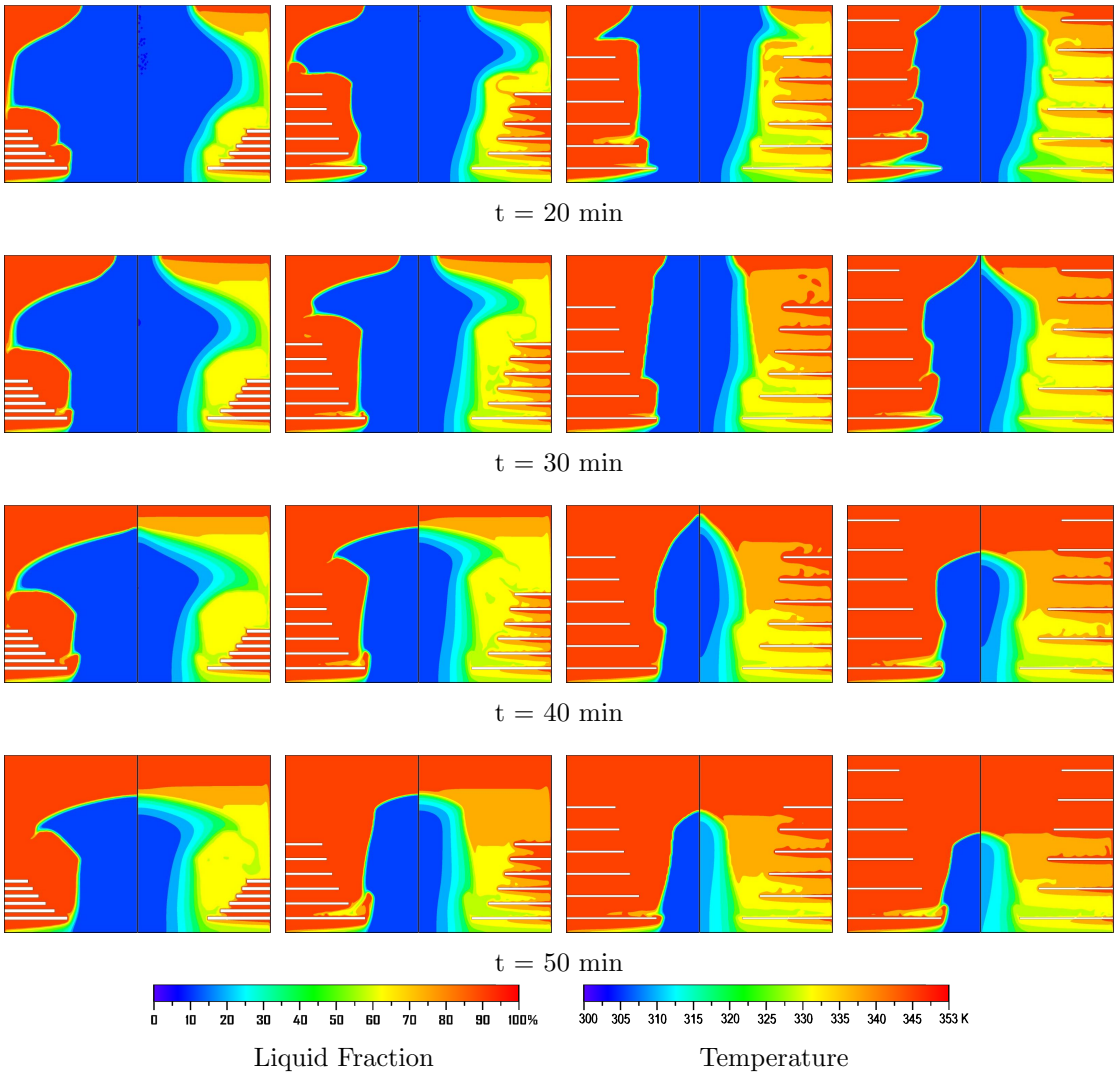


FIGURE 6.12: Contours of PCM melt fraction and temperature for different fin displacements at $A_r = 1.5$.

In cases $A_r = [15, 1.25, 1.0]$, during the initial conduction phase at the start of the melting process the melting rate is similar for fin displacements $f_d = [10, 15, 20]$. After PCM melts and natural convection gradually strengthens, the melting rate starts to vary and after about 60% liquid fraction, the configuration with $f_d = 20$ starts to dominate and melting rate increases due to better heat transfer of the strong convection.

In other configurations, melting is slower than the reference case. Even for $A_r = 0.5$ container geometry aspect ratio, the configuration with smaller fin displacement ($f_d$) performed worse than the reference case. As was observed from contour plots, due to concentrated heat pockets around the fins, weak natural convection

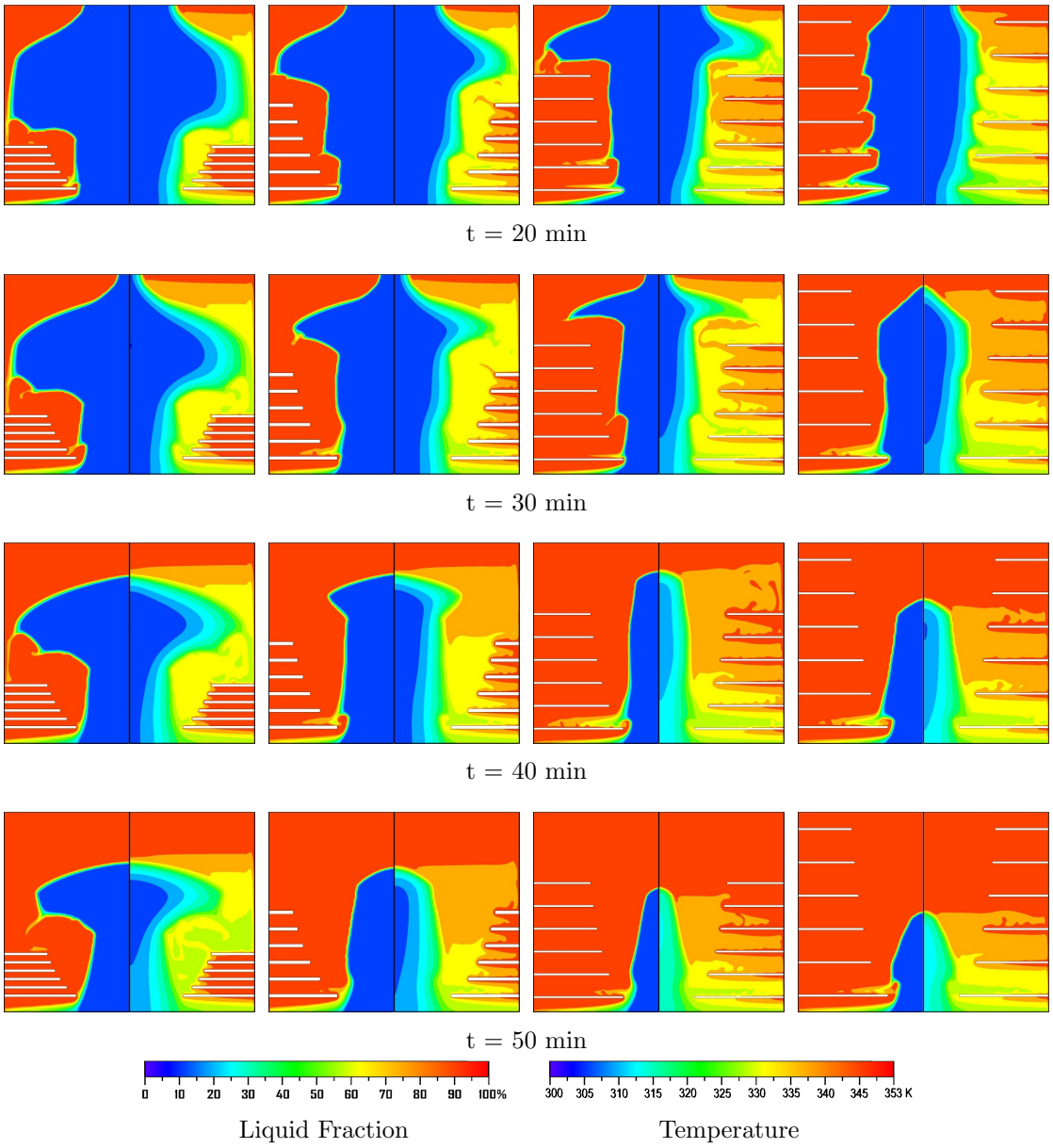


FIGURE 6.13: Contours of PCM melt fraction and temperature for different fin displacements at $A_r = 1.25$.

builds up and heat transfer is slow for this configuration and the LHTES devices performed poorly.

The other fin displacements $f_d = [10, 15, 20]$, all performed better with higher melting rate from the start of the melting process compared to the reference case.

More detailed analysis of the performance of different LHTES designs is obtained with the help of enhancement ratio of melting and energy storage compared to the reference case. These melting enhancement ratio $E_{mr}$, and energy enhancement

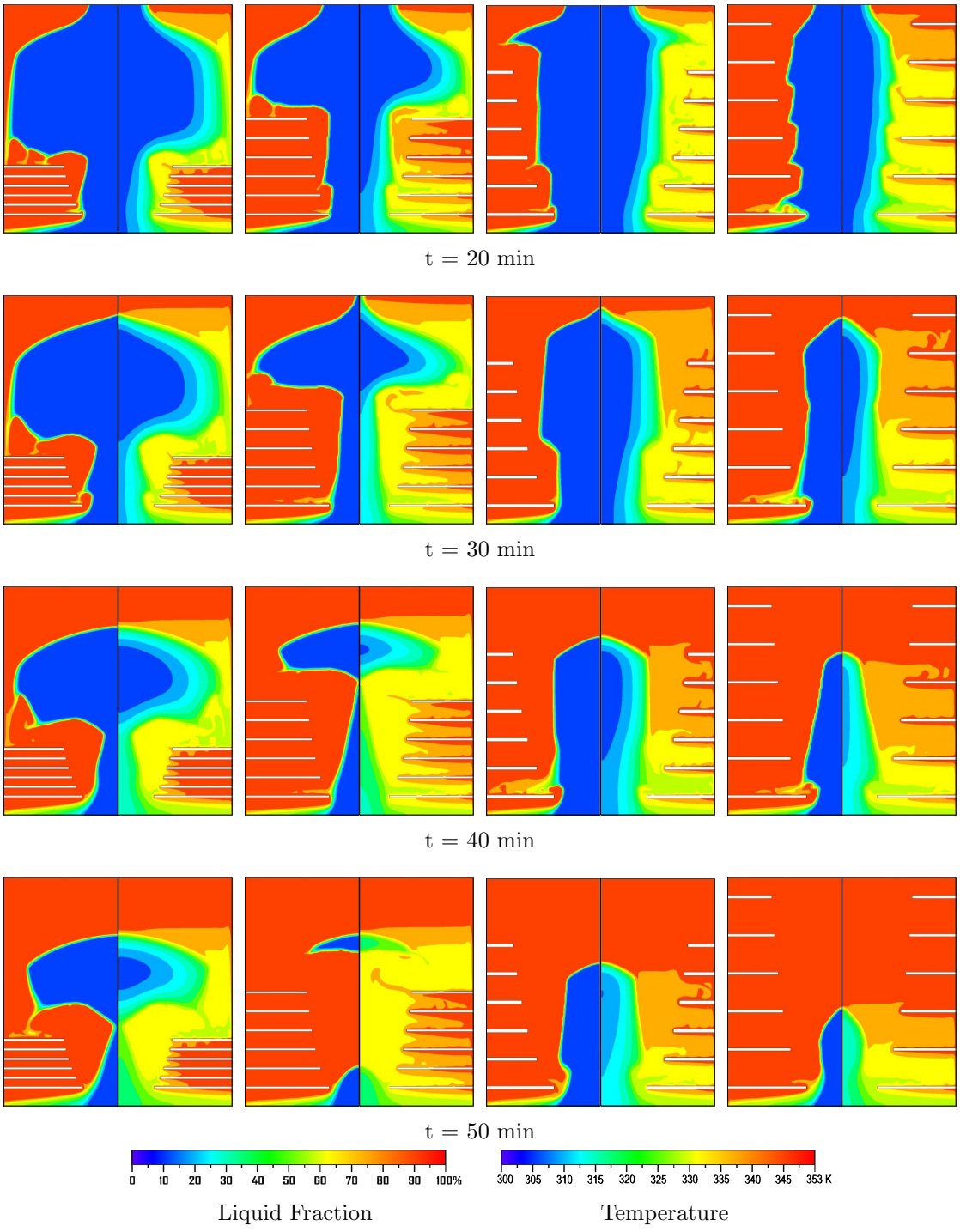


FIGURE 6.14: Contours of PCM melt fraction and temperature for different fin displacements at $A_r = 1.0$.

ratio $E_{er}$ are shown in Figure 6.18 and 6.20 respectively. The same conclusion is drawn from the enhancement ratio plots as well.

The analysis of the results reveals that the thermal performance of the LHTES device in various configurations is predominantly influenced by two factors: the

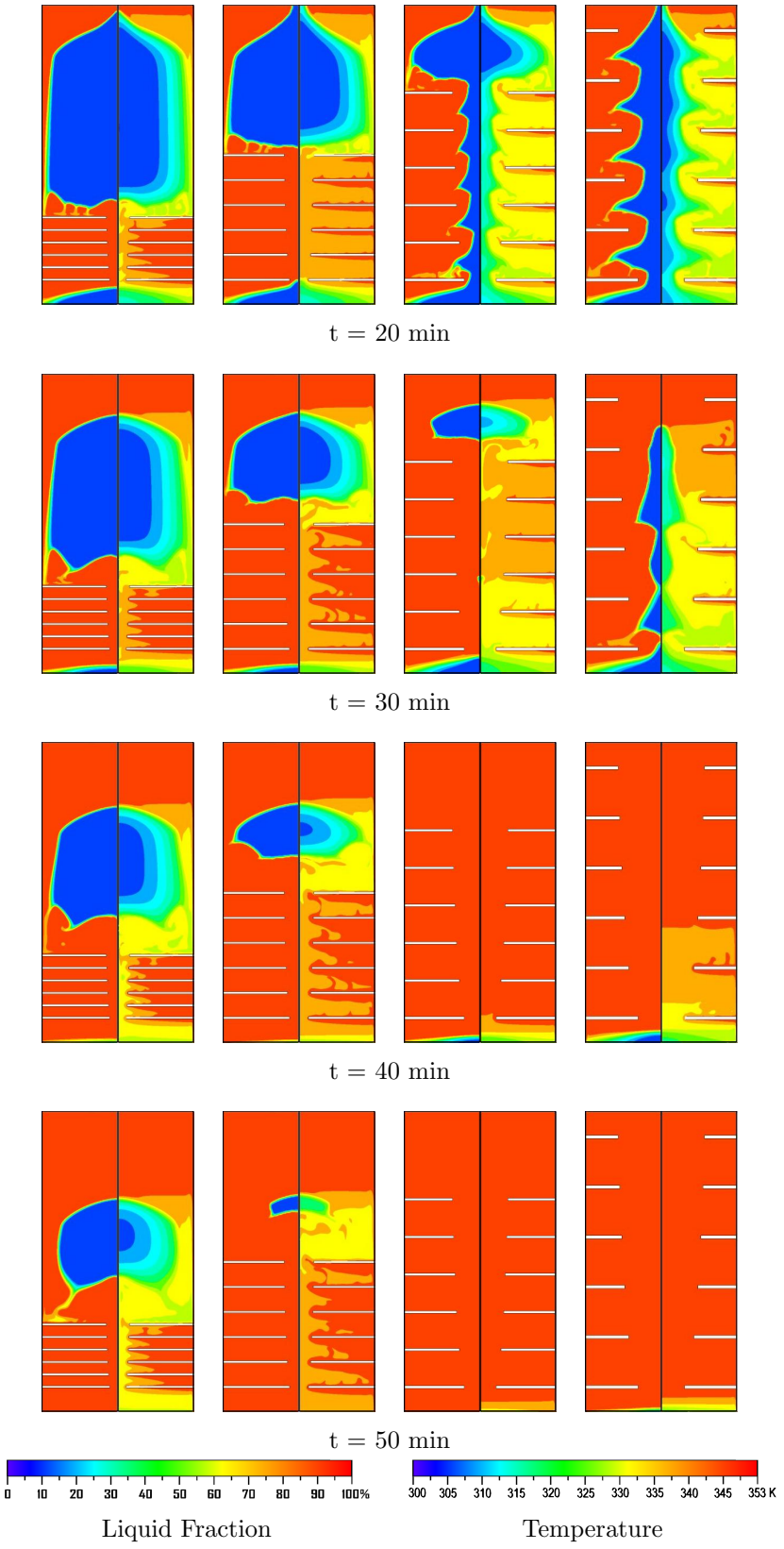


FIGURE 6.15: Contours of PCM melt fraction and temperature for different fin displacements at $A_r = 0.5$.

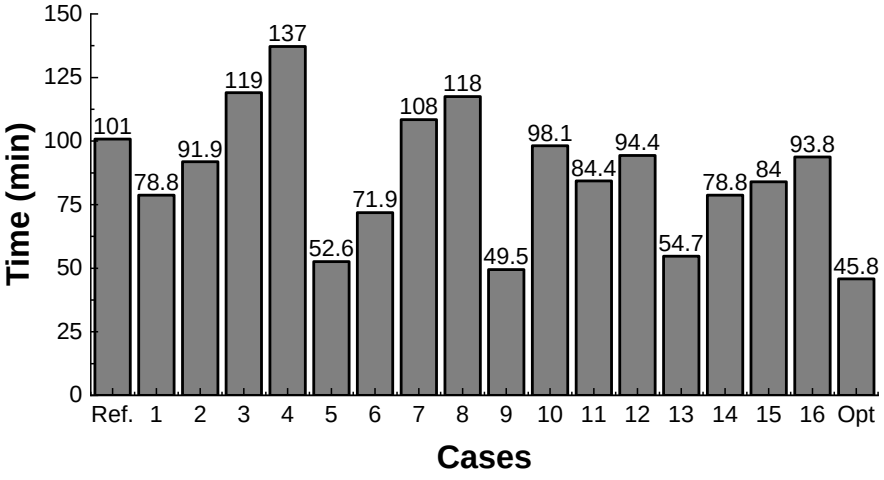


(a)

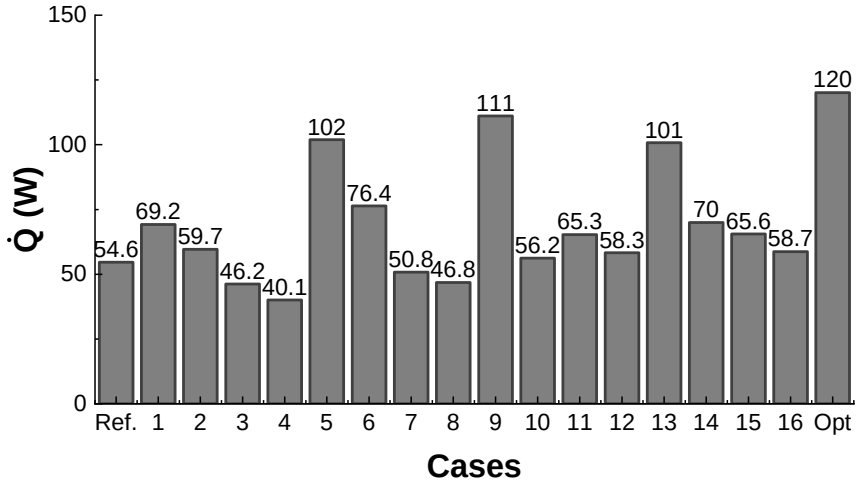


(b)

FIGURE 6.16: Performance of LHTES device for Taguchi experiments (a) Total melting time, (b) Total energy storage rate.

container aspect ratio $A_r$ and the fin displacement on the heated wall $f_d$. On the other hand, the effect of fin thickness $f_t$ on the thermal performance is found to be relatively less significant.

The container aspect ratio $A_r$ refers to the ratio of the length to the width of the container housing the LHTES system. The results indicate that variations in the container aspect ratio have a substantial impact on the thermal performance. Changes in this parameter can significantly influence the heat transfer characteristics and overall performance of the LHTES device.

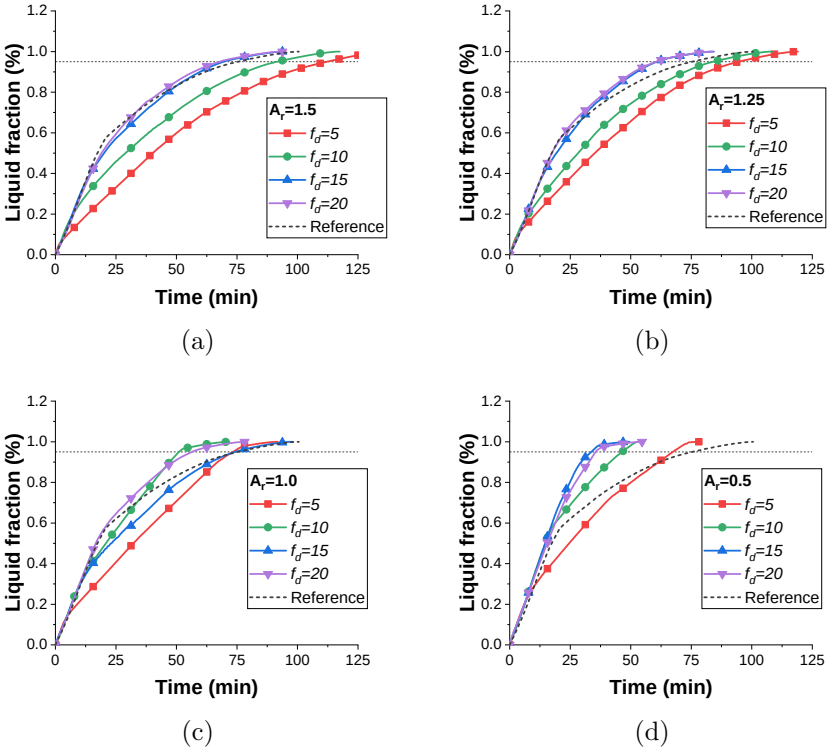


FIGURE 6.17: Transient progress of melting fraction (a) $A_r = 1.5$, (b) $A_r = 1.25$, (c) $A_r = 1.0$, (d) $A_r = 0.5$.

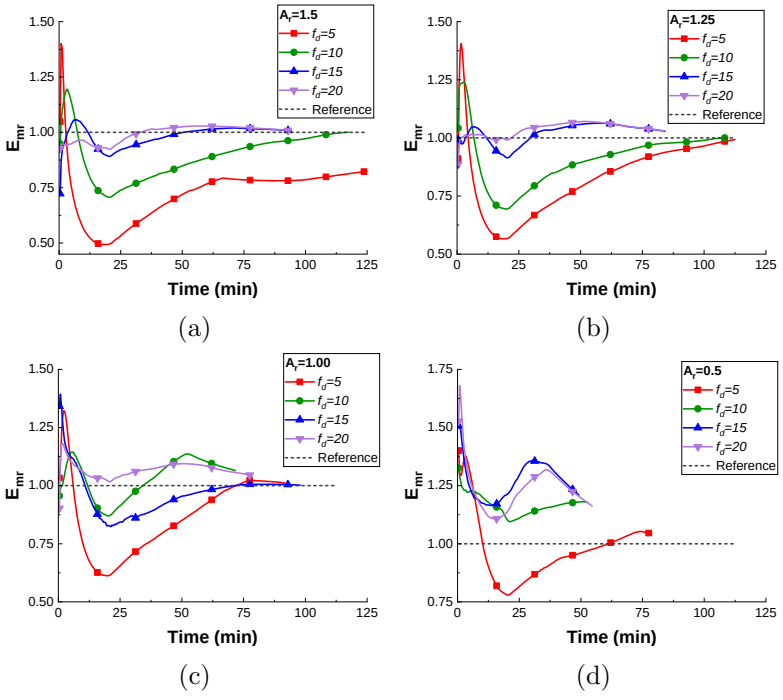


FIGURE 6.18: Melting enhancement ratio (a) $A_r = 1.5$, (b) $A_r = 1.25$, (c) $A_r = 1.0$, (d) $A_r = 0.5$.

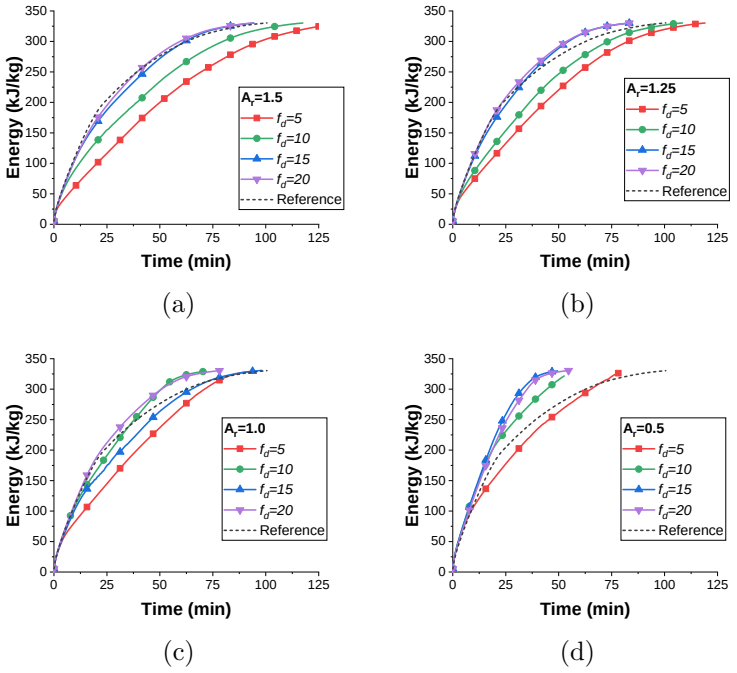


FIGURE 6.19: Transient progress of stored energy (a) $A_r = 1.5$, (b) $A_r = 1.25$, (c) $A_r = 1.0$, (d) $A_r = 0.5$.

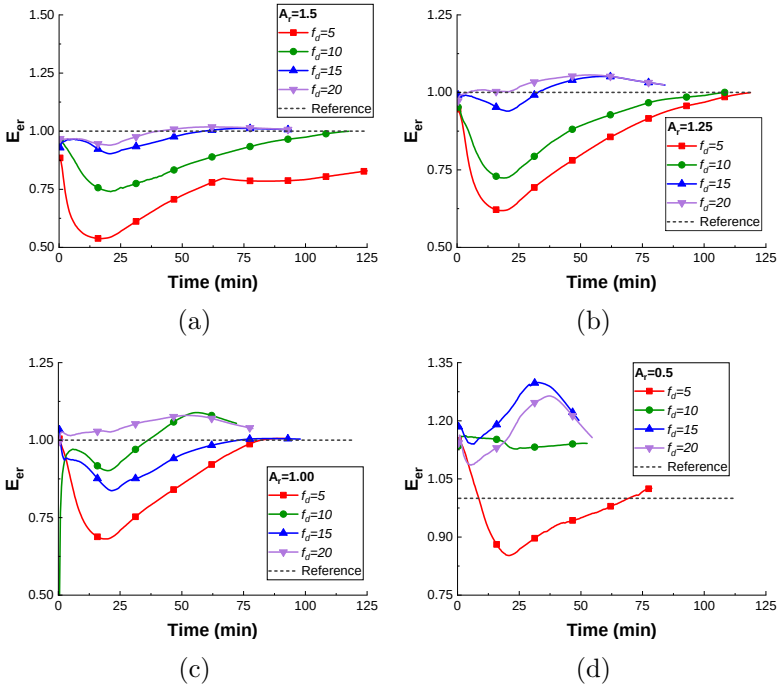


FIGURE 6.20: Energy storage enhancement ratio (a) $A_r = 1.5$, (b) $A_r = 1.25$, (c) $A_r = 1.0$, (d) $A_r = 0.5$.

Similarly, the fin displacement on the heated wall $f_d$, which refers to the spacing between the fins on the heated wall of the LHTES system, is identified as another critical parameter affecting the thermal performance.

The results suggest that adjusting the fin displacement can have a notable influence on the heat transfer process and, consequently, the device's overall performance.

On the other hand, the effect of fin thickness $f_t$ on the thermal performance is deemed relatively less significant. Although variations in fin thickness can affect heat transfer to some extent, the results indicate that it is not as influential as the container aspect ratio and fin displacement.

These findings highlight the importance of considering the container aspect ratio and fin displacement when optimizing the thermal performance of LHTES devices. Engineers and researchers can prioritize these parameters in the design process to achieve improved heat transfer efficiency and overall system performance. While fin thickness should not be disregarded entirely, its impact may be comparatively smaller.

In summary, the analysis of the results indicates that the thermal performance of LHTES devices is primarily influenced by the container aspect ratio and fin displacement, while the effect of fin thickness is relatively less significant.

This insight can guide further optimization efforts and help prioritize design parameters to enhance the efficiency and performance of LHTES systems.

## 6.5 Melting Performance Analysis of the Optimal Configuration

In this section, melting and thermal performance of the optimal design is studied and compared with the reference and default cases. The reference and default cases were selected from the previous chapter where mathematical functions were used for fin length distribution from top to bottom. The case where fin length were constant and the exponential function based configuration was taken as the default case in this section for comparison with the optimal design configuration. Table 6.12 lists design parameters and fin lengths for all these cases.

TABLE 6.12: Design parameters and corresponding fin lengths.

| **Configuration** | **Parameters** | | | **Fin length** | | | | | |
|---|---|---|---|---|---|---|---|---|---|
| | $f_d$ | $A_r$ | $f_t$ | $f_1$ | $f_3$ | $f_5$ | $f_7$ | $f_9$ | $f_{11}$ |
| Reference | 20 | 1.25 | 1.25 | 40 | 40 | 40 | 40 | 40 | 40 |
| Default | 20 | 1.25 | 1.25 | 35.47 | 36.80 | 38.37 | 40.30 | 42.78 | 46.27 |
| Optimal | 20 | 0.50 | 1.25 | 38.52 | 38.87 | 39.30 | 39.88 | 40.77 | 42.66 |

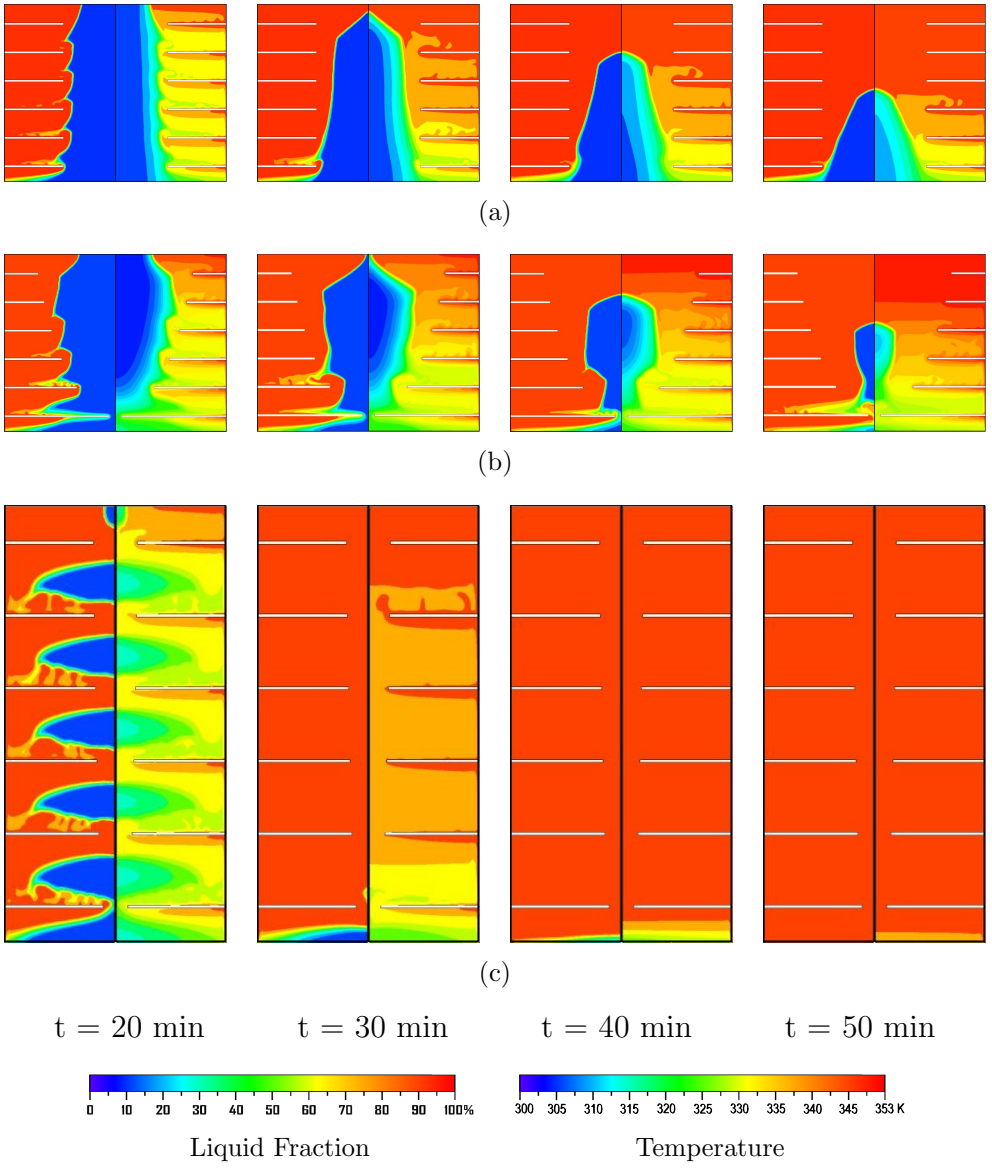


FIGURE 6.21: Contours of PCM melt fraction and temperature for (a) reference, (b) default, and (c) optimal cases.

The contours of melting fraction and temperature for the reference, default, and optimal design cases are shown in Figure 6.21. It can be seen from these contours that the melting is faster in both default (exponential) and optimal design

configurations. The optimal configuration has large fin displacements and fins are uniformly distributed along the heated walls and result in much better heat transfer, higher rate of natural convection and faster melting. The total melting time and energy storage rate for these cases are shown in Figure 6.22.

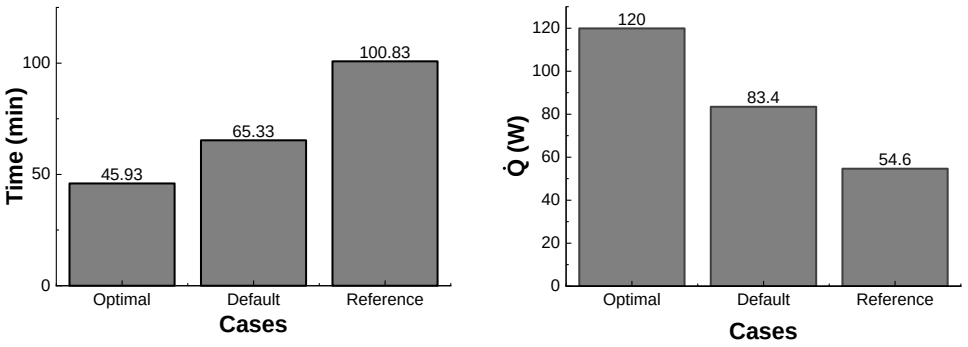


(a) (b)

FIGURE 6.22: Performance of optimal LHTES configuration (a) Total melting time, (b) Total energy storage rate

The transient progression of melt-fraction and stored energy in all cases is visualized in Figure 6.23a and Figure 6.23b, respectively. These figures provide an overview of the time-dependent behavior of the melt-fraction and stored energy for different configurations.

To further analyze the performance of the optimal design, enhancement ratios for melting and energy storage are employed, comparing them to a reference case. The melting enhancement ratio $E_{mr}$ and energy enhancement ratio $E_{er}$ are illustrated in Figure 6.24a and Figure 6.24b, respectively.

By examining Figure 6.23a, it can be observed that the optimal configuration significantly improves conduction, as the fins are uniformly distributed and cover a substantial portion of the phase change material (PCM). This improved conduction facilitates more efficient heat transfer within the system.

The implementation of an intelligent fin arrangement based on the exponential function has proven effective in enhancing convection heat transfer, resulting in improved melting performance. The optimized configuration demonstrates a higher melt-fraction compared to the reference case, indicating the superior heat transfer

characteristics achieved through the intelligent fin arrangement. The exponential function provides a tailored distribution of fins, maximizing the convective heat transfer surface area and facilitating efficient heat transfer from the surrounding environment to the PCM. This enhanced heat transfer contributes to a faster and more complete melting process, highlighting the potential of intelligent fin arrangements as a means to optimize thermal energy storage systems and increase their overall performance.

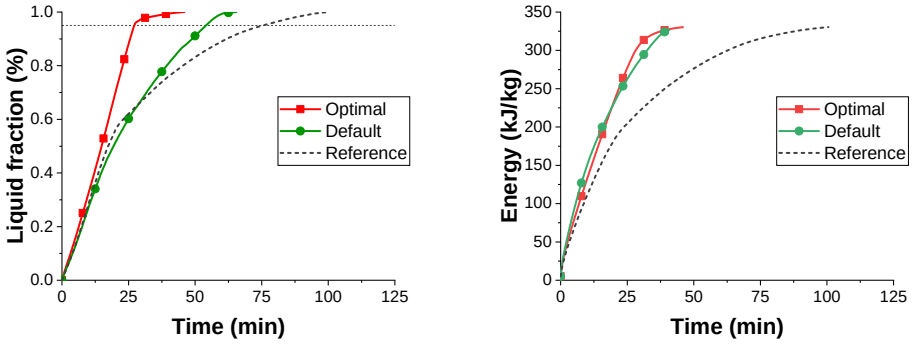


(a) (b)

FIGURE 6.23: Transient progress of (a) melting fraction and (b) energy storage.

The findings presented in Figure 6.23b support the notion that the optimal configuration, enabled by the intelligent fin arrangement, achieves the highest energy storage rate. This outcome is attributed to the improved heat transfer characteristics facilitated by the optimized fin configuration. The enhanced convective heat transfer from the surrounding environment to the PCM enables a more efficient and rapid energy storage process. As a result, the optimal configuration offers the advantage of a higher energy storage rate, making it a favorable choice for applications that require quick and effective thermal energy storage. These results highlight the significance of intelligent fin arrangements in enhancing energy storage performance and optimizing the overall efficiency of thermal energy storage systems.

The melting enhancement ratio $E_{mr}$ in Figure 6.24a and the energy enhancement ratio $E_{er}$ in Figure 6.24b further emphasize the improved performance of the

optimal design compared to the reference case. These enhancement ratios quantitatively highlight the superiority of the optimal configuration in terms of both melting and energy storage.

In summary, the transient progression of melt-fraction and stored energy, as well as the enhancement ratios, provide a comprehensive understanding of the performance of the optimal design. The optimized fin arrangement improves conduction and convection heat transfer, resulting in enhanced melting performance and energy storage rates. The overall performance of the optimal configuration surpasses that of the reference case, highlighting the effectiveness of the design improvements achieved through the Taguchi method and subsequent analysis.

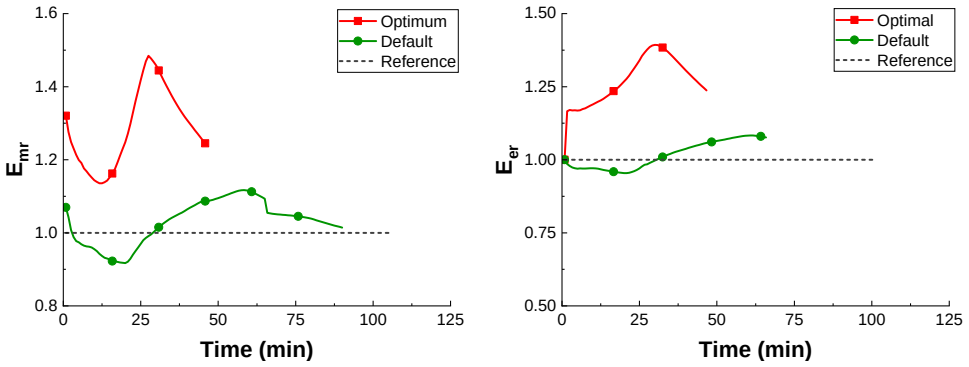


(a) (b)

FIGURE 6.24: (a) Melting and (b) Energy enhancement ratio comparison of optimal configuration.

## 6.6 Regression Analysis using Machine Learning Techniques

Recently Machine Learning (ML) based methods have gained wide adoption in a variety of fields, including flow dynamics, electronics, defense, medicine, banking, telecommunications, and transportation. Machine learning provides a multitude of methods for deriving knowledge from data that may be applied to the fluid dynamics at play. Melting time and thermal performance prediction through geometric optimization of PCM based LHTES systems. Additionally, ML systems

can automate operations linked to flow control and optimization and supplement domain expertise [161, 162].

Recently a successful implementation of the ML model for thermal performance prediction of PCM integrated roof building was implemented by Bhamare et al [163]. The five machine learning models employed in their work were Catboost, Gradient Boosting, Extreme Gradient Boosting, Random Forest Regression, and Extra Trees Regression. The results showed that, when compared to other machine learning models, gradient boosting regression had the best performance.

In recent studies machine learning has been used to study the melting and heat transfer process of PCM [164, 165]. In the last part of this study different machine learning and methods were applied to obtain improved regression model and results were compared to previously performed investigation using Taguchi method.

### 6.6.1 Machine Learning Linear Regression Method

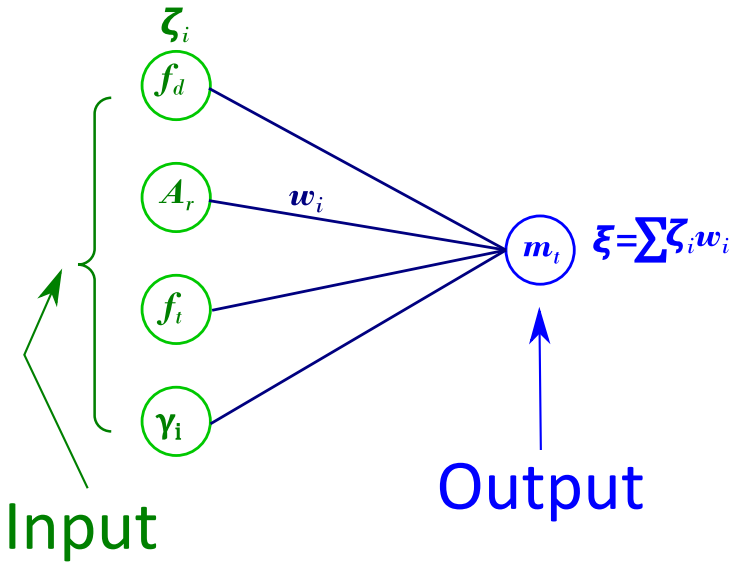


FIGURE 6.25: Basic machine learning model.

The simplest ML method was intended for regression in which the target value was expected to be a linear combination of the input parameters [166]. The model as illustrated in Figure 6.26, can be mathematically represented as shown in Equation (6.7). The ML algorithm fits a linear model as shown in Figure 6.26, by finding

coefficients $w = (\omega_1, \cdots, \omega_n)$ in such a way that the residual sum of squares between the target and prediction are minimized. The cost function $J$ that the ML technique minimizes can be represented as shown in Equation (6.8)

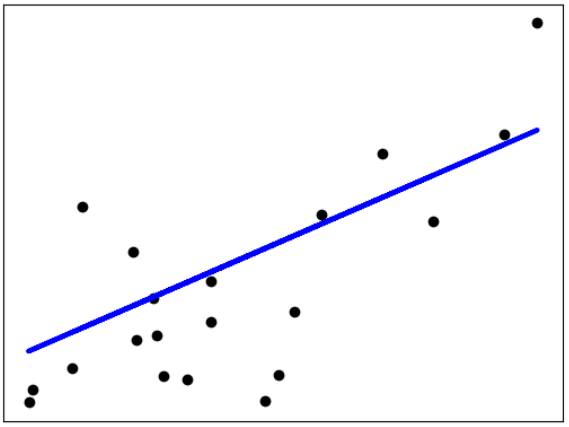

FIGURE 6.26: Linear regression.

$$\xi(\omega, x) = \omega_0 + \omega_1\zeta_1 + \cdots + \omega_n\zeta_n \tag{6.7}$$

$$J = ||\xi(\omega, \zeta) - \xi_t||^2 \tag{6.8}$$

Where $\xi(\omega, \zeta)$ is the expected value and $\xi_t$ is the target value of the output. The experimental data gathered from the Taguchi DoE was used in the implementation of ML linear regressions. Fin displacement $f_d$, fin thickness $f_t$, geometry aspect ratio $A_r$, and liquid fraction $\gamma$ were used as features and complete melting time of the PCM in LHTES was the desired output.

The training data set was obtained from all the simulation runs and each record in the set comprised of data recorded during each time step of the simulation. There were a total of 6788 records in the data set used in the training of machine learning model.

A selected subset of the data used in in ML linear regressions analysis is listed in Table 6.13. The table only shows record for $\gamma = 1.0$ liquid fraction. Complete data set contains all records of melting time ($m_t$) for intermediate liquid fraction ($\gamma$) values.

TABLE 6.13: Training data for ML linear regression.

| **Features** | | | | **Output** |
|---|---|---|---|---|
| $f_d$ | $A_r$ | $f_t$ | $\gamma$ | $m_t$ |
| 5 | 0.5 | 1.2 | 1.0 | 4725.00 |
| 5 | 1 | 1.25 | 1.0 | 5512.50 |
| 5 | 1.25 | 1.5 | 1.0 | 7143.75 |
| 5 | 1.5 | 2 | 1.0 | 8231.25 |
| ⋮ | ⋮ | ⋮ | ⋮ | ⋮ |
| 10 | 0.5 | 1.25 | 1.0 | 3156.25 |
| 10 | 1 | 1.2 | 1.0 | 4312.50 |
| 10 | 1.25 | 2 | 1.0 | 6506.25 |
| 10 | 1.5 | 1.5 | 1.0 | 7050.00 |
| ⋮ | ⋮ | ⋮ | ⋮ | ⋮ |
| 15 | 0.5 | 1.5 | 1.0 | 2968.75 |
| 15 | 1 | 2 | 1.0 | 5887.50 |
| 15 | 1.25 | 1.2 | 1.0 | 5062.50 |
| 15 | 1.5 | 1.25 | 1.0 | 5662.50 |
| ⋮ | ⋮ | ⋮ | ⋮ | ⋮ |
| 20 | 0.5 | 2 | 1.0 | 3281.25 |
| 20 | 1 | 1.5 | 1.0 | 4725.00 |
| 20 | 1.25 | 1.25 | 1.0 | 5037.50 |
| 20 | 1.5 | 1.2 | 1.0 | 5625.00 |

MATLAB R2019b was used to implement additional machine learning regression models [167, 168]. MATLAB has support for about 20 types of regression models that can be trained. These models are grouped into five different categories - Linear regression [169], Regression trees [170], Support vector machines [171], Ensembles of Trees [172], and Gaussian process regressions [173] as listed in Table 6.14.

### 6.6.2 ML Model Performance Analysis

After training the models in Regression learner, these were assessed based on the overall score of each model. The score estimated the performance of the trained

TABLE 6.14: MATLAB Regression learner models and training results.

| Category | Model | $R^2$ | RMSE | MSE | MAE |
|---|---|---|---|---|---|
| Linear Regression Models | Linear | 0.87 | 662.79 | 439290 | 529.23 |
| | Interactions Linear | 0.92 | 524.34 | 274940 | 427.03 |
| | Robust Linear | 0.87 | 667.72 | 445850 | 515.85 |
| | Stepwise Linear | 0.92 | 524.51 | 275110 | 426.95 |
| Regression Trees | Fine Tree | 1.00 | 42.78 | 1830.2 | 35.597 |
| | Medium Tree | 1.00 | 81.704 | 6675.5 | 66.181 |
| | Coarse Tree | 0.99 | 209.84 | 44032 | 162.94 |
| Support Vector Machines | Linear SVM | 0.86 | 681.55 | 464520 | 506.19 |
| | Quadratic SVM | 0.97 | 309.99 | 96091 | 240.65 |
| | Cubic SVM | 0.896 | 354.1 | 125390 | 279.18 |
| | Fine Gaussian SVM | 0.99 | 165.36 | 27345 | 152.92 |
| | Medium Gaussian SVM | 0.99 | 153.14 | 23452 | 130.48 |
| | Coarse Gaussian SVM | 0.97 | 310.36 | 96321 | 234.23 |
| | Optimizable SVM | | | | |
| Ensembles of Trees | Boosted Tree | 0.98 | 258.02 | 66573 | 201.1 |
| | Bagged Tree | 1.00 | 97.237 | 9454.9 | 62.968 |
| Gaussian Process Regressions | Rational Quadratic | 1.0 | 11.19 | 125.21 | 5.2733 |
| | Squared Exponential | 1.00 | 12.443 | 154.84 | 6.6285 |
| | Matern 5/2 | 1.00 | 9.8457 | 96.938 | 4.0343 |
| | Exponential | 1.00 | 3.4008 | 11.566 | 0.86883 |
| | Optimizable GPR | | | | |

model. The score used to choose the best model is Root Mean Square Error (RMSE) on the validation set. Additional statistics used for the comparison of the performance of models are listed in Table 6.15.

TABLE 6.15: Regression learner models statistics.

| Statistic | Description | Test |
|---|---|---|
| $RMSE$ | Root mean square error | Smaller is better. |
| $R^2$ | Coefficient of determination. $0 > R^2 > 1.0$ | Check values close to 1. |
| $MSE$ | Mean square error. $MSE = RMSE^2$ | Smaller is better. |
| $MEA$ | Mean absolute error. | Smaller is better. |

The values of these statistics for each model are also listed in Table 6.14. The best performing model from the performance comparison was found to be Exponential GPR.

Following the training of regression models, a comparison was conducted based on various model statistics to evaluate their performance. The results were visualized using response plots, where the actual responses were plotted against the

predicted responses. Additionally, the models were assessed using residual plots to gain insights into the distribution and patterns of the residuals. To determine

TABLE 6.16: Prediction results and errors for different ML models with $f_d$=20 and $\gamma = 1.0$

| $\mathbf{A_r}$<br>$\mathbf{f_t}$ | 0.5<br>1.25 | 1.25<br>2.0 | 1.25<br>1.25 | 0.5<br>1.5 | 0.5<br>1.2 | Avg Error |
|---|---|---|---|---|---|---|
| Numerical | **2756.25** | **5900** | **5037.5** | **2868.75** | **2787.5** | |
| Fine Tree | 3218.7 | 6443.7 | 5003.7 | 3218.7 | 3218.7 | |
| | (17%) | (9%) | (1%) | (12%) | (15%) | (10.8%) |
| Exponential GPR | 2901.9 | 5225.7 | 5005.3 | 2838.1 | 2929.0 | |
| | (5.%) | (11%) | (1%) | (1%) | (5%) | (4.6%) |
| Medium Gaussian SVM | 2581.2 | 5532.7 | 4666.5 | 2548.5 | 2614.9 | |
| | (6%) | (6%) | (7%) | (11%) | (6%) | (7.2%) |
| Interactions Linear | 1765.2 | 4611.9 | 3608.3 | 2042.8 | 1709.7 | |
| | (36%) | (22%) | (28%) | (29%) | (39%) | (30.8%) |

the best model among the trained regression models, model performance scores were calculated using the RMSE on the validation set. The RMSE provides an estimation of the performance of the trained models on new, unseen data. The model with the lowest RMSE score was selected as the best-performing model.

Table 6.14 presents the different machine learning models utilized for the regression analysis, along with their respective performance metrics. These metrics include the RMSE score, which serves as an indicator of the overall accuracy and predictive power of the models.

The evaluation process involved assessing the statistical measures of the models, examining the response plots to compare actual and predicted responses, and analyzing the residual plots to understand the quality of the models' predictions. In summary, the regression models were compared and evaluated based on model statistics, response plots, and residual plots. The performance of the models was quantified using the RMSE score, and the model with the lowest RMSE was identified as the best-performing model. The results and metrics for each model are summarized in Table 6.14, providing valuable insights into the performance and accuracy of the regression models.

The best performing model in each category was used to predict the melting time using additional data that was not part of the training set. The results are listed in Table 6.16 and the corresponding errors of the prediction and average error for all validation data are listed in Table 6.17. These results also indicate that exponential GPR is predicted quite close to the actual values.

TABLE 6.17: Prediction results obtained for different ML models.

| **Features** | | | | **Numerical** | **Prediction Error** | | | |
|---|---|---|---|---|---|---|---|---|
| $f_d$ | $A_r$ | $f_t$ | $\gamma$ | | F-Tree | Exp-GPR | Med-SVM | Int-Lin |
| 20 | 0.5 | 1.25 | 1 | **2756.25** | 17% | 5% | 6% | 36% |
| 20 | 1.25 | 2 | 1 | **5900** | 9% | 11% | 6% | 22% |
| 20 | 1.25 | 1.25 | 1 | **5037.5** | 1% | 1% | 7% | 28% |
| 20 | 0.5 | 1.5 | 1 | **2868.75** | 12% | 1% | 11% | 29% |
| 20 | 0.5 | 1.25 | 1 | **2787.5** | 15% | 5% | 6% | 39% |
| | | | | Average error | 11% | 5% | 7% | 31% |

### 6.6.3 ML Model Analysis using Performance Plots

The comparison of predicted, actual and residual plots manifest the model performance by making predictions for different response values. The predicted response of the models are plotted against the actual, true response. The actual response was the melting time obtained by the simulations that were carried out to collect all the data. 25% was not provided to the regression learner and it was used to predict melting times for this 25% data.

A perfect regression model has a predicted response equal to the true response, so all the points lie on a diagonal line. The vertical distance from the line to any point is the error of the prediction for that point. A good model has small errors, and so the predictions are scattered roughly symmetrically around the diagonal line.

The residuals plot displays the difference between the predicted and true responses. Usually a good model has residuals scattered roughly symmetrically around 0. Following types of patterns in the residuals plot indicate that the model can be improved with advanced tweaking of ML algorithm hyper parameters:

- Residuals are not symmetrically distributed around 0.
- Residuals change significantly in size from left to right in the plot.

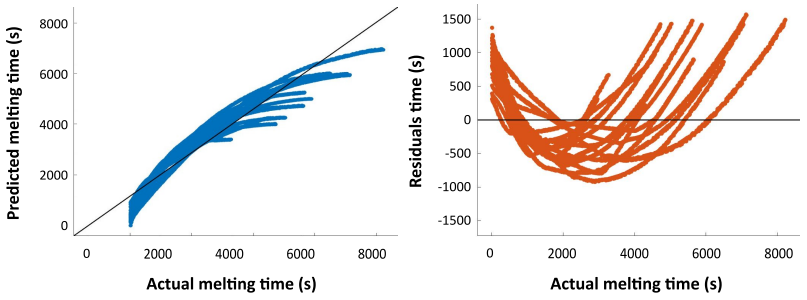


(a)

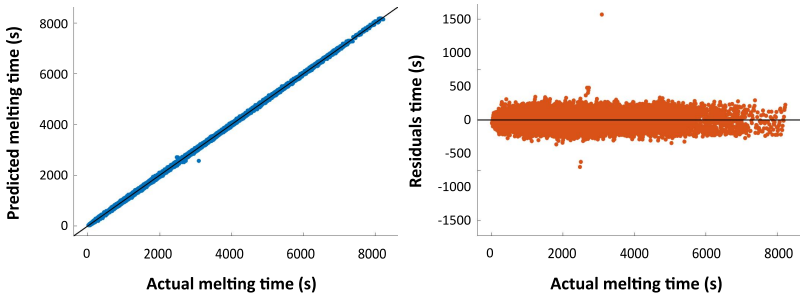


(b)

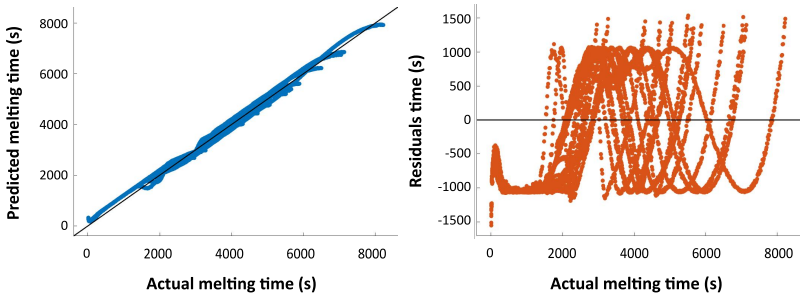


(c)

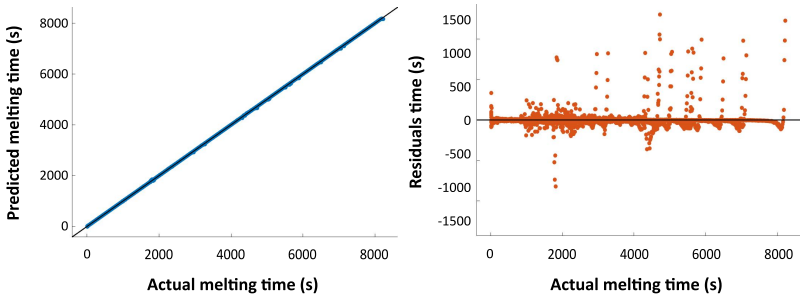


(d)

FIGURE 6.27: Performance plots showing residuals and predicted vs. actual values for (a) Interactions linear, (b) Fine tree, (c) Fine Guassian SVM, and (d) Exponential GPR machine learning regressions models.

- Outliers occur, that is, residuals that are much larger than the rest of the residuals.

- Clear, nonlinear pattern appears in the residuals.

Predicted vs. actual, and residual plots for the best performing model in each category are shown in Figure 6.27. It can be concluded from the figure that Exponential Gaussian Process Regression (GPR) is the best model. The plot of predicted values vs. experimental response for this model is almost linear. Similarly, the residuals plot is symmetrically scattered around the zero line. The average error for this model was 5% whereas the maximum error obtained in case of exponential GPR model was about 11%. The mathematical formulation of exponential GPR model is described in Appendix B.

### 6.6.4 ML Model Parameters

Table 6.18 lists parameters used for the training of the model.

TABLE 6.18: Parameters for machine learning regression analysis.

| **Parameters** | **Specification** |
|---|---|
| Network Model | Exponential Gaussian process regression |
| Data observations | 6788 |
| No. of Predictors | 4 |
| Predictors | $f_d, A_r, f_t, \gamma$ |
| Response variable | Melting time ($m_t$) |
| Validation | 5-folds Cross-validation |

Cross-validation protects against overfitting by partitioning data set into folds and estimating accuracy on each fold. Moreover, the training data set was also divided into two parts - training set and test set. 75% of the data set was used for training the ML model while remaining 25% was used for validation and tuning of the trained model. The performance statistics obtained for the Exponential GPR trained model are listed in Table 6.19:

TABLE 6.19: Exponential GPR performance statistics.

| **Statistic** | **Value** |
|---|---|
| $RMSE$ | 3.4008 |
| $R^2$ | 1.00 |
| $MSE$ | 11.566 |
| $MAE$ | 0.86883 |
| Prediction speed | 5100 obs/s |
| Training time | 323.74 sec |

### 6.6.5 Prediction of Melting Time using Trained Model

The selected model was employed to predict the melting time of various LHTES configurations. These predictions encompass a range of configurations, including some that were used during the model's training, as well as others that were not included in the training process. The comprehensive list of these predictions is presented in Table 6.20.

By leveraging the trained model, these predictions offer valuable insights into the expected melting times for different LHTES configurations. The model's ability to make accurate predictions for both trained and unseen configurations demonstrates its capability to generalize and extrapolate beyond the training data. This provides confidence in the model's potential for reliable melting time estimations for various LHTES designs. These predicted melting times serve as a valuable resource for engineers and researchers involved in LHTES system design and optimization. They facilitate informed decision-making, enabling the selection of configurations that meet specific performance requirements or achieve desired thermal energy storage goals. Furthermore, these predictions can expedite the design process by reducing the need for extensive experimental testing, saving time and resources.

Among the listed predictions in Table 6.20, the highlighted rows indicate design configurations that were not included in the training phase of the ML model. These configurations were new to the model, allowing for an assessment of its generalization capability.

TABLE 6.20: Prediction results using exponential GPR machine learning model for $\gamma = 0.90$.

| $\mathbf{f_d}$ | $\mathbf{A_r}$ | $\mathbf{f_t}$ | **Melting time** | | **Error** |
|---|---|---|---|---|---|
| | | | Numerical | ML Prediction | |
| 10 | 1.5 | 1.5 | 4725.00 | 4718.85 | 0.13% |
| 5 | 1 | 1.25 | 4012.50 | 4016.95 | 0.11% |
| 15 | 1.5 | 1.25 | 3587.50 | 3581.65 | 0.16% |
| 20 | 0.5 | 1.2 | 1550.50 | 1667.28 | 7.55% |
| 5 | 0.5 | 1.2 | 3687.50 | 3685.40 | 0.06% |
| 20 | 0.5 | 2 | 1962.50 | 1964.52 | 0.10% |
| 20 | 1 | 1.5 | 2925.00 | 2919.18 | 0.20% |
| 5 | 1.25 | 1.5 | 4893.75 | 4894.74 | 0.02% |
| 15 | 1.25 | 1.2 | 3156.25 | 3153.65 | 0.08% |
| 10 | 1.25 | 2 | 4350.00 | 4347.03 | 0.07% |
| 5 | 1.5 | 2 | 5787.50 | 5790.25 | 0.05% |
| 15 | 1 | 2 | 3850.00 | 3856.03 | 0.16% |
| 20 | 1.25 | 1.25 | 3081.25 | 3079.27 | 0.06% |
| 20 | 0.5 | 1.25 | 1556.25 | 1645.80 | 5.72% |
| 10 | 0.5 | 1.25 | 2487.50 | 2488.35 | 0.03% |
| 15 | 0.5 | 1.5 | 1775.00 | 1773.70 | 0.07% |
| 20 | 1.25 | 2 | 3793.75 | 4067.00 | 7.20% |
| 10 | 1 | 1.2 | 2831.25 | 2829.99 | 0.04% |
| 20 | 1.5 | 1.2 | 3425.00 | 3425.02 | 0.00% |
| 20 | 0.5 | 1.5 | 1593.75 | 1621.38 | 1.73% |

An analysis of the predicted complete melting times compared to the corresponding numerical results reveals promising accuracy. The average error in the prediction of the melting time is reported to be 1.16%, indicating a close agreement between the model's predictions and the numerical data. Additionally, the maximum error observed is less than 10%, further affirming the model's reliability in estimating melting times for unseen design configurations.

These results suggest that the ML model has effectively learned the underlying patterns and relationships within the training data, allowing it to make accurate predictions for new LHTES configurations. The low average and maximum errors reflect the model's ability to generalize and provide reliable estimations of the complete melting time.

The performance of the ML model in accurately predicting melting times offers

significant advantages, including time and cost savings, as it reduces the reliance on extensive numerical simulations or experimental testing. Engineers and researchers can utilize the model as a valuable tool for efficient and reliable estimation of melting times for a wide range of LHTES designs, even those that were not part of the training dataset. The model trained in the current study used temporal data

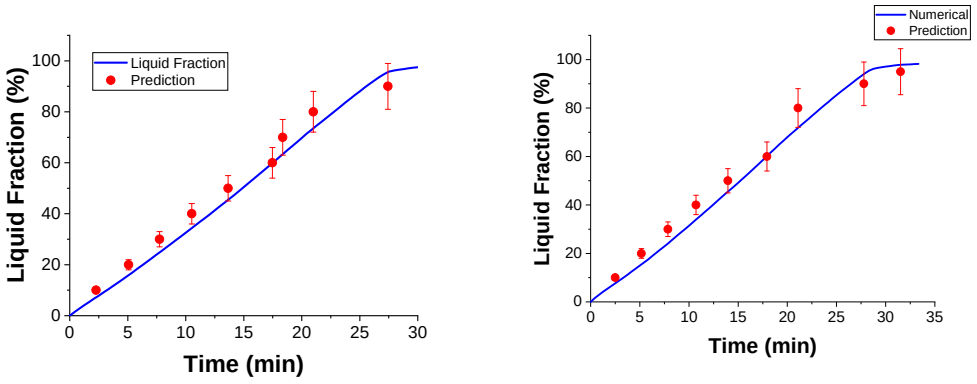


(a) (b)

FIGURE 6.28: Predicted and numerical results for configurations (a) $[f_d = 20, A_r = 0.5, f_t = 1.25]$ and (b) $[f_d = 20, A_r = 0.5, f_t = 1.2]$.

from the start of the melting ($\gamma = 0$) until the complete melting ($\gamma = 1.0$). The performance of the model for liquid fraction prediction other than the complete melting is shown in Figure 6.28. From the table and figures, it can be concluded that machine learning models can be used for predicting thermal performance of latent heat thermal energy storage device to an acceptable accuracy.

## 6.7 Conclusion

In this chapter LHTES design parameters were optimized initially performing Taguchi analysis for melting time and energy storage of LHTES. The $L_{16}$ DoE matrix was generated by Taguchi method and simulations were conducted for each combination in the DoE table row.

Optimal parameters were identified by generating main effects plot for S/N ratios and means. The optimal configuration with $A_r = 0.5$, $f_d = 20\,mm$, and

$f_t = 1.2\,mm$ parameter values was determined. The PCM total melting time of $28.3\,min$ and an average energy rate of $120\,W$ was found for this design.

The results provide specific information on the design parameters that resulted in the optimal performance of the LHTES device. The identified optimal configuration with specific parameter values can be used as a basis for the design and production of LHTES devices for various applications. This information is critical for engineers and manufacturers who aim to develop LHTES devices with optimal performance, as it provides a specific set of parameters to target and optimize. In the case of reference configuration with 6 fins on heated walls, the PCM melted completely in $100.83\,min$ with a charging rate of $54.6\,W$. Hence, it can be said that the optimal configuration of the LHTES system has a fast charging rate of PCM based thermal energy storage bank. The fast charging rate and reduced full charging time make it an efficient device.

Based on these results a linear regression model is obtained. The average error of the linear regression model of the Taguchi method was about 13%. To improve the model that could predict better results, machine learning and artificial intelligence techniques were used. Various regression models were analyses and their performance was compared with the experimental results. The best machine learning regression model obtained was Exponential Gaussian Process Regression. This model resulted in average error of 5%.

The importance of using optimization techniques such as the Taguchi method and machine learning methods for the design and optimization of LHTES devices, is that they can provide specific parameter values that result in optimal performance and can help to improve the efficiency and effectiveness of energy storage systems.

The optimization process and parameters used for the method have been thoroughly explained. Moreover, the results are validated by comparing with the simulated results. This ensures that the results are reliable.

# Chapter 7

# Conclusion and Future Work

In this study different parameters for the design of a rectangular Phase Change Material (PCM) based thermal energy storage device were investigated to obtain parameters values that would optimize the thermal performance of the energy storage device. Initially a reference experimental setup was prepared and multiple experiments of PCM melting were conducted. Stearic acid was used as PCM and differential scanning calorimetry was used to obtain solidus temperature, liquidus temperature, and enthalpy of fusion. Side walls were isothermal that supplied $353K$ uniform temperature to transfer heat into PCM and connected fins. During these experiments, temperature, liquid fraction, and melt fraction interface were recorded as PCM underwent phase transition from solid to liquid. The parametric variation in the design of Latent Heat Thermal Energy Storage (LHTES) device was studied numerically using a CFD software. First of all a numerical 2D design was developed that replicated the experimental setup. The CFD software settings were configured such that the results of the numerical simulations matched with the experimental results. After validation of numerical models following design parameters were studied:

- Container geometry aspect ratio
- Fin length
- Fin thickness

- Fin shape
- Fin angles
- Fin displacement
- Fin distribution

The metrics used for performance analysis in these experiments were melting time, time saving, enhancement ratio of melting rate and energy storage rate, and the rate of heat transfer into the PCM. All these metrics were compared with the reference cases to identify the behavior of different design parameters on the performance of LHTES.

Initially, various design parameters of fins, including angles (A), shapes (S), and lengths (L), were investigated while maintaining a constant volume of PCM. The base case consisted of six horizontal fins, three on each of the heated walls. Configuration-A, which involved variations in fin angles, resulted in a significant increase in the melting time of PCM by 16% and a reduction in the average energy storage rate by 14.2%.The hybrid fin configuration-S, which combined straight and angled fins, demonstrated noticeable improvements in the thermal performance of the LHTES device. The melting rate increased by 18%, and the average energy storage rate improved by 19.8%. Configuration-L, which involved combinations of straight fins with different lengths and thicknesses while maintaining a constant PCM volume, proved to be the most effective. The optimum case of configuration-L exhibited a 39.5% enhancement in the melting performance of the gls*lhtes and a 65.07% increase in the average energy storage rate.

Later fin length and intelligent length distribution for top and bottom halves were selected after first set of simulation experiments. In the second phase of numerical studies fin lengths were calculated using different length distribution functions $x = g(y)$. Moreover, the impact of fin thickness and container geometry aspect ratio were also analyzed in this phase. The design variables selected for optimization purpose at the end the numerical studies were fin displacement ($f_d$), fin thickness ($f_t$), and geometry aspect ratio ($A_r$).

The lengths of the fins were arranged using linear, quadratic, cubic, and exponential distribution functions, with decreasing slopes along the heated walls. Subsequently, the impact of geometry aspect ratios of the enclosure on the performance of the LHTES (Latent Heat Thermal Energy Storage) system was investigated. Simulations were conducted using the enthalpy-porosity model, and the numerical results were validated against experimental data. Compared to the reference case, the linear and quadratic fin configurations demonstrated improvements in the melting times of the PCM by 31.7% and 24.3% respectively. Moreover, these configurations also exhibited enhanced average energy storage rates, with improvements of 46% and 31.4% respectively when compared to the reference case.

In the last phase of the study Taguchi method was used to develop design of experiments matrix employing three design variables as factors with four levels for each factors. The optimal parameters were then used to develop a regression correlation. The regression was further improved by machine learning regression models. Gaussian process regression (GPR) model was selected with best results and average error of 5%.

Statistical and machine learning methods are used to identify the optimal configuration. In order to find optimal parameters that improve the thermal performance of the energy storage device, the design parameters for a thermal energy storage device were examined numerically. The design variables selected at the end of the studies were used to evaluate optimal values using Taguchi Method and later improved the prediction model by applying machine learning techniques. Exponential Gaussian Process Regression is found to predict the performance of LHTES device designed based on the base configuration and defined parameters.

The key points drawn from this study are described below.

1. It was found that some fin configurations could also negatively impact the melting performance of PCM. This was observed in case of orientation of fins in configurations A1, A2, A3. The performance of these configurations was worse than the reference case.

2. Experimental measurements including the photographs of solid-liquid interface and temperatures can be employed to verify numerical approaches for PCM melting. The experimental results were helpful in establishing the validity of numerical simulations as the simulations results matched reasonably with the experimental results.

3. It was observed that during the melting process of the design with function based fin length distributions, the case where fin lengths were calculated using cubic function was found to be worst. The exponential function based fin length distribution was the best performing case. The cubic configuration represented the case where the top and bottom fins created an inflection point in the middle of the chamber. It was observed that in this case heat was trapped and both convection and conduction were slow, resulting in longer melting time

4. The impact of aspect geometry aspect ratio was inversely proportional to the total melting time of PCM in LHTES device. The lower ratio decreased the distance between the heated walls and resulted in improving the overall performance of the PCM melting time.

5. With a given container geometry aspect ratio, and exponential based fin length distribution, the effect of fin thickness was also found to be inversely proportional to the thermal performance of the thermal energy storage device. The PCM volume was constant throughout the research. The larger thickness required shorter length for fins to keep the PCM volume fixed. The longer fins improve performance of the LHTES device.

Following objectives have been achieved in the research. Design parameter for LHTES system were identified. Mathematical functions based fin length profiles utilized that helped investigate the impact of these variations on the thermal performance of energy storage unit. throughout the course of the study dual walled heated rectangular LHTES system with fins was studied. Optimization the primary design parameters of LHTES system and a machine learning model for the melting performance prediction of different LHTES design units was developed.

## 7.1 Research Contributions

The core contributions of this dissertation are as follows:

- The influence of different designs of the fins on the performance enhancement of a double-wall-heated rectangular latent heat thermal energy storage unit is studied numerically. The study included variation in fin angles, shapes, and lengths while maintaining constant PCM volume.

- A novel fin distribution tool based on mathematical functions (linear, quadratic, cubic, and exponential) is developed while keeping the volume of PCM and total fin area constant. The melting and energy storage performance enhancements of each of the fin distribution configuration is investigated in detail and optimal function is identified.

- The LHTES system is optimized by considering aspect ratio of the container, location of fins along the wall, and optimal mathematical fin distribution function. Taguchi optimization method is used with four level variation of each of the design parameter, forming an $L_{16}$ orthogonal array. A regression model is also developed by employing machine learning methods to predict the transient behavior of melting progression of PCM for a different design configuration based on parameters considered in this study.

## 7.2 Future Recommendations

The design of LHTES is a complex problem as many variables influence the performance of thermal energy storage in PCM. In the current study, some of the most important design parameters were studied in detail and a design of LHTES based on significant improvements in melting and energy storage performance was proposed. However, in the future, the performance of the LHTES may further be improved by exploring the following design prospects.

1. The performance of LHTES is highly dependent on fins designs. Therefore, different fin shapes such as perforated or textured fins, fins enhanced with dimples, triangular fins, convex fins, concave fins, and branched fins may be investigated.

2. The orientation and size of the heated surface affect the natural convection in the PCM and thus alter the thermal behavior of the PCM. Therefore, different orientations and shapes of the enclosure can also be studied.

3. The deep learning techniques could provide quick estimations of the melting time, energy storage performance, and the limitations of a particular design of LHTES.

# Bibliography


[1] International Energy Agency, Paris, "World energy statistics 2017." Available at: https://www.iea.org/reports/world-energy-outlook-2017, 2017. (Accessed: 2022-05-02, License: CC BY 4.0).

[2] N. Zhang, Y. Yuan, X. Cao, Y. Du, Z. Zhang, and Y. Gui, "Latent heat thermal energy storage systems with solid–liquid phase change materials: a review," *Advanced Engineering Materials*, vol. 20, no. 6, p. 1700753, 2018.

[3] S. Kan, B. Chen, and G. Chen, "Worldwide energy use across global supply chains: Decoupled from economic growth?," *Applied Energy*, vol. 250, no. April, pp. 1235–1245, 2019.

[4] M. Höök and X. Tang, "Depletion of fossil fuels and anthropogenic climate change-A review," *Energy Policy*, vol. 52, pp. 797–809, 2013.

[5] Á. Campos-Celador, G. Diarce, J. T. Zubiaga, T. V. Bandos, A. M. García-Romero, L. M. López, and J. M. Sala, "Design of a finned plate latent heat thermal energy storage system for domestic applications," *Energy Procedia*, vol. 48, pp. 300–308, 2014.

[6] IEA (2022), "Buildings: A source of enormous untapped efficiency potential." Available at: https://www.iea.org/reports/buildings. (Accessed: 6 Oct 2022; License: CC BY 4.0).

[7] A. Sharma, V. V. Tyagi, C. Chen, and D. Buddhi, "Review on thermal energy storage with phase change materials and applications," *Renewable and Sustainable energy reviews*, vol. 13, no. 2, pp. 318–345, 2009.

[8] M. V. Shoubi and M. V. Shoubi, "Solar wall system, the Sun-centered approach toward ecosystem," *Journal of Green Building*, vol. 8, no. 4, pp. 39–54, 2013.

[9] Sanford S. Smith, "Renewable and nonrenewable resources." Available at: https://extension.psu.edu/renewable-and-nonrenewable-resources, June 2006. (Accessed: 6 Aug 2022).

[10] K. Start, "Renewable and Non Renewable Energy Sources Explained." Available at: https://www.kqed.org/science/renewable-and-non-renewable-energy-resources-explained, September 2019. (Accessed: 11 Mar 2022).

[11] United Nations, Climate Action, "What is renewable energy?." Available at: https://www.un.org/en/climatechange/what-is-renewable-energy. (Accessed: 6 Oct 2022).

[12] H. Ritchie, M. Roser, and P. Rosado, "Energy, our world in data," *Our World in Data*, 2022. (Accessed: 19 Fev 2023).

[13] BP, "BP Statistical Review of World Energy, 2022," tech. rep., 2022. (Accessed: 4 Oct 2022).

[14] Tyson Brown, National Geographic Society, "Nonrenewable resources." Available at: https://education.nationalgeographic.org/resource/nonrenewable-resources. (Accessed: 6 Oct 2022).

[15] A. Meghwar, Latif-Ul-Haq, and N. Irshad, "Techno Economic Evaluation of Off-grid Hybrid Solar-Wind Power System for Village Malo Bheel, Tharparkar Sindh Pakistan," *American Journal of Energy Research, Vol. 5, 2017, Pages 28-34*, vol. 5, no. 2, pp. 28–34, 2017.

[16] G. Kuo, "When Fossil Fuels Run Out, What Then?." Available at: https://mahb.stanford.edu/library-item/fossil-fuels-run/, May 2019. (Accessed: 6 Aug 2022).

[17] S. Shafiee and E. Topal, "When will fossil fuel reserves be diminished?," *Energy Policy*, vol. 37, no. 1, pp. 181–189, 2009.

[18] Tyson Brown, National Geographic Society, "Renewable resources." Available at: https://education.nationalgeographic.org/resource/renewable-resources. (Accessed: 6 Oct 2022).

[19] The Welding Institute (TWI), "What is renewable energy? definition, types, benefits and challenges." Available at: https://www.twi-global.com/technical-knowledge/faqs/renewable-energy. (Accessed: 5 Sep 2022).

[20] K. Rutledge, M. McDaniel, S. Teng, H. Hall, T. Ramroop, E. Sprout, J. Hunt, D. Boudreau, and H. Costa, "Tidal energy." Available at: https://education.nationalgeographic.org/resource/tidal-energy. (Accessed: 6 Oct 2022).

[21] EDF Energy, "Types of renewable energy." Available at: https://www.edfenergy.com/for-home/energywise/renewable-energy-sources. (Accessed: 6 Oct 2022).

[22] A. F. O. Falcão, "Wave energy utilization: A review of the technologies," *Renewable and Sustainable Energy Reviews*, vol. 14, no. 3, pp. 899–918, 2010.

[23] D. Madan, P. Rathnakumar, S. Marichamy, P. Ganesan, K. Vinothbabu, and B. Stalin, "A technological assessment of the ocean wave energy converters," in *Advances in Industrial Automation and Smart Manufacturing* (A. Arockiarajan, M. Duraiselvam, and R. Raju, eds.), (Singapore), pp. 1057–1072, Springer Singapore, 2021.

[24] "Solar Energy Technologies Office", "Solar radiation basics." Available at: https://www.energy.gov/eere/solar/solar-radiation-basics. (Accessed: 6 Oct 2022).

[25] United States Environmental Protection Agency, "Overview of greenhouse gases." Available at: https://www.epa.gov/ghgemissions/overview-greenhouse-gases. (Accessed: 6 Oct 2022).

[26] Melissa Denchak, "Greenhouse Effect 101." Available at: https://www.nrdc.org/stories/greenhouse-effect-101, July 2019. (Accessed: 12 Sep 2022).

[27] P. Moriarty and D. Honnery, "What is the global potential for renewable energy?," *Renewable and Sustainable Energy Reviews*, vol. 16, no. 1, pp. 244–252, 2012.

[28] A. Shahsavari and M. Akbari, "Potential of solar energy in developing countries for reducing energy-related emissions," *Renewable and Sustainable Energy Reviews*, vol. 90, no. June 2017, pp. 275–291, 2018.

[29] I. Hamilton and O. Rapf, "Executive summary of the 2020 global status report for buildings and construction," *Global Alliance for Buildings and Construction*, pp. 1–7, 2020.

[30] M. A. Umbark, S. K. Alghoul, and E. I. Dekam, "Energy Consumption in Residential Buildings: Comparison between Three Different Building Styles," *Sustainable Development Research (ISSN 2690-9898 e-ISSN 2690-9901)*, vol. 2, no. 1, p. p1, 2020.

[31] R. Perez and M. Perez, "A Fundamental Look At Energy Reserves For The Planet," *The International Energy Agency SHC programme Solar Update*, vol. 50, no. April, pp. 4–6, 2009.

[32] Perez, "Energy Reserves from page 4," *Int. Energy Agency SHC Program. Sol. Updat*, vol. 62, no. Nov 2015, 2015.

[33] E. Kabir, P. Kumar, S. Kumar, A. A. Adelodun, and K. H. Kim, "Solar energy: Potential and future prospects," *Renewable and Sustainable Energy Reviews*, vol. 82, no. September 2016, pp. 894–900, 2018.

[34] N. Kannan and D. Vakeesan, "Solar energy for future world: - A review," *Renewable and Sustainable Energy Reviews*, vol. 62, pp. 1092–1105, 2016.

[35] Time and Date, "Day and night world map." Available at: https://www.timeanddate.com/worldclock/sunearth.html/. (Accessed: 6 Sep 2022).

[36] A. Crespo, C. Barreneche, M. Ibarra, and W. Platzer, "Latent thermal energy storage for solar process heat applications at medium- high temperatures – A review," *Solar Energy*, no. October 2017, pp. 1–32, 2018.

[37] L. Fan and J. M. Khodadadi, "Thermal conductivity enhancement of phase change materials for thermal energy storage: a review," *Renewable and sustainable energy reviews*, vol. 15, no. 1, pp. 24–46, 2011.

[38] F. K. Malik, M. M. Khan, H. F. Ahmed, M. Irfan, and I. U. Ahad, "Performance characteristics of PCM based thermal energy storage system for fluctuating waste heat sources," *Case Studies in Thermal Engineering*, vol. 34, no. April, p. 102012, 2022.

[39] E. Paroutoglou, A. Afshari, N. Bergsøe, P. Fojan, and G. Hultmark, "A pcm based cooling system for office buildings: a state of the art review," in *CLIMA 2019 Congress*, vol. 111 of *E3S Web of Conferences*, (France), pp. 1–8, EDP Sciences, Aug. 2019.

[40] H. Faraji, A. Benkaddour, K. Oudaoui, M. El Alami, and M. Faraji, "Emerging applications of phase change materials: A concise review of recent advances," *Heat Transfer*, vol. 50, no. 2, pp. 1443–1493, 2021.

[41] L. B. Kong, T. Li, H. H. Hng, F. Boey, T. Zhang, and S. Li, *Waste energy harvesting*. Springer, 2014.

[42] M. Costa, D. Buddhi, and A. Oliva, "Numerical simulation of a latent heat thermal energy storage system with enhanced heat conduction," *Energy Conversion and Management*, vol. 39, no. 3-4, pp. 319–330, 1998.

[43] M. M. A. Khan, N. I. Ibrahim, I. M. Mahbubul, H. Muhammad. Ali, R. Saidur, and F. A. Al-Sulaiman, "Evaluation of solar collector designs

with integrated latent heat thermal energy storage: A review," *Solar Energy*, vol. 166, no. March, pp. 334–350, 2018.

[44] R. Karami and B. Kamkari, "Experimental investigation of the effect of perforated fins on thermal performance enhancement of vertical shell and tube latent heat energy storage systems," *Energy Conversion and Management*, vol. 210, no. March, p. 112679, 2020.

[45] G. Chen, Y. Su, D. Jiang, L. Pan, and S. Li, "An experimental and numerical investigation on a paraffin wax/graphene oxide/carbon nanotubes composite material for solar thermal storage applications," *Applied Energy*, vol. 264, no. March, p. 114786, 2020.

[46] Á. Campos-Celador, G. Diarce, P. Larrinaga, and A. M. García-Romero, "A simple method for the design of thermal energy storage systems," *Energy Storage*, no. December 2019, pp. 1–11, 2020.

[47] X. Huang and S. Yao, "Solidification performance of new trapezoidal longitudinal fins in latent heat thermal energy storage," *Case Studies in Thermal Engineering*, vol. 26, no. June, p. 101110, 2021.

[48] L. Kalapala and J. K. Devanuri, "Influence of operational and design parameters on the performance of a PCM based heat exchanger for thermal energy storage – A review," *Journal of Energy Storage*, vol. 20, no. July, pp. 497–519, 2018.

[49] L. A. Khan and M. M. Khan, "Influence of Angular Orientation of Fins on Thermal Charging and Discharging Performance of Latent Heat Storage Unit," *High Temperature*, vol. 60, no. 2, pp. 238–251, 2022.

[50] B. J. Jones, D. Sun, S. Krishnan, and S. V. Garimella, "Experimental and numerical study of melting in a cylinder," *International Journal of Heat and Mass Transfer*, vol. 49, no. 15-16, pp. 2724–2738, 2006.

[51] S. P. Prashanth, D. Dandotiya, and A. M. Surendra Kumar, "State of the Art of Phase Change Material (PCM) for the Purpose of Heat Storage and

Transfer in Cylindrical and Rectangular/Square Shells/Tubes - A Review," *IOP Conference Series: Materials Science and Engineering*, vol. 1013, no. 1, 2021.

[52] P. Gadhave, F. Pathan, S. Kore, and C. Prabhune, "Comprehensive review of phase change material based latent heat thermal energy storage system," *International Journal of Ambient Energy*, 2021.

[53] M. M. Umair, Y. Zhang, K. Iqbal, S. Zhang, and B. Tang, "Novel strategies and supporting materials applied to shape-stabilize organic phase change materials for thermal energy storage–A review," *Applied Energy*, vol. 235, no. October 2018, pp. 846–873, 2019.

[54] B. Zalba, J. M. Marín, L. F. Cabeza, and H. Mehling, "Review on thermal energy storage with phase change: Materials, heat transfer analysis and applications," *Applied Thermal Engineering*, vol. 23, no. 3, pp. 251–283, 2003.

[55] A. Abhat, "Low temperature latent heat thermal energy storage: heat storage materials," *Solar energy*, vol. 30, no. 4, pp. 313–332, 1983.

[56] M. M. Kenisarin, "Thermophysical properties of some organic phase change materials for latent heat storage. A review," *Solar Energy*, vol. 107, pp. 553–575, 2014.

[57] L. Cabeza, I. Martorell, L. Miró, A. Fernández, and C. Barreneche, "Introduction to thermal energy storage (tes) systems," in *Advances in thermal energy storage systems*, pp. 1–28, Elsevier, 2015.

[58] J. Pereira da Cunha and P. Eames, "Thermal energy storage for low and medium temperature applications using phase change materials - A review," *Applied Energy*, vol. 177, pp. 227–238, 2016.

[59] D. W. Hawes, D. Banu, and D. Feldman, "Latent heat storage in concrete. II," *Solar Energy Materials*, vol. 21, no. 1, pp. 61–80, 1990.

[60] A. M. Abdulateef, S. Mat, J. Abdulateef, and K. Sopian, "Geometric and design parameters of fi ns employed for enhancing thermal energy storage systems : a review," *Renewable and Sustainable Energy Reviews*, vol. 82, no. June 2016, pp. 1620–1635, 2018.

[61] M. K. Rathod and J. Banerjee, "Thermal performance enhancement of shell and tube latent heat storage unit using longitudinal fins," *Applied thermal engineering*, vol. 75, pp. 1084–1092, 2015.

[62] J. M. Khodadadi and S. F. Hosseinizadeh, "Nanoparticle-enhanced phase change materials (NEPCM) with great potential for improved thermal energy storage," *International Communications in Heat and Mass Transfer*, vol. 34, no. 5, pp. 534–543, 2007.

[63] I. Sarbu and A. Dorca, "Review on heat transfer analysis in thermal energy storage using latent heat storage systems and phase change materials," *International Journal of Energy Research*, vol. 43, no. 1, pp. 29–64, 2019.

[64] A. M. Abdulateef, J. Abdulateef, S. Mat, K. Sopian, B. Elhub, and M. A. Mussa, "Experimental and numerical study of solidifying phase-change material in a triplex-tube heat exchanger with longitudinal/triangular fins," *International Communications in Heat and Mass Transfer*, vol. 90, pp. 73–84, 2018.

[65] Q. Huang, X. Li, G. Zhang, J. Zhang, F. He, and Y. Li, "Experimental investigation of the thermal performance of heat pipe assisted phase change material for battery thermal management system," *Applied Thermal Engineering*, vol. 141, pp. 1092–1100, 2018.

[66] J. M. Maldonado, A. de Gracia, and L. F. Cabeza, "Systematic review on the use of heat pipes in latent heat thermal energy storage tanks," *Journal of Energy Storage*, vol. 32, no. April, p. 101733, 2020.

[67] H. F. Öztop, Ö. Akbal, F. Selimefendigil, and N. H. Abu-Hamdeh, "Analysis of the Melting Time of Phase Change Material in a Heat Exchanger with Sinusoidal Inner Duct," *Symmetry*, vol. 15, no. 1, 2023.

[68] A. M. Abed, H. I. Mohammed, I. Patra, J. M. Mahdi, A. Arshad, R. Sivaraman, R. K. Ibrahem, F. A. Al-Qrimli, S. Dhahbi, and P. Talebizadehsardari, "Improving the melting performance in a triple-pipe latent heat storage system using hemispherical and quarter-spherical fins with a staggered arrangement," *Frontiers in Chemistry*, vol. 10, no. October, 2022.

[69] Y. Tian, C. Zhao, and A. Lapkin, "Exergy Optimisation for Cascaded Thermal Storage," in *Innostock 2012 The 12th International Conference on Energy Storage*, 2012.

[70] Y. Cao, N. Farouk, H. Ayed, A. A. Aly, F. Jarad, M. Dahari, M. Waehayee, and B. Saleh, "Heat transfer improvement between a pair of heater and cooler inside an energy storage by using nano-encapsulated phase change material/water: A numerical modeling," *Case Studies in Thermal Engineering*, vol. 30, no. January, p. 101770, 2022.

[71] H. Nazir, M. Batool, F. J. Bolivar Osorio, M. Isaza-Ruiz, X. Xu, K. Vignarooban, P. Phelan, Inamuddin, and A. M. Kannan, "Recent developments in phase change materials for energy storage applications: A review," *International Journal of Heat and Mass Transfer*, vol. 129, pp. 491–523, 2019.

[72] M. Aramesh and B. Shabani, "Metal foam-phase change material composites for thermal energy storage: A review of performance parameters," *Renewable and Sustainable Energy Reviews*, no. April, p. 111919, 2021.

[73] X. Xiao, P. Zhang, and M. Li, "Preparation and thermal characterization of paraffin/metal foam composite phase change material," *Applied Energy*, vol. 112, pp. 1357–1366, 2013.

[74] V. Joshi and M. K. Rathod, "Experimental and numerical assessments of thermal transport in fins and metal foam infused latent heat thermal energy storage systems: A comparative evaluation," *Applied Thermal Engineering*, vol. 178, no. March, p. 115518, 2020.

[75] Z. Ding, W. Wu, and M. Leung, "Advanced/hybrid thermal energy storage technology: material, cycle, system and perspective," *Renewable and Sustainable Energy Reviews*, vol. 145, no. March, p. 111088, 2021.

[76] M. M. Heyhat, S. Mousavi, and M. Siavashi, "Battery thermal management with thermal energy storage composites of PCM, metal foam, fin and nanoparticle," *Journal of Energy Storage*, vol. 28, no. December 2019, p. 101235, 2020.

[77] A. De Gracia and L. F. Cabeza, "Phase change materials and thermal energy storage for buildings," *Energy and Buildings*, vol. 103, pp. 414–419, 2015.

[78] S. Ručevskis, P. Akishin, and A. Korjakins, "Parametric analysis and design optimisation of PCM thermal energy storage system for space cooling of buildings," *Energy and Buildings*, vol. 224, 2020.

[79] A. A. Ghoneim, S. A. Klein, and J. A. Duffie, "Analysis of collector-storage building walls using phase-change materials," *Solar Energy*, vol. 47, no. 3, pp. 237–242, 1991.

[80] L. E. Bourdeau, "Study of two passive solar systems containing phase change materials for thermal storage," 1980.

[81] L. Xu, J. I. Torrens, F. Guo, X. Yang, and J. L. Hensen, "Application of large underground seasonal thermal energy storage in district heating system: A model-based energy performance assessment of a pilot system in Chifeng, China," *Applied Thermal Engineering*, vol. 137, no. November 2017, pp. 319–328, 2018.

[82] R. Stropnik, R. Koželj, E. Zavrl, and U. Stritih, "Improved thermal energy storage for nearly zero energy buildings with PCM integration," *Solar Energy*, vol. 190, no. August, pp. 420–426, 2019.

[83] Frank Bruno, "Using Phase Change Materials PCMs for Space Heating and Cooling in Buildings," in *Proceedings of the AIRAH performance enhanced*

*buildings environmentally sustainable design conference*, no. March, pp. 26–31, 2005.

[84] A. Ecevit, A. Al-Shariah, and E. Apaydin, "Triangular built-in-storage solar water heater," *Solar Energy*, vol. 42, no. 3, pp. 253–265, 1989.

[85] S. F. Ahmed, M. Khalid, W. Rashmi, A. Chan, and K. Shahbaz, "Recent progress in solar thermal energy storage using nanomaterials," *Renewable and Sustainable Energy Reviews*, vol. 67, pp. 450–460, 2017.

[86] J. Prakash, H. P. Garg, and G. Datta, "A solar water heater with a built-in latent heat storage," *Energy Conversion and Management*, vol. 25, no. 1, pp. 51–56, 1985.

[87] M. T. Chaichan, A. H. Al-Hamdani, and A. M. Kasem, "Enhancing a Trombe wall charging and discharg- ing processes by adding nano-Al 2 O 3 to phase change materials," *International Journal of Scientific and Engineering Research*, vol. 7, no. 3, pp. 736–741, 2016.

[88] B. Huang and M. Toksoy, "Design and analysis of greenhouse solar systems in agricultural production," *Energy in Agriculture*, vol. 2, pp. 115–136, 1983.

[89] K. Hung, C. Abrams Jr, L. Coasts, and C. Bowers Jr, "Development of greenhouse bulk drying systems for solar energy utilization and planted mechanization. ahare paper no. 75-1018," *Am. Soc. Agric. Eng., St. Joseph, MI*, 1975.

[90] M. Kern and R. A. Aldrich, "Phase change energy storage in a greenhouse solar heating system," *Paper-American Society of Agricultural Engineers (USA)*, 1979.

[91] U. K. Sasidharan and R. Bandaru, "Thermal management of photovoltaic panel with nano-enhanced phase change material at different inclinations," *Environmental Science and Pollution Research*, vol. 29, no. 23, pp. 34759–34775, 2022.

[92] M. M. Younes, A. S. Abdullah, Z. M. Omara, and F. A. Essa, "Enhancement of discs' solar still performance using thermal energy storage unit and reflectors: An experimental approach," *Alexandria Engineering Journal*, vol. 61, no. 10, pp. 7477–7487, 2022.

[93] Z. Liu, Z. J. Yu, T. Yang, D. Qin, S. Li, G. Zhang, F. Haghighat, and M. M. Joybari, "A review on macro-encapsulated phase change material for building envelope applications," *Building and Environment*, vol. 144, pp. 281–294, 2018.

[94] S. Arunachalam, "Latent Heat Storage: Container Geometry, Enhancement Techniques, and Applications-A Review," *Journal of Solar Energy Engineering, Transactions of the ASME*, vol. 141, no. 5, 2019.

[95] Z. A. Qureshi, H. M. Ali, and S. Khushnood, "Recent advances on thermal conductivity enhancement of phase change materials for energy storage system: A review," *International Journal of Heat and Mass Transfer*, vol. 127, pp. 838–856, 2018.

[96] L. A. Khan and M. M. Khan, "Role of orientation of fins in performance enhancement of a latent thermal energy storage unit," *Applied Thermal Engineering*, vol. 175, no. December 2019, p. 115408, 2020.

[97] L. A. Khan, M. M. Khan, H. F. Ahmed, M. Irfan, D. Brabazon, and I. U. Ahad, "Dominant roles of eccentricity, fin design, and nanoparticles in performance enhancement of latent thermal energy storage unit," *Journal of Energy Storage*, vol. 43, no. August, p. 103181, 2021.

[98] R. Qaiser, M. M. Khan, L. A. Khan, and M. Irfan, "Melting performance enhancement of PCM based thermal energy storage system using multiple tubes and modified shell designs," *Journal of Energy Storage*, vol. 33, no. August 2020, p. 102161, 2021.

[99] P. Ding and Z. Liu, "Numerical investigation of natural convection enhancement in latent heat energy storage units with punched-fin and slit-fin," *International Journal of Thermal Sciences*, vol. 163, p. 106834, 2021.

[100] A. Rahimi, A. Dehghan Saee, A. Kasaeipoor, and E. Hasani Malekshah, "A comprehensive review on natural convection flow and heat transfer: The most practical geometries for engineering applications," *International Journal of Numerical Methods for Heat and Fluid Flow*, vol. 29, no. 3, pp. 834–877, 2019.

[101] F. Agyenim, N. Hewitt, P. Eames, and M. Smyth, "A review of materials , heat transfer and phase change problem formulation for latent heat thermal energy storage systems ( LHTESS )," *Renewable and Sustainable Energy Reviews*, vol. 14, pp. 615–628, 2010.

[102] L. T. Benos, E. G. Karvelas, and I. E. Sarris, "Crucial effect of aggregations in CNT-water nanofluid magnetohydrodynamic natural convection," *Thermal Science and Engineering Progress*, vol. 11, no. February, pp. 263–271, 2019.

[103] K. Venkateshwar, N. Joshy, H. Simha, and S. Mahmud, "Quantifying the nanoparticles concentration in nano-PCM," *Journal of Nanoparticle Research*, vol. 21, no. 12, 2019.

[104] B. Kok and M. Gürtürk, "Determining Effects Of Heat Transfer Fins On The Solidification Process Of Pcm And Nano-Pcm With A Rectangular Cooler," *European Journal of Technique (EJT)*, vol. 9, no. 2, pp. 263 – 274, 2019.

[105] M. Gürtürk and B. Kok, "A new approach in the design of heat transfer fin for melting and solidification of PCM," *International Journal of Heat and Mass Transfer*, vol. 153, p. 119671, 2020.

[106] D. Guerraiche, K. Guerraiche, Z. Driss, A. Chibani, S. Merouani, and C. Bougriou, "Heat Transfer Enhancement in a Receiver Tube of Solar Collector Using Various Materials and Nanofluids," *Engineering, Technology & Applied Science Research*, vol. 12, no. 5, pp. 9282–9294, 2022.

[107] L. L. Tian, X. Liu, S. Chen, and Z. G. Shen, "Effect of fin material on PCM melting in a rectangular enclosure," *Applied Thermal Engineering*, vol. 167, no. November 2019, 2020.

[108] M. M. Kenisarin, K. Mahkamov, S. C. Costa, and I. Makhkamova, "Melting and solidification of PCMs inside a spherical capsule: A critical review," *Journal of Energy Storage*, vol. 27, no. November 2019, p. 101082, 2020.

[109] M. Akgün, O. Aydın, and K. Kaygusuz, "Thermal energy storage performance of paraffin in a novel tube-in-shell system," *Applied Thermal Engineering*, vol. 28, pp. 405–413, apr 2008.

[110] R. Qaiser, M. M. Khan, H. F. Ahmed, F. K. Malik, M. Irfan, and I. U. Ahad, "Performance enhancement of latent energy storage system using effective designs of tubes and shell," *Energy Reports*, vol. 8, no. November, pp. 3856–3872, 2022.

[111] R. Sabir, M. M. Khan, N. A. Sheikh, and I. U. Ahad, "Effect of dimple pitch on thermal-hydraulic performance of tubes enhanced with ellipsoidal and teardrop dimples," *Case Studies in Thermal Engineering*, vol. 31, p. 101835, 2022.

[112] M. J. Hosseini, M. Rahimi, and R. Bahrampoury, "Experimental and computational evolution of a shell and tube heat exchanger as a PCM thermal storage system," *International Communications in Heat and Mass Transfer*, vol. 50, pp. 128–136, 2014.

[113] J. M. Mahdi, S. Lohrasbi, D. D. Ganji, and E. C. Nsofor, "Accelerated melting of PCM in energy storage systems via novel configuration of fins in the triplex-tube heat exchanger," *International Journal of Heat and Mass Transfer*, vol. 124, pp. 663–676, sep 2018.

[114] F. ul Hasnain, M. Irfan, M. M. Khan, L. A. Khan, and H. F. Ahmed, "Melting performance enhancement of a phase change material using branched fins and nanoparticles for energy storage applications," *Journal of Energy Storage*, vol. 38, no. March, p. 102513, 2021.

[115] J. Zhang, Z. Cao, S. Huang, X. Huang, K. Liang, Y. Yang, H. Zhang, M. Tian, M. Akrami, and C. Wen, "Improving the melting performance of

phase change materials using novel fins and nanoparticles in tubular energy storage systems," *Applied Energy*, vol. 322, no. June, p. 119416, 2022.

[116] K. Reddy, "Thermal modeling of pcm-based solar integrated collector storage water heating system," *Transactions of the ASME*, vol. 129, pp. 458–464, 2007.

[117] V. K. Sonker, J. P. Chakraborty, A. Sarkar, and R. K. Singh, "Solar distillation using three different phase change materials stored in a copper cylinder," *Energy Reports*, vol. 5, pp. 1532–1542, 2019.

[118] N. S. Bondareva, N. S. Gibanov, and M. A. Sheremet, "Computational study of heat transfer inside different PCMs enhanced by Al2O3 nanoparticles in a copper heat sink at high heat loads," *Nanomaterials*, vol. 10, no. 2, 2020.

[119] M. Fadl and P. C. Eames, "A comparative study of the effect of varying wall heat flux on melting characteristics of phase change material RT44HC in rectangular test cells," *International Journal of Heat and Mass Transfer*, vol. 141, pp. 731–747, 2019.

[120] N. Soares, A. R. Gaspar, P. Santos, and J. J. Costa, "Experimental study of the heat transfer through a vertical stack of rectangular cavities filled with phase change materials," *Applied Energy*, vol. 142, pp. 192–205, 2015.

[121] V. V. Tyagi and D. Buddhi, "PCM thermal storage in buildings: A state of art," *Renewable and Sustainable Energy Reviews*, vol. 11, no. 6, pp. 1146–1166, 2007.

[122] B. Kamkari and H. Shokouhmand, "Experimental investigation of phase change material melting in rectangular enclosures with horizontal partial fins," *International Journal of Heat and Mass Transfer*, vol. 78, pp. 839–851, 2014.

[123] P. H. Biwole, D. Groulx, F. Souayfane, and T. Chiu, "Influence of fin size and distribution on solid-liquid phase change in a rectangular enclosure," *International Journal of Thermal Sciences*, vol. 124, no. October 2017, pp. 433–446, 2018.

[124] C. Ji, Z. Qin, S. Dubey, F. H. Choo, and F. Duan, "Simulation on PCM melting enhancement with double-fin length arrangements in a rectangular enclosure induced by natural convection," *International Journal of Heat and Mass Transfer*, vol. 127, pp. 255–265, 2018.

[125] A. Abdi, V. Martin, and J. N. Chiu, "Numerical investigation of melting in a cavity with vertically oriented fins," *Applied Energy*, vol. 235, no. July 2018, pp. 1027–1040, 2019.

[126] B. Yazicioğlu and H. Yüncü, "Optimum fin spacing of rectangular fins on a vertical base in free convection heat transfer," *Heat and Mass Transfer/Waerme- und Stoffuebertragung*, vol. 44, no. 1, pp. 11–21, 2007.

[127] T. Bouhal, S. ed Dîn Fertahi, O. Limouri, Y. Agrouaz, T. Kousksou, Y. Zeraouli, and A. Jamil, "Numerical analysis of PCM melting filling a rectangular cavity with horizontal partial fins," *MATEC Web of Conferences*, vol. 307, p. 01011, 2020.

[128] M. E. Nakhchi and J. A. Esfahani, "Improving the melting performance of PCM thermal energy storage with novel stepped fins," *Journal of Energy Storage*, vol. 30, no. November 2019, p. 101424, 2020.

[129] M. S. Mahdi, H. B. Mahood, A. N. Campbell, and A. A. Khadom, "Natural convection improvement of PCM melting in partition latent heat energy storage: Numerical study with experimental validation," *International Communications in Heat and Mass Transfer*, vol. 126, p. 105463, 2021.

[130] L. Kasper, D. Pernsteiner, M. Koller, A. Schirrer, S. Jakubek, and R. Hofmann, "Numerical studies on the influence of natural convection under inclination on optimal aluminium proportions and fin spacings in a rectangular

aluminium finned latent-heat thermal energy storage," *Applied Thermal Engineering*, p. 116448, 2020.

[131] B. Fekadu and M. Assaye, "Enhancement of phase change materials melting performance in a rectangular enclosure under different inclination angle of fins," *Case Studies in Thermal Engineering*, vol. 25, no. April, p. 100968, 2021.

[132] A. Arshad, M. Ibrahim Alabdullatif, M. Jabbal, and Y. Yan, "Towards the thermal management of electronic devices: A parametric investigation of finned heat sink filled with PCM," *International Communications in Heat and Mass Transfer*, vol. 129, no. October, p. 105643, 2021.

[133] N. Sinaga, H. Moria, K. S. Nisar, C. M. Vu, B. Heidarshenas, A. Arsalanloo, and M. M. Youshanlouei, "Melting performance enhancement of thermal storage system by utilizing shape and position of double fin," *Case Studies in Thermal Engineering*, vol. 23, no. October 2020, p. 100813, 2021.

[134] G. Wang, L. Feng, M. Altanji, K. Sharma, K. Sooppy Nisar, and S. Khorasani, "Proposing novel "L" shaped fin to boost the melting performance of a vertical PCM enclosure," *Case Studies in Thermal Engineering*, vol. 28, no. July, p. 101465, 2021.

[135] B. Kamkari, H. Shokouhmand, and F. Bruno, "Experimental investigation of the effect of inclination angle on convection-driven melting of phase change material in a rectangular enclosure," *International Journal of Heat and Mass Transfer*, vol. 72, pp. 186–200, 2014.

[136] B. Kamkari and D. Groulx, "Experimental investigation of melting behaviour of phase change material in finned rectangular enclosures under different inclination angles," *Experimental Thermal and Fluid Science*, vol. 97, pp. 94–108, 2018.

[137] T. Sathe and A. S. Dhoble, "Experimental investigations of phase change material filled rectangular enclosure with inclined top and side heating mode," *Journal of Energy Storage*, vol. 32, no. August, p. 101799, 2020.

[138] J. Duan, Y. Xiong, and D. Yang, "On the melting process of the phase change material in horizontal rectangular enclosures," *Energies*, vol. 12, no. 16, 2019.

[139] A. Laouer, K. Al-Farhany, M. F. Al-Dawody, and A. L. Hashem, "A numerical study of phase change material melting enhancement in a horizontal rectangular enclosure with vertical triple fins," *International Communications in Heat and Mass Transfer*, vol. 137, p. 106223, 2022.

[140] V. Safari, B. Kamkari, K. Hooman, and J. M. Khodadadi, "Sensitivity analysis of design parameters for melting process of lauric acid in the vertically and horizontally oriented rectangular thermal storage units," *Energy*, vol. 255, p. 124521, 2022.

[141] M. Barthwal and D. Rakshit, "No fins attached? Numerical analysis of internal–external fins coupled PCM melting for solar applications," *Applied Thermal Engineering*, vol. 215, no. November 2021, p. 118911, 2022.

[142] Y. Xu, H. Yin, C. He, Y. Wei, M. Cui, and Z. J. Zheng, "Structure Optimization of Longitudinal Rectangular Fins to Improve the Melting Performance of Phase Change Materials through Genetic Algorithm," *Energies*, vol. 15, no. 24, 2022.

[143] H. Zhang, "12 - heat-insulating materials and sound-absorbing materials," in *Building Materials in Civil Engineering* (H. Zhang, ed.), Woodhead Publishing Series in Civil and Structural Engineering, pp. 304–423, Woodhead Publishing, 2011.

[144] Y. Li and S. Ren, "16 - acoustic and thermal insulating materials," in *Building Decorative Materials* (Y. Li and S. Ren, eds.), Woodhead Publishing Series in Civil and Structural Engineering, pp. 359–374, Woodhead Publishing, 2011.

[145] S. J. Kline, "Describing uncertainties in single-sample experiments," *Mechanical Engineering*, vol. 75, pp. 3–8, 1953.

[146] M. S. Shafiq, M. M. Khan, and M. Irfan, "Performance enhancement of double-wall-heated rectangular latent thermal energy storage unit through effective design of fins," *Case Studies in Thermal Engineering*, vol. 27, no. May, p. 101339, 2021.

[147] V. Voller and C. Prakash, "A fixed grid numerical modelling methodology for convection-diffusion mushy region phase-change problems," *International Journal of Heat and Mass Transfer*, vol. 30, no. 8, pp. 1709–1719, 1987.

[148] J. Vogel and A. Thess, "Validation of a numerical model with a benchmark experiment for melting governed by natural convection in latent thermal energy storage," *Applied Thermal Engineering*, vol. 148, pp. 147–159, 2019.

[149] A. Brent, V. R. Voller, and K. Reid, "Enthalpy-porosity technique for modeling convection-diffusion phase change: application to the melting of a pure metal," *Numerical Heat Transfer, Part A Applications*, vol. 13, no. 3, pp. 297–318, 1988.

[150] M. Kumar and D. J. Krishna, "Influence of Mushy Zone Constant on Thermohydraulics of a PCM," *Energy Procedia*, vol. 109, no. November 2016, pp. 314–321, 2017.

[151] V. Safari, H. Abolghasemi, L. Darvishvand, and B. Kamkari, "Thermal performance investigation of concentric and eccentric shell and tube heat exchangers with different fin configurations containing phase change material," *Journal of Energy Storage*, vol. 37, no. December 2020, p. 102458, 2021.

[152] Y. Zhou, S. Zheng, and G. Zhang, "A review on cooling performance enhancement for phase change materials integrated systems—flexible design and smart control with machine learning applications," *Building and Environment*, vol. 174, no. March, p. 106786, 2020.

[153] F. Keramat, A. Azari, H. Rahideh, and M. Abbasi, "A CFD parametric analysis of natural convection in an H-shaped cavity with two-sided inclined porous fins," *Journal of the Taiwan Institute of Chemical Engineers*, vol. 114, pp. 142–152, 2020.

[154] S. S. Ajarostaghi, S. Poncet, M. A. Delavar, and K. Sedighi, "Numerical simulation of the melting process in a shell and coil tube ice storage system for air-conditioning application," *Refrigeration Science and Technology*, vol. 2018-May, pp. 157–165, 2018.

[155] S. Yao and X. Huang, "Study on solidification performance of PCM by longitudinal triangular fins in a triplex-tube thermal energy storage system," *Energy*, vol. 227, p. 120527, 2021.

[156] H. Faraji, M. El Alami, and A. Arshad, "Investigating the effect of single and hybrid nanoparticles on melting of phase change material in a rectangular enclosure with finite heat source," *International Journal of Energy Research*, vol. 45, no. 3, pp. 4314–4330, 2021.

[157] A. Kaushal, R. Alexander, P. T. Rao, J. Prakash, and K. Dasgupta, "Artificial neural network, Pareto optimization, and Taguchi analysis for the synthesis of single-walled carbon nanotubes," *Carbon Trends*, vol. 2, p. 100016, 2021.

[158] S. Ajith Arul Daniel, R. Pugazhenthi, R. Kumar, and S. Vijayananth, "Multi objective prediction and optimization of control parameters in the milling of aluminium hybrid metal matrix composites using ANN and Taguchi -grey relational analysis," *Defence Technology*, vol. 15, no. 4, pp. 545–556, 2019.

[159] T. Dagdevir, "Multi-objective optimization of geometrical parameters of dimples on a dimpled heat exchanger tube by Taguchi based Grey relation analysis and response surface method," *International Journal of Thermal Sciences*, vol. 173, no. November, p. 107365, 2022.

[160] I. Kotcioglu, A. Cansiz, and M. Nasiri Khalaji, "Experimental investigation for optimization of design parameters in a rectangular duct with plate-fins heat exchanger by Taguchi method," *Applied Thermal Engineering*, vol. 50, no. 1, pp. 604–613, 2013.

[161] S. L. Brunton, B. R. Noack, and P. Koumoutsakos, "Machine Learning for Fluid Mechanics," *Annual Review of Fluid Mechanics*, vol. 52, pp. 477–508, 2020.

[162] S. Ray, "A Quick Review of Machine Learning Algorithms," *Proceedings of the International Conference on Machine Learning, Big Data, Cloud and Parallel Computing: Trends, Prespectives and Prospects, COMITCon 2019*, pp. 35–39, 2019.

[163] D. K. Bhamare, P. Saikia, M. K. Rathod, and D. Rakshit, "A machine learning and deep learning based approach to predict the thermal performance of phase change material integrated building envelope," *Building and Environment*, vol. 199, no. April, p. 107927, 2021.

[164] R. Baby and C. Balaji, "A neural network-based optimization of thermal performance of phase change material-based finned heat sinks-an experimental study," *Experimental Heat Transfer*, vol. 26, no. 5, pp. 431–452, 2013.

[165] S. Motahar and M. Jahangiri, "Transient heat transfer analysis of a phase change material heat sink using experimental data and artificial neural network," *Applied Thermal Engineering*, vol. 167, p. 114817, 2020.

[166] F. Pedregosa, G. Varoquaux, A. Gramfort, V. Michel, B. Thirion, O. Grisel, M. Blondel, P. Prettenhofer, R. Weiss, V. Dubourg, J. Vanderplas, A. Passos, D. Cournapeau, M. Brucher, M. Perrot, and E. Duchesnay, "Scikit-learn: Machine learning in Python," *Journal of Machine Learning Research*, vol. 12, pp. 2825–2830, 2011.

[167] MathWorks, "Regression: Linear, generalized linear, nonlinear, and nonparametric techniques for supervised learning." Available at: https://www.mathworks.com/help/stats/regression-and-anova.html?s_tid=CRUX_lftnav. (Accessed: 7 Mar 2022).

[168] G. Bonaccorso, *Machine Learning Algorithms*. Packt Publishing, 2017.

[169] D. Maulud and A. M. Abdulazeez, "A Review on Linear Regression Comprehensive in Machine Learning," *Journal of Applied Science and Technology Trends*, vol. 1, no. 4, pp. 140–147, 2020.

[170] J. Elith, J. R. Leathwick, and T. Hastie, "A working guide to boosted regression trees," *Journal of Animal Ecology*, vol. 77, no. 4, pp. 802–813, 2008.

[171] S. Muthukrishnan, H. Krishnaswamy, S. Thanikodi, D. Sundaresan, and V. Venkatraman, "Support vector machine for modelling and simulation of heat exchangers," *Thermal Science*, vol. 24, no. 1PartB, pp. 499–503, 2020.

[172] F. Schiltz, C. Masci, T. Agasisti, and D. Horn, "Using regression tree ensembles to model interaction effects: a graphical approach," *Applied Economics*, vol. 50, no. 58, pp. 6341–6354, 2018.

[173] E. Schulz, M. Speekenbrink, and A. Krause, "A tutorial on Gaussian process regression: Modelling, exploring, and exploiting functions," *Journal of Mathematical Psychology*, vol. 85, pp. 1–16, 2018.

[174] C. E. Rasmussen, "Gaussian Processes in machine learning," *Lecture Notes in Computer Science (including subseries Lecture Notes in Artificial Intelligence and Lecture Notes in Bioinformatics)*, vol. 3176, pp. 63–71, 2004.

[175] R. B. Gramacy, *Surrogates: Gaussian Process Modeling, Design and Optimization for the Applied Sciences*. Boca Raton, Florida: Chapman Hall/CRC, 2020.

# Appendix A

# Code Scripts used for Image Processing

## A.1 Contour Mirroring

The following MATLAB code processes liquid fraction and temperature contour images. It combines each frame of liquid fraction and temperature into a single image with one half showing liquid fraction and solid-liquid interface, while the second half showing temperature distribution.

```
%%%%%%%%%%%%%%%%%%%%%%%%%%%%,
%   The following routine mirrors the image frames
%   left half is LF and right half is temp
%%%%%%%%%%%%%%%%%%%%%%%%%%%%
%% Initialize
clear

%% Define images

%home = "G:\My Drive\Edu\PHD\thesis-cust\ME\Chapters\chapter7\images\snaps\";
cropList = struct('exp1',[308,27,142,564],...
'exp2',[223,27,282,564],...
'exp3',[228,25,323,516],...
'exp4',[191,25,388,516],...
'exp5',[308,27,142,564],...
'exp6',[223,27,282,564],...
```

```
'exp7',[228,25,323,516],...
'exp8',[191,25,388,516],...
'exp9',[345,25,130,516],...
'exp10',[266,25,259,516],...
'exp11',[228,25,323,516],...
'exp12',[191,25,388,516],...
'exp13',[345,25,130,516],...
'exp14',[223,27,282,564],...
'exp15',[181,27,353,564],...
'exp16',[191,25,388,516],...
'ref',[130,32,314,502],...
'def',[130,42,313,501],...
'mint',[345,25,130,516]);

base = "refdef";
ptrn_lf = base+"\"+"ref-L-*.png";
%crop = patterns{config,4};

% get file list
imlist_lf = dir(ptrn_lf);
count = size(imlist_lf,1);

for i = 1:count
imgname = imlist_lf(i).name;
fprintf('Processing %s...\n', imgname);

idx = extractBefore(imgname, "-");
image_lf = strcat(imlist_lf(i).folder,"\",imlist_lf(i).name);
image_tmp = strcat(imlist_lf(i).folder,"\",strrep(imlist_lf(i).name, "-L-", "-T-"));
%image_vel = strcat(imlist_lf(i).folder,"\",strrep(imlist_lf(i).name, "-L-", "-V-"));
im_lf = imread(image_lf);
im_tmp = imread(image_tmp);
%im_vel = imread(image_vel);

crop = cropList.(idx);
%im_lf = flip(imcrop(im_lf, crop), 2);
im_lf = imcrop(im_lf, crop);
%im_tmp = imcrop(im_tmp, crop);
im_tmp = flip(imcrop(im_tmp, crop), 2);
%im_vel = imcrop(im_vel, crop);

imsize = size(im_tmp);
width = imsize(2);
height = imsize(1);

%im_out = imtile({im_lf, im_tmp});
im_out = cat(2, im_lf, im_tmp);
%im_out = cat(2, im_lf, im_tmp, im_vel);
```

```
im_out = insertShape(im_out, 'rectangle', [2 1 width-1 height-2; width+1 1 width-2 height-2],'Li
%im_out = imresize(im_out, [240 320]);

[p, f, x] = fileparts(image_lf);
%f = replace(f, "scene", "scn");
imwrite(im_out, fullfile(".\", strrep(f, "-L-", "-X-")+x), 'jpg');
imshow(im_out);
%break;
end

fprintf('Ready.\n');
```

## A.2 Clipping and Gray scale Image Processing

The photographs taken during the PCM melting experiments in the LHTES were processed using a MATLAB script for identifying solid and liquid fractions. The script cropped the images remove extra view and focus on the LHTES device. Then the images were converted to gray scale and then black and white for easier identification of solid and liquid phase-fractions.

```
%%%%%%%%%%%%%%%%%%%%%%%%%%%
%   The following routine converts the images to
%   grayscale and then binarize.
%   The ratio of black and white pixels is also evaluated.
%
%%%%%%%%%%%%%%%%%%%%%%%%%%%
%% Initialize
clear

%% Define images

source = "D:\Google Drive\Edu\PHD\Experimental Work\First\Cropped\clipped";
dest = "D:\Google Drive\Edu\PHD\Experimental Work\First\Cropped\clipped";
images = [
"scn130710c.JPG" "scn133100c.JPG"  "scn133847c.JPG" "scn135020c.JPG"...
"scn135959c.JPG" "scn141033c.JPG" "scn142019c.JPG" "scn142731c.JPG"
];

imarea = 2000*855;
finarea = 6*740*40;
pcmarea = imarea-finarea;
count = size(images,2);
```

```
        s.wh = zeros(count, 1);
        s.bk = zeros(count, 1);
        s.lf = zeros(count, 1);
        s.total= zeros(count, 1);

        for i = 1:count
        imgname = images(i);
        image1 = source+imgname;
        display('Processing '+imgname+' ...');
        im1 = imread(image1);
        res = improcess(im1, true);

        s.wh(i) = sum(res.bw(:));
        s.bk(i) = sum(~res.bw(:));
        s.total(i) = s.wh(i) + s.bk(i);
        s.lf(i) = s.bk(i) / pcmarea;

        [p, f, x] = fileparts(image1);
        imwrite(res.bw, fullfile(dest,f + "_bw"+x), 'jpg');
        imwrite(res.imgray, fullfile(dest,f + "_gs"+x), 'jpg');
end
```

## A.3 Prediction Using ML Model

The Gaussian Process Regression model was trained by Matlab. The trained model was then saved as MATLAB function, ***ml_expgprc.mat***, and was used to make prediction by the following script.

```
clear

% Gaussian Process Regression
% Exponential GPR
%

load('ml_expgprc.mat')

% prediction
T = table([20 20 20 20 20]', ...
[0.5 1.25 1.25 0.5 0.5]', ...
[1.25 2 1.25 1.5 1.2]', ...
[1.0 1.0 1.0 1.0 1.0]', ...
'VariableNames', {'fd','ar','ft','lf'});
```

```
yt = [
2756.25
5900.00
5037.50
2868.75
2787.5
];

yfit = ml_expgprc.predictFcn(T)
```

## A.4 Training Data for Machine Learning

All the data recorded during simulations of Taguchi DoE cases is combined into a single large file containing features and results using the following python script.

```
# -*- coding: utf-8 -*-
"""
Created on Sat Dec 11 17:04:00 2021

@author: SShafiq
"""

import glob
import pandas as pd

path = ''
#'D:/My Drive/Edu/PHD/taguchi/v1.2/data/'
files_lf = glob.glob(path + '*-lf-rfile.out', recursive=False)

result = pd.DataFrame(columns=[75,80,85,90,95,100])
i = 0
for f in files_lf:
df = pd.read_csv(f,
header=3,
sep=' ',
names=['step', 'lf', 'time'])

ef = f.replace('-lf-', '-energy-')
en = pd.read_csv(ef,
header=3,
sep=' ',
names=['step', 'energy', 'time'])

ra = []
```

```
for r in range(75, 105, 5):
flt = r/100
sb = df[(df['lf'] >= flt) & (df['lf'] < flt+0.01)]
idx = sb.iloc[0]['time']
es = en[en['time']==idx]['energy']
ra.append(es.iloc[0])

print(ra)
t = pd.DataFrame([ra], columns=[75,80,85,90,95,100])
result = pd.concat([result, t], ignore_index=True)

print(result)

#sys.exit()
```

# Appendix B

# Gaussian Process Regression Model

Gaussian process regression (GPR) models [174, 175] are nonparametric kernel-based probabilistic models. Consider the training set $(x_i, y_i); i = 1, 2, \cdots, n$, where $x_i \in \mathbb{R}^d$ and $y_i \in \mathbb{R}$, drawn from an unknown distribution. A GPR model addresses the question of predicting the value of a response variable $y_{new}$ given the new input vector $x_{new}$, and the training data. A linear regression model is of the form

$$y = x^T \beta + \epsilon,$$

where $\epsilon \sim N(0, \sigma^2)$. The error variance $\sigma^2$ and the coefficients $\beta$ are estimated from the data. A GPR model explains the response by introducing latent variables, $f(x_i), i = 1, 2, \cdots, n$, from a Gaussian process (GP), and explicit basis functions, $h$. The covariance function of the latent variables captures the smoothness of the response and basis functions project the inputs $x$ into a p-dimensional feature space.

A GP is a set of random variables, such that any finite number of them have a joint Gaussian distribution. If $f(x), x \in \mathbb{R}^d$ is a GP, then given $n$ observations $x_1, x_2, \cdots, x_n$, the joint distribution of the random variables $f(x_1), f(x_2), \cdots, f(x_n)$ is Gaussian. A GP is defined by its mean function $m(x)$ and covariance function,

$k(x, x')$. That is, if $f(x), x \in \mathbb{R}^d$ is a Gaussian process, then $E(f(x)) = m(x)$ and $Cov[f(x), f(x')] = E[f(x) - m(x)f(x') - m(x')] = k(x, x')$.

Now consider the following model.

$h(x)^T\beta + f(x)$,

where $f(x) \sim GP(0, k(x, x'))$, that is $f(x)$ are from a zero mean GP with covariance function, $k(x, x').h(x)$ are a set of basis functions that transform the original feature vector $x \in \mathbb{R}^d$ into a new feature vector $h(x)$ in $\mathbb{R}^p$. $\beta$ is a $p$-by-1 vector of basis function coefficients. This model represents a GPR model. An instance of response $y$ can be modeled as

$P(y_i|f(x_i), x_i) \sim N(y_i|h(x_i)^T\beta + f(x_i), \sigma^2)$

Hence, a GPR model is a probabilistic model. There is a latent variable $f(x_i)$ introduced for each observation $x_i$, which makes the GPR model nonparametric. In vector form, this model is equivalent to

$P(y|f, X) \sim N(y|H\beta + f, \sigma^2 I)$,

where

$$X = \begin{Bmatrix} x_1^T \\ x_2^T \\ \vdots \\ x_n^T \end{Bmatrix}, y = \begin{Bmatrix} y_1 \\ y_2 \\ \vdots \\ y_n \end{Bmatrix}, H = \begin{Bmatrix} h(x_1^T) \\ h(x_2^T) \\ \vdots \\ h(x_n^T) \end{Bmatrix}, f = \begin{Bmatrix} f_(x_1) \\ f_(x_2) \\ \vdots \\ f_(x_n) \end{Bmatrix}$$

The joint distribution of latent variables $f(x_1), f(x_2), \cdots, f(x_n)$ in the GPR model is as follows:

$P(f|X) \sim N(f|0, K(X, X))$,

close to a linear regression model, where $K(X, X)$ looks as follows:

$$K(X, X) = \begin{bmatrix} k(x_1, x_1) & k(x_1, x_2) & \cdots & k(x_1, x_n) \\ k(x_1, x_1) & k(x_1, x_2) & \cdots & k(x_1, x_n) \\ \vdots & \vdots & \vdots & \vdots \\ k(x_1, x_1) & k(x_1, x_2) & \cdots & k(x_1, x_n) \end{bmatrix}$$

The covariance function $k(x, x')$ is usually parameterized by a set of kernel parameters or hyperparameters, $\theta$. Often $k(x, x')$ is written as $k(x, x'|\theta)$ to explicitly indicate the dependence on $\theta$.